UNIVERSIDAD DE CANTABRIA

PROGRAMA DE DOCTORADO EN BIOLOGÍA MOLECULAR Y BIOMEDICINA

TESIS DOCTORAL

CARACTERIZACIÓN DE RETRIEVER-SNX17, UN COMPLEJO MULTIPROTEICO IMPLICADO EN EL RECICLAJE ENDOSOMAL DE CARGOS

PhD THESIS

CHARACTERIZATION OF RETRIEVER-SNX17, A MULTIPROTEIN COMPLEX FOR ENDOSOMAL CARGO RECYCLING

Aurora Martín González

Instituto de Biomedicina y Biotecnología de Cantabria (IBBTEC)

Supervisora: María Jesús Lucas Gay

Santander, 2024

Agradecimientos

Esta tesis ha sido posible gracias a todas esas personas que me han acompañado durante toda mi estancia en el IBBTEC, tanto dentro como fuera del centro.

Agradezco a todas y cada una de las personas con las que he convivido en el IBBTEC durante estos años. Desde el primer grupo que me acogió lleno de gente estupenda (Yelina, Fer, Laura Giner, Esther, Lorena, Candela, Judit, Carol, Jorge Grande, Óscar...). Una pena que sus etapas en el centro acabaran al poco de yo empezar.

También agradezco a la gente de mi laboratorio: Eva (¡¡¡cómo te he echado y echo de menos!!!), Sara, Iván y Arturo. Arturo, queda pendiente enseñarnos más música de la *wena*. Iván, gracias por todo el apoyo y la ayuda que me has dado siempre que la he necesitado, ¡ánimo que tú eres el siguiente! Y, por supuesto, a mi directora de tesis, María Lucas, por haberme dado esta oportunidad de realizar un doctorado, en un tema además tan interesante para mí, y por todo lo que me ha enseñado.

También a los grupos de laboratorios con los que he compartido tiempo y espacio, que siempre te enseñan nuevas cosas y se hace más divertido; el laboratorio de Gabi, de Fernando Calvo, de Alberto Sánchez y Magda, de Ana Villar, y de Mapi. Anavi, muchas gracias por tus consejos. Y gracias a Víctor Campa por el apoyo técnico con el microscopio de fluorescencia. Y para ayuda la que me ha dado María Subijana, sobre todo con todo el papeleo para el depósito de la tesis, evitar pasarme los plazos gracias a ti fue todo un detalle... Jeje

Gracias también a la gente del CIC Biogune de Bilbao y del Instituto de Biofisika (UPV/EHU), que cada vez que fuimos nos hicieron sentir tan cómodos. Sobre todo, gracias a Diego Charro, Issac Santos, Adriana Rojas e Idoia Iturrioz por la ayuda con la crio-ME, a Elsa por la ayuda con la colecta de los datos y a David Albesa por la ayuda con la cristalización.

Gracias también a mi profesor de biología Carlos del instituto, porque sin él nunca habría acabado aquí.

Agradezco al grupo ya ancianito al que tanto cariño tengo, con Alex, María, Thais, Carlos, Sofía, Víctor y Alfonso. Por todos los buenos momentos y los que quedan. ¿Al final Thais se fue se fue, o se quedó?

Y vaya convivencia en La Moraleda, ¡bendita casa! Y todavía mejora cuando convives con la Lidi: cocinera / organizadora de eventos / cómica y vividora como ella sola. ¿Te aburres? ¡Imposible! En esta casa se juega a videojuegos y se ven series con Alfonsito, y se canta y baila con la DJ (y doctora) Zdral. O te hacen un análisis de grasa corporal al completo, o haces tiro con arco en la cocina, lo que tú prefieras.

Además, mi última etapa ha sido acompañada de un grupo extraordinario, lleno de energía y siempre SIEMPRE con ganas de hacer mil planes, y te contagian las ganas, la verdad: Pablo, Lolu, Andrea, David, Dani, Mariadel, Irene, Arancha, Antonio, Marina, Luisa, Carlos... mil gracias. Me he ganado un buen manteo, ¿no?

Y es que esta etapa en Cantabria ha sido estupenda, esta ciudad tiene un potencial increíble y mil opciones diferentes:
Pablo, ¿para cuándo otro safari nocturno?
Ivancito, ¿subimos al Urriellu? (aunque esté en Asturias)
Helenilla, cogeremos entradas para el próximo concierto de Robe, ¿no?
Thais y Carlitos, ¿unas olitas?
Subi, ¿partidito de tenis?

Thais y María, porque simplemente sois las mejores, no puedo decir mucho más. GRACIAS.

También agradezco a mis amigos de la montaña, porque es gente muy guay y me han alegrado cada fin de semana: Kike, Jose Alberto, Poo, Víctor Vélez, Reini, Greta, Zeta, Micro, el Abu, Jorrín, Sonia, Jorge, Marta, Ibone, Sergio, Aída, Copper, Carla... Y al trepa, al Quality y al Indian.

Y a mis amigos de Madrid: Laura, Elena, Dani, Perales y Zayas, os echo mucho de menos.
Y, por supuesto, a mi grupo de las 8 islas: Adri, Roman, Carl, Rebe!!!! Febrero is coming! Y encima el grupo va a aumentar!!!

Y, evidentemente, doy las gracias a Iván, por cuánto y cómo me quiere, y por la actitud optimista que nunca pierde. Y a su ratón del ordenador, que también me ha ayudado tela. Ivansito, próximo viaje a Yosemite, ¿no?

Y a mí familia, a mis primos y a mis primas. A mí tía Pili y a mi tía Ana Mari, por darme jamón serrano (y cariño). A mi padre y a mi madre, por su paciencia (cercana a infinita) y su apoyo. Y a mi hermano, que, aunque no haga caso a sus consejos (algo me comentó sobre no hacer una tesis), siempre me intenta ayudar con todo. Y sus dibujos molan mogollón.

Y a Nessy y a Goku, que sois muy majos.

Resumen

La abundancia y distribución de las proteínas integrales de membrana en la superficie celular regulan un amplio rango de funciones celulares, como la señalización, adhesión, migración y el transporte de nutrientes, todas ellas esenciales para mantener la homeostasis e integridad celular. Las proteínas integrales de membrana, conocidas como cargos, son internalizadas por endocitosis y posteriormente dirigidas a los lisosomas para su degradación, o bien son recicladas de nuevo a la membrana plasmática o la red trans del Golgi. Las alteraciones en este proceso de reciclaje se han relacionado con enfermedades neurodegenerativas como el Alzheimer y el Parkinson. Además, proteínas efectoras virales, como la proteína L2 del virus del papiloma humano (VPH), explotan estas vías de reciclaje para su transporte intracelular durante la infección.

En esta tesis, hemos investigado una vía de reciclaje endosomal que depende del complejo multiproteico Retriever, junto con *sorting nexin* 17 (SNX17) y otros complejos proteicos adicionales. Se sabe que la proteína adaptadora de cargo SNX17 está implicada en la ruta de reciclaje de Retriever; sin embargo, su mecanismo molecular y su función siguen poco definidos.

Esta tesis describe una serie de estudios bioquímicos, biofísicos y de mutagénesis dirigida mediante modelos estructurales con el objetivo de elucidar las interacciones entre SNX17, Retriever y diversos cargos. Hemos examinado la unión de cargos como LRP1 (*low-density lipoprotein receptor-related protein L1*), ITGB1 (*β1-integrin*) y APP (*amyloid precursor protein*), además de la proteína L2 del VPH, a SNX17. Nuestros resultados muestran que la proteína viral puede competir con los cargos fisiológicas debido a su mayor afinidad de unión. Además, hemos demostrado que existe una interacción directa entre SNX17 y Retriever en solución, específicamente entre la región C-terminal de SNX17 y la interfaz de las subunidades de Retriever VPS35L y VPS26C. Esta interacción se ve aumentada cuando SNX17 se une al cargo, debido a la interrupción de una interacción autoinhibitoria intramolecular entre la región C-terminal de SNX17 y su bolsillo de unión del cargo. Asimismo, utilizando vesículas gigantes unilamelares y liposomas, hemos observado que SNX17 se une a membranas que contienen fosfatidilinositol-3-fosfato (PI3P), lo cual promueve el reclutamiento del complejo Retriever. Nuestros hallazgos respaldan un mecanismo de autoinhibición hasta ahora no identificado en SNX17 que mantiene el sistema de reciclaje en un estado “apagado”, que puede cambiar a un estado “encendido” por medio de dos mecanismos diferentes: mediante la unión selectiva con un cargo o mediante asociaciones específicas con membranas que contienen PI3P. Proponemos que este mecanismo regulador permite asegurar un control espaciotemporal de la vía de reciclaje de Retriever, evitando el ensamblaje prematuro de toda la maquinaria de reciclaje cuando SNX17 se encuentra en el citoplasma o asociado débilmente con membranas inespecíficas.

Abstract

The abundance and distribution of integral membrane proteins on the cell surface regulate a wide range of cellular functions, including cell signaling, adhesion, migration, and nutrient transport, all of which are essential for maintaining cellular homeostasis and integrity. Integral membrane proteins, known as cargos, are internalized through endocytosis, and subsequently directed either to lysosomes for degradation or recycled back to the plasma membrane or the trans-Golgi network. Disruptions in this recycling process have been linked to neurodegenerative diseases such as Alzheimer's and Parkinson's. Additionally, viral effector proteins, such as the L2 protein from human papillomavirus (HPV), exploit these recycling pathways for intracellular transport during infection.

In this thesis, we have investigated the endosomal recycling pathway which relies on the multiprotein complex Retriever, alongside sorting nexin 17 (SNX17) and additional protein complexes. While it was previously established that SNX17 is implicated in the Retriever recycling pathway, the molecular mechanisms underlying their interaction and function remained unclear.

This thesis presents a range of biochemical, biophysical and structural model-guided mutagenesis studies aimed to elucidating the interactions between SNX17, Retriever, and various cargos. We have examined the binding of cargos, such as low-density lipoprotein receptor-related protein L1 (LRP1), β1-integrin (ITGB1), and amyloid precursor protein (APP), and the HPV L2 protein, to SNX17. Our findings reveal that the viral protein outcompetes physiological cargos due to its higher binding affinity. Furthermore, we have demonstrated a direct interaction between SNX17 and Retriever in solution, specifically between the C-terminal region of SNX17 and the interface of the Retriever subunits VPS35L and VPS26C. This interaction is enhanced upon SNX17 binding to its cargo, due to the disruption of an intramolecular autoinhibitory interaction between the C-terminal region of SNX17 and its cargo-binding pocket. Moreover, using giant unilamellar vesicles and liposomes, we discovered that SNX17 binds to membranes containing phosphatidylinositol-3-phosphate (PI3P), which promotes the recruitment of the Retriever complex. Our findings support a previously unidentified autoinhibition mechanism in SNX17 that holds the recycling system in an "off" state, which can be switched to an "on" state by two different mechanisms: either through selective engagement with a cargo protein or specific association with PI3P-containing membranes. We propose that this regulatory mechanism ensures proper spatiotemporal control of the Retriever recycling pathway, preventing the premature assembly of the recycling machinery when SNX17 is in the cytoplasm or loosely associated with nonspecific membranes.

Table of contents

Abbreviations

Ɛ: Extinction coefficient

AF: AlphaFold

APP: Amyloid Precursor Protein

APS: Ammonium PerSulfate

ArPIKfyve: Associated Regulator of PIKfyve

BAR: Bin/Amphiphysin/Rvs

C16orf62: Chromosome 16 open reading frame 62

CCC: CCDC22, CCDC93, and ten COMMD

CCDC: Coiled-Coil Domain-Containing

CD: Circular Dichroism

CME: Clathrin-Mediated Endocytosis

COMMD: COpper-Metabolism Murr1 Domain

Cryo-EM: Cryo-Electron Microscopy

CT: C-Terminal

DENN: Differentially Expressed in Normal and Neoplastic cells

DOPC: 1,2-DiOleoyl-sn-glycerol-3-PhosphoCholine

DOPE: 1,2-DiOleoyl-sn-glycerol-3-PhosphoEthanol-amine

DOPS: 1,2-DiOleoyl-sn-glycerol-3-Phospho-l-Serine

DSCR: Down Syndrome Critical Region

ECM: ExtraCellular Matrix

ED: Extracellular Domain

EEA1: Early Endosomal Antigen 1

ER: Endoplasmic Reticulum

ESCPE-1: Endosomal SNX-BAR Sorting Complex for Promoting Exit 1'

ESCRT: Endosomal Sorting Complex Required for Transport

FAM: N-terminal 5-carboxyfluorescein

FBR: FERM-Binding Region

FBS: Fetal Bovine Serum

FYVE finger: Fab1p, YOTB, Vac1p and EEA1

FERM: Four-point-one/Ezrin/Radixin/Moesin

GA: Golgi Apparatus

GAP: GTPase-Activating Protein

GEF: Guanine nucleotide Exchange Factor

GFP: Green Fluorescent Protein

GLUT1: Glucose Transporter type 1

GST: Glutathione S-Transferase

GUV: Giant Unilamellar Vesicle

HEAT: Huntington/Elongation factor 3/Protein phosphatase 2A/TOR1

HPV: Human PapillomaVirus

HRV 3C: Human RhinoVirus 3C

ICD: IntraCellular Domain

ILV: IntraLuminal Vesicle

IPTG: IsoPropyl-ß-D-ThioGalactopyranoside

ITG: Integrin

KDELR: KDEL Receptors

LB medium: Luria Broth medium

LB-SDS: SDS Loading Buffer

LDLR: Low-Density Lipoprotein Receptor

LE: Late Endosome

LRP: Low-density Lipoprotein Receptor-related Protein

LUV: Large Unilamellar Vesicle

MBP: Maltose Binding Protein

MCS: Membrane Contact Site

MET: Mesenchymal-Epithelial Transition

MLV: Multilamellar Lipid Vesicle

MS: Mass Spectrometry

MTMR2: Myotubularin-Related protein-2

MW: Molecular Weight

MWCO: Molecular Weight CutOff

NB: No Binding

NN-CH: NDC80 and NUF2 Calponin Homology

ORF: Open Reading Frame

PAE: Predicted Aligned Error

PCR: Polymerase Chain Reaction

PDLIM: PDZ and LIM domain-containing

PDZ: PSD-95/Discs-large/ZO-1

PDZbm: PDZ-binding motifs

pI: Isoelectric Point

PIs: PhosphoInositides

PI3P: PhosphatidylInositol 3-Phosphate

PI(3,5)P2: PhosphatidylInositol 3,5-bisPhosphate

PI5P: PhosphatidylInositol 5-Phosphate

PIKfyve: PhosphoInositide Iinase, FYVE-type Zinc Finger containing

PIP: PhosphatidylInositol Phosphate

pLDDT: Predicted Local Distance Difference Test

PMSF: PhenylMethylSulphonyl Fluoride

PX: Phox-homology

qPCR: real-time PCR

SD: Standard Deviation

SDS-PAGE: Sodium Dodecyl-Sulfate PolyAcrilamide Gel Electrophoresis

SEC-SAXS: Size-Exclusion Chromatography coupled with Small-Angle X-ray Scattering

Senp2: Sentrin-specific protease 2

SNX: Sorting NeXin

SWIP: Strumpellin and WASH Interacting Protein

TEMED: N,N,N′,N′-TEtraMethylEthyleneDiamine

TEV: Tobacco Etch Virus

TGN: Trans-Golgi Network

TM: Transmembrane Domain

Tm: Melting Temperature

TrxA: Thioredoxin

VEGFR1: Vascular Endothelial Growth Factor Receptor 1

VPS: Vacuolar Protein Sorting

WASH: Wiskott–Aldrich syndrome protein and SCAR Homologue

WASP: Wiscott-Aldrich Syndrome Protein

Wls: Wntless

WT: Wild-Type

XLID: X-Linked Intellectual Disability

YFP: Yellow Fluorescent Protein

Chapter 1: INTRODUCTION

1.1. Intracellular trafficking

The emergence of **compartmentalization** through membranes represents a pivotal development in the evolution of eukaryotic cells. This structural innovation that arose around two billion years ago facilitated the segregation of cellular processes into distinct microenvironments, enhancing the efficiency and regulation of metabolic pathways and biochemical reactions. Unlike prokaryotes, eukaryotic cells possess a complex system of membrane-bound organelles, including the nucleus, endoplasmic reticulum (ER), Golgi apparatus (GA), mitochondria, and lysosomes, each with specialized functions that contribute to cellular homeostasis and adaptability (Gabaldón & Pittis, 2015).

The origin of these membrane-bound compartments is intimately tied to the endosymbiotic theory and membrane invagination processes. The biologist Mereschowsky in 1910 was one of the first to propose the symbiotic origin of certain organelles found in eukaryotic cells (Kowallik & Martin, 2021). Through endosymbiosis, ancestral prokaryotic cells were integrated into a host cell, leading to the formation of mitochondria and chloroplasts, organelles that possess their own genetic material and double membranes, indicative of their evolutionary origins. Simultaneously, the internal membrane system, including the nuclear envelope and ER, likely arose from the invagination of the plasma membrane, thereby creating isolated environments for transcription and translation processes (Cavalier-Smith, 2010).

This compartmentalization enables a high degree of control over the cellular environment, facilitating intricate regulatory mechanisms that are essential for complex life forms. For instance, the separation of genetic material within the nucleus allows for sophisticated regulation of gene expression, while the segregation of distinct metabolic pathways in mitochondria and chloroplasts underscores the division of labor critical for energy production and biosynthesis. It has been proposed that the advent of mitochondria allowed for a redistribution of DNA in relation to bioenergetic membranes, leading to a 200,000-fold expansion in the number of genes expressed. While the energetic cost of maintaining genes is minimal, the energy required to express them as proteins is substantial and accounts for the majority of the cell's energy expenditure. Mitochondria increased the number of proteins a cell can evolve, inherit, and produce by four to six orders of magnitude (Lane & Martin, 2010). These adaptations illustrate the evolutionary advantage conferred by cellular compartmentalization, which has driven the diversity and complexity observed in eukaryotic life.

However, compartmentalization has a side effect: it limits communication within the cell. As a result, cells require a **transport system** that regulates the traffic of molecules (Bar-Peled & Kory, 2022). In this context, regulated pathways are essential for targeting proteins to their final

subcellular destinations. Through membrane contact sites (MSCs), organelles in close proximity, typically within less than 30 nm, can exchange certain molecules and ions (Prinz et al., 2019). However, the transport of larger molecules to distant organelles or other cells cannot be achieved via MCSs; instead, it relies on vesicle trafficking. Vesicular transport allows various molecules to reach different compartments of the cell. With the exception of the few proteins encoded by mitochondrial and plastid genomes, most proteins are synthesized by ribosomes in the cytosol or attached to the rough endoplasmic reticulum and are then directed to their final destinations through a complex network of sorting pathways. This subcellular sorting mechanism consists of two main components. The first is a targeting signal, which can be embedded either within the polypeptide chain or the folded structure of the protein. The second component involves specific soluble receptors that recognize these sorting signals and direct the proteins to a membrane-associated translocation machinery. These translocons then inserts the protein into the lumen or membrane of the appropriate compartment. The sorting code is dynamic, with post-translational modifications and conformational changes capable of activating or deactivating a signal. Notably, the same protein is often targeted to multiple compartments, possibly under different physiological conditions, suggesting that various targeting signals can coexist within a single protein (Cui et al., 2022; Gabaldón & Pittis, 2015).

Within the **intracellular trafficking**, there are two major pathways: the exocytic (or secretory pathway), which transports material synthesized in the ER to the GA and subsequently to other compartments or the extracellular environment; and the endocytic pathway, which internalizes material from the external environment into the cell. **Endosomes** operates as carriers in both pathways and are connected to each other and the plasma membrane via endocytic vesicles. This endosomal network ensures the precise delivery of proteins, lipids, and other molecules to their appropriate destinations within the cell, playing a crucial role in coordinating cellular processes, signal transduction and response, cellular homeostasis, adaptation, stress response, immune function, and pathogen defense (Mellman & Warren, 2000). Endosomes orchestrate the fate of proteins and lipids, acting as cellular sorting stations. However, while endosomes are involved in lipid transport, other non-vesicular mechanisms such as lipid transfer proteins (LTPs) and direct MSCs play a more significant role in the lipid distribution within cells (Prinz, 2010; Wong et al., 2019). Additionally, soluble proteins are often released directly into the cytoplasm, where they move randomly by simple diffusion or are actively transport via motor proteins (Sartori et al., 2020). In contrast, the transport of membrane proteins does heavily rely on the endosomal system (Cullen & Steinberg, 2018), as they contain hydrophobic regions that must be shielded from the aqueous cellular environment, thus requiring a lipid bilayer. The human genome encodes approximately 5,500 to 7,500 membrane proteins, which stresses the importance of a correct regulation of their transport among the cells through these intracellular pathways (Uhlén et al., 2015).

1.1.1. The endolysosomal system

Within the cell, there are multiple pathways for the trafficking of membrane proteins, and the endosome serves as a central checkpoint in most of them. Endosomes exist in various types depending on their maturation stage: early endosomes (EE), late endosomes (LE), recycling endosomes, and multi-vesicular bodies (MVB). Together with lysosomes, endosomes form the endolysosomal system (Naslavsky & Caplan, 2018).

It is important to note that endosomes are mobile, and their movement is closely linked to their maturation stage and function. Research suggests that their position within the cytoplasm, particularly their distance from the nucleus, significantly influences the number, size, and cargo content of endosomes, aligning with the spatial and temporal progression of their maturation (Collinet et al., 2010). Endosomes rely on dynein and kinesin motors for motility along microtubules, with these motors generating opposing forces that move endosomes in opposite directions. This bidirectional transport is essential for distributing endosomes within the cell and delivering them to various cellular locations. Additionally, it has been proposed that the tug-of-war created by various weak dyneins and a single strong kinesin facilitates endosome fission, a process required to produce smaller vesicles during endosomal maturation, which can then be further processed or sorted (Soppina et al., 2009).

The **endocytic pathway** facilitates the inward movement of vesicles from the cell's exterior into the cytosol, serving several functions including nutrient uptake, regulation of membrane composition, signal transduction, and debris removal. However, some pathogens, such as animal viruses, exploit this pathway to enter the cell, as the endocytic route provides a means for penetration into the cytosol (Mercer et al., 2010). The use of the endosomal network by human pathogens will be explored further in section 1.4.

Membrane proteins entering the endocytic pathway, referred to as cargos, are initially internalized from the cell surface through membrane invagination, forming primary endocytic vesicles via endocytosis. These primary vesicles then transfer their contents and membrane components to EEs located in the peripheral cytoplasm. EEs vary in morphology, localization, composition, and function, with their distribution being dependent on cell type. Typically, EEs are small and exhibit saltatory movement along microtubules in the peripheral cytoplasm near the plasma membrane (Huotari & Helenius, 2011).

EEs maintain a slightly acidic environment (pH 5.9 - 6.8), which is crucial for their function (Maxfield & Yamashiro, 1987). This acidity promotes the dissociation of ligands from their receptors, allowing receptors to be recycled back to the plasma membrane while ligands are directed

toward degradation pathways. Moreover, the mildly acidic conditions help prevent premature activation of enzymes and avoid aggregation or precipitation of certain cargo molecules, partly due to the relatively low Ca^{2+} concentration in EEs (Gerasimenko et al., 1998).

In these **early endosomes** is where the fate of the cargos is going to be defined (**Figure 1**). Proteins that are internalized follow one of **two pathways**: the degradative pathway or the recycling pathway. In the degradative pathway, proteins are directed towards lysosomal degradation, whereas in the recycling pathway, they are transported to various destinations such as the plasma membrane, the trans-Golgi network (TGN), or specialized endosomal compartments.

Integral membrane cargos that have undergone lysine-63-linked ubiquitination (Shaid et al., 2013), are recognized by ESCRT (Endosomal Sorting Complex Required for Transport) complexes. These cargos are then delivered into LE via intralumenal vesicles (ILVs), which eventually fuse with lysosomes to form a transient hybrid organelle known as the endolysosome. This organelle provides a controlled acidic environment essential for the degradation of the cargos (Christ et al., 2017). While ubiquitination is a key signal for cargo destined for degradation, it is important to note that ubiquitin-independent mechanisms for cargo incorporation into ILVs have also been observed (Bissig & Gruenberg, 2014).

The **degradative pathway** is necessary for the removal of damaged, misfolded, or excess proteins and lipids, thus preventing the accumulation of potentially harmful aggregates. It should be noted that protein levels within cells are regulated not only by rates of synthesis, but also by rates of degradation. The degradative pathway also plays a role in pathogen defense, cellular development, differentiation, and the regulation of membrane receptor levels. For instance, by degrading cell surface receptors, the pathway controls the sensitivity of cells to external signals, thereby modulating responses to hormones, growth factors, and other signaling molecules (Huber & Teis, 2016).

Conversely, in the **recycling pathway**, internalized proteins are identified by specific sequence-dependent motifs, and are transported back to the plasma membrane, the TGN, or other organelles such as melanosomes. The current thesis focuses on the recycling pathway, which will be discussed in detail in the following section.

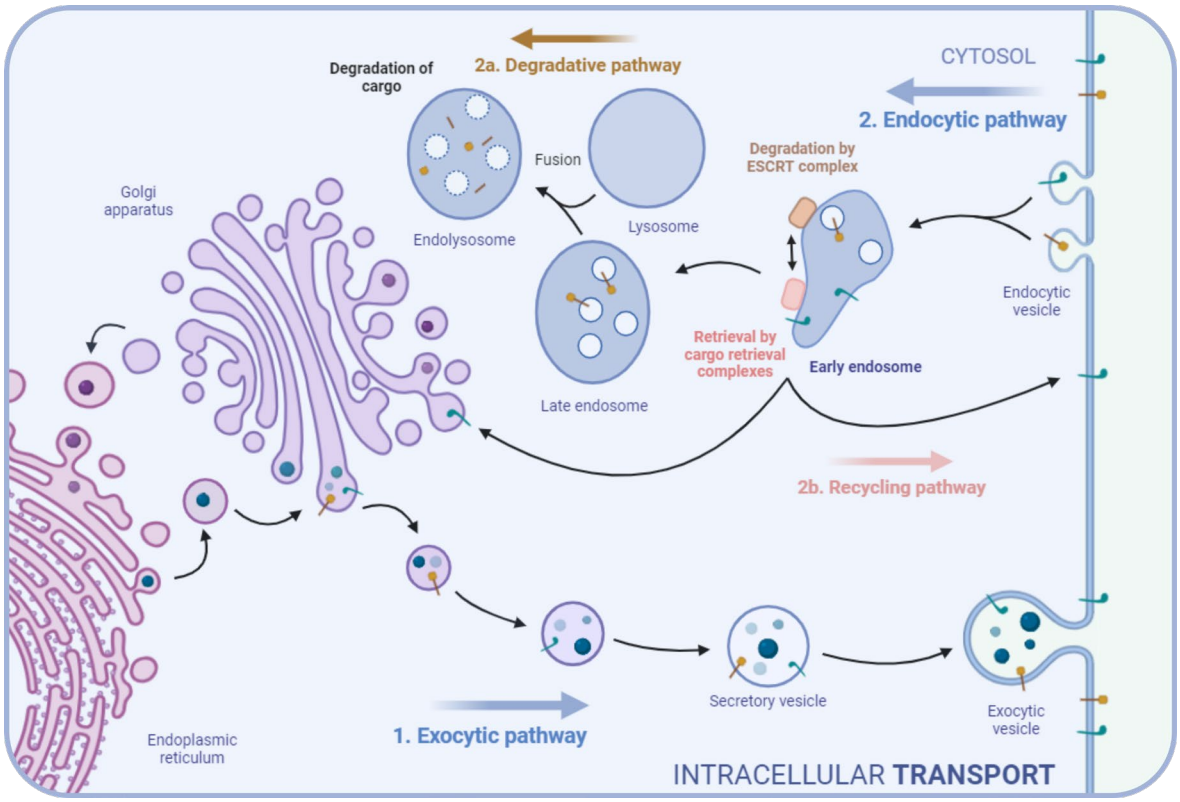

Figure 1. Simplified overview of intracellular trafficking pathways. Membrane protein cargos from the plasma membrane enter the endosomal system through the endocytic pathway. Within the endosomal system, these cargos are sorted either for degradation or for retrieval to avoid degradation. Cargo retrieval complexes localize to specific sub-domains within the endosome that are distinct from the sub-domains where ESCRT complexes operate. Cargos recognized by cargo retrieval complexes, based on sequence-dependent motifs from cytosolic-facing regions, are spared from lysosomal degradation and are recycled back to the plasma membrane or to the TGN via the recycling pathway. Figure created with BioRender.com.

Early endosomes play a role in both the degradative pathway and the recycling pathways (either directly or via recycling endosomes). They accumulate cargo for approximately 8 to 15 minutes maturing into LEs. The LEs carry a selected subset of endocytosed cargo accumulated from EEs, along with newly synthesized lysosomal hydrolases and membrane components from the secretory pathway (Huotari & Helenius, 2011).

LEs grow in size through homotypic fusion reactions and acquire more ILVs, effectively amplifying the degradative compartment. The maturation process continues with the aim of delivering this mixture of endocytic and exocytic components to lysosomes. Upon fusion of the endosome with a lysosome, forming an endolysosome, further maturation occurs, converting the endolysosome into a dense lysosome. This dense lysosome serves as a storage organelle for lysosomal hydrolases and membrane components (Huotari & Helenius, 2011).

The internalization of molecules from the plasma membrane is commonly carried out by **clathrin-mediated endocytosis** (CME). This process starts with the recruitment of clathrin, a trimeric protein that forms a lattice-like structure on the inner surface of the plasma membrane. Adaptor proteins, such as AP-2, recognize and bind to specific cargo molecules, incorporating them into forming clathrin-coated pits. As the clathrin coat assembles, it induces membrane curvature, leading to the invagination of the plasma membrane. Dynamin, a GTPase, then constricts and pinches off the neck of the invaginated pit, releasing a clathrin-coated vesicle (CCV) into the cytoplasm (Doherty & McMahon, 2009). Once internalized, the vesicle rapidly sheds its clathrin coat, a process facilitated by auxilin and Hsc70, allowing the uncoated vesicle to fuse with early endosomes (McMahon & Boucrot, 2011). CME is crucial not only for nutrient uptake and receptor downregulation but also for synaptic vesicle recycling and immune responses (Conner & Schmid, 2003). The specificity and regulation of CME are finely tuned by multiple accessory proteins and lipid modifications, ensuring efficient internalization of a wide array of cargos (Mayor & Pagano, 2007). Early endosomes (EEs) also acquire cargo through non-clathrin-mediated routes, including caveolar, GEEC, and ARF6-dependent pathways. EEs have a complex structure with tubular and vacuolar regions; the tubular regions account for most of the membrane surface area, while the vacuolar regions make up a significant portion of the internal volume. The limiting membrane of EEs contains various subdomains with distinct compositions and functions, including areas enriched with Rab5, Rab4, Rab11, Arf1/COPI, Retromer, and caveolae. Many of these domains are found in the tubular extensions and are involved in molecular sorting and vesicle formation for different organelles (Huotari & Helenius, 2011). The composition and sorting activity of Rab GTPases in endosomes change during maturation, which involves a gradual transformation of the organelle and extensive remodeling of the endosomal membrane (Gopaldass et al., 2024). This is achieved, in part, because Rab proteins act as “molecular switches”, cycling between GDP- and GTP-bound states. Rab effectors preferentially bind to the GTP-bound, active state, forming higher-order molecular assemblies that define endomembrane identity and regulate vesicle formation, targeting, and fusion, thereby ensuring the directionality of transport (Elkin et al., 2016).

Within the endosomal network, **phosphoinositides (PIs)** play a remarkable role. Phosphatidylinositol phosphates (PIPs) are phosphorylated derivatives of phosphatidylinositol, synthesized in the endoplasmic reticulum and delivered to endomembrane compartments through endosomal transport. Although they are present in mammalian cells only in minute quantities, their levels in membranes are critical as they provide docking sites for various proteins involved in endosomal trafficking and sorting (Elkin et al., 2016). Specifically, PIs recruit several effector proteins with PI-binding domains, including FYVE finger (Fab1p, YOTB, Vac1p and EEA1), PH (plekstrin homology), ENTH (epsin N-terminal homology), PX (Phox-homology), GRAM (glucosyltransferases, Rab-like GTPase activators and myotubularins) and PHD (plant homeo

domain) domains, which are involved in vesicular budding, cargo sorting, and fusion processes (Shisheva, 2008). Additionally, PIs regulate endosomes movement within the cell by interacting with motor proteins and other cytoskeletal components. Increases in several PI species have been associated with the accumulation of endosomal F-actin.

There are seven different PPIs, defined by their phosphorylation status at positions 3, 4, or 5 of the inositol ring (Elkin et al., 2016). Among them, **PI3P** (phosphatidylinositol 3-phosphate) **and PI(3,5)P2** (phosphatidylinositol 3,5-bisphosphate) are particularly significant PI3P contributes to the identity of early endosome (EE) membranes, while PI(3,5)P2 is important for late endosome (LE) function and endosome maturation. PI3P is predominantly found on the cytosolic leaflet of EE membranes and plays a central role in recruiting effector proteins to early endosomes (Singla et al., 2019).

Three main enzymes are involved in the metabolism of PI3P and PI(3,5)P2: VPS34 kinase, PIKfyve kinase, and myotubularin phosphatases. PI3P is primarily generated by **VPS34**, a class III PI 3-kinase, which is recruited by Rab5-GTP and forms a core complex together with p150 and Beclin-1. Inhibition of VPS34 activity results in enlarged LEs with fewer ILVs, indicating that PI3P is essential for maintaining the unique identity of early endosomes (Balla, 2013; Huotari & Helenius, 2011).

In contrast, PI(3,5)P2 plays a role later in the degradative pathway, and it is generated by the evolutionary conserved **PIKfyve enzyme**, a phosphoinositide kinase, FYVE-type Zinc Finger containing enzyme, that converts PI3P to PI(3,5)P2. PIKfyve forms an active complex by associating with its activator ArPIKfyve (associated regulator of PIKfyve), also known as Vac14, and the phosphatase Fig4, called de PIKfyve complex. This complex is required for both kinase and phosphatase activities. PIKfyve also serves as the primary source of cellular pools of phosphatidylinositol 5-phosphate (PI5P), likely through the activity of lipid phosphatases on PI(3,5)P2 and potentially through direct synthesis as well (Giridharan et al., 2022). PIKfyve dysfunction leads to endosome enlargement and significant cytoplasmic vacuolation due to impaired endosome processing and membrane exit (Shisheva, 2008). Finally, PI3P dephosphorylation is catalyzed by **myotubularin** family members, particularly myotubularin-related protein-2 (MTMR2), which dephosphorylates PI3P back to PI (Singla et al., 2019). Thus, the composition of phosphoinositides is a hallmark of different endosomal compartments.

1.1.2. The recycling pathway

Those cargos that are destined for recycling must first avoid inclusion into ILVs, a process termed cargo retrieval. The majority of internalized cargos are recycled, typically back to the cell surface via an **anterograde pathway** (outward flux; movement from the early endosomes towards more distal compartments). This sorting process tightly regulates the composition of signaling receptors, adhesion proteins, ion channels and nutrient transporters at the cell surface, and thereby modulates the ability of the cell to respond to external signals (Cullen & Steinberg, 2018; McNally & Cullen, 2018). Studies have shown that between 50% and 100% of the surface area of the plasma membrane in human cells can be internalized and replaced within an hour. This indicates a high turnover rate, essential for various cellular functions such as nutrient uptake, receptor recycling, and response to signaling events (Doherty & McMahon, 2009). In macrophages, the recycling pathway has special relevance, as they require a tight regulation of surface receptors, such as those involved in antigen presentation or receptors for cytokines, chemokines, and pathogens. Interestingly, the amount of fluid internalized by macrophages corresponds to 30% of cell volume per hour, with about two-thirds being returned to the extracellular space within 10 to 15 minutes (Huotari & Helenius, 2011).

Moreover, membrane proteins coming from the synthetic pathway, including lysosomal hydrolase receptors, are also retrieved by sorting complexes within endosomes and recycled back to the TGN via **retrograde transport** (inward flow). This trafficking is required for the efficient delivery of newly synthesized lysosomal hydrolases to the endosomal lumen (Buser & Spang, 2023). Retrograde trafficking is also implicated in other processes, such as the regulation of cell polarity, retrieval of resident proteins, and the redirection of mis-localized proteins (Bingham et al., 2024).

For instance, β1 integrin, a cell surface receptor, undergoes retrograde transport from the plasma membrane to the TGN when a migratory phenotype in highly polarized cells is needed, where it is subsequently re-secreted specifically to the leading edge of the cells. Disruption of the retrograde transport in mouse embryos via conditional *Rab6a* knockout led to lethality at a stage when cell–matrix interaction became dependent on a functional β1 integrin system (Shafaq-Zadah et al., 2016). This contrasts with the recycling of β1 integrin via an anterograde pathway, which maintains β1 integrin at the leading edge in a more random fashion (White et al., 2007).

Retrograde movements are also implicated in retrieving resident proteins, such as Wntless (Wls), a transmembrane sorting receptor. Wls has a function in the anterograde transport of Wnt signaling proteins from the TGN to the plasma membrane. To enable repeated rounds of this transport, Wls must be recycled back to the TGN by retrograde movements (Franch-Marro et al., 2008). In addition, v-SNARE proteins involved in the tethering of cargo from the ER to the Golgi,

needs to be retrieved back to the ER to maintain a functional pool of v-SNAREs for subsequent rounds of secretion (Hong, 2005).

Finally, proteins that mistakenly enter the wrong compartment during anterograde trafficking are recognized and transported back to their proper location. For instance, ER-resident chaperone proteins, which can mistakenly remain in the Golgi after trafficking from the ER, must be retrieved back to the ER via COPI-mediated retrograde transport. To identify these mislocalized ER-resident proteins, they possess a C-terminal Lys-Asp-Glu-Leu (KDEL) sequence. This sequence is recognized by KDEL receptors (KDELR) in the cis-Golgi, where the pH is around 6. The KDELR binds strongly to the KDEL motif on the protein in the acidic environment of the cis-Golgi. This binding triggers the incorporation of the protein into COPI vesicles that transport it back to the ER. In the ER, where the pH is approximately 7, the higher pH causes the protein to dissociate from the KDELR.

Thus, the recycling pathway plays a role in delivering molecules by both anterograde (outward secretion) and retrograde (inward flow) trafficking routes, which work together to maintain cellular homeostasis (Bingham et al., 2024).

Cargos destined for recycling are recognized by **cargo retrieval complexes** such as Retromer, ESCPE-1 (Endosomal SNX-BAR Sorting Complex for Promoting Exit 1), AP5/SPG11/SPG15, and Retriever complexes. Notably, when these cargo retrieval complexes are suppressed or knocked out, cargos are directed to lysosomal degradation. This suggests that in the absence of these sorting complexes, cargo degradation may be the default pathway (McNally & Cullen, 2018). For this reason, recycling complexes are referred to as “retrieval complexes”, as they are essential for diverting cargos away from lysosomal degradation.

Consistent with the critical role of endosomal protein sorting in cellular physiology, homeostasis, and lysosomal health, defects in this process have been linked to a wide array of human disorders, including neurodegenerative diseases, developmental disorders, cancer, and diabetes (McMillan et al., 2017), which will be discussed later.

1.2. Cargo retrieval complexes

For cargo recycling, specific domains of the endosomal membrane recruit membrane coats that shape the membrane into tubular or vesicular forms and gather targeted cargo proteins. These regions pinch off from the endosomes to form endosomal carriers, which then travel to the Golgi or the plasma membrane (Gopaldass et al., 2024). Several different coat membrane complexes have been described so far. The most studied complex to date is Retromer, which, in combination with other proteins or complexes, is responsible for delivering cargos to various compartments. Until recently, it was believed that cargo recycling was exclusively mediated by Retromer; however, Retromer-independent pathway have now been described. This has revealed **five major pathways** (**Figure 2**), each characterized by specific proteins that recognize sorting motifs in the cargos and deliver them to distinct destinations. Although each cargo retrieval complex undertakes distinct itineraries, they all localize to the same endosomal retrieval sub-domain (McNally et al., 2017), which is separate from the complexes involved in the degradative pathway.

Three of these recycling pathways send cargos back to the cell membrane: Retromer in combination with sorting nexin 27 (SNX27), Retriever together with SNX17, or SNX4 alone. In contrast, when Retromer forms a complex with SNX3, or when the ESCPE-1 complex is involved, the final destination of the attached cargos is the Golgi apparatus. ESCPE-1, first described by Simonetti *et al.*, consists of heterodimeric combinations of either SNX5 or SNX6 dimerized with either SNX1 or SNX2 (Simonetti et al., 2017). Notably, each pathway utilizes specific members of the sorting nexin (SNX) family, which are essential for associating with endosomes and selecting the appropriate cargo.

In addition to the mentioned proteins, other protein complexes are involved in the assembly of the recycling machinery. While the Wiskott–Aldrich syndrome protein and SCAR homologue (WASH) complex is required in both Retromer and Retriever-related pathway, the CCDC22, CCDC93, and COMMD (CCC) complex is exclusive of the Retriever pathway. Additionally, Rab GTPase proteins play a role in coordinating vesicular trafficking processes, with Rab5 and Rab7 specifically required in the Retromer context (Rojas et al., 2008).

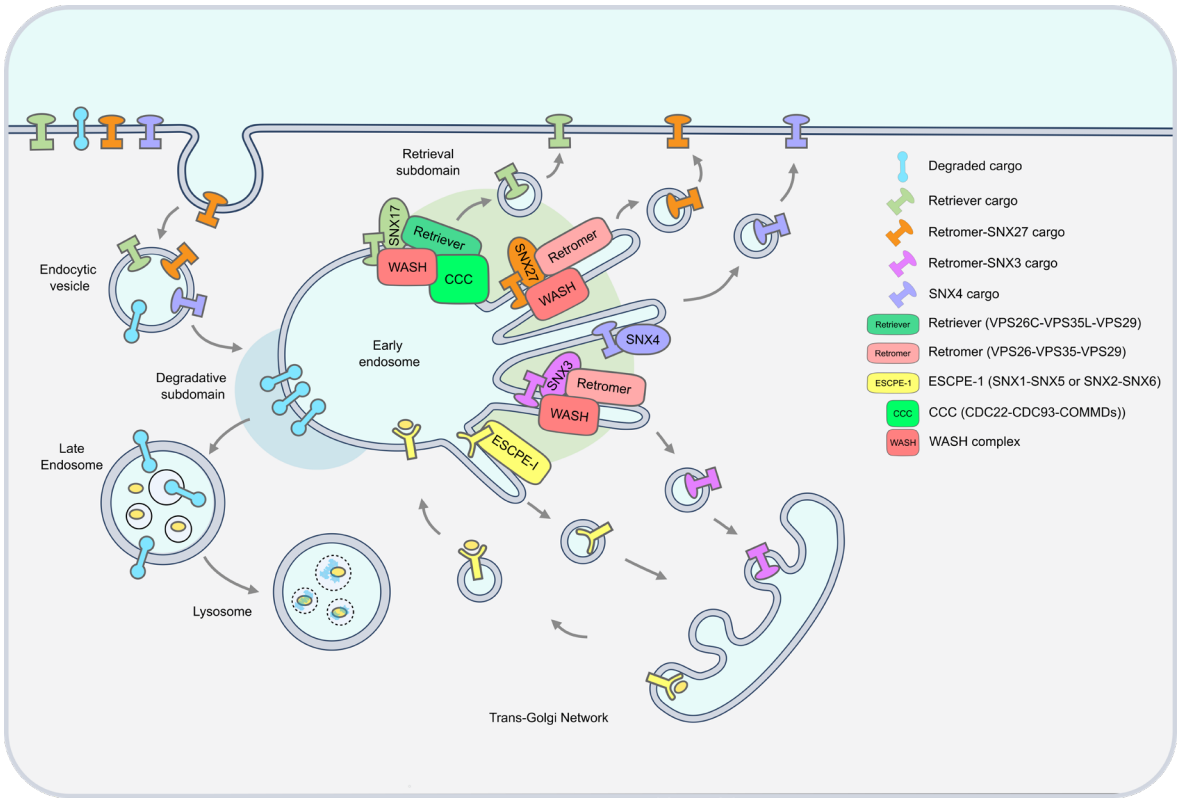

Figure 2. Major endosomal trafficking pathways in mammalian cells. Membrane proteins undergo endocytosis to reach early endosomes. Through the recognition of specific and different sorting signals, cargo induces the recruitment of certain endosomal carriers. SNX27 or SNX3 in combination with Retromer, SNX17 assembled with Retriever, SNX4 alone, or the ESCPE-1 complex associates with this endosomal compartment to serve as a membrane scaffold. The forming coat enables the formation of tubular carriers and the recruitment of cargo into them. The composition of the coat will determine the final destination of the cargo.

The **Retromer complex** was first identified in the yeast *Saccharomyces cerevisiae* two decades ago (Seaman et al., 1998). Retromer is an ancient endosomal sorting complex conserved in all eukaryotes, indicative of an ancient origin before the Last Eukaryotic Common Ancestor (LECA). In mammals, the genes encoding Retromer have undergone duplication and divergence (Koumandou et al., 2011). The complex consists of three subunits: VPS26A/B (Vacuolar Protein Sorting), VPS29 and VPS35. The structure of the Retromer complex, as well as the mechanisms for cargo recognition and tubular vesicle formation, have been widely described (Chen et al., 2019; Lucas et al., 2016). In human cultured cells, Retromer regulates the cell surface levels of more than 100 integral plasma membrane proteins and mediates the recycling of cargo from the endosome to the TGN and lysosomal-related organelles, including proteins involved in cell adhesion, ion transport, and amino acid transport (Steinberg et al., 2013).

As previously mentioned, the **SNX family** plays a remarkable role in the cargo recycling process by associating with endosomes and recognizing cargo. SNXs determine the fate of the

recycling machinery they are associated with; depending on the specific SNX member, cargos will be transported either back to the plasma membrane or to the TGN (Chi et al., 2015). While *S. cerevisiae* possesses 10 different SNXs, humans have 33 different members (Teasdale & Collins, 2012), which can be divided into three classes (**Figure 3**). The overarching characteristic of these classes is the presence of a PX domain (Cullen & Steinberg, 2018). The PX domain, binds specific phosphoinositides and is crucial for targeting (Xu et al., 2001).

One class of sorting nexins contains only a PX domain and no additional defined domains (SNX-PX). Another class includes proteins with a PX domain and a C-terminal BAR (Bin/Amphiphysin/Rvs) domain (SNX-BAR). The third class of sorting nexins contains a PX domain along with other defined domains, excluding BAR (SNX-others). All three classes of SNXs are well-conserved across eukaryotes (examined using a Hidden Markov Model profile of the 33 human sorting nexins) (Koumandou et al., 2011).

The BAR domain functions in dimerization and sensing membrane curvature. Dimerization of BAR domains results in a banana-shaped structure with positively charged surface residues that interact with negatively charged membrane phospholipids to promote membrane association and curvature formation (Frost et al., 2009). It is also noteworthy that other domains, such as short amphipathic helices, can induce membrane curvature. These helices insert shallowly into the membrane and cause localized deformation. Additional domains observed in SNXs members include the PSD-95/discs-large/ZO-1 (PDZ) domain, which facilitates protein-protein interactions, and the FERM-like domain, which interacts with cargo and/or lipids.

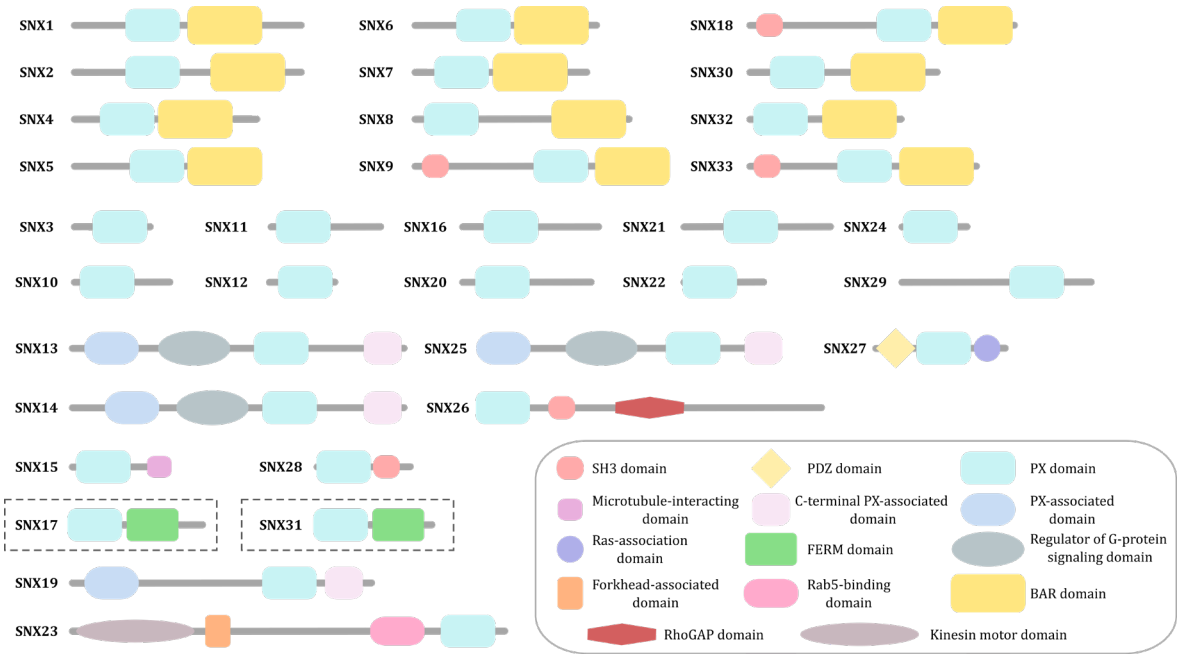

Figure 3. Diagram of the predicted domain structures of the 33 mammalian SNXs proteins. All family members contain an evolutionarily conserved PX domain that recognizes PI3P. The figure is adapted from (Yang et al., 2021). SNX17 and SNX31, the members used in this thesis, are highlighted with a dashed line.

Among the five described recycling pathways, this thesis focuses on the recently discovered route mediated by Retriever-SNX17, and its molecular details will be described later.

1.2.1. Mechanism of action of the cargo retrieval complexes

Retromer and Retriever complexes share certain similarities, but the molecular mechanism of action of Retriever has been poorly described so far. However, the accumulated knowledge of the Retromer complex can help to elucidate the mechanism of action of Retriever (McGough & Cullen, 2011).

A general diagram of the **Retromer-dependent pathway** is displayed (**Figure 4**). Initially, SNXs identify and bind to cargo proteins, with the mechanism of cargo binding varying depending on the recycling pathway. For instance, membrane proteins recycled by Retromer with SNX3 contain a sequence-specific sorting motif composed of an ΩΦ[Leu/Met] motif (where Ω represents an aromatic amino acid and Φ represents a hydrophobic amino acid) located in the cytosolic-facing 'tail' regionc(Collins et al., 2005, 2008; Shi et al., 2006; Wang et al., 2005) (Seaman, 2007; Tabuchi et al., 2010). SNX3 attaches to the VPS26–VPS35 interface via its flexible N-terminal region and PX domain. When Retromer binds to SNX3, it induces a conformational change in VPS26, exposing a hydrophobic pocket for cargo binding. Recycling cargos then bind to this site at the interface between SNX3 and VPS26 (Lucas et al., 2016).

In contrast, cargos recognized by Retromer associated with SNX27 contain a characteristic sequence; [-][-]x[-][Ser-Thr]xΦ (where [-] refers to any negatively charged such Asp or Glu, or a phosphorylated Ser or Thr, and x to any amino acid) (Gallon et al., 2014; Lauffer et al., 2010). SNX27 interacts directly with VPS26 through its PDZ domain, which facilitates cargo binding at a different site within the domain. SNX27's ability to bind cargo is enhanced when associated with VPS26, linking cargo recognition with Retromer binding. Interestingly, many cargos regulated by SNX27 do not possess the acidic residues typically required to form a stable electrostatic interaction with a key residue in SNX27 (Arg58). Instead, these cargos contain phosphorylation sites that mimic the acidic side chains required for high-affinity binding, suggesting a post-translational regulatory mechanism (Clairfeuille et al., 2016).

Finally, cargos recycled by ESCPE-1 complex contain the motif ΦxΩ0xΦ[x_n]Φ. ESCPE-1 comprises SNX1/2 heterodimers with SNX5/6. These proteins possess a PX domain followed by a

BAR domain, and form heterodimers of SNX5 or SNX6 with SNX1 or SNX2 through the C-terminal BAR domain structure. The PX domains of SNX5 and SNX6 feature a unique extended helical structure and no membrane-binding capacity. Instead, this helical extension provides a docking site for cargo sorting peptide motifs. Interestingly, cargo retrieval often relies on interactions that cannot occur simultaneously. For instance, the motifs in the CI-MPR cargo recognized by SNX3-Retromer and ESCPE-1 overlap. Therefore, these interactions need to be dynamic and adaptable depending on the specific context (Lopez-Robles et al., 2023; McNally & Cullen, 2018; Singla et al., 2019; Van Weering et al., 2010; Weeratunga et al., 2020).

The interaction of cargo with SNX triggers the recruitment of Retromer subunits to the membrane. Retromer itself lacks membrane-binding capacity and depends on accessory proteins for this recruitment (Baños-Mateos et al., 2019). This process leads to membrane deformation and the formation of tubulovesicles. The Retromer complex assembles into a loosely symmetrical coat, consisting of head-to-head Retromer dimers that connect to the SNX coat via VPS26A/B. This cooperation facilitates the formation of tubular transport intermediates (Kovtun et al., 2018). Retromer functions as a scaffold, acting as a bridge between different complexes: it promotes membrane remodeling through its arch-shaped polymers and recruits additional factors. Conceptually, Retromer can be compared to the clathrin cage in its scaffolding role (Kendall et al., 2020).

Scission occurs through an as-yet-unknown mechanism, with longitudinal force generated through interactions with microtubule motors and/or actin polymerization. The association of SNXs with either minus-end- or plus-end-directed microtubule motors enables long-distance transport of cargo to its target compartment. In the example depicted in the figure, minus-end-directed movement delivers the vesicle to the TGN. Upon reaching the final destination, other SNXs interact with a tethering factor localized there, facilitating carrier recognition. Before the vesicle fuses with the target compartment for cargo retrieval, the carrier undergoes uncoating, which may be driven by specific myotubularins. Once the vesicle reaches its target compartment, the Retromer complex disassembles, allowing it to function again (McGough & Cullen, 2011).

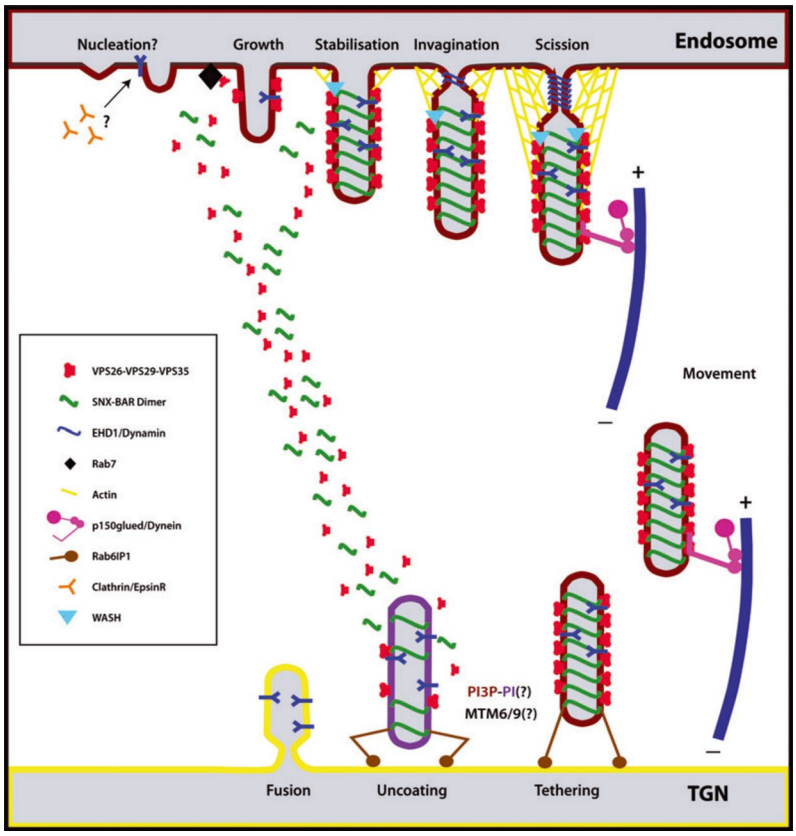

Figure 4. Mechanism of action the Retromer pathway and cryo-ET reconstruction of the Retromer complex. Mechanistic details of the TGN-targeted recycling of cargo by the mammalian Retromer pathway. Specific combinations of SNXs initiate membrane tabulation, which is coupled with sorting by the VPS26–VPS29–VPS35 complex interacting with the cytosolic tails of targeted cargos. Once the vesicle is formed, it travels to the target compartment, such as the TGN, and establishes a physical connection with the acceptor membrane through a tether protein. Following this connection, docking and fusion occur, with the opposing membranes merging to form an expanding fusion pore. Figure from (McGough & Cullen, 2011).

The structure of Retromer has been elucidated by various research groups in recent years, significantly advancing our understanding of the assembly architecture of this recycling machinery and its interaction with membranes (**Figure 5**). Multiple crystal structures of mammalian Retromer subunits have been determined (Collins et al., 2005, 2008; Shi et al., 2006; D. Wang et al., 2005), as well as sub-complexes (Hierro et al., 2007; Lucas et al., 2016). Additionally, the first cryo-electron microscopy (cryo-EM) structure of the mammalian Retromer complex was solved at an average resolution of 5.7 Å from 26,369 particles (Kendall et al., 2020). Moreover, atomic models of the fungal Retromer:Vps5 complex (Kovtun et al., 2018) and the metazoan Retromer:SNX3 complex (Leneva et al., 2021) have been determined by cryo-electron tomography (cryo-ET) and sub-tomogram averaging.

The VPS35 subunit acts as an extended central scaffold within the Retromer complex, with VPS26 and VPS29 binding independently to the amino- and carboxyl terminals of VPS35, respectively. At the carboxyl terminus of VPS35, its solenoid structure wraps around VPS29 with a high binding affinity of approximately 200 nM, while VPS26 binding occurs through the N-terminal of VPS35 with an even higher affinity constant (with a K_D of ~ 4 nM observed by Norwood (2011), and ~ 1 nM observed by Lucas (2016)). Notably, no cooperativity has been observed in this process, as VPS29 and VPS26 do not form additional contact with each other within the trimeric core complex, nor do they alter VPS35's structure in a way that affects the binding of the other (Norwood et al., 2011). The Retromer trimer can dimerize through VPS35, forming arch-like structures. Additionally, cryo-EM studies have described Retromer tetramers, suggesting that this oligomeric state might serve as a soluble cytosolic pool for rapid assembly on membranes in the presence of sorting nexins and cargos, though experimental validation is still required (Kendall et al., 2020).

As the largest protein of the complex, **VPS35** consists of 33 helices arranged into 16 pairs of antiparallel α-helices, forming a domain structure known as a Huntington/EF3/PP2A/TOR1 (HEAT) repeat. These HEAT repeats create an elongated, slightly curved α-helical solenoid structure. HEAT repeats, which are common in many eukaryotic proteins, are highly flexible and can undergo significant conformational changes when interacting with various binding partners or subjected to external forces. This flexibility is attributed to their unusual hydrophobic core, which facilitates intramolecular helix–helix interactions (Yoshimura & Hirano, 2016).

VPS29 adopts a fold similar to that found in phosphoesterases, which initially suggested that the Retromer complex might regulate retrograde trafficking through cargo dephosphorylation (Damen et al., 2006). However, VPS29 lacks the critical histidine residue required for enzymatic activity, and in the context of the Retromer complex, its catalytic site is inaccessible due to its interaction with VPS35 (Hierro et al., 2007). Additionally, no phosphoesterase activity has been observed *in vitro* (Swarbrick et al., 2011). These findings ultimately refuted the phospho-peptides model. Instead, VPS29 is believed to function primarily as a scaffold, aiding in the correct folding of other proteins. Furthermore, VPS29 acts as a multi-adaptor protein, interacting with various partners through a second conserved pocket located on the side opposite the VPS35 binding surface. This interaction may help regulate activity and facilitate crosstalk among different recycling systems (Baños-Mateos et al., 2019).

VPS26A and VPS26B are paralogues, with VPS26B arising from interchromosomal duplication, and they exhibit some overlapping but also distinct functions (Bugarcic et al., 2011). These proteins share approximately 70% sequence identity and both adopt arrestin-like folds consisting of two β-sandwich domains connected by a flexible linker and a polar core. Arrestin family proteins are generally involved in receptor internalization at the plasma membrane. The polar core,

located centrally within the protein, is known in arrestins for facilitating conformational changes. However, such conformational changes have not been observed in VPS26A/B; mutations disrupting the polar core interaction did not prevent protein folding, leaving the functional significance of the polar core in VPS26 unclear (Aubry et al., 2009; Shi et al., 2006). The C-terminal domain of VPS26A interacts with VPS35 N-terminal domain through a broad binding surface that includes both polar and apolar interactions (Lucas et al., 2016). Both VPS26A and VPS26B bind to the VPS35-VPS29 complex with nanomolar affinity and compete for a single binding site in a mutually exclusive manner. Although both paralogues show identical endosomal membrane localizations in the HeLa cell line and are expressed at various stages of development, they are not functionally redundant; for example, an insertion mutation in VPS26A alone is embryonically lethal. It was suggested that their C-terminal 'tails', composed of 30 to 40 residues, which are poorly conserved, may be crucial for their differential function (Collins et al., 2008), a hypothesis that was, indeed, later confirmed (Bugarcic et al., 2011).

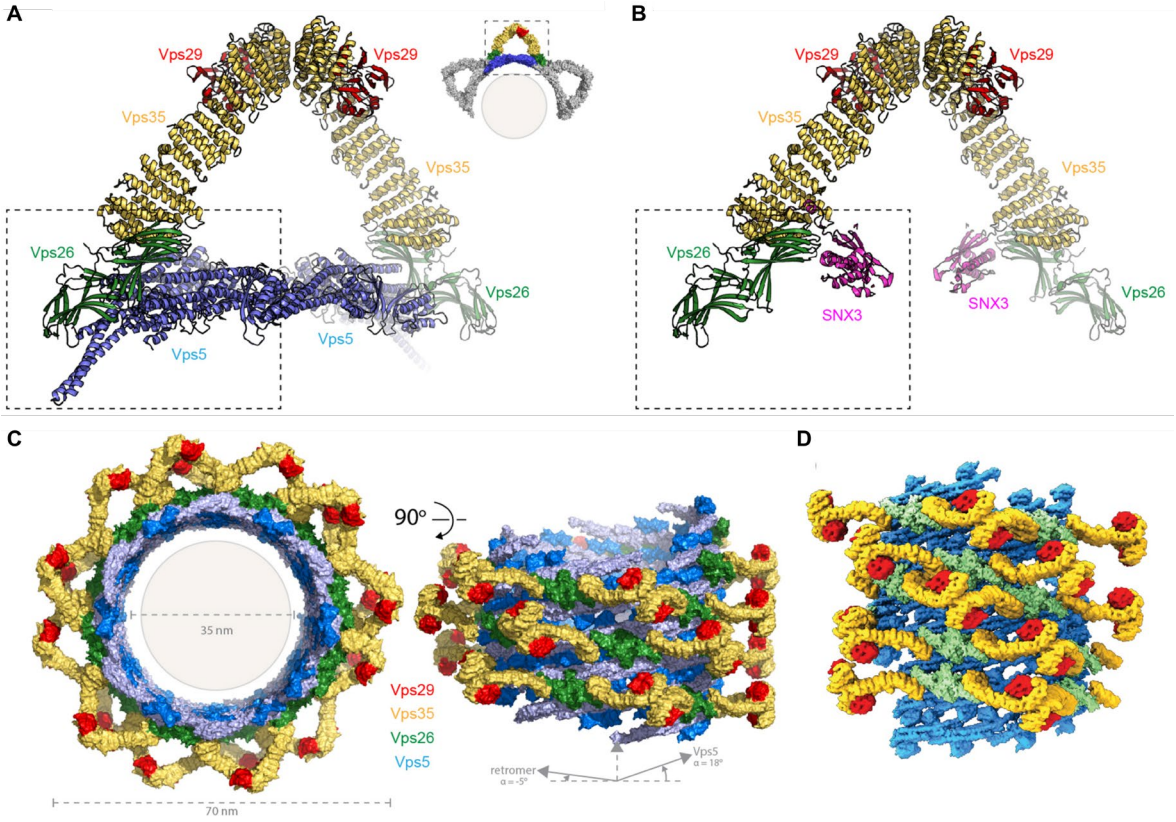

Figure 5. Cryo-ET reconstructions of the Retromer complex and its membrane-associated assemblies. (**A**) The structure of *C. thermophilum* Retromer in complex with the SNX-BAR protein Vps5 (a homologue of SNX1 in humans) determined by cryo-ET (PDB entry: 6H7W, Kovtun et al., 2018). The SNX proteins Vps5 form an inner layer of the coat made up of Vps5–Vps5 homodimers through tip-to-tip contacts between the BAR domains and lateral interactions of the PX domains between adjacent helical rows. In the cell, Vps5–Vps17 heterodimers are formed, and due to the similarity between Vps5 and Vps17, these heterodimers likely organize into a SNX array similar to Vps5–Vps5 homodimers. Retromer interacts with Vps5 via its VPS26

subunit, which remains positioned on top of the SNX layer without direct membrane interaction. (**B**) A model of SNX3 (magenta) bound to the arch-like dimer of Retromer trimers, generated by fitting the crystal structures of SNX3 bound to VPS35 and VPS26 (PDB ID: 5F0J) and VPS29-VPS35C (PDB ID: 2R17, Hierro et al., 2007) with experimental SAXS data (Lucas et al., 2016). The mode of SNX3 interaction is significantly different to that of the SNX-BAR protein Vps5. Unlike fungi, SNX3 lacks a BAR domain and does not self-interact. Here, Retromer has direct membrane contact through its VPS26 subunit, and SNX3, along with the cytosolic tail of transmembrane cargo, shows cooperative membrane binding. The arches formed by Retromer, SNX3, and cargo induce a tubular shape in the bilayer. (**C**) A simulated model of a Retromer coat, with the sub-tomographic structure of Retromer-Vps5 iteratively aligned. In this model, Vps5 forms a right-handed pseudo-helical inner layer, while Retromer creates a left-handed pseudo-helical outer layer. (**D**) A segment of a Retromer-Vps5 coated membrane tubule observed by cryo-ET showing the relatively heterogeneous structure of the assembled coat (Kovtun et al., 2018). Figure taken from (Chen et al., 2019).

1.2.2. Identification of the Retriever complex

Retriever was identified seven years ago as an additional player in the endosomal cargo recycling process of integral membrane proteins from the endosomes to the plasma membranes (McNally et al., 2017). The discovery was achieved through a comparative interactome analysis between wild-type SNX17 and SNX17 knock-down. The study identified a subset of proteins, including Retriever subunits, as interactors of SNX17 (McNally et al., 2017). The Retriever complex, along with additional partner complexes, provides an alternative mechanism for Retromer-independent endosomal sorting of cargos. This finding sparked significant interest in the scientific community studying endosomal trafficking. Since the discovery of the complex, 11 review articles have been published over the past 7 years (Chen et al., 2019; Cullen & Steinberg, 2018; Filippone & Praticò, 2021; Gershlick & Lucas, 2017; Gopaldass et al., 2024; Laulumaa & Varjosalo, 2021; McDonald, 2021; McNally & Cullen, 2018; Rabouille, 2017; Saitoh, 2022; Wang et al., 2018), highlighting its significance as a novel transport pathway for integral membrane proteins from endosomes to the plasma membrane.

Retriever is an ancient and evolutionary conserved complex, present in the last eukaryotic ancestor, and is ubiquitously expressed in nearly every human cell type examined so far (Mallam & Marcotte, 2017). This conservation and broad expression underscore Retriever's critical role in the endosomal trafficking machinery (Gershlick & Lucas, 2017). Indeed, defects in the Retriever complex have been associated with various human diseases, which will be discussed in section 1.4.

Retriever is composed of three subunits that form a stable complex: VPS29, VPS26C (previously named Downs syndrome critical region 3 or DSCR3), and VPS35L (previously known as chromosome 16 open reading frame 62 or C16orf62). The trimer complex was identified as stable

by co-elution following size-exclusion chromatography (McNally et al., 2017). Retromer and Retriever are recognized as forming independent pathways because an analysis of surface proteomes following the knockdown of SNX17 and VPS35 (a Retromer subunit) revealed that, although some cargos were shared, many other cargos were uniquely recycled by one complex but not the other, and vice versa. For instance, suppression or knockout of Retriever subunits resulted in the lysosomal degradation of cargos such as $\alpha_5\beta_1$ integrin, while knockout of VPS35 did not produce this phenotype (McNally et al., 2017).

The sequences of the Retromer and the Retriever subunits differ widely; however, they are predicted to be structurally similar, which suggests that their functions and mechanism of action may be similar. The most obvious similarity in their structural composition is that the VPS29 subunit is shared by both Retromer and Retriever. However, whether VPS29's role in controlling the assembly of retrieval complexes with regulatory components is maintained in the Retriever context remains unknown (Baños-Mateos et al., 2019). Additionally, VPS26C is a paralogue of the Retromer subunits VPS26A/B (Koumandou et al., 2011). VPS26C shares 17% sequence identity with VPS26A and 16% with VPS26B and is predicted to fold into two curved β-sheet sandwiches, similar to VPS26A/B (Laulumaa & Varjosalo, 2021). Furthermore, although VPS35L and VPS35 share little residue conservation (with only 11% sequence similarity), VPS35L is predicted to fold into an alpha solenoid containing HEAT repeats, similar to those found in VPS35. Therefore, Retriever and Retromer are hetero-trimers that contain a VPS29 subunit, a protein with an arrestin-like fold (either VPS26C or VPS26A/B, respectively), and a protein containing a series of HEAT-repeats (VPS35L or VPS35, respectively). When this thesis was started, many questions remained unanswered about this newly discovered recycling complex. The atomic structure of the complex, the molecular details of its interactions, its role in cargo recognition, and its ability to induce membrane curvature for the formation of trafficking vesicles were all unknown. Despite the described potential similarity, experimental evidence was required to determine the interaction mechanism of this complex.

The study and comparison of Retromer and Retriever from an evolutionary perspective is intriguing. Both complexes are ubiquitously expressed and trace back to the last common eukaryotic ancestor (Koumandou et al., 2011). However, while Retromer is conserved from yeast to humans, Retriever subunits VPS26C and VPS35L, as well as the WASH complex and the CCC complexes, have been selectively lost in all fungi (Wang et al., 2018). Although Retriever is present in amoeba (*Dictyostelium*), its absence in yeast and presence only in higher eukaryotes suggests that Retriever may represent a "*higher evolved"* form of Retromer. *VPS26C* belongs to the subset of about 20 genes located on locus 21q22, called the Down Syndrome Critical Region (DSCR), which is involved in the partial or full trisomy of chromosome 21 that is responsible for Down syndrome (Aubry et al., 2009).

1.2.2.1. Structure of the Retriever complex

Retriever is composed of VPS35L and VPS26C subunits, which are structurally similar to VPS35 and VPS26 of Retromer, and it shares VPS29 with Retromer. While the structure of Retromer is well-known, the structure of Retriever remained unsolved for most of my thesis period. Recently, the structure of the Retriever complex was resolved at both low and high resolution by cryo-EM, and the structure of VPS29:VPS35L$_{16-38}$ subcomplex was elucidated by X-ray crystallography (Boesch et al., 2024; Healy et al., 2023; Laulumaa et al., 2024).

Here I briefly describe the recently solved structure of the Retriever complex (**Figure 6**). The overall structural arrangement of the three Retriever subunits resembles that of Retromer. Healy *et al.* observed that both VPS35 and VPS35L are comprised of 16 HEAT-like α-helical repeat structures (Healy et al., 2023). In Retromer, the C-terminus of VPS35L is located at the VPS29-binding end. In Retriever, the major interaction of VPS29 with VPS35L is supported by the C-terminal region of VPS35L α-solenoid, which partially wraps around VPS29, similar to Retromer (Hierro et al., 2007). Residues H826 and S781 from VPS35L and residues I91 and W93 from VPS29 are important for this interaction. However, a significant difference was identified: unlike VPS35, VPS35L contains an additional conserved N-terminal sequence of about 180 residues that interacts with both the last three α-helical repeats of VPS35L and VPS29 (Healy et al., 2023). This N-terminal extension notably increases the binding interface between VPS35L and VPS29 from 1,984 Å² to 2,903 Å². This interface, composed of the C-terminal and N-terminal regions, is nearly double the size of that in Retromer (1,479 Å^2), suggesting stronger binding in the Retriever complex (Laulumaa et al., 2024). An X-ray crystal structure of the complex between VPS29 and a synthetic VPS35L peptide (E16-I38) confirmed these interactions, as L27 to L35 of VPS35L interact with two hydrophobic pockets on VPS29 (PDB ID: 8ESE, (Healy et al., 2023) (**Figure 6C**). The conserved ^{34}PL^{35} side chains of VPS35L bind the VPS29 pocket defined by V174 and L152, respectively. It is worth noting that the PL motif of VPS35L blocks a binding site on VPS29 and thereby prevents Retriever from engaging accessory proteins that Retromer recruits through VPS29, including VARP and TBC1D5. Thus, the incorporation of VPS29 into Retriever is mutually exclusive with its ability to function in canonical Retromer-mediated transport. Interestingly, a mutation in VPS29 (Y169), which decreases VPS29 binding to VPS35L, simultaneously increased binding to Retromer components VPS35 and VPS26A/B, suggesting potential competition between Retriever and Retromer for the same pool of VPS29 in cells (Boesch et al., 2024).

In addition to the structural insights into the Retriever complex provided by the Commander studies (Healy et al., 2023; Laulumaa et al., 2024), a few months later, another research group (Boesch et al., 2024) reported a high-resolution structure of the Retriever complex at 2.9 Å, determined through cryo-EM using single-particle reconstruction (**Figure 6A,B**). This study

confirmed the presence of a 37-residue motif at the N-terminus of VPS35L which acts as a "belt" surrounding VPS29. Another distinct feature of Retriever, compared to Retromer, is the long unstructured peptide linker in VPS35L that follows the "belt" sequence. The serine-rich sequence of this unstructured linker is highly conserved among vertebrates, hinting at its potential role in regulatory interactions or post-translational modifications, which are yet to be explored.

VPS26C, on the other hand, interacts with the second and third α-helical repeats in VPS35L through its C-terminal β-sandwich subdomain. The residue R293 in VPS35L is essential for VPS26C binding, while it is not required for interactions with VPS29 or the CCC complex (Healy et al., 2023). In the model of Retriever within the Commander complex, the α-solenoid appears more compact and bent at the VPS26-binding region compared to Retromer (Laulumaa et al., 2024). Notably, Retriever adopts a more compact and twisted conformation than Retromer, being approximately 40 Å shorter in its longest dimension. Additionally, Retriever has a less negatively charged molecular surface compared to Retromer. Both VPS35L and VPS26C exhibit more compact structures than their homologues, VPS35 and VPS26A, respectively. In contrast, the globular VPS29 subunit maintains an almost identical structure in both Retriever and Retromer (Boesch et al., 2024).

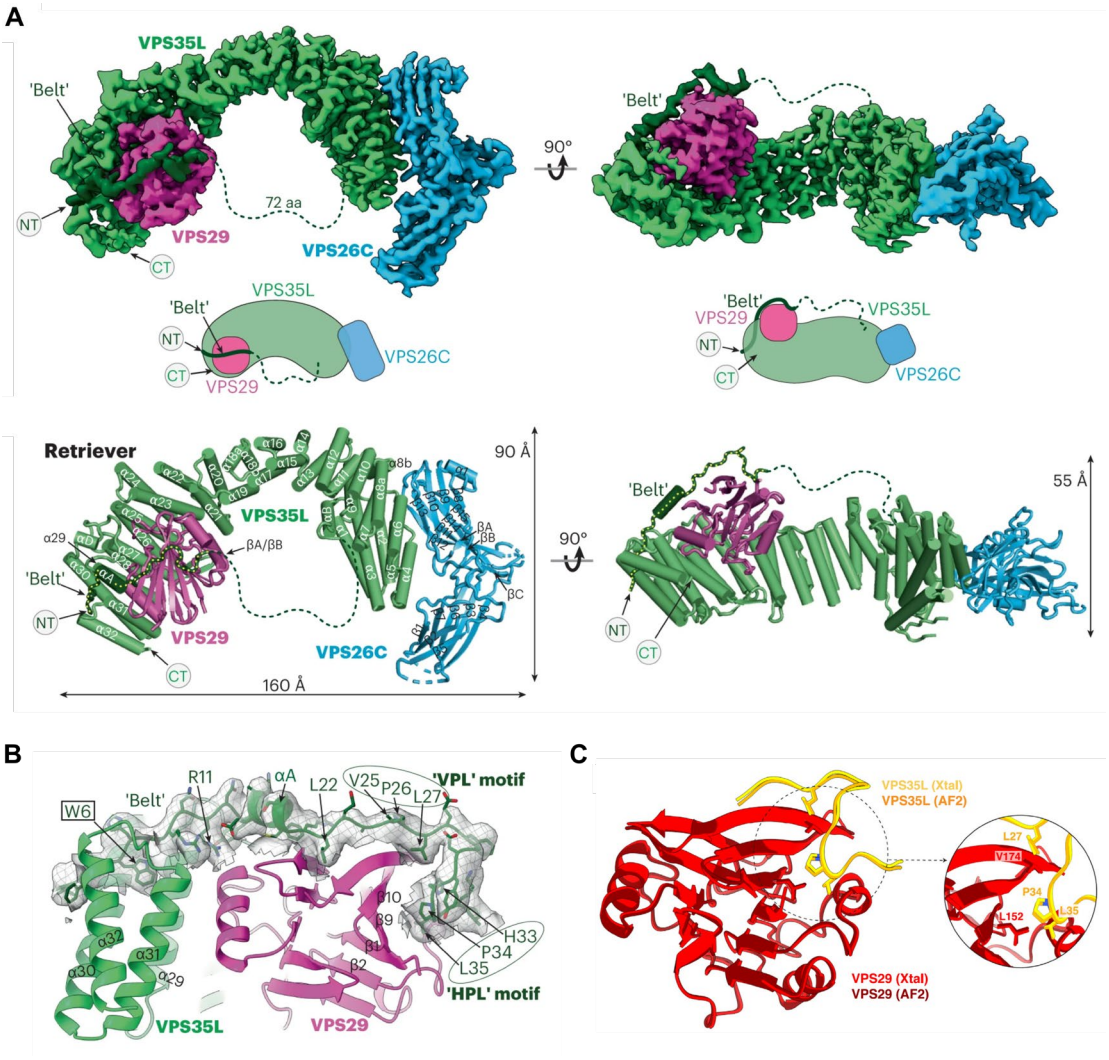

Figure 6. Cryo-EM structure of the Retriever complex. (**A**) Top panel: Cryo-EM map (EMD: 40886; PDB: 8SYO) and schematic of the Retriever complex, with VPS35L colored in green, VPS29 in pink, and VPS26C in blue. Bottom panel: The Retriever structure is displayed in cartoon representation. Secondary structural elements are labeled. Dotted lines represent the putative flexible linker sequence in VPS35L not observed in the map. The "belt" sequence unique to VPS35L is traced by yellow dotted lines (Boesch et al., 2024). (**B**) Cryo-EM density of the 'belt' sequence interacting with VPS35L and VPS29 (Boesch et al., 2024). (**C**) A 1.35-Å crystal structure of VPS29 bound to VPS35L (16-38) confirms the binding of the core 34PL35 motif to VPS29 and the extended interaction of adjacent residues predicted by AF2. The crystal structure is aligned with the AF2 model and represented in carton, with VPS29 colored red and VPS35L peptide in yellow (Healy et al., 2023).

1.2.2.2. Cargos of the Retriever complex

Potential **cargos of Retriever** were identified through proteomic analysis after silencing SNX17 and comparing the cell surface proteome in HeLa cells with a control (McNally et al., 2017). Over 120 cell surface proteins were identified that require SNX17 to avoid lysosomal degradation, including numerous integrins, signaling receptors, solute transporters, and cell adhesion proteins. All these cargos contain an NPxY sorting motif in their cytosolic tails, which is the conserved 4-residue sequence recognized by SNX17. Additionally, another study identified numerous cargos of SNX17 and SNX31 by performing an array screen comprised of multiple peptides containing NPxY motifs derived from transmembrane proteins incubated with these SNXs (Ghai et al., 2013a). Consistent with this, 236 membrane proteins showed altered levels in *VPS35L* knockout cells (Boesch et al., 2024).

Based on the previously described proteomic study (McNally et al., 2017), it is noteworthy that various membrane proteins have been related to both Retromer and Retriever complexes, such as APP (amyloid precursor protein), CD97 (cluster of differentiation 97), ITGA7 (integrin α7), and ITGB8 (integrin β8). However, the recognition mechanisms differ, as Retromer and Retriever are associated with different SNXs. Conversely, there are other cargos specific to either Retromer or Retriever, and not recognized by any other recycling machinery. For instance, ITGA1, ITGA4, ITGB1, LRP1, VAPB (VAMP associated protein B and C), and TYRO3 (tyrosine-protein kinase receptor) seem to be Retriever-specific (as their levels were only affected by SNX17 suppression), while cargos like GLUT1 (glucose transporter 1), LRP10 (LDL receptor-related protein 10), LRP5, or CD70 are likely Retromer-specific (as their levels were altered upon VPS35 or SNX27 suppression, proteins not associated with Retriever). However, it should be noted that a direct association between most of these cargos and the retrieval complexes has not yet been experimentally confirmed.

Currently, evidence for Retriever involvement in the SNX17-defined cargo is available so far only for ß1-integrin (ITGB1), LRP1 (low-density lipoprotein receptor-related protein L1) (McNally et al., 2017), and LDLR (low-density lipoprotein receptor) (Vos et al., 2023). In the absence of SNX17 or Retriever, these cargos have been shown to undergo lysosome-mediated degradation (McNally et al., 2017).

This thesis focuses on the following four potential Retriever cargos: **LRP1, APP, ITGB1** and **VEGFR1** (vascular endothelial growth factor receptor 1). This choice is based on the clinical relevance of proper trafficking of these cargos, as alterations in their membrane levels contribute to the development of severe diseases.

LRP1 is a multifunctional receptor involved in various physiological processes, particularly in lipid metabolism, cellular signaling, and protein homeostasis. It plays a key role in the uptake of lipoproteins, such as low-density lipoproteins (LDL), which helps regulate cholesterol levels in the body. LRP1 is also responsible for the uptake of other extracellular molecules, including proteases, protease-inhibitor complexes, and other protein debris, contributing to maintain tissue homeostasis. Additionally, LRP1 interacts with multiple ligands, such as growth factors and integrins, and is involved in a variety of cell signaling pathways (Sizova et al., 2023).

Dysregulation of the LRP1 receptor has been linked to neurodegenerative diseases, atherosclerosis, and cancer. For example, LRP1 regulates the endocytosis and subsequent spread of the tau protein in the brain, with tau misfolding and aggregation playing a role in several forms of dementia (Rauch et al., 2020). Animal models of CCC deficiency and patients with *CCDC22* hypomorphic mutations present LDLR mis-trafficking, resulting in hypercholesterolemia due to lower uptake of LDL-cholesterol, the LDLR ligand (Bartuzi et al., 2016). Additionally, certain cancer cell lines including brain, liver, and lung exhibit elevated levels of LRP1 expression, suggesting its upregulation in tumors (Sizova et al., 2023).

APP is a type I transmembrane protein involved in several critical cellular processes, particularly in the brain. APP plays a role in maintaining synaptic structure and function, promoting neurite outgrowth, and mediating cell adhesion and migration. Notably, APP enhances synaptic plasticity, which allows neurons to modify synaptic connections based on activity levels. This is crucial for learning and memory. Neurite outgrowth is vital for neuronal development, growth, and regeneration following injury (Z. Zhou et al., 2011). APP is also implicated in metal ion homeostasis, especially in regulating copper and zinc levels in the brain, which plays a role in oxidative stress and neuronal injury (Wild et al., 2017). APP undergoes enzymatic processing through two competitive pathways. The non-amyloidogenic pathway involves α-secretase processing, producing soluble APP-α, which is neuroprotective. In contrast, the amyloidogenic pathway is initiated when APP is

processed by BACE1 (β-site APP-cleaving enzyme 1), a β-secretase. This triggers the production β-amyloid peptides, which are neurotoxic and widely associated with Alzheimer's disease (Tan & Gleeson, 2019). A lack of APP recycling increases the tendency to follow this amyloidogenic pathway, leading to the accumulation of these toxic peptides (Cam & Bu, 2006).

SNX17 plays a role in regulating APP levels. Experiments have shown that overexpression of a dominant-negative mutant of SNX17 and RNA interference knockdown of endogenous SNX17 both reduced APP levels at the plasma membrane. This decrease in APP at the plasma membrane was accompanied by a concomitant increase in Aβ production (J. Lee et al., 2008). Notably, LRP1 closely is linked to APP, as LRP1 can affect APP trafficking and processing through interactions with both extracellular and intracellular domains (Filippone & Praticò, 2021).

Additionally, **ITGB1** is of interest because integrins control cell adhesion and migration, which are vital for maintaining normal physiological processes (Wozniak et al., 2004). Through the dynamic regulation of focal adhesion complexes, integrins on the cell surface connect the intracellular actin network to the extracellular matrix (Vicente-Manzanares et al., 2009). Integrins are heterodimers of α and β chains, and β1-integrin is the most commonly found integrin β subunit. In mammals, 24 different α/β heterodimeric combinations exist, found in active or inactive conformations with high or low affinity for their extracellular matrix (ECM) ligands (Hynes 2002). Integrins continuously cycle between the plasma membrane and internal compartments, with low lysosomal degradation rates (Shafaq-Zadah et al., 2016). It has been shown that integrin levels at the cell surface are controlled by both their endocytosis into endosomes and their subsequent recycling back to the plasma membrane (Moreno-Layseca et al., 2019). Thus, understanding how integrin recycling is controlled is of great interest. Evidence suggests that the Retriever-SNX17 recycling pathway recycles ITGB1 from endosomes to the plasma membrane, playing key roles in regulating synaptic function and plasticity (Rivero-Ríos et al., 2023).

Finally, **VEGFR1** is a critical receptor in humans that regulates vascular development, angiogenesis, and inflammation. Its altered expression or signaling is linked to various pathological conditions, including cancer, retinal diseases, cardiovascular disorders, and complications in pregnancy like preeclampsia (Laakkonen et al., 2019; Penn et al., 2008).

1.2.2.3. Partners of the Retriever complex

Several partners of the Retriever complex have been identified through proteomics screenings, including **SNX17, SNX31, the WASH complex, the CCC complex, and DENND10** (Singla et al., 2019) (**Figure 7**).

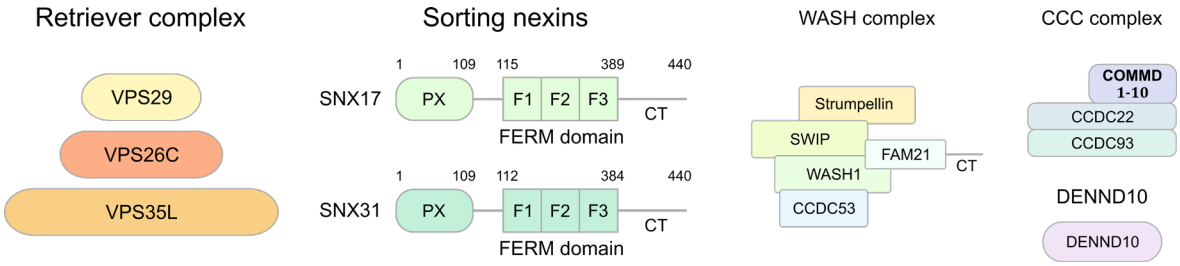

Figure 7. Diagram of Retriever subunits and associated proteins implicated in the Retriever-dependent recycling pathway. The Retriever complex comprises the proteins VPS26C, VPS29 and VPS35L. The WASH complex contains the subunits Strumpellin, SWIP, WASH, FAM21 and CCDC53 subunits, while the CCC complex is formed by CCDC22, CCDC93, and 10 members of the COMMD protein family. The SNXs related to Retriever, SNX17 and SNX31, both contain a PX domain, which binds PI3P, a lipid enriched in endosomal membranes, a FERM-like domain responsible for cargo recognition and binding, and a C-terminal tail suggested to associate with Retriever. *VPS*, Vacuolar Protein Sorting; *WASH*, Wiskott–Aldrich syndrome protein or WASP and SCAR homologue; *SNX*, Sorting Nexin; *PX*, Phox-homology; *FERM*, band 4.1/ezrin/radixin/moesin domain; *CT*, C-Terminal; *DENND*, DENN(differentially expressed in normal and neoplastic cells) domain-containing protein; *CCC*, CCDC22, CCDC93, and COMMD; *COMMD*, Copper Metabolism MuRR1 Domain; *CCDC*, Coiled-Coil Domain-Containing.

SNX17 and SNX31

Similar to Retromer, Retriever interacts with specific members of the **sorting nexin (SNX) family**, which play a crucial role in the recycling pathway. The sorting nexin members associated with Retriever are **SNX17 and SNX31.**

SNX17 and SNX31 are the most closely related SNXs, sharing 37% sequence identity in mice, but SNX31 is a poorly characterized homolog of SNX17. In addition, SNX31 is important for the recycling of cargos such as certain β1 integrins, similar to SNX17, so their mechanisms of cargo recognition are expected to be similar. It should be noted that while SNX17 is ubiquitously expressed, its paralog SNX31 is found mainly in the urinary tract (Tseng et al., 2014).

Both SNXs contain a PX domain, a FERM-like domain, and a C-terminal tail (CT) (**Figure 3**). The PX domain binds preferentially to PI3P, a lipid that is enriched in endosomal membranes (Chandra et al., 2019; Knauth et al., 2005). The FERM-like domain plays an important role as it

interacts with the cargo through the recognition of NPxY or NxxY sorting motifs located in the cytosolic tails of the cargos (Ghai et al., 2013a). It is named "FERM-like" because it differs subtly from the canonical FERM domain. FERM domains are composed of three subdomains called F1, F2 and F3 modules. Unlike classical FERM domains, SNX17 and SNX31 possess an altered F2 module. The F2 modules of SNX17 and SNX31 are predicted to contain three helices instead of the usual four and are shorter than the standard F2 structure, being about 50 residues long instead of the typical 100. Therefore, SNX17 and SNX31 have all the characteristics of a FERM domain but with a slightly modified F2 module (Ghai et al., 2011). The F3 module is responsible for binding to cargos, so the role of the domain seems consistent with canonical FERM domains. For this reason, the "FERM-like" domains of SNX17 and SNX31 have been referred to as "FERM" for simplicity in this thesis. It is worth noting that none of the Retriever-associated SNXs identified so far (SNX17 and SNX31) contains a BAR domain, so it is unknown whether Retriever can induce membrane curvature on its own or if it requires additional protein interactions for this purpose.

It is noteworthy that SNX27, a specific SNX from Retromer, also contains a FERM domain, with a sequence identity of around 25% compared to SNX17. The presence of a FERM domain suggests that SNX27 is presumably able to recognize NPxY motifs. However, there is controversy in the literature regarding the mechanism of cargo recognition by SNX27 (Wang et al., 2022). Some studies have shown binding affinity of SNX27 to the cargos P-selectin and APP by GST pull-downs, and this binding was abrogated by mutating the F3 region of SNX27 (W475A and K520Q mutations), where the binding site for recognition of NPxY cargo is located (Ghai et al., 2013a). Notably, certain proteins identified in SNX27 proteomics do not possess PDZ motifs: some possess NPxY sequences, whereas others may be recruited through as-yet-undetermined mechanisms. Other studies have determined that the PDZ domain of SNX27, located at its N-terminus, binds directly to VPS26 as well as to cargo proteins with PDZ-binding motifs including GLUT1 and the β2-adrenergic receptor (β2AR). These studies demonstrated that the function of the SNX27 FERM domain involves binding to WASH complex and SNX-BAR complex components SNX1 or SNX2 (Clairfeuille et al., 2016; Steinberg et al., 2013). Therefore, whether SNX27 is able to recognize certain cargos through an NPxY motif, as occurs with SNX17 and SNX31, remains unresolved.

It has been suggested that the C-terminal region of SNX17 and SNX31 interacts with Retriever through the VPS26C subunit, particularly through the last four residues of the C-terminus. However, it was unknown whether this interaction is direct or indirect (McNally et al., 2017). Some researchers have proposed that an unidentified intermediate protein between Retriever and SNX17 might be involved, suggesting that the binding could be indirect (Healy et al., 2022). Chen *et al.* discussed the potential involvement of a PDZ binding-motif (PDZbm) domain (formed by the C-terminal sequence DEDL) in the interaction with Retriever, either directly or via another protein (Chen et al., 2019). However, the exact mechanism of interaction remained unknown. Interestingly, in addition to

potentially interacting directly or indirectly with the Retriever complex, the DEDL region of SNX17 has been shown to interact with several members of the PDZ and LIM domain-containing (PDLIM) protein family, including PDLIM1, PDLIM4, and PDLIM7 (Healy et al., 2022). PDLIM proteins are multi-domain scaffolds typically associated with actin and its accessory proteins, such as α-actinins and myotilin. Given that the major function of PDLIMs is to regulate actin-mediated processes, it has been speculated that SNX17, Retriever/CCC, PDLIMs, and the WASH complex could be cooperating to control normal endosomal trafficking, with PDLIM possibly serving as an intermediate protein linking SNX17 with Retriever. However, no direct interaction between Retriever and PDLIM has been reported. If SNX17 interacts with both Retriever and PDLIM through its C-terminal peptide, it remains unclear whether Retriever and PDLIM bind competitively or cooperatively (Wang et al., 2022).

WASH complex

Two additional complexes are involved in the Retriever recycling pathway: the CCDC22, CCDC93, and COMMD (CCC) complex, and the Wiskott–Aldrich syndrome protein or WASP and SCAR homologue (WASH) complex. Retriever requires both the CCC and WASH complexes for endosomal localization and function.

The **WASH complex** is an evolutionarily conserved complex present in many eukaryotic taxa, including some unicellular organisms, although it is absent in the yeast *S. cerevisiae* (as is the Retriever complex, as previously described), and is ubiquitously expressed in mammalian tissues (Li et al., 2014; Seaman et al., 2013). The WASH complex facilitates the formation of branched F-actin on endosomal membranes, which is required for vesicle formation in both Retromer and Retriever-dependent pathways. The role of the WASH complex in Retromer-independent pathways was confirmed because VPS35-KO cells showed a reduction in the amount of endosomal-localized WASH complex, although a significant amount was still present (McNally et al., 2017). The induction of branched patches by the WASH complex creates a platform of discrete domains where specific proteins are sorted for transport. Through the elongation of actin filaments, a localized force is generated that may be involved in the production and/or scission of endosomal tubules, along with other proteins such as dynamin II(Seaman et al., 2013). Without WASH-dependent actin polymerization, cargos are trapped in the endosomal compartment, leading to their default trafficking to lysosomes for degradation (Boesch et al., 2024).

The WASH complex comprises five proteins that operate as an obligate complex (with new nomenclature for the subunits in parentheses): SWIP (Strumpellin and WASH interacting protein), also known as KIAA1033 (WASHC4), Strumpellin, also known as KIAA0196 (WASHC5), WASH1

(WASHC1), FAM21A/B/C (WASHC2A/B/C), and CCDC53 (WASHC3) (Jia et al., 2010). Although some controversy exists, generally, depletion of individual subunits impacts the stability of the other subunits (Wang et al., 2018).

To achieve its role, **WASH1** subunit activates the ubiquitously expressed actin-related protein 2/3 (Arp2/3) complex, a nucleation-promoting factor (Derivery et al., 2009). **Strumpellin** and **CCDC53** subunits play structural roles in maintaining complex stability and functionality. The **SWIP** subunit interacts with several PI species such as PI3P and PI(3,5)P2, demonstrating an intrinsic ability to associate with liposomes (Dostál et al., 2023). FAM21 is also comprised of a head domain (~220 amino acids), necessary for interacting with other members of the WASH complex, and a long C-terminal disordered tail harboring 21 repeats of leucine-phenylalanine (LFa) acidic motifs. The FAM21 tail is believed to act as an endosomal signaling hub, recruiting numerous proteins, including the actin-capping protein CapZ, ANKRD50, FKBP15, TBC1d23, RME-8, Retromer complex, and the CCC complex (Jia et al., 2012). A direct interaction of FAM21 with VPS35 and VPS29 provides a link between the WASH complex and Retromer (Guo et al., 2024; Jia et al., 2012; Romano-Moreno et al., 2024). In fact, a mutation in VPS35 (D620N), associated with early onset Parkinson's disease, diminishes the interaction of the WASH complex with Retromer and consequently impairs Retromer-mediated cargo trafficking (McGough et al., 2014; Zavodszky et al., 2014). WASH is linked with the Retriever pathway through a direct interaction to the subunit CCDC93 from the CCC complex. The WASH complex also has ability to bind to ESCPE-1 through the SNX1-interacting DNAJ protein RME8 and to the SNX27 FERM domain. In a FAM21 KO HeLa cell line, VPS35L endosomal localization was found to be abrogated (McNally et al., 2017).

CCC Complex

CCC complex is another large multiprotein complex linked to Retriever. It consists of twelve subunits: ten members of the Copper Metabolism MuRR1 Domain (COMMD) family, **COMMD1-COMMD10**, and the coiled-coil domain-containing (CCDC) proteins **CCDC22 and CCDC93**. The CCC complex can be co-eluted as a 600 kDa complex in size-exclusion chromatography (Wan et al., 2015a).

COMMD1 was discovered first and initially named MURR1 (Van De Sluis, 2002). Later, it was renamed Copper-metabolism Murr1 Domain (COMMD1) after its identified role in regulating copper homeostasis (Burstein et al., 2005). COMMD proteins are approximately 20 kDa in size and generally contain a C-terminal COMM domain and an N-terminal HN domain. The exception is COMMD6, which has a shortened HN domain. Although the HN domain varies in sequence, it retains a conserved globular structure composed of six α-helices (α1-α6). In contrast, the COMM

domain exhibits high sequence similarity across the ten proteins and consists of three antiparallel β-strands (β1- β3), and a C-terminal α-helix. The COMM domain forms obligate dimers, resulting in the formation of elongated homo- and heterodimers (Healy et al., 2018). When individual COMMD proteins are knocked out, there is a significant decrease in the levels of all COMMD proteins, indicating that they likely form a larger complex and do not function independently (Fedoseienko et al., 2018). All ten *COMMD* genes in vertebrates are 90% conserved in mammals, while individual *COMMD* genes are found in genomes of lower metazoans such as insects and worms (Van De Sluis, 2002).

CCDC22 and CCDC93 belong to the group of microtubule-associated proteins. They contain an N-terminal microtubule binding NDC80 and NUF2 calponin homology domain (NN-CH) and a C-terminal coiled-coil domain. Structural information about these proteins was not available until recently. CCDC proteins often serve as scaffolds in larger protein complexes. Using cross-linking mass spectrometry, COMMD9 was shown to interact with the NN-CH domain of CCDC93 (Healy et al., 2018).

Cellular functions of COMMD proteins, such as hypoxia response (Van De Sluis, 2002) and nuclear factor-κB activation (Maine & Burstein, 2007), have been reported for some time. However, the role of the CCC complex in recycling pathways has only recently been identified. The CCC complex functions as a negative regulator of WASH complex recruitment to endosomes. Branched F-actin deposition induced by the WASH complex is essential for maintaining the structure of the endolysosomal network, promoting the effective fission of membrane tubules and trafficking of cargo proteins. However, excess endosomal F-actin accumulation hinders endosomal cargo recycling, and the CCC complex plays a role in regulating this process (Singla et al., 2019).

CCC function is achieved through the modulation of PI3P levels on endosomal membranes via recruitment of the lipid phosphatase MTMR2, which converts PI3P to PIs. Hypomorphic mutations in MTMR2 are associated with Charcot–Marie–Tooth syndrome, a genetic disorder affecting peripheral nerves. However, the spectrum of defects associated with CCC deficiency is broader and more severe, including neurological impairments and congenital heart defects, suggesting the CCC complex has functions beyond MTMR2 regulation (Singla et al., 2019). Indeed, CCC complex components interact with other proteins, including direct binding between the FAM21 subunit of the WASH complex and CCDC93 of the CCC complex. This interaction is supposed to be responsible for the recruitment of the CCC complex to endosome (Phillips-Krawczak et al., 2015). The CCC complex, largely conserved throughout evolution (Burstein et al., 2005), exhibits close co-evolution with the WASH complex (Li et al., 2014). Notably, defects in either complex lead to similar pathologies. For instance, mutations in CCDC22 in humans cause intracellular copper accumulation and modest copper alterations due to impaired trafficking of the copper transporter ATP7A (Phillips-

Krawczak et al., 2015). Furthermore, these individuals are hypercholesterolemic due to deregulated cholesterol homeostasis and low-density lipoprotein receptor (LDLR) trafficking. Similar defects are observed in *Commd1* knockout mice, hepatic COMMD9-deficient mice, and humans with mutations in WASH complex component Strumpellin (Bartuzi et al., 2016), highlighting the interaction between the WASH and CCC complexes. In addition, other cargos, such as Notch receptors, are also altered upon CCC deficiency, but the affected pathway is unknown (Singla et al., 2019).

Additionally, the CCC complex is functionally linked to recycling events mediated by either Retromer/SNX27 or Retriever/SNX17 (Laulumaa et al., 2024; Singla et al., 2019). Loss of CCC complex components, as well as Retromer subunit VPS35 or SNX27, impairs endosome-to-plasma membrane recycling of ATP7A, indicating CCC is essential for certain Retromer/SNX27 cargo recycling (Phillips-Krawczak et al., 2015). Conversely, COMMD1-deficient mice show reduced surface levels of LDLR, a Retriever-SNX17 cargo (Bartuzi et al., 2016). Proteomic studies have also shown interactions between the CCC complex and Retriever components (Singla et al., 2019), as well as SNX17 (McNally et al., 2017). However, a direct interaction between CCC complex and Retromer and/or SNX27 has not been described so far.

Interestingly, VPS35L has been identified as a shared protein between the CCC and Retriever complexes (Singla et al., 2019). In some studies, the CCC complex, Retriever, and DENND10 are considered to form a single large multisubunit assembly known as the **Commander complex** (Boesch et al., 2024; Healy et al., 2023; Wan et al., 2015). This complex is implicated in recycling various internalized cargos such as ATP7A, ATP7B, GLUT1, LDLR, and NOTCH2 (neurogenic locus notch homolog protein 2) (Bartuzi et al., 2016; McNally et al., 2017; Singla et al., 2019). The recruitment mechanism of the Commander complex to endosomal membranes has not yet been elucidated. To narrow down this broad question, this thesis has focused on the Commander subcomplex Retriever. To date, it is unclear whether Retriever can function independently of the Commander complex. Although the Commander complex has been purified as a single multiprotein assembly, some studies have isolated only the Retriever subcomplex, suggesting that the Commander complex might disassemble during sample preparation or that Retriever and CCC may function independently (Boesch et al., 2024; Healy et al., 2023; Laulumaa et al., 2024; Singla et al., 2019). This latter hypothesis is supported by findings that CCC complex silencing does not affect Retriever expression (McNally et al., 2017), and that CCC regulates the trafficking of Retriever-independent cargos, such as ATP7A and TGN46 (Phillips-Krawczak et al., 2015). Additionally, Singla *et al.* demonstrated that CCC components COMMD1 and CCDC22 migrated around 700 kDa, whereas VPS35L appeared in two complexes: one ~700 kDa and another ~250 kDa (Singla et al., 2019). Similarly, Boesch *et al.* found that VPS35L partitioned into two distinct complexes: a smaller one (~240 kDa) corresponding to Retriever, and a larger one (~720 kDa), containing CCC, confirmed by

COMMD1 immunoblotting (Boesch et al., 2024). These findings suggest that the interaction between Retriever and CCC is not constitutive; Retriever may exist either as part of the Commander complex or independently, highlighting the importance of studying Retriever in isolation.

DENND10

In addition to the twelve subunits of the CCC complex and the three subunits of the Retriever complex, a 16th subunit has recently been incorporated into the large Commander complex: **DENND10**, also known as FAM45A. DENND10 was identified as a partner of the CCC and Retriever complexes through co-immunoprecipitation assays, though it is not required for Commander stability, and its deletion does not affect recycling of cargos such as α5 integrin (Singla et al., 2019).

DENND10 contains a single DENN (differentially expressed in normal and neoplastic cells) domain and belongs to a family of guanine nucleotide exchange factors (GEFs) that activate Rab proteins to coordinate intracellular trafficking. However, the exact role of this protein in the Commander complex remains unknown (Healy et al., 2023). DENND10 has been proposed to interact with Rab27A or Rab27B, participating in the homeostasis of late endosomes (J. Zhang et al., 2019). However, comparison to the structure of DENND1B in complex with Rab35 revealed that the putative Rab binding site of DENND10 is obstructed when bound to the Commander complex, suggesting that DENND10 may be inactive in this conformation (Laulumaa et al., 2024). Nevertheless, the inherent flexibility of this region may enable Rab binding in another conformation that exposes the binding site, or DENND10 may bind Rabs in an unconventional manner. For now, the exact role of DENND10 remains unknown.

1.2.3. Structure of the Commander complex

Until recently, only the structure of COMMD9 had been solved using X-ray crystallography (Healy et al., 2018). Based on the known structure of COMMD9, the remaining subunits of the COMMD proteins were modelled with AlphaFold (Laulumaa & Varjosalo, 2021). However, the complete structure of the Commander complex remained uncharacterized and the stoichiometry of its various subunits was unknown until last year. Three different research groups made significant strides in understanding the complex's structural organization by combining data from cryo-electron microscopy (cryo-EM), X-ray crystallography, *in silico* predictions, and mutational analysis (Boesch et al., 2024; Healy et al., 2023; Laulumaa et al., 2024) (**Figure 8**).

The Commander complex contains a single copy of each subunit. CCDC22 and CCDC93 adopt a coiled-coil structure and extensive interact with the COMMD proteins, Retriever, and DENND10. CCDC22 and CCDC93 stabilize the hetero-decameric ring formed by five specific heterodimers of COMMD proteins. Additionally, they recruit DENND10 and connect the CCC and Retriever assemblies through a conserved C-terminal region of VPS35L, which is distal from VPS26C and VPS29. In fact, VPS35L$_{R661A}$ and VPS35L$_{I710D}$ mutants abolished CCC complex association (Healy et al., 2023). Surprisingly, disrupting the interaction between VPS29 and VPS35L also eliminated the interaction between VPS35L and CCDC22-CCDC93, suggesting an interdependence between VPS29-VPS35L and Retriever-CCC interactions. Conversely, the association of VPS26C with VPS35L does not contribute to the Retriever-CCC interaction. Since VPS29 does not bind directly to CCDC22-CCDC93, it is suggested that VPS29 facilitates a favorable conformation of VPS35L necessary for its interaction with CCC (Boesch et al., 2024).

They cryo-EM structure of the Commander complex was recently published by Laulumma *et al.* (Laulumaa et al., 2024). They found that the complex is divided into two distinct halves, each with different functions. The lower half features two main effectors that link it to SNX-coated PI3P-rich membranes and connect it spatially and temporally to DENND10 and the WASH complex. This lower half is more variable in both composition and conformation. In contrast, the upper half of the complex is more rigid at its core and may serve either as a cargo recognition site or as a platform for assembling protein complexes in the cytosol, due to the flexible binding sites on the COMMD N-terminal domains. Additionally, they analyzed the interactome of the Commander complex using mass spectrometry-based proteomics, and identified a set of biological processes in which Commander components are involved, including transcriptional regulation, vesicle exocytosis, and microtubule-based cell remodeling. Furthermore, they discovered associations with other processes such as cilium assembly, as well as centrosome and centriole functions.

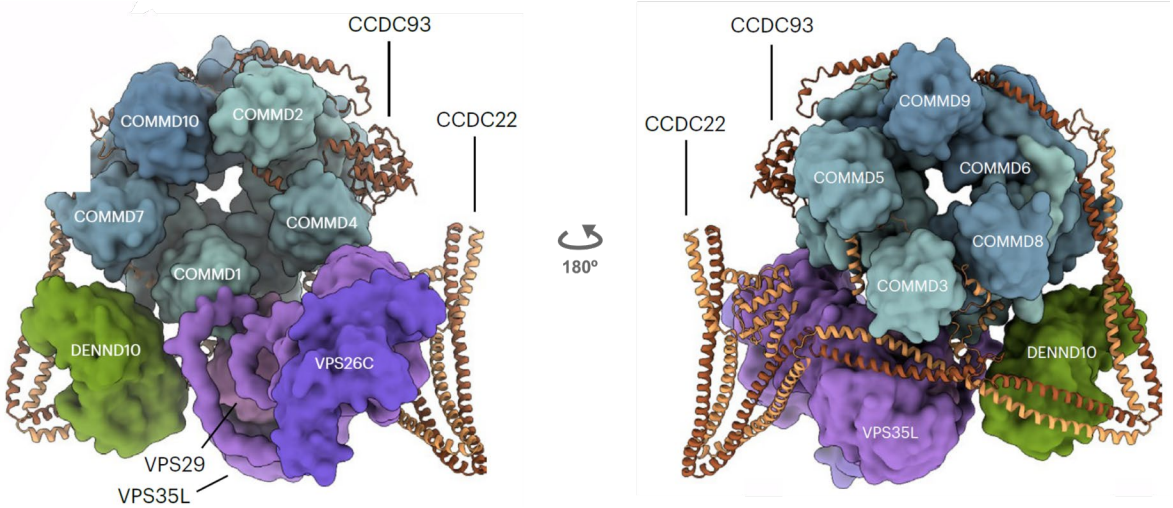

Figure 8. Overall structural model of the Retriever-CCC-DENND10 complex. Model of the Commander complex, combining a composite map from cryo-EM and AlphaFold2 (AF2) modeling, showing two orientations of the complex. The COMMD1-10 ring is tethered between the CCDC proteins and Retriever, binding extensively to the linkers between the CCDC CH domains and the coiled-coil regions. The CH domain of CCDC22 interacts with the C-terminal coiled-coil region adjacent to Retriever, helping to maintain a relatively compact configuration of the entire complex. Additionally, CCDC22 and CCDC93 recruit DENND10. Figure taken from Laulumaa *et al.* (Laulumaa et al., 2024).

However, it remains unknown how the Commander complex interacts with the membrane and forms endosomal coats, as well as the conformation it assumes during these processes (Gopaldass et al., 2024).

1.3. Defects in the Retriever recycling pathway in human health

The recycling pathway determines the localization and relative quantity of many proteins in the plasma membrane. Recent studies have identified several human diseases associated with mutations in the Retriever recycling pathway, highlighting the importance of this pathway in the biogenesis and homeostasis of eukaryotic cells and organelles. Biallelic loss-of-function variants (c.1097dup; p.Cys366Trpfs*28 and c.2755G>A; p.Ala919Thr) in *VPS35L* have been recently identified as the cause of a cranio-cerebello-cardiac dysplasia, similar to a syndrome known as Ritscher-Schinzel/3C (Kato et al., 2020). Additionally, a homozygous nonsense variant (c.178G>T; p.Glu60*) in the *VPS26C* gene has been associated with a novel syndrome characterized by neurodevelopmental deficits, growth failure, skeletal abnormalities, and distinctive facial features (Beetz et al., 2020). Moreover, the *VPS26C* gene is codified in the Down Syndrome Critical Region, which is associated with the pathogenesis of Down Syndrome, and is overexpressed in individuals with this syndrome (Lockstone et al., 2007). The significance of Retriever in endosomal sorting is underscored by its critical role during fetal development, as evidenced by the embryonic lethality resulting from homozygous knockout of the *VPS35L* gene in mice (Kato et al., 2020).

The structural analysis of the Commander complex by Healy *et al.* has enabled the identification of mutation locations associated with XLID and RSS. Most missense mutations are found in crucial structural elements or at inter-subunit interfaces, and all tested mutations result in a substantial decrease in overall Commander protein levels. In contrast, deletions and frameshift mutations in VPS35L near the VPS29 binding site specifically affect VPS29 interaction without significantly disrupting the overall assembly of the Commander complex. This demonstrates that XLID/RSS mutations can cause either general instability of the Commander complex or disruption of specific interactions within it, underscoring the critical role of VPS29 in Commander function (Healy et al., 2023).

A comprehensive analysis of the COSMIC (Catalogue Of Somatic Mutations In Cancer) database has revealed two somatic mutations in VPS35L linked to cancer: G902E, which disrupts binding to VPS29, and G325E, which impairs binding to VPS26C. Both mutations affect the assembly of the Retriever complex. Notably, the frequency of somatic mutations associated with cancer in VPS35L exceeds that in its closest paralog, VPS35, across all tumor types. Furthermore, the cancer-associated mutations in VPS35L replicate many of the alterations observed in the cell membrane proteome of *VPS35L* knockout cells (Boesch et al., 2024).

There have also been descriptions of mutations in CCC complex and WASH complex subunits that result in different syndromes with similar patient phenotypes and at least one common feature: neurodevelopmental defects, suggesting a shared mechanism of pathology. A missense variant in *CCDC22* from CCC complex is the cause of an X-linked recessive intellectual disability (XLID)

(Kolanczyk et al., 2015). Within the WASH complex, a splice-site mutation in *KIAA0196* gene (which encodes Strumpellin) is linked to Ritscher-Schinzel/3C syndrome (Elliott et al., 2013). Patients with mutations in either *CCDC22* or *KIAA0196* also suffer from hypercholesterolemia, as both the CCC and WASH complexes are crucial for endosomal sorting of low-density lipoprotein receptor (LDLR) and its function, affecting cholesterol homeostasis (Bartuzi et al., 2016). Moreover, missense mutations in *KIAA0196* gene has been linked to hereditary spastic paraplegia type SPG8 (Lee et al., 2020). A single point mutation (c.3056C>G; Pro1019Arg) in *KIAA1033* gene, which encodes for SWIP subunit of WASH complex, has been shown to be cause non-syndromic autosomal recessive intellectual disability (ID) (Ropers et al., 2011). Additionally, some variants of this gene have been linked to late-onset Alzheimer's disease (Vardarajan et al., 2012). The mechanism by which deregulation of WASH and CCC complexes contributes to the pathology of ID syndromes remains to be determined but likely involves the regulation of vesicle recycling of proteins involved in neuronal maturation, survival, or function during brain development (Wang et al., 2018).

Defects in the SNX family have also been associated with various disorders. A complete deletion of *Snx17* in mice, achieved by CRISPR/CAS9-strategy, was found to be embryonically lethal. Mice with *Snx17* haploinsufficiency exhibited anxiety-like behavior and a low preference for social novelty (Cui et al., 2024). Further studies showed that ablation of SNX17 in rats resulted in heart defects, which may be the cause of the observed embryonic lethality during mid-gestation (Wu et al., 2021). Lastly, somatic mutations in SNX31 are associated with melanoma. These mutations predominantly occur within the FERM domain, with one specific mutation present in two different melanoma cases. Over 60% of non-silent mutations are located within a 48-residue segment of this 440-residue protein. Furthermore, a significant proportion of mutations in the SNX31 gene are C>T transitions, indicating a potential involvement in UVB-induced melanoma development (Hodis et al., 2012).

From a regulatory perspective, it is noteworthy that the phosphorylation of SNX proteins regulates membrane targeting. For instance, a cancer-related phosphorylation of a conserved serine in the PI3P-binding pocket of SNX3 was found to completely inhibit PIP-binding, leading to SNX3's release into the cytosol. This effect underscores how protein kinases influence membrane assemblies and suggests a mechanism by which protein complexes are detached from organelle membranes. This regulatory feature is conserved across the PX superfamily and throughout evolution, including in fungi and plants. Notably, SNX17 and SNX31 each contain a conserved serine (S38 and S39, respectively) that is subject to phosphorylation. Interestingly, melanoma cells often exhibit phosphorylation of the corresponding serine in SNX12, SNX17, and SNX21. This suggests that cancer may involve the dysregulation of PIP-binding elements, presenting a potential new cause and target for intervention (Lenoir et al., 2018; Stuart et al., 2015).

1.4. Manipulation of endosomal protein sorting by pathogens

Given the importance of endosomal sorting pathways for cellular homeostasis and other cellular functions, these pathways emerge as opportune targets for a variety of viral and bacterial pathogens (Personnic et al., 2016). Indeed, within the Retromer-dependent pathway, various human pathogens have already been identified that target key sorting protein machineries to promote cellular entry, replication during infection, and evade degradation. For instance, human papillomavirus (HPV) type 16 targets SNX27 (Pim et al., 2015; Popa et al., 2015), while human immunodeficiency virus (HIV) type-1 (Groppelli et al., 2014) and herpesvirus saimiri (Kingston et al., 2011) both bind directly to the Retromer complex. Bacterial effector proteins such as *Legionella pneumophila* RidL have also been described to block retrograde transport by interacting with Retromer, in particular with the VPS29 subunit (Romano-Moreno et al., 2017). Additionally, *Chlamydia trachomatis* targets SNX5/SNX6 (Mirrashidi et al., 2015). The Retromer complex and SNX27, along with COMMD2, COMMD3, and COMMD4 from the CCC complex, have also been identified as necessary for endosomal recycling of SARS-CoV-2 (Daniloski et al., 2021; Zhu et al., 2021). Pathogens such as vaccinia virus have also been observed to target the WASH complex to exploit this recycling route during infection (Hsiao et al., 2015).

To date, **human papillomavirus** is the only human pathogen linked to the Retriever-dependent pathway. HPV specifically infects human epithelial cells in the anal and genital regions, as well as oral cavities. Over 200 HPV types have been reported; while most cause no symptoms, various types such as HPV 6 and HPV 11 can cause benign tumors called papillomas or warts. Most importantly, some HPV types, including HPV 16 and HPV 18, can lead to carcinomas or cancer of the epithelial cells. Cervical cells in women are particularly at high risk, being HPV the main etiological agent of cervical cancer, with this malignancy being the fourth most common cancer in women, after breast, colorectal, and lung cancer. The carcinogenic process is initiated when the E6 and E7 proteins of the virus disrupt the tumor suppressor pathway by interacting with p53 and retinoblastoma protein (pRB), respectively, both of which are responsible for preventing uncontrolled growth of epithelial cells.

HPV belongs to the group of non-enveloped DNA viruses and has an 8 Kb double-stranded circular genome that encodes both early and late proteins. The HPV genome consists of 8 overlapping open reading frames (ORFs). The early ORFs encode E1, E2, E5, E6, and E7, while the late ORFs encode E4, L1, and L2. The *L1* gene is responsible for determining the HPV type and encodes the main capsid protein, which forms the outer rigid layer of the virion. The *L2* gene encodes the minor capsid protein, which is crucial for intracellular viral trafficking.

During the HPV viral cycle (**Figure 9**), the virus first binds to the cell membrane of human cells. L1 facilitates the virus's attachment to the ECM and to cell surface receptors. This binding triggers conformational changes in the capsid, exposing the L2 N-terminus. The virions are then internalized into endosomes, where endosomal acidification plays a critical role in virus uncoating. This process causes most of the L1 protein to separate from the L2/viral DNA complex, targeting L1 for degradation in lysosomes. The L2 and viral DNA (L2/vDNA), along with a small portion of L1, are delivered to the TGN, which allows them to escape lysosomal degradation and enter the nucleus when the nuclear membrane breaks down during mitosis. The L2/vDNA complex ultimately localizes to promyelocytic leukemia nuclear bodies, believed to support early viral gene expression necessary for establishing infection (Day et al., 2004, 2013; Siddiqa et al., 2018).

Trafficking to the TGN is facilitated by L2 recruitment. Structural predictions suggest that L2 is primarily an unstructured, disordered protein, with only about 20% predicted to form secondary structure elements. A significant portion of L2 is externalized from the endosome into the cytoplasm due to a hydrophobic C-terminal membrane-destabilizing segment with membrane-penetrating activity, although the exact mechanism of L2 membrane penetration remains unknown. Consequently, L2 becomes accessible on the cytosolic side of intracellular membranes, allowing interaction with cytosolic factors, including SNX17 and SNX27 (Bergant et al., 2017; Bronnimann et al., 2013; Siddiqa et al., 2018). Additionally, L2 directly interacts with Retromer, and this complex is considered to be critical for retrograde trafficking of the virus. Mutations of the L2 binding sites in Retromer lead to accumulation of L2/vDNA in early endosomes and block the trafficking of viral cargo to the TGN (Popa et al., 2015). SNX27 has also been shown to be involved in L2/vDNA trafficking via binding to L2 (residues 192–292) through its PDZ domain (Pim et al., 2015).

Similar to physiological cargo, the L2 protein contains an NPxY sorting motif recognized by **SNX17 and SNX31**. Mutants in L2 that impair SNX17 interaction, or the siRNA ablation of SNX17 expression, significantly enhanced L2 degradation and reduce viral capsid stability (Bergant Marušič et al., 2012). While the exact role of the Retriever complex in HPV infection remains unclear, studies have shown that silencing this complex significantly reduced infection rates in HaCaT cells (McNally et al., 2017). Moreover, it has been observed that Retriever colocalizes with L2 during infection in HeLa cells infected with HPV16 pseudovirions. Additionally, pull-down assays with a GST fusion protein of the last 106 amino acids of L2 and whole-cell extracts showed weak interactions of VPS35L with L2. (Pim et al., 2021).

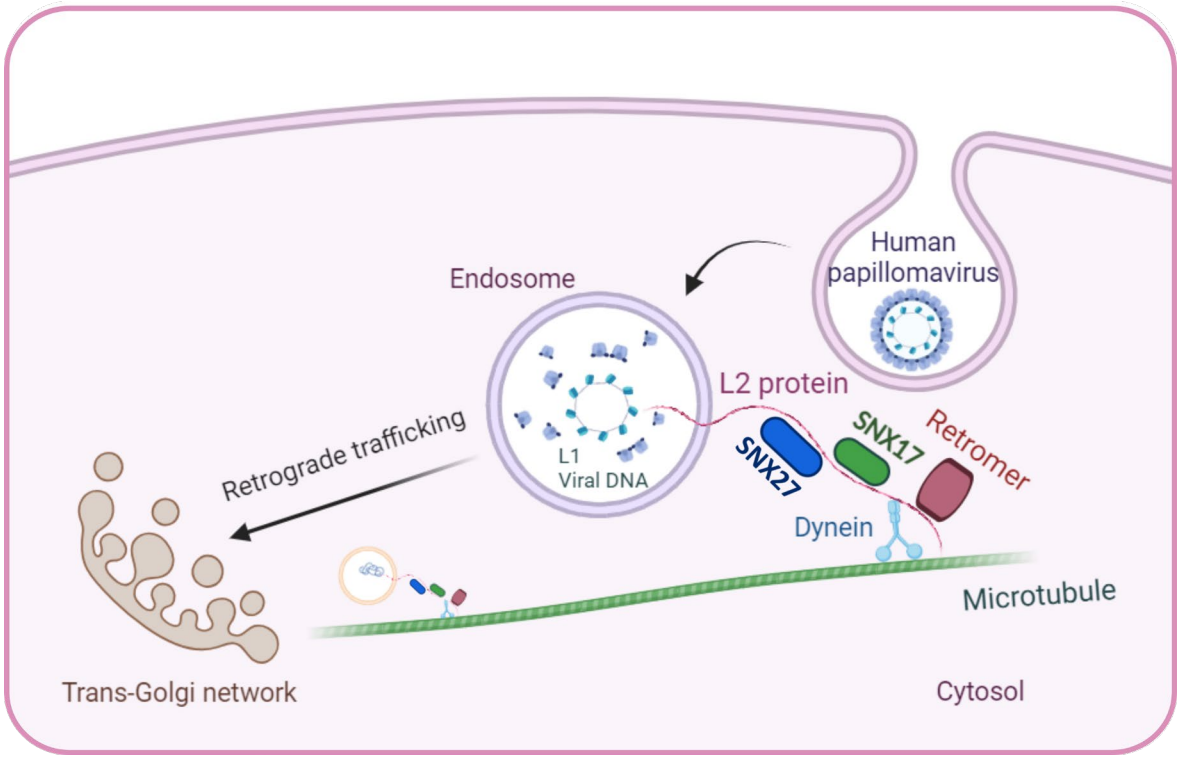

Figure 9. Simplified overview of the role of the L2 protein during HPV infection. The diagram illustrates HPV entry from the cell surface to the trans-Golgi network. After internalization, virions enter the endolysosomal pathway, with the L2 protein recruiting cytosolic sorting factors, including SNX17, SNX27, and Retromer to facilitate trafficking to the TGN. This process allows the viral DNA to enter the endocytic pathway and escape lysosomal degradation, ultimately aiming to reach the nucleus. Figure created with BioRender.com.

Chapter 2: OBJECTIVES

The main objective of this thesis is to elucidate the molecular mechanism underlying the recycling of integral membrane proteins by the Retriever complex in combination with sorting nexin 17 (SNX17).

The Retriever-CCC-SNX17 pathway plays a crucial role in cargo recycling from endosomes to the plasma membrane. Despite its significance, the precise molecular mechanisms by which SNX17 acts as a cargo adaptor and facilitates the recruitment of the Retriever complex to endosomal membranes remain an unanswered question in the field. Furthermore, it remains unclear whether SNX31, a protein closely related to SNX17, plays a similar role in the Retriever-mediated recycling. Lastly, although DENND10 has been identified as a potential partner of Retriever, its specific role within this recycling pathway is yet to be fully determined. Understanding the involvement and precise roles of these proteins in transmembrane protein recycling from endosomes to the plasma membrane is expected to offer new insights into their contributions to cellular processes and disease mechanisms.

To address these knowledge gaps, the following specific objectives were established:

- **Aim 1. Define the structural organization of the Retriever complex**.
- **Aim 2**. **Investigate the cargo recognition mechanism by SNX17.**
- **Aim 3**. **Examine the assembly of the Retriever-SNX17 complex.**
- **Aim 4. Explore the membrane association of SNX17 and the Retriever complex.**
- **Aims 5 and 6. Clarify the roles of SNX31 and DENND10 within the Retriever-mediated recycling pathway.**

Chapter 3: MATERIALS AND METHODS

3.1. Materials

3.1.1. Bacterial strains

The *Escherichia coli* (*E. coli*) strains Top10 and BL21(DE3) were the most commonly used strains for cloning and protein expression, respectively. The Top10 strain was routinely employed for obtaining and maintaining constructs as stability of plasmids is improved in this strain because of the absence of the natural *E. coli* recombinase system. The BL21(DE3) strain was used for protein overexpression, as it contains a chromosomal copy of the phage T7 RNA polymerase gene, which is regulated by an isopropyl-β-D-thiogalactopyranoside (IPTG)-inducible promoter, facilitating efficient expression of genes under the control of a T7 promoter. In addition, constructs that were not successfully overexpressed in BL21(DE3) were introduced into other BL21(DE3) derivative strains (**Table 1**).

Table 1. *E. coli* strains used for cloning and expression of the proteins used in this work.

Name	Genotype	Source
Top10	*E. coli* F$^-$ *mcrA* Δ(*mrr-hsdRMS-mcrBC*) φ80*lac*ZΔM15 Δ*lac*X74 nupG *rec*A1 *ara*D139 Δ(*ara-leu*)7697 *gal*E15 *gal*K16 *rps*L (StrR) *end*A1 λ-	Thermo Cat# C404003
BL21(DE3)	*E. coli* B F$^-$ *dcm ompT hsdSB*(r_B^- m_B^-) *gal* λ (DE3)	(Studier & Moffatt, 1986) Thermo Cat# C600003
Rosetta™ (DE3)	*E. coli* B F$^-$ *ompT hsdS*$_B$(r_B^- m_B^-) *gal dcm* (DE3) pRARE (Cam^R)	Novagen
ArticExpress™ (DE3)	*E. coli* B F$^-$ *ompT hsdS*(r_B^- m_B^-) *dcm*$^+$ Tet^r *gal* λ(DE3) *endA* Hte [*cpn10 cpn60* Gent^r]	Agilent Technologies
SHuffle® T7	F′ *lac, pro, lacIq / Δ(ara-leu)7697 araD139 fhuA2 lacZ::T7 gene1 Δ(phoA)PvuII phoR ahpC* galE (or U) galK λatt::pNEB3-r1-cDsbC* ($Spec^R$, *lacIq*) *ΔtrxB rpsL150*(Str^R) *Δgor Δ(malF)3*	New England Biolabs
Origami™ B(DE3)	F$^-$ *ompT hsd*S$_B$(r_B^- m_B^-) *gal dcm lacY1 ahpC* (DE3) *gor522*:: Tn*10 trxB* (Kan^R, Tet^R)	
BL21(DE3)pLysS	F$^-$ *omp*T *hsd*S$_B$ (r_B^- m_B^-) *dcm gal* λ(DE3) pLysS Cm^r	
C41 (DE3)	F$^-$ *ompT gal dcm hsdS$_B$* (r_B^- m_B^-) (DE3)	(Miroux & Walker, 1996)
C43 (DE3)	F$^-$ *ompT gal dcm hsdS$_B$* (r_B^- m_B^-) (DE3)	(Miroux & Walker, 1996)
DH10EmBacY	F$^-$ *mcr*A Δ(*mrr*-hsdRMS-*mcr*BC) Φ80*lac*ZΔM15 Δ*lac*X74 *rec*A1 *end*A1 *ara*D139 Δ(*ara*, *leu*)7697 *gal*U *gal*K λ$^-$ *rps*L *nup*G/pMON14272/pMON7124	Geneva Biotech

For instance, Rosetta was used to enhance the expression of eukaryotic proteins with codons rarely used in *E. coli*; it contains tRNAs for 7 rare codons (AUA, AGG, AGA, CUA, CCC, GGA, CGG).

ArcticExpress(DE3) contains genes for cold-adapted chaperonins (in particular, cpn60 and cpn10). This strain was employed to improve protein folding and yield of soluble proteins at low temperatures.

SHuffle and Origami strains, e engineered with mutant thioredoxin reductase (*trxB*) and glutathione reductase (*gor*) genes, were selected to optimize cytosolic disulfide bond formation.

BL21(DE3)pLysS, containing the T7 lysozyme gene, which inhibits T7 RNA polymerase and allows tighter expression control, was used to reduce the expression levels of potential toxic proteins before induction.

C41 and C43 strains shown to be effective for expression of toxic and membrane proteins, were also used to optimize protein expression.

3.1.2. Insect cells

Insect cell strains Sf21 and High Five (H5) (Thermo Fisher Scientific) were grown in HyClone SFX-Insect cell culture medium (Cytiva).

3.1.3. Plasmids

The plasmids used in this study are listed in **Table 8**. The DNA sequence for the genes *VPS26C*, *VPS35*L, SNX31, *LRP1* and *ITGB1* were obtained from commercial synthesis services. The nucleotide sequences were optimized for bacterial expression using the Invitrogen GeneArt Synthesis Service, except for ITGB1 which was optimized using the IDT Codon Optimization Tool. All the DNA constructs generated in this thesis, are detailed in **Table 9**.

3.1.4. Peptides

The peptides used in binding assays were synthesized by GenScript with an HPLC purity of ≥95%. These peptides are listed in **Table 2**. To predict peptide solubility, the tool Pepcalc was used (Lear & Cobb, 2016) (https://pepcalc.com/peptide-solubility-calculator). Lyophilized peptides were resuspended in 100 mM Hepes pH 7.5 at a concentration of 5 mg/ml. The peptides used in fluorescence anisotropy assays were synthesized with an N-terminal 5-Carboxyfluorescein (FAM) label.

Table 2. Peptides used in this work.

Mutations are shown in red.

Peptide	Sequence region	Sequence	Molecular weight (Da)
$L2_{14\text{-mer}}$	248-261	KLITYDNPAYEGID	1611.75
FAM-$L2_{14\text{-mer}}$	248-261	5-FAM-KLITYDNPAYEGID	1970.06
FAM-$L2_{14\text{-mer(D261A)}}$	248-261	5-FAM-KLITYDNPAYEGIA	1926.05
FAM-$L2_{14\text{-mer(E258A)}}$	248-261	5-FAM-KLITYDNPAYAGID	1912.02
FAM-$L2_{14\text{-mer(Y252A)}}$	248-261	5-FAM-KLITADNPAYEGID	1877.96
$LRP1_{14\text{-mer}}$	4464-4477	MNVEIGNPTYKMYE	1688.93
FAM-$LRP1_{14\text{-mer}}$	4464-4477	5-FAM-MNVEIGNPTYKMYE	2047.23
$APP_{14\text{-mer}}$	753-766	QQNGYENPTYKFFE	1764.85
FAM-$APP_{14\text{-mer}}$	753-766	5-FAM-QQNGYENPTYKFFE	2123.16
FAM-$APP_{14\text{-mer(K763E)}}$	753-766	5-FAM-QQNGYENPTYEFFE	2124.10
FAM-$INTB_{D\text{-}13\text{-mer}}$	786-798	5-FAM-AVTTVVNPKYEGK	1763.90
FAM-$INTB_{P\text{-}14\text{-mer}}$	774-787	5-FAM-KWDTGENPIYKSAV	1966.07
FAM-$VEGFR1_{14\text{-mer}}$	1044-1057	5-FAM-ARDIYKNPDYVRKG	2053.20
FAM-$DMT1_{19\text{-mer}}$	550-568	5-FAM-AQPELYLLNTMDADSLVSR	2494.70
FAM-$SNX17_{CT\text{-}18\text{-mer}}$	453-470	5-FAM-ASDVHGNFAFEGIGDEDL	2251.24
FAM-$SNX31_{D\_18\text{-mer}}$	423-440	5-FAM-IKIAKDDCVFGNIKEEDL	1763.90
FAM-$SNX31_{P\_18\text{-mer}}$	409-426	5-FAM-QQKDYSSFLSRKSKIKIA	2485.76

3.1.5. Lipids

The lipids used in this work for the preparation of giant unilamellar vesicles (GUVs) and liposomes are listed in **Table 3**. All lipids, with the exception of 18:1 PI3P and Marina Blue™ DHPE, were solubilized directly in chloroform, and stock solutions were prepared at 1 mg/ml. 18:1 PI3P was solubilized in a 20:9:1 mixture of chloroform:methanol:Milli-Q water followed by brief sonication, and the stock solution was prepared at 0.2 mg/ml. Marina Blue™ DHPE was dissolved in a 1:1 mixture of chloroform:methanol at 1 mg/ml. All lipid mixtures were stored at -20 ºC in amber glass vials (Thermo), flushed with argon gas to prevent oxidative damage, and sealed with assembled target™ caps (Thermo). Lipid manipulation was performed with Hamilton® syringes (Sigma, USA) and glass containers.

Table 3. Lipids used for either GUV or liposome preparation.

Abbreviation	Lipid name	Source	Reference	Molecular weight
DOPC	1,2-dioleoyl-sn-glycerol-3-phosphocholine	Avanti Polar Lipids	850375C	786.113
DOPE	1,2-dioleoyl-sn-glycerol-3-phosphoethanol-amine	Avanti Polar Lipids	850725C	744.034
DOPS	1,2-dioleoyl-sn-glycerol-3-phospho-l-serine	Avanti Polar Lipids	840035C	810.025

PI3P	1,2-dioleoyl-sn-glycero-3-phospho-(1′-myo-inositol-3′-phosphate	Avanti Polar Lipids	850150P	977.147
Marina Blue™ DHPE	Marina Blue™ 1,2-Dihexadecanoyl-sn-Glycero-3-Phosphoethanolamine	Invitrogen	M12652	944.140
Liss Rhod PE	1,2-dioleoyl-sn-glycero-3-phosphoethanolamine-N-(lissamine rhodamine B sulfonyl)	Avanti Polar Lipids	810150C	1,301.715

3.2. Molecular cloning

3.2.1. DNA amplification by PCR

The amplification of vectors and inserts of interest, was performed using the polymerase chain reaction (PCR) technique with Phusion High-Fidelity polymerase (Thermo) on a C1000 Touch™ thermal cycler (Bio-Rad, USA). Oligonucleotides were dissolved in nuclease-free Milli-Q water, and their annealing temperatures were calculated with the Tm calculator server from Thermo. The OligoAnalyzer tool from Integrated DNA Technologies (https://eu.idtdna.com/calc/analyzer), was also used to calculate specific features of the oligos, such as GC content and the potential formation of structures like hairpins, homodimers or heterodimers by terms of spontaneity (Delta G). The PCR protocol used is shown in **Table 4**.

Table 4. Mix of the reagents required for one PCR run (A) and amplification cycles (B).

A.

Components	**Volume (µl)**
Phusion High Fidelity Buffer (Thermo) (5X)	10
dNTPs (Thermo) (10 mM)	1
Forward primer (10 µM)	1
Reverse primer (10 µM)	1
Template plasmid (1 ng/µl)	1
Phusion DNA polymerase (Thermo)	0.5
Nuclease-free Milli-Q water	35.5

B.

Steps	**Time (s)**	**Temperature (ºC)**	**Cycles**
Initial denaturation	30	98	1
Denaturation	10	98	30
Annealing	30	At	
Extension	Et	72	
Final extension	300	72	1

At: Annealing temperature, calculated using the Tm calculator from Thermo .

Et: Extension time, which is 30 s/Kb for PCRs with products of less than 2000 nt and 20s/Kb for PCRs with products greater than 2000 nt.

3.2.2. DNA digestion by DpnI

PCR products were digested with DpnI nuclease for 1 h at 37 ºC, which digests methylated DNA, with the aim of removing the DNA template. 45 µl of amplified DNA was mixed with 5 µl of Fast Digest Buffer 10x and 1 µl of DpnI FD (Fast Digest) enzyme (Thermo). After digesting the template DNA, the PCR was purified with Clean-up system kit (Thermo). The DNA concentration was measured by spectrophotometric analysis at 260 nm using a Nanodrop 2000c (Thermo), with 2 µl of sample. Extracted DNA purity was confirmed by ensuring $A_{260/280}$ nm and $A_{260/230}$ nm ratios were greater than 1.8 and 2, respectively.

3.2.3. DNA electrophoresis in agarose gel

DNA fragments were visualized and analyzed using 1% (w/v) agarose gel electrophoresis. For gel preparation, D1 low EEO agarose (Condalab) was dissolved in 1X TAE buffer (40 mM acetate, 1 mM EDTA, 40 mM Tris-HCl pH 8.0). Prior to gel polymerization, SafeView™ Classic DNA stain (abm) was added to the gel for DNA visualization. DNA samples were mixed with 6X TriTrack DNA loading dye (Thermo), and GeneRuler Plus 1kb DNA Ladder (Thermo) was used as a molecular weight marker. Gels were typically run for 30 minutes at 120 V using a horizontal electrophoretic running system (Bio-Rad) with 1X TAE buffer and ChemiDoc XRS gel imaging system (Bio-Rad) was used for gel visualization.

3.2.3. Isothermal Assembly

The nucleotidic fragments were joined by Isothermal Assembly (Gibson et al., 2009), thanks to the presence of an overlapping region between both fragments. The reaction was performed in the thermal cycler at 50 ºC for 1 hour. PCR products were mixed as shown in **Table 5**. Site-directed mutagenesis was also performed with the Gibson Isothermal DNA Assembly method using mutagenic primers. A set of cloning plasmids, designated as pIA ("Isothermal Assembly"), were constructed in this study for the efficient cloning of a single PCR product into various vectors using Gibson assembly. These vectors facilitate the expression of the desired sequence with either a His-, Sumo3-, GST- (Glutathione S-transferase), TrxA- (Thioredoxin), MBP- (Maltose Binding Protein), Strep-, Twin-Strep- (that contains two Strep-tag moieties), or Zbasic- tag, along with the TEV (Tobacco Etch Virus), SenP2 (Sentrin-specific Protease 2), or HRV3C (Human Rhinovirus 3C protease) protease recognition site at the N-terminus. The sequences of the oligonucleotides and template DNA used for construct generation are summarized in **Table 10**.

Table 5. Mix of PCR products for the Isothermal Assembly reaction (A) and components of the Isothermal mixture (B).

A.

Isothermal Mix (10X)	5X Isothermal buffer composition*
40 µl Isothermal reaction buffer 5X	3 ml 1M Tris-HCl pH 7.5
1.5 µl T5 exonuclease 1 U/µl (NEB)	300 µl 1M MgCl2
2.5 µl Phusion polymerase (Thermo)	600 µl 10 mM each dNTP
10 µl Taq Ligase (NEB)	300 µl 1M DTT (Thermo)
96 µl Milli-Q	1.5 g PEG-8000
	20 mg NAD
	Milli-Q to 6 ml

B.

Reagents (20 µl)	
x µl vector PCR	50 – 100 ng
x µl insert PCR	2 – 5X molar excess
+ 15 µl Isothermal mix	
+ x µl Milli-Q (if required to complete volume)	

3.2.4. Test PCR and sequencing

To confirm that the antibiotic-resistant colonies contained the insert of interest in the plasmid, a test PCR was performed. Around six different colonies for each construct were subjected to the PCR protocol described in **Table 6**, using PCR Taq MasterMix with dye containing Taq DNA Polymerase (abm).

Table 6. Mix of the reagents required for one test PCR run (A) and amplification cycles (B).

A.

Components	Volume (µl)
Forward primer (10 µM)	1
Reverse primer (10 µM)	1
2X PCR Taq MasterMix with dye	10
Nuclease-free Milli-Q water	8
Colony 1-6	

B.

Steps	Time (s)	Temperature (ºC)	Cycles
Initial denaturation	180	94	1
Denaturation	30	94	30
Annealing	30	At	
Extension	Et	72	
Final extension	300	72	1

At: Annealing temperature was set at 5 ºC below the lowest primer melting temperature.

Et: Extension time, which is 60s/Kb.

Positive colonies were isolated by streak-plate procedure on a new agar plate. Plasmid DNA was extracted from a 10 ml *E. coli* cell culture grown with the selective antibiotic and purified with GeneJet Plasmid Miniprep Kit (Thermo). A final verification of the construct was achieved by Sanger sequencing of the insert and surrounding regions using the Eurofins sequencing service (Ebersberg, Germany). For sequencing, 5 µl of the plasmid at 50-100 ng/µl, and 2.5 µl primer at 5 µM were provided, with a final volume of 10 µl, adjusted with Milli-Q water. Sequencing results were analyzed using CLC Sequence Viewer (Qiagen, Denmark) and SnapGene Viewer (Dotmatics; available at https://www.snapgene.com/).

3.2.5. Generation of recombinant baculovirus

The Retriever subunits were cloned into the pLIB vector and then combined into the pBIG1a plasmid using the biGBac method (Weissmann et al, 2016). The pBIG1a recombinant vectors were introduced by heat shock into DH10EMBacY competent cells that harbors a baculovirus shuttle vector and a helper plasmid, to generate recombinant baculoviral genomes via Tn7 transposition. After plating the transformants on agar plates containing 100 µg/ml 5-Bromo-4-chloro-3-indolyl β-D-galactopyranoside (X-gal) (VWR), 0.1 mM isopropyl β-d-1-thiogalactopyranoside (IPTG) (Thermo), 50 µg/ml kanamycin, 10 µg/ml tetracycline, and 10 µg/ml gentamycin, white colonies were selected. Bacmid DNA was extracted by lysing the cells with the GeneJet Plasmid Miniprep Kit solutions, followed by isopropanol precipitation of the supernatant, and washing of the pellet with 70% ethanol. Sf9 cells were seeded at $4x10^5$ cells/well in a 6-well plate. Bacmid DNA was transfected into the insect cells using FuGENE HD Transfection Reagent (Promega) according to the manufacturer's protocol and incubated at 27 ºC for at least 72 hours. Transfection efficiency was monitored by observing the fluorescence of the yellow fluorescent protein (YFP) through fluorescence microscopy and measuring the cell concentration in the Neubauer chamber (Sigma), which contains cells from the cell culture mixed with Trypan blue stain (Gibco) in a 1:1 ratio. After centrifugation of the cells at 700 g for 5 minutes at 4 ºC, 2% of Fetal Bovine Serum (FBS) (PAN-Biotech) was added to the supernatant and was then used to infect a 25 ml suspension culture of Sf9 cells at $1x10^6$ cells/ml. At 72 hours post-infection, the P1 generation of virus was harvested by collecting the supernatant again and 2% FBS was added. For further virus amplification, 2 ml of P1 was used to infect a 100 ml culture of Sf9 cells at $1x10^6$ cells/ml. The supernatant, termed P2, was harvested after 72 hours, 2% FBS was added, filtered with 0.2 µm-filters (Whatman GE Healthcare Life Sciences), and stored at 4 ºC in the dark.

3.3. Microbiological methods

3.3.1. General culture conditions

E. coli was routinely grown at 37 °C in Luria broth (LB) medium (10g/l tryptone, 5 g/l yeast extract, 5 g/l NaCl; Pronadisa, Spain) with shaking. For growth on solid medium plates, LB was supplemented with 1.5% (w/v) of bacterial agar (Pronadisa). For antibiotic selection, medium was supplemented with ampicillin (Amp) at a final concentration of 100 µg/ml (Sigma), chloramphenicol (Cm) at 25 µg/ml (Sigma) or kanamycin (Km) at 50 µg/ml (Sigma), depending on the vector resistance. Cultures were incubated at 37 ºC and 180 rpm. To induce the expression of the protein of interest, 1 mM of IPTG was added, and the culture was grown overnight at 15 ºC or 18 ºC and 180 rpm.

3.3.2. Bacterial glycerol stock

Stocks of cell cultures were prepared by mixing 0.8 ml of overnight culture with 0.8 ml of glycerol-peptone (50% glycerol (v/v), 0.15% peptone (w/v)), and stored frozen at -80 ºC.

3.3.3. Bacterial growth measurement

The bacterial growth was measured by determining the OD_{600} in a Nanodrop 2000c spectrophotometer (Thermo), with 1 ml samples taken from the culture.

3.3.4. Bacterial transformation by heat shock

Two methods of transformation were used: electroporation and heat shock transformation. Heat shock was used for the majority of the transformations. Around 100 ng of the plasmid of interest was added to the cells and incubated on ice for 30 minutes. Following the incubation, cells were subjected to a 45 seconds heat-shock at 42 ºC and afterwards to a 10 minute-cool down on ice. 500 µl of LB was added and cells were incubated for 1 hour at 37 ºC with agitation at 180 rpm. Following incubation, the bacterial culture was plated on selective medium and incubated at 37 ºC.

3.3.5. Preparation of competent cells for heat shock

For the preparation of competent cells, a pre-inoculum is incubated overnight at 37 ºC with shaking. 1 ml from the pre-inoculum is transferred into 100 ml of LB with the corresponding bacteria-resistant

antibiotic and incubated at 37 ºC with shaking until the OD reaches 0.5-0.6. Once reached, the culture is cooled on ice for 15 minutes and centrifuged at 4 ºC for 10 minutes at 3,000 rpm. The pellet is resuspended with 30 ml ice-cold TFB1 buffer (100 mM KCl, 50 mM $MnCl_2$, 30 mM potassium acetate, 10 mM $CaCl_2$ and 15% glycerol; with pH adjusted to 5.8 with 10% acetic acid). The solution is kept on ice for 10 minutes and cells are collected by centrifugation (10 minutes, 3,000 rpm, 4 °C). The cells are resuspended with 2 ml of ice-cold TFB2 buffer (10 mM MOPS, 10 mM KCl, 75 mM $CaCl_2$ and 15% glycerol; pH adjusted to pH 7.0 with 1M NaOH). The competent cells are then aliquoted, frozen in liquid nitrogen and stored at -80 °C.

3.3.6. Bacterial transformation by electroporation

For transformation by electroporation, DNAs from enzymatic reactions such as isothermal assembly required a previous microdialysis step, as the samples must be salt-free, while DNAs from plasmid purification were used directly. Electrocompetent cells were purchased from the IBBTEC's research support platform. 100 ng of DNA was added to 80 µl of the ice-cold competent cells and the mixture was transferred to an ice-cold 0.2 cm electroporation cuvette Gene Pulser (Bio-Rad). A single pulse was applied at a field strength of 2.5 kV, 200 Ω resistance, and 25 µF capacitance, using a MicroPulser TM electroporator (Bio-Rad). Immediately after the electric pulse, 1 ml of previously preheated LB medium was added and cells were incubated at 37 °C for 1 hour with shaking at 180 rpm. After that, the cultures were plated on a selective medium according to the plasmid resistance. Antibiotic resistant colonies were selected after 18h-incubation at 37 ºC.

3.4. Protein characterization

3.4.1. Determination of the physicochemical parameters

To estimate certain protein parameters, such as the isoelectric point (pI), the extinction coefficient (Ɛ), and the molecular weight, the online ProtParam tool from Expasy was used (https://web.expasy.org/protparam/) (Gasteiger et al., 2005).

Absorbance at 280 nm has been the method of choice for protein quantification because of its simplicity and cost-effectiveness relation. Absorbance at 280 nm was measured using Nanodrop 2000c (Thermo). The concentration of purified protein samples was estimated by applying the Beer-Lambert law, $A_{280} = Ɛ_{prot} \cdot C \cdot l$, where A is the absorbance at 280, Ɛ is the extinction coefficient, C the concentration, and l is the path length.

3.4.2. Protein overexpression and cell lysis

For protein overexpression in bacteria, *E. coli* BL21(DE3) strain was primarily used. Cells were grown in LB medium at 37 ºC until reaching an optical density at 600 nm of 0.6-0.8. After cooling for 30 minutes, protein expression was induced with 0.5 mM IPTG at 18 ºC for 16 hours. Cells were harvested by centrifugation at 4,500 rpm for 20 minutes at 4 ºC using Avanti J-30I centrifuge (Beckman Coulter) with JA10 rotor, and the cell pellet was resuspended in buffer A (50 mM Tris-HCl pH 8.0, 300-500 mM NaCl, 1 mM DTT), supplemented with 0.5 mM phenylmethylsulphonyl fluoride (PMSF) (VWR), 5 mM benzamidine (Thermo), 25 µg/ml DNAse (PanReac), and 1 mg/ml lysozyme (Sigma). For the purification of His-tagged proteins, 20 mM imidazole (Sigma) was also included. After a 30-minute incubation, the bacteria were disrupted by sonication in an ice bath at 60% amplitude using 24 cycles of 5 seconds on and 25 seconds off to avoid sample overheating. The lysate was then cleared by centrifugation at 20,000 rpm for 45 minutes using Avanti J-30I centrifuge (Beckman Coulter) with JA30.50 rotor. Lysates containing SNXs were mixed with 1% of the non-denaturing detergent Triton X-100 (Thermo) prior to centrifugation to further lyse cell membranes and reduce protein aggregation (Walker 2009).

For baculovirus-insect cell expression, 250 ml suspension cultures of High Five insect cells at $1x10^6$ cells/ml were infected with a P2 baculovirus solution containing the Retriever constructs or VPS35L. At 48- or 72-hours post-infection, when YFP fluorescence reached a plateau, cells were harvested by centrifugation at 1,000 x g for 5 minutes at 4 ºC. Insect cells were lysed using probe sonication in the same lysis buffer as used for bacteria, without the addition of lysozyme, at 20% amplitude with 10 cycles of 5 seconds on and 25 seconds off. The lysate was then ultracentrifuged at 163,000 x g for 45 minutes using the T-865 rotor in the Sorvall-WX Ultra 100 ultracentrifuge (Thermo).

3.4.3. Small-scale protein purification test

Prior to large-scale protein purification, a test was conducted using a 50-ml cell culture. Before adding IPTG for protein overexpression, a 1-ml sample of the culture was taken, centrifuged at 4,000 rpm, 5 minutes, 4 ºC, and the pellet was resuspended in 100 µl of 1% SDS (sodium dodecyl-sulfate) (for OD = 1). After 16-hour protein overexpression, another 1-ml sample was taken before centrifuging the culture to verify that the host efficiently overexpressed the protein of interest. The culture was then centrifuged at 4,000 rpm for 10 minutes at 4 ºC. The pellet was frozen, thawed, and resuspended in 1.5 ml of buffer A. Lysis was performed by sonication at 4ºC using a Bioruptor® Plus sonication device (Diagenode) at 10% amplitude with 6 cycles of 5 seconds on and 15 seconds off. The lysate was then centrifuged at 14,000 rpm for 20 minutes at 4 ºC. For pellet lysate sample

(insoluble fraction), before centrifugation, 40 µl of lysate was taken out and centrifuged at 4,000 rpm for 15 minutes at 4 ºC. The pellet was then resuspended in 40 µl of 1% SDS. A 40-µl sample of the supernatant (soluble fraction) was collected, and the remaining supernatant was applied to a small column containing 50 µl of the resin of interest, depending on the protein tag, and was washed with 1 ml of buffer A. Samples of 40 µl each of the flow-through, wash, and resin were taken and analyzed using SDS-PAGE.

3.4.4. Protein purification

The lysis supernatant was incubated in batch with PureCube Glutathione agarose (Cube Biotech), PureCube Ni-INDIGO agarose (Cube Biotech), or Streptactin-XT-4Flow beads (IBA Lifesciences) depending on whether the protein of interest had a GST-tag, His-tag, or Strep-tag, respectively. This was followed by extensive washing with buffer A using a gravity column. The protein linker was proteolytically removed by overnight incubation at 4 °C in the presence of Sentrin-specific Protease 2 (SenP2), Human Rhinovirus 3C protease (HRV 3C) or Tobacco Etch Virus (TEV) proteases, depending on the cleavage site of the protein, in 25 mM Tris-HCl pH 8.0, 300 mM NaCl, and 1 mM DTT. For buffer exchange, dialysis was performed with membranes with a molecular weight cutoff (MWCO) of 6-8 kDa (Spectrum Laboratories Inc.). Following tag removal, reversed affinity chromatography was performed using a gravity column, and the protein of interest was collected in the flow-through, while the unwanted tag was captured on the affinity matrix. In this thesis, tags were retained on certain proteins to enhance their stability and solubility. For further purification, some proteins were subjected to ion exchange chromatography (HitrapQ, Cytiva), employing a salt gradient ranging from 100 to 1000 mM NaCl. This was followed by size exclusion chromatography (Superdex75 10/300, Superdex200 10/300, or Superdex200 16/60; Cytiva) in buffer B (25 mM Hepes pH 7.5, 150-300 mM NaCl, and 1 mM TCEP (GoldBio)), a step carried out for the purification of all the proteins except SNX17. These chromatographic separations were performed on an ÄKTA™ Pure protein purification system (GE Healthcare). The steps performed for the purification of each protein are detailed in **Table 11**. The sequences of the resulting recombinant proteins purified in this thesis are listed in **Table 12**.

3.4.5. Denaturing gel electrophoresis SDS-PAGE

Successful protein purification was confirmed by denaturing gel electrophoresis SDS-PAGE (SDS Polyacrylamide Gel Electrophoresis), with the gel components detailed in **Table 7**. For protein visualization, samples were mixed with a home-made 5X SDS Loading Buffer (LB-SDS), composed of 10% SDS, 500 mM DTT, 50% glycerol, 250 mM Tris-HCl 6.8, and 0.025% bromophenol blue dye. PageRuler™ Plus Prestained Protein Ladder (Thermo) was used as the molecular weight (MW)

marker. All samples were incubated for 5 minutes at 95 ºC, and the electrophoresis was run at 180V for 45-60 minutes in SDS-PAGE 1X buffer (25 mM Tris, 192 mM glycine, 1% (w/v) SDS, pH 8.4). Afterwards, gel was stained with Coomassie staining solution(composed of 10% acetic acid, 40% ethanol, and 0.1% Coomassie Blue R250 dye), destained with distilled water, and visualized with the Odyssey CLx imaging system (LI-COR).

Table 7. Components for running (A) and stacking (B) gel in SDS-PAGE.

A.

% acrylamide	**8%**	**10%**	**12%**	**15%**
Running 2x*	20 ml	20 ml	20 ml	20 ml
40% acrylamide / bis acrylamide (37.5:1) (Bio-Rad)	8 ml	10 ml	12 ml	15ml
Milli-Q	12 ml	10 ml	8 ml	5 ml
10% (w/v) APS (Sigma)	400 µl	400 µl	400 µl	400 µl
TEMED (Sigma)	24 µl	16 µl	16 µl	16 µl

B.

% acrylamide	**5%**
Stacking 2x**	10 ml
40% acrylamide / bis acrylamide (37.5:1)	2.5 ml
Milli-Q	7.5 ml
10% (w/v) APS	200 µl
TEMED	20 µl

*Running buffer 2x: Composed of 0.75 M Tris pH 8.8 and SDS 0.2% (w/v).

**Stacking buffer 2x: Composed of 0.25 M Tris pH 6.8 and SDS 0.2% (w/v).

The SDS was added after pH adjustment since the pH electrode is sensitive to SDS.

APS, Ammonium persulfate; TEMED, N,N,N′,N′-Tetramethylethylenediamine.

3.4.6. Protein concentration

When required, the protein was concentrated using Amicon Ultra Centrifugal filters (Merck Millipore) and quantified by measuring the absorbance at 280nm and applying the theoretical extinction coefficient. In the purification of SNX17 and GFP-SNX17 (both wild-type and mutant forms), the concentration method differed due to the impossibility of using centrifugal filters because of protein precipitation. Instead, the protein was concentrated by binding to a Q column and then eluted with a pronounced salt gradient. This approach ensured that all the protein of interest eluted within the same fraction at a high enough concentration to allow the experiments to be performed.

3.4.7. Mass spectrometry (MS)

Purified proteins were subjected to mass spectrometry at the UPV-EHU Mass Spectrometry Service (University of the Basque Country, Spain) to obtain structural and functional insights, such as potential loss of protein regions during purification or potential post-translational modifications (e.g., phosphorylation, glycosylation). The samples were processed using C4 and C18 micro spin-columns (Harvard Apparatus). First, the C4 column was used, and the flow-through was collected and then passed through the C18 column. The two resulting samples were combined, desiccated using a Speed-Vac, and rehydrated in 25 µl of a solution containing 50% acetonitrile and 0.25% formic acid. The mixture was injected by direct infusion into the SYNAPT G2-S HDMS mass spectrometer (Waters).

3.4.8. Thermal stability assay

A thermal stability assay was performed to assess the stability of our proteins of interest in the presence of various compounds, with the aim of finding potential stabilizers. This technique measures changes in the melting temperature (Tm), which represents the temperature at which half of the protein is denatured. For each condition, 45 µl of protein at a concentration of 5 µM was mixed with 5 µl of each additive (1:10 ratio), and SYPRO Orange dye 10x (Invitrogen). The mixture was added to a MicroAmp Fast 96-well reaction plate (Applied Biosystems) and the plate was sealed using Diamond ClearSeal (Thermo) in ALPS Microplate Heat Sealing Instrument (Thermo). SYPRO Orange binds to hydrophobic regions exposed during protein unfolding, resulting in fluorescence. The fluorescent dye is quenched in the aqueous environment, so only basal fluorescence emission is detected at 555 nm upon excitation at 470 nm. As the temperature increases and the protein unfolds, the increase in fluorescence is continuously monitored in a real-time PCR (qPCR) machine (Thermo), and the melting temperature (Tm) is calculated. The starting temperature was set at 25 ºC, with increments of 0.5 ºC per step.

3.5. Structural analysis of proteins

3.5.1. Circular Dichroism (CD)

The structural comparison of the WT and mutant SNXs was performed using CD analysis at the Biophysics Unit (Basque Country, Spain). Far-UV CD spectra were acquired at 25 °C using a JASCO J-810 CD spectropolarimeter. Proteins were dialyzed overnight at 4 °C against 100 mM sodium phosphate buffer (pH 7.5), and measured at a concentration of 2 μM. Data were collected using a 0.1-cm path length quartz cuvette, scanning from 200 to 260 nm at 0.5 nm intervals with a scanning speed of 50 nm/min. A total of 50 scans were accumulated to generate the final spectrum, which was baseline-corrected by subtracting the buffer spectrum. Ellipticity values were converted to mean residue ellipticity.

3.5.2. Small-angle X-ray scattering (SAXS)

SAXS experiments were conducted at the B21 bioSAXS beamline at the Diamond Light Source synchrotron in Oxfordshire, which is equipped with an EigerX 4M detector (Dectris) (Cowieson et al, 2020). A Shodex KW-403 gel-filtration column, equilibrated in 50 mM Tris pH 7.5, 200 mM NaCl, and 1 mM TCEP, was coupled to SAXS measurement setup. Details of the SAXS collection are provided in **Table 13**. For DENND10, 600 frames were recorded with a 3.0 s exposure time per frame using an X-ray wavelength of λ = 0.954 Å in flow mode at 15 ºC. Data processing was assisted by Iván Méndez Guzmán, a lab member from my group. The 2D to 1D radial averaging was performed using the dedicated the DAWN software. The 1D scattering intensities of the SEC-SAXS data were computed as $I(q)$ *versus* q, where $q = (4\ \pi * \sin\theta)/\lambda$ with 2θ being the scattering angle and λ the X-ray wavelength. Buffer subtraction, quality assessment, and subsequent analysis were carried out using ATSAS (Manalastas-Cantos et al., 2021) and BioXtas RAW (Hopkins et al, 2017). Forward scattering, $I(0)$, and the radius of gyration, R_g, were calculated through Guinier analysis and the inverse Fourier transformation method implemented in GNOM. The D_{max} was derived from the pair distance distribution obtained with GNOM. To build low-resolution bead models of the SAXS data, we employed *ab initio* modeling techniques. The DENND10 protein was modeled using GASBOR, with the best-scoring model selected. The averaged model was filtered with DAMSTART and refined using DAMMIN. The envelope of the *ab initio* model was generated with the Molmap function of UCSF ChimeraX (Pettersen et al., 2021). The AF2 model was aligned with the GASBOR-generated envelopes for visual comparison. All visualizations were done using UCSF ChimeraX (Pettersen et al, 2021).

3.5.3. X-ray crystallography

To identify initial crystallization conditions, the proteins of interest were screened using various commercially available sitting-drop vapor diffusion screens: Hampton Research Crystal Screen 1 and 2 (Hampton Research, catalogue numbers HR2-110 and HR2-112), PACT *premier*™ (Molecular Dimensions MD1-36), JCSG-*plus*™ (Molecular Dimensions MD1-40), AmSO4 Suite (Qiagen), PGA Eco (Molecular Dimensions MD1-51-ECO), ProPlex™ (Molecular Dimensions MD1-42), Morpheus™ (Molecular Dimensions MD1-46), MIDAS*plus*™ (Molecular Dimensions MD1–107) and Stura Footprint Screen™ + MacroSol™ (Molecular Dimensions MD1-43). These kits contain reagents covering a broad range of precipitants, pH levels, and organic compounds.

50 µl of the crystallization solutions were pipetted into the reservoirs of 96-well sitting-drop plates. A 0.5 µl drop of protein was then placed into each well, and 0.5 µl of the corresponding precipitant from the reservoir was added to the drop without further mixing. If crystal formed in any of these conditions, the successful condition was replicated in a 24-well hanging-drop plate, with slight variations in precipitant and protein concentrations, the ratio of protein to precipitant, or the pH of the buffer solution.

The proteins subjected to crystallization trials included $SNX17_{FL}$, $SNX17_{FERM-CT}$, $SNX17_{FERM-CT(del406-442)}$, $SNX17_{FERM-CT}$-$L2_{FBR}$, $SNX17_{FERM-CT}$-$APP_{739-770}$, $SNX17_{109-388}$-$L2_{FBR}$, $SNX31_{FERM-CT}$, Retriever, Retriever-MBP, VPS26C and DENND10. Before using the commercial screens, the proteins were subjected to a pre-crystallization test (PCT™, Hampton Research, catalogue number HR2-140), to determine the appropriate protein concentration.

Additionally, several approaches were employed to increase the likelihood of crystal formation. Glycerol at 10% was added as an additive to all proteins in some conditions. Different constructs of SNX17 and SNX31 were also incubated with the peptide L2 to potentially enhance protein stability and, promote crystallization.

In some crystallization trials, 0.5 µl of seed stocks from previous crystals was added to drops containing 1.5 µl of protein and 1 µl of reservoir solution. Microseeding is often required to initiate crystal growth or induce nucleation (McPherson & Gavira, 2014). Seed stocks were prepared by crushing crystal fragments using a crystal crusher (Hampton Research, HR4-216), and placing them in a seed bead tube (Hampton Research, HR2-320) in a 50-µl volume of the reservoir solution where the crystals were grown, followed by four rounds of vortex for 30 seconds each. Serial dilutions of 1:10, 1:100 and 1:1,000 were prepared from the stock to reduce the number of nuclei introduced into the new drop.

Crystals were harvested from the drop using Mounted CryoLoops (Hampton Research) and transferred into a cryoprotectant solution, which, for most crystals, comprised the crystallization solution supplemented with 15-25% ethylene glycol or 15-25% glycerol. After soaking, the crystals were harvested again and flash-frozen in liquid nitrogen. X-ray diffraction data were collected using an X-ray beam from beamline BL13-XALOC at the ALBA Synchrotron (Barcelona, Spain). The diffraction pattern was recorded at various positions as the crystal gradually rotated, typically 360°, with incremental rotations of 0.1°. X-ray diffraction data were processed with several crystallographic programs. Data sets from individual crystals were indexed, integrated, and scaled using XDS (Kabsch, 2010) or iMOSFLM and SCALA (Battye et al., 2011) from the CCP4 package.

3.5.4. Cryo-electron microscopy (Cryo-EM)

With the assistance of our collaborators at the Electron Microscopy Platform at CIC bioGUNE (Basque Country, Spain), preliminary vitrification tests with Retriever samples were conducted at different concentrations for cryo-electron microscopy studies, using a buffer composed by 25 mM Hepes pH 7.5, 200 mM NaCl, and 1 mM TCEP. Quantifoil Holey Carbon R2/2 Mesh 300 copper grids (Quantifoil Micro Tools, Großlöbichau, Germany) were glow-discharged for 40 seconds at 8.6 mA before applying 4 µl of the sample and plunge-freezing it in liquid ethane using a Vitrobot™ System (Thermo) with 75-85% chamber humidity at 16 °C. The sample was incubated with the grids for 15 seconds, followed by blotting the grids for 2 seconds. A dataset of micrographs was collected using a JEM-2200FS/CR transmission electron microscope (JEOL, Japan), equipped with an UltraScan 4000 SP (4008×4008 pixels) cooled slow-scan CCD camera (GATAN, UK). From the collected data, a preliminary 2D classification of the Retriever complex was performed, and an initial 3D model was created from the selected 2D particles using Relion (Zivanov et al., 2018).

In addition, two other cryo-EM studies were performed. The first study involved the Retriever complex with an MBP tag in VPS29. The second study analyzed a protein complex composed of Retriever-MBP, MBP-SNX17, and $L2_{FBR}$. After optimizing the micrograph for the Retriever-MBP:MBP-SNX17:$L2_{FBR}$ complex, grids were prepared and sent to eBIC (Electron Bio-Imaging Centre) at Diamond Light Source (Didcot, United Kingdom). Data were collected using the Titan Krios IV microscope, equipped with a Gatan K3 camera. Fifty-frame super-resolution movies were recorded with a 2-second exposure time, a total dose of 52.7 $e^-/Å^2$, and a pixel size of 0.829 Å/px at the specimen level. Isaac Santos and Diego Charro from CIC bioGUNE was responsible for processing the electron microscopy data using cryoSPARC (Punjani et al., 2017).

3.6. Protein-protein interaction studies

3.6.1. Fluorescence anisotropy assay

The peptides used for binding assays (**Table 2**) were synthesized with an N-terminal 5-Carboxyfluorescein (FAM) and HPLC purified (≥95%) by GenScript. The lyophilized peptides were resuspended in 100 mM Hepes pH 7.5 at 5 mg/ml and further diluted in the assay buffer (50 mM Hepes pH 7.5, 300 mM NaCl and 1 mM DTT). 50 µl-binding reactions were prepared by serial dilutions of purified protein with final concentrations ranging between 0.25 µM to 128 µM and a fixed ligand concentration of 0.1 µM. The mixture was incubated at 25 ºC for at least 30 minutes and then transferred to 96 well, black, flat bottom microplates (Tecan). Fluorescence anisotropy was measured at 25 ºC using Spark 10M Plate Reader (Tecan) with a 485/20 excitation filter and 535/35 emission filter. The dissociation constants were calculated in GraphPad Prism by nonlinear regression fitting of the experimental data to a one-site total binding model. The final K_D measurement is the mean of at least two independent experiments.

3.6.2. Pull-down assays

For pull-down assays, proteins of interest at 5 µM were incubated in binding buffer (25 mM Hepes pH 7.5, 300 mM NaCl, 1 mM DTT, and 0.01% Triton X-100) either with GST-tagged or MBP-tagged ligands at 2.5 mM in the presence of glutathione agarose beads (Cube Biotech), amylose resin beads (NEB) or Ni-INDIGO agarose beads (Cube Biotech), respectively. The nonionic detergent triton X-100 was added to reduce non-specific hydrophobic. A volume of 50 µl of the mixture, along with 10 µl of pre-equilibrated beads, was incubated on a rotating wheel for 1 hour at 4 °C. Beads were washed three times with 0.5 ml binding buffer and resuspended in SDS-PAGE loading buffer. Protein controls and resin samples were loaded on a precast NuPAGE 4-12% Bis-Tris SDS-PAGE gel (Invitrogen) or self-made 15% SDS-PAGE gels (Mini-PROTEAN, Bio-Rad), together with PageRuler Plus Prestained Protein Ladder 10 to 250 kDa (Thermo) in NuPAGE™ MOPS SDS Running buffer 1X (Thermo) or SDS-PAGE running buffer, respectively. After Coomassie blue staining, gels were scanned with the Odyssey CLx imaging system. For each experiment, two, three or four independent pull-downs were performed. Non-fused GST or non-fused MBP proteins were used as negative controls. The quantification of pull-down gel results was conducted by assessing background-subtracted band intensities using Fiji/ImageJ software(Schindelin et al, 2012). Statistical analyses were performed with GraphPad Prism, using unpaired Student's t-test.

3.7. Protein-lipid interaction studies

3.7.1. GUV preparation

For the study of Retriever binding to membranes, a GUV lipid mixture was prepared that contain DOPC:DOPE:DOPS:PI3P:Marina Blue™ DHPE in a 45:29.3:20:5:0.7 molar ratio, and the final mix concentration was prepared at 1.5 mM. All lipids were purchased from Avanti Polar Lipids (Alabaster, AL, USA) and are detailed in **Table 3**. First, multilamellar lipid vesicles (MLVs) were prepared. All lipids were mixed, incubated for 1 hour at 37 ºC, desiccated in spin vacuum to remove organic solvents such as chloroform and methanol, rehydrated with a previously degassed working buffer (20 mM Hepes pH 7.5, 200 mM NaCl, 1 mM TCEP), and the mixture was incubated for 1 hour at 60 ºC. Argon gas was added when tubes were opened to avoid oxidative damage from air. From MLVs, GUVs were generated following the method developed by Velasco-Olmo *et al.* (Velasco-Olmo et al., 2019), with the use of 41 µm-diameter plain silica microspheres (Corpuscular Inc). Briefly, 2 µl-drops of the lipid mixture were placed on a Teflon surface. 1 µl of plain silica microspheres was brought into contact with the lipid drops and fell into the drop without the need for pipetting. The drops were dried in vacuum and mixed with 6 µl of 1 M trehalose (Sigma) using a cut plastic pipette tip. The tip was then introduced into a home-made humidity chamber, which consists of a 1.5 ml-Eppendorf tube halfway filled with Milli-Q water and with a hole in its cap, and incubated in this chamber for 10 minutes at 60 ºC.

3.7.2. GUV assays and imaging

Marina Blue™ labeled GUV membranes were incubated with 2 µM of purified proteins for 15 minutes at room temperature in binding buffer (20 mM Hepes pH 7.5, 200 mM NaCl, 1 mM TCEP). The mixture was examined by fluorescence microscopy in 18-well uncoated chambered coverslips (Ibidi, Cat# 81811), which were previously treated with bovine serum albumin (BSA) at 1 mg/ml (Sigma) for 2 hours. For image acquisition, an ECLIPSE Ti2 inverted microscope (NIKON) was used, equipped with an APO TIRF 60x 1.49 lens, with LED as light source and an sCMOS camera (Hamamatsu Orca-Flash4.0). The fluorescence of Marina Blue™ fluorophore was detected using a Zeiss G 365 excitation filter and a BP 445/50 emission filter; the fluorescence of EGFP with a Zeiss BP 470/40 excitation filter and a BP 525/50 emission filter; and mKate2 was detected with a Zeiss BP 546/12 excitation filter and a BP 575-640 emission filter. Images were processed with Fiji (Schindelin et al., 2012). For the same experiment, all the images were settled with the same values of brightness and contrast, and a representative GUV image from each condition was selected and scale bar was added (which belongs to 5 µm).

3.7.3. Liposomes preparation

The liposomes were composed of a mixture of lipids with the following final molar ratios: 44.7% DOPC, 29.3% DOPE, 20.0% DOPS, 5.0% 18:1 PI3P, and 1.0% 18:1 Liss Rhod PE. These vesicles were prepared using a thin-film hydration technique similar to that used for GUVs, followed by extrusion to get a more homogeneous vesicle population. Large Unilamellar Vesicles (LUVs) were produced using a mini extruder (Avanti Polar Lipids) and Whatman Nucleopore track-etched membranes with a 0.4 µm pore size (Cytiva). The extrusion buffer, consisting of 25 mM Hepes (pH 7.5) and 1 mM TCEP, was supplemented with 250 mM Raffinose pentahydrate (Thermo Fisher) to create vesicles filled with raffinose. These vesicles can be separated from the aqueous solution using co-sedimentation assays via centrifugation (Julkowska et al., 2013). A 2 mM liposome suspension was diluted with three volumes of working buffer (25 mM Hepes pH 7.5, 200 mM NaCl, 1 mM TCEP) and then ultracentrifuged at 50,000 g for 15 minutes at 22 ºC in a Sorvall-WX Ultra 100 ultracentrifuge (Thermo). The pellet, which contained the vesicles, was resuspended in an equal volume of working buffer. The liposomes were stored in an argon atmosphere at 21 ºC for up to 7 days.

3.7.4. Liposome co-sedimentation assays

For co-sedimentation experiments, 0.5 ml tubes were sequentially filled with the working buffer (25 mM Hepes pH 7.5, 200 mM NaCl, 1 mM TCEP), proteins (Retriever, His-Sumo-SNX17, and His_{10}-$L2_{FBR}$ or His_{10}-$LRP1_{ICD}$ in a 2:2:4 µM ratio), and liposomes (1 mM final concentration). To remove potential aggregates, proteins were first centrifuged at 21,100 g for 30 minutes at 4 ºC. The resulting mixtures were then incubated at room temperature on a rotating wheel for 1 hour. Following incubation, the samples were centrifuged at 16,000 g for 30 minutes at 21 ºC. The pellet obtained was washed with 500 µl of working buffer without resuspension and subjected to a second round of centrifugation. The supernatant (S sample) was collected, mixed with 5X loading buffer, and 500 µl was discarded. The pellet (P sample) was resuspended in 1X loading buffer. Both S and P samples were loaded onto a 15% SDS-PAGE gel along with PageRuler Plus Prestained Protein Ladder (Thermo) and electrophoresed at 150 V for 90 minutes. Protein bands were visualized using Coomassie staining and imaged with an Odyssey CLx. Signal intensity was quantified using Empiria Studio Software (LI-COR). Each co-sedimentation experiment was conducted in triplicate under the same conditions, and statistical analyses were performed using GraphPad Prism with one-way ANOVA followed by Tukey's post hoc test.

3.8. Computational modeling and bioinformatic analyses

3.8.1. Modeling with AlphaFold2 multimer

The AlphaFold2 multimer algorithm (Jumper et al., 2021; Varadi et al., 2022) from the Neurosnap web tool and Colabfold (Mirdita et al., 2022) was used to model the SNX17-cargo (SNX17:L2$_{FBR}$, SNX17:L2$_{14\text{-}mer}$, SNX17:LRP1$_{14\text{-}mer}$, SNX17:APP$_{14\text{-}mer}$, SNX17:ITGB1$_{P\text{-}14\text{-}mer}$, SNX17:ITGB1$_{D\text{-}13\text{-}mer}$, SNX17:L2$_{CT\text{-}18}$) and SNX17-Retriever (SNX17:VPS26C:VPS35L:VPS29, SNX17$_{CT\text{-}18}$:VPS26C:VPS35L$_{110\text{-}598}$, SNX17:L2$_{17\text{-}mer}$: VPS26C:VPS35L$_{110\text{-}598}$) structures. Five models were generated without templates, through ten iterative refinement recycles, and relaxed using AMBER. The model with the highest pLDDT score was selected. ChimeraX was and PyMol Molecular Graphics System (Schrödinger, LLC) were used to generate all the figures depicting the predicted protein structures and the corresponding PAE plots.

3.8.2. Characterization of the energetic contribution of each residue

To determine the energetic contribution of each residue to the surface interaction of a protein complex, computational mutagenesis to alanine was screened using the resEnergy pyDock web server (Romero-Durana et al., 2020). The scoring function of the docking energy from this server accounts for electrostatics, desolvation, and van der Waals energy terms. These terms are analyzed for each individual residue, providing a detailed description of the docking energy landscape. AF3 models of SNX17:L2$_{248\text{-}261}$, SNX17:LRP1$_{4464\text{-}4477}$, SNX17:APP$_{753\text{-}766}$ and SNX17:ITGB1$_{774\text{-}787}$ were submitted as input, and the residue contribution from each cargo were calculated.

3.8.3. Evolutionary conservation analysis

Evolutionary conservation analysis was conducted using the ConSurf web server (Ashkenazy et al., 2016) (https://consurf.tau.ac.il/consurf_index.php), with the AF2 models as the query and default parameters. The results were mapped onto the structure. Multiple sequence alignments were generated using the structure-based alignment tool PROMALS3D (Pei et al., 2008) and plotted with ESPript 3 (Robert & Gouet, 2014).

3.8.4. Databases

Nucleic acids sequences used in this work were retrieved from the NCBI database (National Center for Biotechnology Information, National Institutes of Health, NIH). Protein sequences and structures were obtained from Protein Data Bank or PDB (Research Collaboratory for Structural Bioinformatics, RCSB). Protein structural models were downloaded from the AlphaFold Protein Structure Database (Google DeepMind and EMBL-EBI). The BLAST (Basic Local Alignment Search Tool) online server (NCBI) was used to identify protein and DNA homologous sequences (Altschul, 1997). Sequence alignment to determine the degree of similarity and conservation among residues of different proteins was performed using the Clustal Omega server (EMBL-EBI) (Madeira et al., 2024) (https://www.ebi.ac.uk/Tools/msa/clustalo/). Information on specific proteins was obtained from Uniprot (The UniProt Consortium et al., 2023) (https://www.uniprot.org/), GeneCards® (The Human Gene Database) (Stelzer et al., 2016) (https://www.genecards.org/), and The Human Protein Atlas (Uhlén et al., 2015) (https://www.proteinatlas.org/).

3.9. Supplementary tables

Table 8. DNA constructs for recombinant protein production used in this thesis.

Identifier	Plasmid construct	Source/reference
	pET28-Sumo3	EMBL, Heidelberg
	pGST-P2	(Sheffield et al., 1999)
	pET28NStrep	KP Hopfner Lab (Gene Center)
	pCDH-CMV-fmKate2-EF1-puro	I. Varela Lab (IBBTEC)
	pLIB	(Weissmann et al., 2016)
	pBIG1a	(Weissmann et al., 2016)
	pHis-MBP-P4	(Sheffield et al., 1999)
pMLG30	pIA-His	This study
pMLG31	pIA-GST	This study
pMLG32	pIA-His-MBP	This study
pMLG34	pIA-Strep	This study
pMLG73	pIA-Twin-Strep	This study
pMLG23	pMK-VPS26C (opt*)	Invitrogen GeneArt
pMLG21	pET28-His-Sumo3-VPS26C (opt)	This study
pMLG6	pGST-VPS29	(Romano-Moreno et al., 2017)
pMLG11	pECE-H2-SNX17	Addgene # 69811
pMLG13	pET28-His-Sumo3-SNX17	This study
pMLG135	pET28-His-Sumo3-SNX17$_{PX}$	This study
pMLG1	pET28-His-Sumo3-SNX17$_{FERM-CT}$	This study
pMLG14	pET28-His-Sumo3-EGFP-SNX17	This study
pMLG159	pIA-His-MBP-SNX17	This study
pMLG179	pIA-His-MBP-SNX17$_{D467X}$	This study
pMLG178	pIA-His-MBP-SNX17$_{L470G}$	This study
pMLG203	pIA-His-MBP-SNX17$_{W321A}$	This study
pMLG204	pIA-His-MBP-SNX17$_{V380D}$	This study
pMLG205	pIA-His-MBP-SNX17$_{H457A}$	This study
pMLG206	pIA-His-MBP-SNX17$_{N459A+F462A}$	This study
pMLG238	pET28-His-Sumo3-EGFP-SNX17$_{R36A+Y37A}$	This study
pMLG248	pET28-His-Sumo3-EGFP-SNX17$_{K431LSSK:AAAAA}$	This study
pMLG250	pET28-His-Sumo3-EGFP-SNX17$_{7-470}$	This study
pMLG29	pET28-His-Sumo3-SNX17$_{FERM-CT}$-TEV-L2$_{FBR}$	This study
pMLG42	pET28-His-Sumo3-SNX17$_{FERM-CT}$-TEV-APP$_{739-770}$	This study
pMLG181	pET28-His-Sumo3-SNX17$_{FERM-CT(del406-442)}$	This study
pMLG146	pET28-His-Sumo3-SNX17$_{109-388}$-L2$_{FBR}$	This study
pMLG20	pET28-His-Sumo3-SNX31$_{FERM-CT}$	This study
pMLG25	pMK-LRP1$_{ICD}$ (opt)	Invitrogen GeneArt
pMLG18	pIA-GST-TEV-LRP1$_{ICD}$ (opt)	This study
pMLG275	pIA-GST-LRP1$_{ICD-mut(N4470A+Y4473A)}$	This study
pMLG124	pIA-GST-3C-His$_{10}$-LRP1$_{ICD}$ (opt)	This study
pMLG165	pIA-His-MBP-His$_{10}$-LRP1$_{ICD}$ (opt)	This study
pMLG173	pIA-MBP-His$_{10}$-LRP1$_{ICD}$ (opt)	This study
pMLG48	pGST-APP$_{ICD}$	A. Hierro Lab (CIC bioGUNE)
pMLG49	pIA-GST-TEV-APP$_{ICD}$	This study
pMLG167	gBlock-ITGB1$_{ICD}$	IDT gBlock

pMLG168	pIA-GST-TEV-ITGB1$_{ICD}$	This study
pMLG28	pIA-GST-TEV-L2$_{FBR}$	This study
pMLG276	pIA-GST-L2$_{FBR\text{-}mut(N254A+Y257A)}$	This study
pMLG131	pIA-GST-3C-His$_{10}$-L2$_{FBR}$	This study
pMLG22	pMK-VPS35L (opt)	Invitrogen GeneArt
pMLG44	pIA-His-VPS35L	This study
pMLG37	pLIB-His-VPS35L (opt)	This study
pMLG05	pET28-His-Sumo3-VPS26C	A. Hierro Lab (CICbioGUNE)
pMLG83	pIA-Twin-Strep-VPS26C	This study
pMLG84	pLIB-Twin-Strep-VPS26C (opt)	This study
pMLG7	pET28-His-Sumo3-VPS29	A. Hierro Lab (CICbioGUNE)
pMLG39	pLIB-VPS29	This study
pMLG85	pBIG1a-His-VPS35L-Twin-Strep-VPS26C-VPS29	This study
pMLG121	pLIB-GST-HRV3C-VPS29	This study
pMLG122	pBIG1a-His-VPS35L-Twin-Strep-VPS26C-GST-VPS29	This study
pMLG156	pLIB-MBP-VPS29	This study
pMLG164	pBIG1a-His-VPS35L-Twin-Strep-VPS26C-MBP-VPS29	This study
pMLG109	pIA-His-VPS35L$_{110\text{-}963}$	This study
pMLG113	pLIB-His-VPS35L$_{110\text{-}963}$	This study
pMLG118	pBIG1a-His-VPS35L$_{110\text{-}963}$-Twin-Strep-VPS26C-VPS29	This study
pMLG107	pIA-His-VPS35L$_{110\text{-}598}$	This study
pMLG111	pLIB-His-VPS35L$_{110\text{-}598}$	This study
pMLG116	pBIG1a-His-VPS35L$_{110\text{-}598}$-Twin-Strep-VPS26C-VPS29	This study
pMLG137	pLIB-His-VPS35L$_{1\text{-}598}$	This study
pMLG138	pBIG1a-His-VPS35L$_{1\text{-}598}$-Twin-Strep-VPS26C-VPS29	This study
pMLG141	pLIB-His-VPS35L$_{1\text{-}436}$	This study
pMLG144	pBIG1a-His-VPS35L$_{1\text{-}436}$-Twin-Strep-VPS26C-VPS29	This study
pMLG151	pBIG1a-His-VPS35L-GST-VPS29	This study
pMLG228	pLIB-HisVPS35L$_{R248E+W280D}$	This study
pMLG231	pBIG1a-HisVPS35L$_{R248E+W280D}$-Twin-Strep-VPS26C-VPS29	This study
pMLG229	pLIB-HisVPS35L$_{K157E+R161E}$	This study
pMLG232	pBIG1a-HisVPS35L$_{K157E+R161E}$-Twin-Strep-VPS26C-VPS29	This study
pMLG15	pET28-His-Sumo3-VPS29-GFP	This study
pMLG59	pET28-His-Sumo3-VPS29-mKate2	This study
pMLG115	pLIB-VPS29-mKate2	This study
pMLG120	pBIG1a-His-VPS35L-Twin-Strep-VPS26C-VPS29-mKate2	This study
pMLG101	pET-50b-His-NusA-DENND10	This study
pMLG8	pET-TEV	Addgene # 92414
pMLG9	pET28-Senp2	KP Hopfner Lab (Gene Center)
pMLG10	pGEx4-T PreScission	F. Blanco Lab (CIB)

*Opt: Optimized for *E. coli* expression.

Table 9. List of all DNA constructs generated in this thesis, including those for which protein purification was unsuccessful.

Constructs that were generated but were unsuccessful due to lack of protein overexpression or solubility are highlighted in red. Constructs with low soluble protein yield are marked in yellow, whereas those for which protein purification was successful are indicated in green. By default, all constructs were overexpressed in bacteria, except those marked with an asterisk ("*"), which were expressed in insect cells.

Protein	ID	Plasmid	Protein	ID	Plasmid
VPS26C	pMLG5	pET28-His-Sumo3-VPS26C	**VPS26C-VPS35L-VPS29**	pMLG143*	pBIG1a-HisVPS35L$_{1-351}$-Twin-StrepVPS26C-GSTVPS29
	pMLG3	pDBHis-GST-VPS26C		pMLG144*	pBIG1a-HisVPS35L$_{1-436}$-Twin-StrepVPS26C-VPS29
	pMLG12	pET29a-VPS26C-His		pMLG145*	pBIG1a-HisVPS35L$_{1-436}$-Twin-StrepVPS26C-GSTVPS29
	pMLG21	pET28-His-Sumo3-VPS26C (opt)		pMLG150*	pBIG1a-HisVPS35L-Twin-StrepVPS26C
	pMLG94	pIA-His-VPS26C		pMLG151*	pBIG1a-HisVPS35L-GST-VPS29
	pMLG95	pIA-His-MBP-VPS26C		pMLG163*	pBIG1a-His-TEV-VPS35L-MBP-VPS26C-VPS29
	pMLG96	pIA-His-TrxA-VPS26C		pMLG164*	pBIG1a-His-TEV-VPS35L-Twin-StrepVPS26C-MBP-VPS29
	pMLG82	pIA-His-Zbasic-VPS26C		pMLG231*	pBIG1a-HisVPS35L$_{W280D+R248E}$-Twin-StrepVPS26C-VPS29
	pMLG83	pIA-Twin-Strep-VPS26C		pMLG232*	pBIG1a-HisVPS35L$_{K157E+ R161E}$-Twin-StrepVPS26C-VPS29
	pMLG97	pIA-GST-VPS26C	**DENND10**	pMLG101	pET-50b-His-NusA-DENND10
	pMLG74	pGEX-6P1-VPS26C (opt)	**SNX31**	pMLG19	pET28-His-Sumo3-SNX31$_{FL}$ (opt)
	pMLG69*	pBIG1a-His-Sumo3-VPS26C		pMLG20	pET28-His-Sumo3-SNX31$_{FERM-CT}$ (opt)
VPS29	pMLG6	pGST-VPS29		pMLG90	pIA-GST-SNX31$_{FERM-CT}$ (opt)
	pMLG7	pET28-His-Sumo3-VPS29		pMLG91	pIA-His-MBP-SNX31$_{FERM-CT}$ (opt)
	pMLG59	pET28-His-Sumo3-VPS29-mKate2		pMLG92	pIA-His-TrxA-SNX31$_{FERM-CT}$ (opt)
VPS35L	pMLG44	pIA-His-VPS35L (opt)		pMLG93	pIA-His-Zbasic-SNX31$_{FERM-CT}$ (opt)
	pMLG36	pIA-Strep-VPS35L (opt)		pMLG99	pIA-His-Zbasic-SNX31$_{110-384}$ (opt)
	pMLG4	pDB-His-GST-VPS35L		pMLG149	pET28-His-Sumo3-SNX31$_{1-116}$ (opt)
	pMLG26	pGST-VPS35L (opt)	**SNX17**	pMLG13	pET28-His-Sumo3-SNX17
	pMLG71	pIA-His-MBP-VPS35L (opt)		pMLG1	pET28-His-Sumo3-SNX17$_{FERM-CT}$
	pMLG72	pIA-His-TrxA-VPS35L (opt)		pMLG98	pIA-GST-TEV-SNX17$_{FERM-CT}$
	pMLG53	pIA-His-VPS35L$_{N617}$ (opt)		pMLG41	pET28-His-Sumo3-SNX17$_{109-388}$
	pMLG16	pIA-GST-VPS35L$_{N617}$ (opt)		pMLG46	pET28-His-Sumo3-SNX17$_{N318}$
	pMLG51	pIA-GST-TEV-VPS35L$_{N617}$ (opt)		pMLG14	pET28-His-Sumo3-GFP-SNX17
	pMLG55	pIA-His-TrxA-VPS35L$_{N617}$ (opt)		pMLG42	pET28-His-Sumo3-SNX17$_{FERM-CT}$-TEV-APP$_{739-770}$
	pMLG57	pIA-His-MBP-VPS35L$_{N617}$ (opt)		pMLG29	pET28-His-Sumo3-SNX17$_{FERM-CT}$-TEV-L2$_{FBR}$

	pMLG54	pIA-His-VPS35L$_{617C}$ (opt)		pMLG146	pET28-His-Sumo3-SNX17$_{109-388}$-TEV-L2$_{FBR}$
	pMLG52	pIA-GST-TEV-VPS35L$_{618C}$ (opt)		pMLG128	pIA-GST-TEV-SNX17$_{109-388}$
	pMLG56	pIA-His-TrxA-VPS35L$_{618C}$ (opt)		pMLG134	pET28-His-Sumo3-SNX17$_{109-388}$
	pMLG58	pIA-His-MBP-VPS35L$_{618C}$ (opt)		pMLG135	pET28-His-Sumo3-SNX17$_{N108}$
	pMLG60	pIA-His-MBP-VPS35L$_{N169}$ (opt)		pMLG136	pET28-His-Sumo3-SNX31$_{N109}$
	pMLG87	pIA-His-Zbasic-VPS35L$_{N169}$ (opt)		pMLG147	pET28-His-Sumo3-SNX17$_{1-405}$
	pMLG61	pIA-His-MBP-VPS35L$_{N222}$ (opt)		pMLG158	pLIB-GST-HRV3C-SNX17$_{FL}$
	pMLG160	pIA-His-MBP-VPS35L$_{1-351}$ (opt)		pMLG159	pIA-His-MBP-SNX17
	pMLG161	pIA-His-MBP-VPS35L$_{1-436}$ (opt)		pMLG178	pIA-His-MBP-SNX17$_{L470G}$
	pMLG62	pIA-His-TrxA-VPS35L$_{110-578}$ (opt)		pMLG179	pIA-His-MBP-SNX17$_{D467X}$
	pMLG63	pIA-His-TrxA-VPS35L$_{110-598}$ (opt)		pMLG181	pET28-His-Sumo3-SNX17$_{FERM-CT (del406-442)}$
	pMLG88	pIA-His-Zbasic-VPS35L$_{110-598}$ (opt)		pMLG203	pIA-His-MBP-SNX17$_{W321A}$
	pMLG64	pIA-His-TrxA-VPS35L$_{110C}$ (opt)		pMLG204	pIA-His-MBP-SNX17$_{V380D}$
	pMLG65	pIA- His-TrxA-VPS35L$_{167C}$ (opt)		pMLG205	pIA-His-MBP-SNX17$_{H457A}$
	pMLG66	pIA-His-TrxA-VPS35L$_{220C}$ (opt)		pMLG206	pIA-His-MBP-SNX17$_{N459A+F462A}$
	pMLG67	pIA-His-TrxA-VPS35L$_{579C}$ (opt)		pMLG211	pIA-His-MBP-TEV-SNX17
	pMLG89	pIA-His-Zbasic-VPS35L$_{579C}$ (opt)		pMLG212	pIA-His-TEV-MBP-3C-SNX17
	pMLG68	pIA-His-TrxA-VPS35L$_{599C}$ (opt)		pMLG228	pET28-His-Sumo3-GFP-SNX17$_{R36A+Y37A}$
	pMLG45*	pIEx6-His-TEV-VPS35		pMLG248	pET28-His-Sumo3-GFP-SNX17$_{K431LSSK:AAAAA}$
	pMLG70*	pBIG1a-His-TEV-VPS35L		pMLG250	pET28-His-Sumo3-GFP-SNX17$_{7-470}$
	pMLG154*	pLIB-His-TEV-MBP-VPS35L	**Cargos**	pMLG43	pGST-APP$_{32}$
VPS26C-VPS35L-VPS29	pMLG40*	pBIG1a-VPS35L-VPS26C-VPS29		pMLG49	pIA-GST-APP$_{ICD}$
	pMLG85*	pBIG1a-HisVPS35L-Twin-StrepVPS26C-VPS29		pMLG18	pIA-GST-LRP1$_{ICD}$ (opt)
	pMLG116*	pBIG1a-HisVPS35L$_{110-598}$-Twin-StrepVPS26C-VPS29		pMLG275	pIA-GST-LRP1$_{ICD-mut(N4470A+Y4473A)}$ (opt)
	pMLG117*	pBIG1a-HisVPS35L$_{599-963}$-Twin-StrepVPS26C-VPS29		pMLG28	pIA-GST-L2$_{FBR}$
	pMLG118*	pBIG1a-HisVPS35L$_{110-963}$-Twin-StrepVPS26C-VPS29		pMLG276	pIA-GST-L2$_{FBR-mut(N254A+Y257A)}$
	pMLG119*	pBIG1a-HisVPS35L$_{1-222}$-Twin-StrepVPS26C-VPS29		pMLG124	pIA-GST-3C-His$_{10}$-LRP1$_{ICD}$ (opt)
	pMLG120*	pBIG1a-HisVPS35L-Twin-StrepVPS26C-VPS29mKate		pMLG125	pIA-GST-3C-His$_{10}$-APP

	pMLG122*	pBIG1a-HisVPS35L-Twin-StrepVPS26C-GSTVPS29
	pMLG123*	pIA-HisTrxAVPS35L-Twin-StrepVPS26C-VPS29
	pMLG138*	pBIG1a-HisVPS35L$_{1-598}$-Twin-StrepVPS26C-VPS29
	pMLG139*	pBIG1a-HisVPS35L$_{1-598}$-Twin-StrepVPS26C-GSTVPS29
	pMLG142*	pBIG1a-HisVPS35L$_{1-351}$-Twin-StrepVPS26C-VPS29
	pMLG143*	pBIG1a-HisVPS35L$_{1-351}$-Twin-StrepVPS26C-GSTVPS29
	pMLG144*	pBIG1a-HisVPS35L$_{1-436}$-Twin-StrepVPS26C-VPS29
	pMLG145*	pBIG1a-HisVPS35L$_{1-436}$-Twin-StrepVPS26C-GSTVPS29
	pMLG150*	pBIG1a-HisVPS35L-Twin-StrepVPS26C
	pMLG151*	pBIG1a-HisVPS35L-GST-VPS29
	pMLG163*	pBIG1a-His-TEV-VPS35L-MBP-VPS26C-VPS29
	pMLG164*	pBIG1a-His-TEV-VPS35L-Twin-StrepVPS26C-MBP-VPS29
	pMLG231*	pBIG1a-HisVPS35L$_{W280D+R248E}$-Twin-StrepVPS26C-VPS29
	pMLG232*	pBIG1a-HisVPS35L$_{K157E+R161E}$-Twin-StrepVPS26C-VPS29
	pMLG126	pIA-GST-3C-His$_{10}$-L2$_{FBR}$
	pMLG129	pIA-GST-3C-His$_{10}$-LRP1$_{ICD}$ (opt)
	pMLG130	pIA-GST-3C-His$_{10}$-APP$_{ICD}$ (opt)
	pMLG131	pIA-GST-3C-His$_{10}$-L2$_{FBR}$
	pMLG152	pIA-His$_{10}$-LRP1$_{ICD}$
	pMLG153	pIA-His$_{10}$-L2$_{FBR}$
	pMLG165	pIA-His-MBP-His$_{10}$-LRP1$_{ICD}$
	pMLG168	pIA-GST-TEV-ITGB1$_{ICD}$
	pMLG169	pIA-GST-3C-His$_{10}$-ITGB1$_{ICD}$
	pMLG173	pIA-MBP-His$_{10}$-LRP1$_{ICD}$
	pMLG174	pIA-MBP-His$_{10}$-APP$_{ICD}$
	pMLG175	pIA-MBP-His$_{10}$-L2$_{FBR}$

Table 10. DNA oligos used in this thesis.

ID: pMLG Plasmid identification number.

ID	Amplification	Template	Primer Identifier and sequence, all 5' to 3'
30	His-TEV	pET28-Sumo3	088: CCGATGAAACGAGAGAGGATGCTCACGATACGGGTTACTG 071: GCCCTGGAAGTACAGGTTTTCGCCGCTGCTGTGATGATGATGATGATG
	His-TEV	pET28-Sumo3	070: GGCGAAAACCTGTACTTCCAGGGCGTGAGCAAGGGCGAGGAGCTG 089: CAGTAACCCGTATCGTGAGCATCCTCTCTCGTTTCATCGG
31	Insert GST	pGST-P2	072: GAAGGAGATATACCATGGGCAGCAGCATGTCCCCTATACTAGGTTATTGGAAAATTAAGGGCC 073: GGAAGTACAGGTTTTCGCCGCTGCTTTTTGGAGGATGGTCGCCACCACC
	Vector	pIA-His	095: GCTGCTGCCCATGGTATATCTCCTTCTTAAAGTTAAAC 096: AGCAGCGGCGAAAACCTGTACTTCCAGGGC
32	His-MBP-TEV	pHis-MBP-P4	088: CCGATGAAACGAGAGAGGATGCTCACGATACGGGTTACTG 074: GGAAGTACAGGTTTTCGCCGCTGCTCCCGAGGTTGTTGTTATTGTTATTGTTGTTGTTG
34	Strep	pET28NStrep	088: CCGATGAAACGAGAGAGGATGCTCACGATACGGGTTACTG 076: GGAAGTACAGGTTTTCGCCGCTGCTAGCGCCTTTTTCGAACTGCGGGTGG
	Vector	pMLG30	096: AGCAGCGGCGAAAACCTGTACTTCCAGGGC 089: CAGTAACCCGTATCGTGAGCATCCTCTCTCGTTTCATCGG
73	Half of the vector	pMLG34	089: CAGTAACCCGTATCGTGAGCATCCTCTCTCGTTTCATCGG 150:CGGTGGATCAGGTGGAAGTGCATGGTCTCATCCTCAGTTTGAGAAAAGCAGCGGCGAAAACCTGTACTTCCAGG
	Half of the vector	pMLG34	088: CCGATGAAACGAGAGAGGATGCTCACGATACGGGTTACTG 151:GGATGAGACCATGCACTTCCACCTGATCCACCGCCAGAACCTCCGCCTTTTTCGAACTGCGGGTGGCTCC
21	Insert VPS26C	pMLG23	053: CGTGTTCCAGCAGCAGACCGGTGGAATGGGCACCGCACTGGATATCAAAATCAAACG 054: CTCAGTGGTGGTGGTGGTGGTGTTAAATGCGGCACAGTTTCAGCGGAAAGTTTTCGG
	Vector	pET28-Sumo3	002: CACCACCACCACCACCACTGAGATCCGGCTGCTAAC 001: TCCACCGGTCTGCTGCTGGAACACGTCGATGGTGTCCTCG
13	Insert SNX17	pMLG11	032: CGACGTGTTCCAGCAGCAGACCGGTGGAATGCACTTTTCCATTCCCGAAACCGAGTCCCGC 007: CCGGATCTCAGTGGTGGTGGTGGTGGTGTTACAGATCCTCATCTCCAATGCCCTCGAAGG
	Vector	pET28-Sumo3	As in 21.
135	Insert $SNX17_{PX}$	pMLG11	032: CGACGTGTTCCAGCAGCAGACCGGTGGAATGCACTTTTCCATTCCCGAAACCGAGTCCCGC 184: GATCTCAGTGGTGGTGGTGGTGGTGTTACTCCTGTTGTGCCCGACGCAGGAAAC
	Vector	pET28-Sumo3	As in 21.
1	Insert $SNX17_{FERM-CT}$	pMLG11	006: CGACGTGTTCCAGCAGCAGACCGGTGGAACACAGCAGGTCCCCACAGAGGAAGTG 007: CCGGATCTCAGTGGTGGTGGTGGTGGTGTTACAGATCCTCATCTCCAATGCCCTCGAAGG
	Vector	pET28-Sumo3	As in 21.
14	Insert SNX17	pMLG13	007: CCGGATCTCAGTGGTGGTGGTGGTGGTGTTACAGATCCTCATCTCCAATGCCCTCGAAGG 034:GGGATCACTCTCGGCATGGACGAGCTCTACAAGGGCGGCGGCGGCAGCATGCACTTTTCCATTCCCGAAACCGAGTCCCGC
	Vector	pET28-Sumo3	002: CACCACCACCACCACCACTGAGATCCGGCTGCTAAC 036: CTTGTAGAGCTCGTCCATGCCGAGAGTGATCCCGGCG
159	Insert SNX17	pMLG11	007: CCGGATCTCAGTGGTGGTGGTGGTGGTGTTACAGATCCTCATCTCCAATGCCCTCGAAGG 208: GACGCGCAGACTAATTCGAGCTCTATGCACTTTTCCATTCCCGAAACCGAGTCC

	Insert MBP	pMLG32	203: GCGAAAACCTGTACTTCCAGGGCATGATCGAAGAAGGTAAACTGGTAATCTGGATTAACG 204: AGAGCTCGAATTAGTCTGCGCGTCTTTCAG
	Vector	pMLG30	002: CACCACCACCACCACCACTGAGATCCGGCTGCTAAC 094: GCCCTGGAAGTACAGGTTTTCGCCGCTGC
179	Insert MBP-$SNX17_{D467X}$	pMLG159	203: GCGAAAACCTGTACTTCCAGGGCATGATCGAAGAAGGTAAACTGGTAATCTGGATTAACG 240: GATCTCAGTGGTGGTGGTGGTGGTGTTATCCAATGCCCTCGAAGGCGAAATTGC
	Vector	pMLG30	As in 159.
178	Insert MBP-$SNX17_{L470G}$	pMLG159	203: GCGAAAACCTGTACTTCCAGGGCATGATCGAAGAAGGTAAACTGGTAATCTGGATTAACG 239: GATCTCAGTGGTGGTGGTGGTGGTGTTAACCATCCTCATCTCCAATGCCCTCGAAGG
	Vector	pMLG30	As in 159.
203	pIA-His-MBP-$SNX17_{W321A}$_1	pMLG159	246: GTCACCCGCATGCGATGCGCGCGGGTCACCTCCTCTGTAC 245: CAGTAACCCGTATCGTGAGCATCCTCTCTC
	pIA-His-MBP-$SNX17_{W321A}$_2	pMLG159	244: GAGAGAGGATGCTCACGATACGGGTTACTG 247: GTACAGAGGAGGTGACCCGCGCGCATCGCATGCGGGTGAC
204	pIA-His-MBP-$SNX17_{V380D}$_1	pMLG159	248: GCAGTCCATGGATGATGAACTGATGGTGAAGAAATCTGGC 245: CAGTAACCCGTATCGTGAGCATCCTCTCTC
	pIA-His-MBP-$SNX17_{V380D}$_2	pMLG159	244: GAGAGAGGATGCTCACGATACGGGTTACTG 249: CACCATCAGTTCATCATCCATGGACTGCAAGCAGATGCTC
205	pIA-His-MBP-$SNX17_{H457A}$_1	pMLG159	250: TGCCAGTGATGTCGCCGGCAATTTCGCCTTCGAGG 245: CAGTAACCCGTATCGTGAGCATCCTCTCTC
	pIA-His-MBP-$SNX17_{H457A}$_2	pMLG159	244: GAGAGAGGATGCTCACGATACGGGTTACTG 251: AAGGCGAAATTGCCGGCGACATCACTGGCACTGGCATCTG
206	pIA-His-MBP-$SNX17_{N459A+F462A}$_1	pMLG159	252: GGTGCTTTCGCTGCTGAGGGCATTGGAGATGAGGATCTG 245: CAGTAACCCGTATCGTGAGCATCCTCTCTC
	pIA-His-MBP-$SNX17_{N459A+F462A}$_2	pMLG159	244: GAGAGAGGATGCTCACGATACGGGTTACTG 253: CCCTCAGCAGCGAAAGCACCGTGGACATCACTGGCAC
238	Half of the vector	pMLG14	298: CCTGCACTGTCGGGTGGCTGCTAGCCAGCTCCTGGGGCTG 245: CAGTAACCCGTATCGTGAGCATCCTCTCTC
	Half of the vector	pMLG14	244: GAGAGAGGATGCTCACGATACGGGTTACTG 299: CCAGGAGCTGGCTAGCAGCCACCCGACAGTGCAGGACTCC
248	Half of the vector	pMLG14	317: TATGGTCGCAGCCGCAGCTGCGCTGAGTGCCGTGAGCTTG 245: CAGTAACCCGTATCGTGAGCATCCTCTCTC
	Half of the vector	pMLG14	244: GAGAGAGGATGCTCACGATACGGGTTACTG 334: TCAGCGCAGCTGCGGCTGCGACCATAGACTCCCGGGTGGC
250	Insert SNX17 and half of the vector	pMLG159	319: GGCGGCGGCGGCAGCGAAACCGAGTCCCGCAGC 245: CAGTAACCCGTATCGTGAGCATCCTCTCTC
	Insert EGFP and half of the vector	pMLG14	244: GAGAGAGGATGCTCACGATACGGGTTACTG 320: GCTGCGGGACTCGGTTTCGCTGCCGCCGCCGCC
29	Insert SNX17 and vector	pMLG1	002: CACCACCACCACCACCACTGAGATCCGGCTGCTAAC 099: CAGATCCTCATCTCCAATGCCCTCGAAGGCGAAATTGCCG
	Insert HPV	pMLG28	086: CCTTCGAGGGCATTGGAGATGAGGATCTGGAAAACCTGTATTTTCAGGGCGATCCGGC 087: GATCTCAGTGGTGGTGGTGGTGGTGTTAGAAGTACAGGGTGTTATCCACATCAATGCCTTCG
42	Insert SNX17 and vector	pMLG1	002: CACCACCACCACCACCACTGAGATCCGGCTGCTAAC 099: CAGATCCTCATCTCCAATGCCCTCGAAGGCGAAATTGCCG
	Insert APP	pMLG49	079: CCTTCGAGGGCATTGGAGATGAGGATCTGGAAAACCTGTATTTTCAGGGCGCCGATG 080: ATCTCAGTGGTGGTGGTGGTGGTGTTAATTCTGCATCTGTTCGAAAAACTTATAGGTCGG
181	Vector and $SNX17_{109-405}$	pMLG1	242: CATCTGTGCTGGGACTGCCAATTCCTCTCAGAGTACCCCCCACCCG 244: GAGAGAGGATGCTCACGATACGGGTTACTG
	Vector and $SNX17_{447-470}$	pMLG1	243: GGAATTGGCAGTCCCAGCACAGATG 245: CAGTAACCCGTATCGTGAGCATCCTCTCTC
146	SNX17-TEV-HPV-Vector	pMLG29	193: GATGGTGAAGAAATCTGAAAACCTGTATTTTCAGGGCGATCCG 089: CAGTAACCCGTATCGTGAGCATCCTCTCTCGTTTCATCGG
	$SNX17_{109-388}$-TEV	pMLG29	088: CCGATGAAACGAGAGAGGATGCTCACGATACGGGTTACTG

			194: GAAAATACAGGTTTTCAGATTTCTTCACCATCAGTTCATCAACC
20	Vector	pET28-Sumo3	As in 21.
	Insert	pMLG24	052: CGTGTTCCAGCAGCAGACCGGTGGATTTGATATTGCAACCAAAAAAGCCTACCTGG 051: CTCAGTGGTGGTGGTGGTGGTGTTACAGATCCTCTTCTTTGATGTTGCCAAACACGC
18	Insert $LRP1_{ICD}$	pMLG25	107: GGCGAAAACCTGTACTTCCAGGGCTATAAACGTCGTGTTCAGGGTGCAAAAGG 108: GATCTCAGTGGTGGTGGTGGTGGTGTTATGCCAGCGGATCACCAATTTCATCTTC
	Vector	pMLG31	002: CACCACCACCACCACCACTGAGATCCGGCTGCTAAC 094: GCCCTGGAAGTACAGGTTTTCGCCGCTGC
275	pIA-GST-$LRP1_{ICDmut\_1}$	pMLG18	339: GAAATTGGTGCCCCGACCGCCAAAATGTATGAAGGTGGTGAACC 245: CAGTAACCCGTATCGTGAGCATCCTCTCTC
	pIA-GST-$LRP1_{ICDmut\_1}$	pMLG18	244: GAGAGAGGATGCTCACGATACGGGTTACTG 340: CATACATTTTGGCGGTCGGGGCACCAATTTCCACATTCATTGC
124	Insert His_{10}-$LRP1_{ICD}$	pMLG18	175: CACCATCATCATCACCATCATCATCATCATTATAAACGTCGTGTTCAGGGTGCAAAAGG 089: CAGTAACCCGTATCGTGAGCATCCTCTCTCGTTTCATCGG
	Vector pIA-GST-HRV3C	pMLG18	088: CCGATGAAACGAGAGAGGATGCTCACGATACGGGTTACTG 174:ATGATGATGATGATGGTGATGATGATGGTGTGGACCTTGAAACAAAACTTCTAAGC CGCTGCTTTTTGGAGGATGGTCGCC
165	Insert His_{10}-$LRP1_{ICD}$	pMLG124	212: GGCGAAAACCTGTACTTCCAGGGCCACCATCATCATCACCATCATCATCATC 108: GATCTCAGTGGTGGTGGTGGTGGTGTTATGCCAGCGGATCACCAATTTCATCTTC
	Vector	pMLG32	002: CACCACCACCACCACCACTGAGATCCGGCTGCTAAC 094: GCCCTGGAAGTACAGGTTTTCGCCGCTGC
173	Vector pIA-MBP-TEV-His_{10}-$LRP1_{ICD}$_1	pMLG165	088: CCGATGAAACGAGAGAGGATGCTCACGATACGGGTTACTG 216: GTAGTACGACATATGTATTCTCCTTCTTAAAGTTAAAC
	Vector pIA-MBP-TEV-His_{10}-$LRP1_{ICD}$_2	pMLG165	089: CAGTAACCCGTATCGTGAGCATCCTCTCTCGTTTCATCGG 215:GTTTAACTTTAAGAAGGAGAATACATATGTCGTACTACATGATCGAAGAAGGTAAA CTGGTAATCTGG
49	Insert APP_{ICD}	pMLG48	102: GGCGAAAACCTGTACTTCCAGGGCAAGAAAAAGCAGTACACCTCTATCCACCACGG 103: GATCTCAGTGGTGGTGGTGGTGGTGTTAGTTCTGCATCTGTTCGAAGAATTTGTAGGTC GGG
	Vector	pMLG31	As in 18.
168	Insert $ITGB1_{ICD}$	pMLG167	214: CACCATCATCATCACCATCATCATCATCATAAACTGCTCATGATTATCCACGACCGTCG T
	Vector	pMLG31	As in 18.
28	Insert $L2_{FBR}$	Overlapping oligos	132: AGCAGCGGCGAAAACCTGTACTTCCAGGGCGATCCG 129: GATTATCATAGGTGATCAGTTTGGTCGGGGTGGTCACAAAGGCCGGATCGCCCTGGAA GT 84: ACCAAACTGATCACCTATGATAATCCGGCGTACGAAGGCATTGATGTGGATAACACCC TG 130: GATCTCAGTGGTGGTGGTGGTGGTGTTAGAAGTACAGGGTGTTATCCACATCAATG
	Vector	pMLG31	As in 18.
276	pIA-GST-$L2_{FBR-mut\_1}$	pMLG28	341: CCTATGATGCTCCGGCGGCAGAAGGCATTGATGTGGATAAC 245: CAGTAACCCGTATCGTGAGCATCCTCTCTC
	pIA-GST-$L2_{FBR-mut\_1}$	pMLG28	244: GAGAGAGGATGCTCACGATACGGGTTACTG 342: CAATGCCTTCTGCCGCCGGAGCATCATAGGTGATCAGTTTGGTCG
131	Insert GST and $L2_{FBR}$	pMLG126	072: GAAGGAGATATACCATGGGCAGCAGCATGTCCCCTATACTAGGTTATTGGAAAATTAA GGGCC 110: GGGTTATGCTAGTTATTGCTCAGCGGTGGC
	Vector	pMLG31	167: GCCACCGCTGAGCAATAACTAGCATAACCC 095: GCTGCTGCCCATGGTATATCTCCTTCTTAAAGTTAAAC
44	Insert VPS35L	pMLG22	065: GGCGAAAACCTGTACTTCCAGGGCATGGCAGTTTTTCCGTGGCATAGCC 066: GATCTCAGTGGTGGTGGTGGTGGTGTTAGGTACGGGTCTGCAGCGGC
	Vector	pMLG30	As in 159.
37	Insert His-VPS35L	pMLG44	063: CCACCATCGGGCGCGGATCCAATGGGCAGCAGCCATCATCATCATCATC

			118:GGTATGGCTGATTATGATCCTCTAGTACTTCTCGACAAGCTTTTAGGTACGGGTCTG CAGCGGCAGGC
	Vector	pLIB	115: GGATCCGCGCCCGATGGTGGG 116: AAGCTTGTCGAGAAGTACTAGAGGATCATAATCAGCCATACCAC
83	Vector	pMLG73	002: CACCACCACCACCACCACTGAGATCCGGCTGCTAAC 094: GCCCTGGAAGTACAGGTTTTCGCCGCTGC
	Insert VPS26C	pMLG05	013: CGGATCTCAGTGGTGGTGGTGGTGGTGTTATATCCTGCAGAGCTTCAGCGGGAAGTTCT CC 154: GGCGAAAACCTGTACTTCCAGGGCATGGGGACCGCCCTGGACATCAAGATTAAAAGAG
84	Insert VPS26C	pMLG83	152: CCACCATCGGGCGCGGATCCATGGCTAGCTGGAGCCACCCGCAG 153:GGTATGGCTGATTATGATCCTCTAGTACTTCTCGACAAGCTTCGGATCTCAGTGGTG GTGGTGGTGGTG
39	Insert VPS29	pMLG7	061: CCACCATCGGGCGCGGATCCAATGTTGGTGTTGGTATTAGGAGATCTGCAC 062:GATGATGTGAAAGTAGAACGAATCGAATACAAAAAACCTTAAAAGCTTGTCGAGA AGTACTAGAGGA
85	Insert VPS35L	pMLG37	055: AACGCTCTATGGTCTAAAGATTTAAATCGACCTACTCCGGAATATTAATAGATC 056: AAACGTGCAATAGTATCCAGTTTATTTAAATGGTTATGATAGTTATTGCTCAGCG
	Insert VPS26	pMLG84	057: AAACTGGATACTATTGCACGTTTAAATCGACCTACTCCGGAATATTAATAGATC 058: AAACATCAGGCATCATTAGGTTTATTTAAATGGTTATGATAGTTATTGCTCAGCG
	Insert VPS29	pMLG39	059: AAACCTAATGATGCCTGATGTTTAAATCGACCTACTCCGGAATATTAATAGATC 060: AACCCCGATTAAGATATAGATTTATTTAAATGGTTATGATAGTTATTGCTCAGCG
121	Insert GST	pGEX-6P-1-H(RBS)	172: CCCACCATCGGGCGCGGATCCAATGTCCCCTATACTAGGTTATTGGAAAATTAAGGGCC 173:GTGCAGATCTCCTAATACCAACACCAACATGGGCCCCTGGAACAGAACTTCCAGAT CCGATTTTGG
	Vector	pMLG39	171: ATGTTGGTGTTGGTATTAGGAGATCTGCACATCCCACACCGG 115: GGATCCGCGCCCGATGGTGGG
122	Insert VPS35L	pMLG37	As in 85.
	Insert VPS26C	pMLG84	As in 85.
	Insert GST-VPS29	pMLG121	059: AAACCTAATGATGCCTGATGTTTAAATCGACCTACTCCGGAATATTAATAGATC 060: AACCCCGATTGAGATATAGATTTATTTAAATGGTTATGATAGTTATTGCTCAGCG
156	Vector	pMLG39	094: GCCCTGGAAGTACAGGTTTTCGCCGCTGC 207:GACGCGCAGACTAATTCGAGCTCTATGTTGGTGTTGGTATTAGGAGATCTGCACAT CC
	Insert	pMLG32	As in 159.
164	Insert VPS35L	pMLG37	As in 85.
	Insert VPS26C	pMLG84	As in 85.
	Insert MBP-VPS29	pMLG156	059: AAACCTAATGATGCCTGATGTTTAAATCGACCTACTCCGGAATATTAATAGATC 060: AACCCCGATTGAGATATAGATTTATTTAAATGGTTATGATAGTTATTGCTCAGCG
109	Insert $VPS35L_{110-963}$	pMLG22	119: GGCGAAAACCTGTACTTCCAGGGCGTGGGTAGCGATTTTGAACCGTGGACC 066: GATCTCAGTGGTGGTGGTGGTGGTGTTAGGTACGGGTCTGCAGCGGC
	Vector	pMLG30	As in 159
113	Insert $VPS35L_{110-963}$	pMLG109	063: CCACCATCGGGCGCGGATCCAATGGGCAGCAGCCATCATCATCATCATC 153: GGTATGGCTGATTATGATCCTCTAGTACTTCTCGACAAGCTTCGGATCTCAGTGGTGGT GGTGGTGGTG
118	Insert $VPS35L_{110-963}$	pMLG113	055: AACGCTCTATGGTCTAAAGATTTAAATCGACCTACTCCGGAATATTAATAGATC 056: AAACGTGCAATAGTATCCAGTTTATTTAAATGGTTATGATAGTTATTGCTCAGCG
	Insert VPS26C	pMLG84	As in 85.
	Insert VPS29	pMLG39	As in 85.
107	Insert $VPS35L_{110-598}$	pMLG22	119: GGCGAAAACCTGTACTTCCAGGGCGTGGGTAGCGATTTTGAACCGTGGACC 126:GATCTCAGTGGTGGTGGTGGTGGTGTTATTGCTGATGTTTGATAAAGGCGTCCATA ATACATTTGCAC
	Vector	pMLG30	As in 159
111	Insert $VPS35L_{110-598}$	pMLG107	063: CCACCATCGGGCGCGGATCCAATGGGCAGCAGCCATCATCATCATCATC 153: GGTATGGCTGATTATGATCCTCTAGTACTTCTCGACAAGCTTCGGATCTCAGTGGTGGT GGTGGTGGTG
116	Insert $VPS35L_{110-598}$	pMLG111	055: AACGCTCTATGGTCTAAAGATTTAAATCGACCTACTCCGGAATATTAATAGATC 056: AAACGTGCAATAGTATCCAGTTTATTTAAATGGTTATGATAGTTATTGCTCAGCG
	Insert VPS26C	pMLG84	As in 85.
	Insert VPS29	pMLG39	As in 85.

137	Insert VPS35L$_{1-598}$	pMLG37	063: CCACCATCGGGCGCGGATCCAATGGGCAGCAGCCATCATCATCATCATC 126:GATCTCAGTGGTGGTGGTGGTGGTGTTATTGCTGATGTTTGATAAAGGCGTCCATAATACATTTGCAC
	Insert VPS35L$_{1-598}$	PCR VPS35L$_{1-598}$	063: CCACCATCGGGCGCGGATCCAATGGGCAGCAGCCATCATCATCATCATC 153:GGTATGGCTGATTATGATCCTCTAGTACTTCTCGACAAGCTTCGGATCTCAGTGGTGGTGGTGGTGGTG
	Vector	pLIB	115: AAGCTTGTCGAGAAGTACTAGAGGATCATAATCAGCCATACCAC 116: GGATCCGCGCCCGATGGTGGG
138	Insert VPS35L$_{1-598}$	pMLG137	055: AACGCTCTATGGTCTAAAGATTTAAATCGACCTACTCCGGAATATTAATAGATC 056: AAACGTGCAATAGTATCCAGTTTATTTAAATGGTTATGATAGTTATTGCTCAGCG
	Insert VPS26C	pMLG84	As in 85.
	Insert VPS29	pMLG39	As in 85.
141	Insert VPS35L $_{1-436}$	pMLG37	063: CCACCATCGGGCGCGGATCCAATGGGCAGCAGCCATCATCATCATCATC 196: GATCTCAGTGGTGGTGGTGGTGGTGTTAACGAAATGCGCTCATAACGCTATTCAGCAGC
	Insert VPS35L $_{1-436}$	PCR VPS35L$_{1-436}$	063: CCACCATCGGGCGCGGATCCAATGGGCAGCAGCCATCATCATCATCATC 153: GGTATGGCTGATTATGATCCTCTAGTACTTCTCGACAAGCTTCGGATCTCAGTGGTGGTGGTGGTGGTG
	Vector	pLIB	As in 137.
144	Insert VPS35L $_{1-436}$	pMLG141	055: AACGCTCTATGGTCTAAAGATTTAAATCGACCTACTCCGGAATATTAATAGATC 056: AAACGTGCAATAGTATCCAGTTTATTTAAATGGTTATGATAGTTATTGCTCAGCG
	Insert VPS26C	pMLG84	As in 85.
	Insert VPS29	pMLG39	As in 85.
151	Insert VPS35L	pMLG37	As in 85.
	Insert GST-VPS29	pMLG121	057: AAACTGGATACTATTGCACGTTTAAATCGACCTACTCCGGAATATTAATAGATC 060: AACCCCGATTGAGATATAGATTTATTTAAATGGTTATGATAGTTATTGCTCAGCG
228	Insert VPS35L$_{R248E+W280D}$	pMLG37	274: CCTTTGGTAAACTGGTGTATGAAGAAATTTTTAGCATGTGTGTTGATAGC 273: CGAATGCTGGCAATTTTGAAAAAATCATTCAGGCAGGTTTCTTTGG
	Vector pLIB-His-VPS35L	pMLG37	272: CCAAAGAAACCTGCCTGAATGATTTTTTCAAAATTGCCAGCATTCG 275: GCTATCAACACACATGCTAAAAATTTCTTCATACACCAGTTTACCAAAGG
231	Insert VPS35L $_{R248E+W280D}$	pMLG228	055: AACGCTCTATGGTCTAAAGATTTAAATCGACCTACTCCGGAATATTAATAGATC 056: AAACGTGCAATAGTATCCAGTTTATTTAAATGGTTATGATAGTTATTGCTCAGCG
	Insert VPS26C	pMLG84	As in 85.
	Insert VPS29	pMLG39	As in 85.
229	Insert VPS35L$_{K157E+R161E}$	pMLG37	280: CCCTGGCAATGAGTGAAGAAGTTCGTACAGAACTGGAAGAACTGGATGATTTTG 093: CTCATGGTTATGGCAGCACTGCATAATTCTCTTACTGTC
	Vector pLIB-His-VPS35L	pMLG37	092: GACAGTAAGAGAATTATGCAGTGCTGCCATAACCATGAG 281: CAAAATCATCCAGTTCTTCCAGTTCTGTACGAACTTCTTCACTCATTGCCAGGG
232	Insert VPS35L$_{K157E+R161E}$	pMLG229	055: AACGCTCTATGGTCTAAAGATTTAAATCGACCTACTCCGGAATATTAATAGATC 056: AAACGTGCAATAGTATCCAGTTTATTTAAATGGTTATGATAGTTATTGCTCAGCG
	Insert VPS26C	pMLG84	As in 85.
	Insert VPS29	pMLG39	As in 85.
15	Insert VPS29	pMLG6	033: ATCGACGTGTTCCAGCAGCAGACCGGTGGAATGTTGGTGTTGGTATTAGGAGATCTGCACA 035:GAACAGCTCCTCGCCCTTGCTCACGGAGCTGCCGCCGCCGCCAGGTTTTTTGTATTCGATTCGTTCTACTTTCACATC
	Vector	pET28-Sumo3	037: TCCACCGGTCTGCTGCTGGAACACGTCGATGGTGTCC 038: TCCGTGAGCAAGGGCGAGGAGCTGTTCACCGGG
59	Insert mKate2	pCDH-CMV-fmKate2-EF1-puro	127: GGCGGCGGCGGCAGCTCCATGGTGAGCGAGCTGATTAAGGAGAACATG 128: GATCTCAGTGGTGGTGGTGGTGGTGTTATCTGTGCCCCAGTTTGCTAGGGAGG
	Vector	pMLG15	002: CACCACCACCACCACCACTGAGATCCGGCTGCTAAC 131: GGAGCTGCCGCCGCCGCC
	Vector	pMLG7	002: CACCACCACCACCACCACTGAGATCCGGCTGCTAAC 143:GCTCGCTCACCATGGAGCTGCCGCCGCCGCCAGGTTTTTTGTATTCGATTCGTTCTACTTTCACATCATCTCC
115	Insert VPS29 and mKate2	pMLG59	061: CCACCATCGGGCGCGGATCCAATGTTGGTGTTGGTATTAGGAGATCTGCAC 153:GGTATGGCTGATTATGATCCTCTAGTACTTCTCGACAAGCTTCGGATCTCAGTGGTGGTGGTGGTGGTG
120	Insert VPS29-mKate2	pMLG115	059: AAACCTAATGATGCCTGATGTTTAAATCGACCTACTCCGGAATATTAATAGATC 060:AACCCCGATTGAGATATAGATTTATTTAAATGGTTATGATAGTTATTGCTCAGCG

	Insert VPS35L	pMLG37	As in 85.
	Insert VPS26C	pMLG84	As in 85.

Table 11. Protein purification workflow for each construct.

Identifier	Protein construct	Steps	Final buffer
pMLG31	GST	GST_1, TEV in roller, GST_2, S200 16/60	Hp150+TCEP
pMLG21	His-Sumo3-VPS26C	Ni_1, SenP2 + dialysis, Ni_2, Q, S75 10/300	Hp150+TCEP
pMLG6	GST-VPS29	GST_1, TEV + dialysis, GST_2, Q, S75 10/300	Hp150+TCEP
pMLG13	His-Sumo3-$SNX17_{FL}$	Ni_1, SenP2 + dialysis, Ni_2 y Q	Hp300+TCEP
pMLG135	His-Sumo3-$SNX17_{N108}$	Ni_1, Senp2 + dialysis, Ni_2, Q, S200 16/60	Hp300+TCEP
pMLG1	His-Sumo3-$SNX17_{FERM-CT}$	Ni_1, Senp2 + dialysis, Ni_2, Q, S200 16/60	Hp300+TCEP
pMLG14	His-Sumo3-EGFP-SNX17	Ni_1, Senp2 + dialysis, Ni_2, Q, S200 16/60	Hp300+TCEP
pMLG159	His-MBP-SNX17	Ni_1, TEV + dialysis, Ni_2, S200 16/60	Hp300+TCEP
pMLG179	His-MBP-$SNX17_{D467X}$	Ni_1, TEV + dialysis, Ni_2, S200 16/60	Hp300+TCEP
pMLG178	His-MBP-$SNX17_{L470G}$	Ni_1, TEV + dialysis, Ni_2, S200 16/60	Hp300+TCEP
pMLG203	His-MBP-$SNX17_{W321A}$	Ni_1, TEV + dialysis, Ni_2, S200 16/60	Hp300+TCEP
pMLG204	His-MBP-$SNX17_{V380D}$	Ni_1, TEV + dialysis, Ni_2, S200 16/60	Hp300+TCEP
pMLG205	His-MBP-$SNX17_{H457A}$	Ni_1, TEV + dialysis, Ni_2, S200 16/60	Hp300+TCEP
pMLG206	His-MBP-$SNX17_{N459A+F462A}$	Ni_1, TEV + dialysis, Ni_2, S200 16/60	Hp300+TCEP
pMLG238	His-Sumo3-EGFP-$SNX17_{R36A+Y37A}$	Ni_1, SenP2 + dialysis, Ni_2, Q, S200 16/60	Hp300+TCEP
pMLG248	His-Sumo3-EGFP-$SNX17_{K431LSSK:AAAAA}$	Ni_1, SenP2 + dialysis, Ni_2, Q, S200 16/60	Hp300+TCEP
pMLG250	His-Sumo3-EGFP-$SNX17_{7-470}$	Ni_1, SenP2 + dialysis, Ni_2, Q, S200 16/60	Hp300+TCEP
pMLG29	His-Sumo3-$SNX17_{1FERM-CT}$-TEV-$L2_{FBR}$	Ni_1, SenP2 + dialysis, Ni_2, Q, S200 16/60	Hp300+TCEP
pMLG42	His-Sumo3-$SNX17_{FERM-CT}$-TEV-$APP_{739-770}$	Ni_1, SenP2 + dialysis, Ni_2, Q, S200 16/60	Hp150+TCEP
pMLG181	His-Sumo3-$SNX17_{FERM-CT\ (del406-442)}$	Ni_1, SenP2 + dialysis, Ni_2, Q, S200 16/60	Hp300+TCEP
pMLG146	His-Sumo3-$SNX17_{109-388}$-$L2_{FBR}$	Ni_1, SenP2 + dialysis, Ni_2, Q, S200 16/60	Hp300+TCEP
pMLG20	His-Sumo3-$SNX31_{FERM-CT}$	Ni_1, SenP2 + dialysis, Ni_2, S200 16/60	Hp300+TCEP
pMLG18	GST-TEV-$LRP1_{ICD}$	GST_1, S200 16/60	Hp150+TCEP
pMLG275	GST-TEV-$LRP1_{ICD-mut(N4470A+Y4473A)}$	GST_1, S200 16/60	Hp150+TCEP
pMLG173	MBP-His_{10}-$LRP1_{ICD}$	Ni_1, TEV + dialysis, Ni_2, Q, S200 16/60	Hp200+TCEP
pMLG49	GST-TEV-APP_{ICD}	GST_1, S200 16/60	Hp150+TCEP
pMLG168	GST-TEV-$ITGB1_{ICD}$	GST_1, S200 16/60	Hp150+TCEP
pMLG28	GST-TEV-$L2_{FBR}$	GST_1, S200 16/60	Hp150+TCEP
pMLG276	GST-TEV-$L2_{FBR-mut(N254A+Y257A)}$	GST_1, S200 16/60	Hp150+TCEP
pMLG131	GST-3C-His_{10}-$L2_{FBR}$	GST_1, HRV 3C in roller, GST_2, Ni_1, S75 10/300	Hp200+TCEP
pMLG85	His-VPS35L-Twin-Strep-VPS26C-VPS29	Ni_1, $Strept_1$, TEV in roller, Ni_2, $Strept_2$, S200 10/300	Hp300+TCEP
pMLG122	His-VPS35L-Twin-Strep-VPS26C-GST-VPS29	Ni_1, TEV + dialysis, GST_1, S200 16/60	Hp300+TCEP
pMLG164	His-VPS35L-Twin-Strep-VPS26C-MBP-VPS29	Ni_1, $Strept_1$, TEV + dialysis, Ni_2, $Strept_2$, S200 10/300	Tr200+TCEP
pMLG118	His-$VPS35L_{110-963}$-Twin-Strep-VPS26C-VPS29	$Strept_1$, Ni_1, TEV + dialysis/in roller, Ni_2, S200 10/300	Hp300+TCEP
pMLG116	His-$VPS35L_{110-598}$-Twin-Strep-VPS26C-VPS29	$Strept_1$, Ni_1, TEV + dialysis, Ni_2, S200 10/300	Hp300+TCEP
pMLG138	His-$VPS35L_{1-598}$-Twin-Strep-VPS26C-VPS29	$Strept_1$, Ni_1, TEV + dialysis, Ni_2, S200 10/300	Hp200+TCEP
pMLG144	His-$VPS35L_{1-436}$-Twin-Strep-VPS26C-VPS29	$Strept_1$, Ni_1, TEV + dialysis, Ni_2, S200 10/300	Hp200+TCEP
pMLG151	His-VPS35L-GST-VPS29	Ni_1, TEV + dialysis, Ni_2, GST_1, HRV 3C in roller, GST_2, S200 10/300	Hp200+TCEP
pMLG231	His-$VPS35L_{R248E+W280D}$-Twin-Strep-VPS26C-VPS29	Ni_1, $Strept_1$, TEV in roller, Ni_2, S200 10/300	Hp300+TCEP
pMLG232	His-$VPS35L_{K157E+R161E}$-Twin-Strep-VPS26C-VPS29	Ni_1, $Strept_1$, TEV in roller, Ni_2, S200 10/300	Hp300+TCEP
pMLG120	His-VPS35L-Twin-Strep-VPS26C-VPS29-mKate2	Ni_1, $Strept_1$, TEV in roller, $Strept_2$, S200 10/300	Hp200+TCEP
pMLG101	His-NusA-His-FAM45A	Ni_1, HRV 3C in roller, Q, S200 16/60	Tr200+TCEP

pMLG8	His-TEV	Ni_1, dialysis	Tr150+DTT+ Gl10
pMLG9	His-Senp2	Ni_1, dialysis, Q, S200 16/60	Tr150¿+ DTT?+Gl10
pMLG10	GST-PreScission	GST_1, S200 16/60	Tr300¿+DTT?

Ni_1: Nickel-based affinity chromatography of His-tagged-protein.

Ni_2: Nickel-based affinity chromatography of His-tagged-protein after protease incubation.

$Strept_1$: Strep-Tactin XT-based affinity chromatography of Twin-Strep-tagged-protein.

$Strept_2$: Strep-Tactin XT-based affinity chromatography of Twin-Strep-tagged-protein after protease incubation.

GST_1: Glutathione S-transferase (GST)-based affinity chromatography of GST-tagged-protein.

GST_2: GST-based affinity chromatography of GST-tagged-protein after protease incubation.

$Amylose_1$: Amylose-based affinity chromatography of Maltose-Binding Protein (MBP)-tagged-protein.

TEV: Incubation with Tobacco Etch Virus (TEV) protease.

Senp2: Incubation with Sentrin-specific protease 2 (Senp2) protease.

HRV 3C: Incubation with Human Rhinovirus (HRV) 3C protease.

Q: Ion exchange chromatography using a gradient of NaCl.

S75 10/300: Size exclusion chromatography with HiLoad 10/300 Superdex 75 column.

S200 10/300: Size exclusion chromatography with HiLoad 10/300 Superdex 200 column.

S200 16/60: Size exclusion chromatography with HiLoad 16/60 Superdex 200 column.

Hp150/200/300+TCEP: 25 mM Hepes pH 7.5, 150/200/300 mM NaCl and 1mM TCEP.

Tr200+TCEP: 50 mM Tris pH 7.5, 200 mM NaCl and 1mM TCEP.

Tr150/200+DTT: 50 mM Tris pH 7.5, 150/200 mM NaCl and 1mM DTT.

Gl10: Glycerol at 10%.

Table 12. Sequences of recombinant proteins used in this thesis.

ID: This column lists the pMLG plasmid identification numbers.

The listed sequences correspond to the cloned proteins before the removal of the affinity tag by protease cleavage. The tag sequences are annotated in blue, the protease recognition sites in orange, the extra sequences resulting from cloning or linkers in green and point mutations from the wild-type sequence in red.

ID	Sequence
31	> GST MGSSMSPILGYWKIKGLVQPTRLLLEYLEEKYEEHLYERDEGDKWRNKKFELGLEFPNLPYYIDGDVKLTQSMAIIRYIADKHNMLG GCPKERAEISMLEGAVLDIRYGVSRIAYSKDFETLKVDFLSKLPEMLKMFEDRLCHKTYLNGDHVTHPDFMLYDALDVVLYMDPMC LDAFPKLVCFKKRIEAIPQIDKYLKSSKYIAWPLQGWQATFGGGDHPPK
21	> His-Sumo3-VPS26C MGSSHHHHHHSSGLVPRGSHMNDHINLKVAGQDGSVVQFKIKRHTPLSKLMKAYCERQGLSMRQIRFRFDGQPINETDTPAQLEM EDEDTIDVFQQQTGGMGTALDIKIKRANKVYHAGEVLSGVVVISSKDSVQHQGVSLTMEGTVNLQLSAKSVGVFEAFYNSVKPIQIINS TIEMVKPGKFPSGKTEIPFEFPLHLKGNKVLYETYHGVFVNIQYTLRCDMKRSLLAKDLTKTCEFIVHSAPQKGKFTPSPVDFTITPET LQNVKERALLPKFLLRGHLNSTNCVITQPLTGELVVESSEAAIRSVELQLVRVETCGCAEGYARDATEIQNIQIADGDVCRGLSVPIYM VFPRLFTCPTLETTNFKVEFEVNIVVLLHPDHLITENFPLKLCRI
6	> GST-TEV-VPS29 MSPILGYWKIKGLVQPTRLLLEYLEEKYEEHLYERDEGDKWRNKKFELGLEFPNLPYYIDGDVKLTQSMAIIRYIADKHNMLGGCPK ERAEISMLEGAVLDIRYGVSRIAYSKDFETLKVDFLSKLPEMLKMFEDRLCHKTYLNGDHVTHPDFMLYDALDVVLYMDPMCLDAF PKLVCFKKRIEAIPQIDKYLKSSKYIAWPLQGWQATFGGGDHPPKIDTTENLYFQGAMGSMLVLVLGDLHIPHRCNSLPAKFKKLLVP GKIQHILCTGNLCTKESYDYLKTLAGDVHIVRGDFDENLNYPEQKVVTVGQFKIGLIHGHQVIPWGDMASLALLQRQFDVDILISGHT HKFEAFEHENKFYINPGSATGAYNALETNIIPSFVLMDIQASTVVTYVYQLIGDDVKVERIEYKKP*
13	> His-Sumo3-SNX17 MGSSHHHHHHSSGLVPRGSHMNDHINLKVAGQDGSVVQFKIKRHTPLSKLMKAYCERQGLSMRQIRFRFDGQPINETDTPAQLEM EDEDTIDVFQQQTGGMHFSIPETESRSGDSGGSAYVAYNIHVNGVLHCRVRYSQLLGLHEQLRKEYGANVLPAFPPKKLFSLTPAEVE QRREQLEKYMQAVRQDPLLGSSETFNSFLRRAQQETQQVPTEEVSLEVLLSNGQKVLVNVLTSDQTEDVLEAVAAKLDLPDDLIGYF SLFLVREKEDGAFSFVRKLQEFELPYVSVTSLRSQEYKIVLRKSYWDSAYDDDVMENRVGLNLLYAQTVSDIERGWILVTKEQHRQL KSLQEKVSKKEFLRLAQTLRHYGYLRFDACVADFPEKDCPVVVSAGNSELSLQLRLPGQQLREGSFRVTRMRCWRVTSSVPLPSGST SSPGRGRGEVRLELAFEYLMSKDRLQWVTITSPQAIMMSICLQSMVDELMVKKSGGSIRKMLRRRVGGTLRRSDSQQAVKSPPLLES PDATRESMVKLSSKLSAVSLRGIGSPSTDASASDVHGNFAFEGIGDEDL
135	> His-Sumo3-SNX17$_{PX}$ MGSSHHHHHHSSGLVPRGSHMNDHINLKVAGQDGSVVQFKIKRHTPLSKLMKAYCERQGLSMRQIRFRFDGQPINETDTPAQLEM EDEDTIDVFQQQTGGMHFSIPETESRSGDSGGSAYVAYNIHVNGVLHCRVRYSQLLGLHEQLRKEYGANVLPAFPPKKLFSLTPAEVE QRREQLEKYMQAVRQDPLLGSSETFNSFLRRAQQE
1	> His-Sumo3-SNX17$_{FERM-CT}$ MGSSHHHHHHSSGLVPRGSHMNDHINLKVAGQDGSVVQFKIKRHTPLSKLMKAYCERQGLSMRQIRFRFDGQPINETDTPAQLEM EDEDTIDVFQQQTGGTQQVPTEEVSLEVLLSNGQKVLVNVLTSDQTEDVLEAVAAKLDLPDDLIGYFSLFLVREKEDGAFSFVRKLQE FELPYVSVTSLRSQEYKIVLRKSYWDSAYDDDVMENRVGLNLLYAQTVSDIERGWILVTKEQHRQLKSLQEKVSKKEFLRLAQTLRH YGYLRFDACVADFPEKDCPVVVSAGNSELSLQLRLPGQQLREGSFRVTRMRCWRVTSSVPLPSGSTSSPGRGRGEVRLELAFEYLMS KDRLQWVTITSPQAIMMSICLQSMVDELMVKKSGGSIRKMLRRRVGGTLRRSDSQQAVKSPPLLESPDATRESMVKLSSKLSAVSLR GIGSPSTDASASDVHGNFAFEGIGDEDL
14	> His-Sumo3-EGFP-SNX17 MGSSHHHHHHSSGLVPRGSHMNDHINLKVAGQDGSVVQFKIKRHTPLSKLMKAYCERQGLSMRQIRFRFDGQPINETDTPAQLEM EDEDTIDVFQQQTGGSVSKGEELFTGVVPILVELDGDVNGHKFSVSGEGEGDATYGKLTLKFICTTGKLPVPWPTLVTTLTYGVQCFS RYPDHMKQHDFFKSAMPEGYVQERTIFFKDDGNYKTRAEVKFEGDTLVNRIELKGIDFKEDGNILGHKLEYNYNSHNVYIMADKQK NGIKVNFKIRHNIEDGSVQLADHYQQNTPIGDGPVLLPDNHYLSTQSALSKDPNEKRDHMVLLEFVTAAGITLGMDELYKGGGGSM HFSIPETESRSGDSGGSAYVAYNIHVNGVLHCRVRYSQLLGLHEQLRKEYGANVLPAFPPKKLFSLTPAEVEQRREQLEKYMQAVRQ DPLLGSSETFNSFLRRAQQETQQVPTEEVSLEVLLSNGQKVLVNVLTSDQTEDVLEAVAAKLDLPDDLIGYFSLFLVREKEDGAFSFV RKLQEFELPYVSVTSLRSQEYKIVLRKSYWDSAYDDDVMENRVGLNLLYAQTVSDIERGWILVTKEQHRQLKSLQEKVSKKEFLRLA QTLRHYGYLRFDACVADFPEKDCPVVVSAGNSELSLQLRLPGQQLREGSFRVTRMRCWRVTSSVPLPSGSTSSPGRGRGEVRLELAF EYLMSKDRLQWVTITSPQAIMMSICLQSMVDELMVKKSGGSIRKMLRRRVGGTLRRSDSQQAVKSPPLLESPDATRESMVKLSSKLS AVSLRGIGSPSTDASASDVHGNFAFEGIGDEDL
159	> His-TEV-MBP-SNX17 MGSSHHHHHHSSGENLYFQGMIEEGKLVIWINGDKGYNGLAEVGKKFEKDTGIKVTVEHPDKLEEKFPQVAATGDGPDIIFWAHDR FGGYAQSGLLAEITPDKAFQDKLYPFTWDAVRYNGKLIAYPIAVEALSLIYNKDLLPNPPKTWEEIPALDKELKAKGKSALMFNLQEP YFTWPLIAADGGYAFKYENGKYDIKDVGVDNAGAKAGLTFLVDLIKNKHMNADTDYSIAEAAFNKGETAMTINGPWAWSNIDTSK

	VNYGVTVLPTFKGQPSKPFVGVLSAGINAASPNKELAKEFLENYLLTDEGLEAVNKDKPLGAVALKSYEEELAKDPRIAATMENAQK GEIMPNIPQMSAFWYAVRTAVINAASGRQTVDEALKDAQTNSSSMHFSIPETESRSGDSGGSAYVAYNIHVNGVLHCRVRYSQLLGL HEQLRKEYGANVLPAFPPKKLFSLTPAEVEQRREQLEKYMQAVRQDPLLGSSETFNSFLRRAQQETQQVPTEEVSLEVLLSNGQKVL VNVLTSDQTEDVLEAVAAKLDLPDDLIGYFSLFLVREKEDGAFSFVRKLQEFELPYVSVTSLRSQEYKIVLRKSYWDSAYDDDVMEN RVGLNLLYAQTVSDIERGWILVTKEQHRQLKSLQEKVSKKEFLRLAQTLRHYGYLRFDACVADFPEKDCPVVVSAGNSELSLQLRLP GQQLREGSFRVTRMRCWRVTSSVPLPSGSTSSPGRGRGEVRLELAFEYLMSKDRLQWVTITSPQAIMMSICLQSMVDELMVKKSGGS IRKMLRRRVGGTLRRSDSQQAVKSPPLLESPDATRESMVKLSSKLSAVSLRGIGSPSTDASASDVHGNFAFEGIGDEDL
179	> His-TEV-MBP-SNX17$_{D467X}$ MGSSHHHHHHSSGENLYFQGMIEEGKLVIWINGDKGYNGLAEVGKKFEKDTGIKVTVEHPDKLEEKFPQVAATGDGPDIIFWAHDR FGGYAQSGLLAEITPDKAFQDKLYPFTWDAVRYNGKLIAYPIAVEALSLIYNKDLLPNPPKTWEEIPALDKELKAKGKSALMFNLQEP YFTWPLIAADGGYAFKYENGKYDIKDVGVDNAGAKAGLTFLVDLIKNKHMNADTDYSIAEAAFNKGETAMTINGPWAWSNIDTSK VNYGVTVLPTFKGQPSKPFVGVLSAGINAASPNKELAKEFLENYLLTDEGLEAVNKDKPLGAVALKSYEEELAKDPRIAATMENAQK GEIMPNIPQMSAFWYAVRTAVINAASGRQTVDEALKDAQTNSSSMHFSIPETESRSGDSGGSAYVAYNIHVNGVLHCRVRYSQLLGL HEQLRKEYGANVLPAFPPKKLFSLTPAEVEQRREQLEKYMQAVRQDPLLGSSETFNSFLRRAQQETQQVPTEEVSLEVLLSNGQKVL VNVLTSDQTEDVLEAVAAKLDLPDDLIGYFSLFLVREKEDGAFSFVRKLQEFELPYVSVTSLRSQEYKIVLRKSYWDSAYDDDVMEN RVGLNLLYAQTVSDIERGWILVTKEQHRQLKSLQEKVSKKEFLRLAQTLRHYGYLRFDACVADFPEKDCPVVVSAGNSELSLQLRLP GQQLREGSFRVTRMRCWRVTSSVPLPSGSTSSPGRGRGEVRLELAFEYLMSKDRLQWVTITSPQAIMMSICLQSMVDELMVKKSGGS IRKMLRRRVGGTLRRSDSQQAVKSPPLLESPDATRESMVKLSSKLSAVSLRGIGSPSTDASASDVHGNFAFEGIG
178	> His-TEV-MBP-SNX17$_{L470G}$ MGSSHHHHHHSSGENLYFQGMIEEGKLVIWINGDKGYNGLAEVGKKFEKDTGIKVTVEHPDKLEEKFPQVAATGDGPDIIFWAHDR FGGYAQSGLLAEITPDKAFQDKLYPFTWDAVRYNGKLIAYPIAVEALSLIYNKDLLPNPPKTWEEIPALDKELKAKGKSALMFNLQEP YFTWPLIAADGGYAFKYENGKYDIKDVGVDNAGAKAGLTFLVDLIKNKHMNADTDYSIAEAAFNKGETAMTINGPWAWSNIDTSK VNYGVTVLPTFKGQPSKPFVGVLSAGINAASPNKELAKEFLENYLLTDEGLEAVNKDKPLGAVALKSYEEELAKDPRIAATMENAQK GEIMPNIPQMSAFWYAVRTAVINAASGRQTVDEALKDAQTNSSSMHFSIPETESRSGDSGGSAYVAYNIHVNGVLHCRVRYSQLLGL HEQLRKEYGANVLPAFPPKKLFSLTPAEVEQRREQLEKYMQAVRQDPLLGSSETFNSFLRRAQQETQQVPTEEVSLEVLLSNGQKVL VNVLTSDQTEDVLEAVAAKLDLPDDLIGYFSLFLVREKEDGAFSFVRKLQEFELPYVSVTSLRSQEYKIVLRKSYWDSAYDDDVMEN RVGLNLLYAQTVSDIERGWILVTKEQHRQLKSLQEKVSKKEFLRLAQTLRHYGYLRFDACVADFPEKDCPVVVSAGNSELSLQLRLP GQQLREGSFRVTRMRCWRVTSSVPLPSGSTSSPGRGRGEVRLELAFEYLMSKDRLQWVTITSPQAIMMSICLQSMVDELMVKKSGGS IRKMLRRRVGGTLRRSDSQQAVKSPPLLESPDATRESMVKLSSKLSAVSLRGIGSPSTDASASDVHGNFAFEGIGDEDG
203	> His-TEV-MBP-SNX17$_{W321A}$ MGSSHHHHHHSSGENLYFQGMIEEGKLVIWINGDKGYNGLAEVGKKFEKDTGIKVTVEHPDKLEEKFPQVAATGDGPDIIFWAHDR FGGYAQSGLLAEITPDKAFQDKLYPFTWDAVRYNGKLIAYPIAVEALSLIYNKDLLPNPPKTWEEIPALDKELKAKGKSALMFNLQEP YFTWPLIAADGGYAFKYENGKYDIKDVGVDNAGAKAGLTFLVDLIKNKHMNADTDYSIAEAAFNKGETAMTINGPWAWSNIDTSK VNYGVTVLPTFKGQPSKPFVGVLSAGINAASPNKELAKEFLENYLLTDEGLEAVNKDKPLGAVALKSYEEELAKDPRIAATMENAQK GEIMPNIPQMSAFWYAVRTAVINAASGRQTVDEALKDAQTNSSSMHFSIPETESRSGDSGGSAYVAYNIHVNGVLHCRVRYSQLLGL HEQLRKEYGANVLPAFPPKKLFSLTPAEVEQRREQLEKYMQAVRQDPLLGSSETFNSFLRRAQQETQQVPTEEVSLEVLLSNGQKVL VNVLTSDQTEDVLEAVAAKLDLPDDLIGYFSLFLVREKEDGAFSFVRKLQEFELPYVSVTSLRSQEYKIVLRKSYWDSAYDDDVMEN RVGLNLLYAQTVSDIERGWILVTKEQHRQLKSLQEKVSKKEFLRLAQTLRHYGYLRFDACVADFPEKDCPVVVSAGNSELSLQLRLP GQQLREGSFRVTRMRCARVTSSVPLPSGSTSSPGRGRGEVRLELAFEYLMSKDRLQWVTITSPQAIMMSICLQSMVDELMVKKSGGSI RKMLRRRVGGTLRRSDSQQAVKSPPLLESPDATRESMVKLSSKLSAVSLRGIGSPSTDASASDVHGNFAFEGIGDEDL
204	> His-TEV-MBP-SNX17$_{V380D}$ MGSSHHHHHHSSGENLYFQGMIEEGKLVIWINGDKGYNGLAEVGKKFEKDTGIKVTVEHPDKLEEKFPQVAATGDGPDIIFWAHDR FGGYAQSGLLAEITPDKAFQDKLYPFTWDAVRYNGKLIAYPIAVEALSLIYNKDLLPNPPKTWEEIPALDKELKAKGKSALMFNLQEP YFTWPLIAADGGYAFKYENGKYDIKDVGVDNAGAKAGLTFLVDLIKNKHMNADTDYSIAEAAFNKGETAMTINGPWAWSNIDTSK VNYGVTVLPTFKGQPSKPFVGVLSAGINAASPNKELAKEFLENYLLTDEGLEAVNKDKPLGAVALKSYEEELAKDPRIAATMENAQK GEIMPNIPQMSAFWYAVRTAVINAASGRQTVDEALKDAQTNSSSMHFSIPETESRSGDSGGSAYVAYNIHVNGVLHCRVRYSQLLGL HEQLRKEYGANVLPAFPPKKLFSLTPAEVEQRREQLEKYMQAVRQDPLLGSSETFNSFLRRAQQETQQVPTEEVSLEVLLSNGQKVL VNVLTSDQTEDVLEAVAAKLDLPDDLIGYFSLFLVREKEDGAFSFVRKLQEFELPYVSVTSLRSQEYKIVLRKSYWDSAYDDDVMEN RVGLNLLYAQTVSDIERGWILVTKEQHRQLKSLQEKVSKKEFLRLAQTLRHYGYLRFDACVADFPEKDCPVVVSAGNSELSLQLRLP GQQLREGSFRVTRMRCWRVTSSVPLPSGSTSSPGRGRGEVRLELAFEYLMSKDRLQWVTITSPQAIMMSICLQSMDDELMVKKSGGS IRKMLRRRVGGTLRRSDSQQAVKSPPLLESPDATRESMVKLSSKLSAVSLRGIGSPSTDASASDVHGNFAFEGIGDEDL
205	> His-TEV-MBP-SNX17$_{H457A}$ MGSSHHHHHHSSGENLYFQGMIEEGKLVIWINGDKGYNGLAEVGKKFEKDTGIKVTVEHPDKLEEKFPQVAATGDGPDIIFWAHDR FGGYAQSGLLAEITPDKAFQDKLYPFTWDAVRYNGKLIAYPIAVEALSLIYNKDLLPNPPKTWEEIPALDKELKAKGKSALMFNLQEP YFTWPLIAADGGYAFKYENGKYDIKDVGVDNAGAKAGLTFLVDLIKNKHMNADTDYSIAEAAFNKGETAMTINGPWAWSNIDTSK VNYGVTVLPTFKGQPSKPFVGVLSAGINAASPNKELAKEFLENYLLTDEGLEAVNKDKPLGAVALKSYEEELAKDPRIAATMENAQK GEIMPNIPQMSAFWYAVRTAVINAASGRQTVDEALKDAQTNSSSMHFSIPETESRSGDSGGSAYVAYNIHVNGVLHCRVRYSQLLGL HEQLRKEYGANVLPAFPPKKLFSLTPAEVEQRREQLEKYMQAVRQDPLLGSSETFNSFLRRAQQETQQVPTEEVSLEVLLSNGQKVL VNVLTSDQTEDVLEAVAAKLDLPDDLIGYFSLFLVREKEDGAFSFVRKLQEFELPYVSVTSLRSQEYKIVLRKSYWDSAYDDDVMEN RVGLNLLYAQTVSDIERGWILVTKEQHRQLKSLQEKVSKKEFLRLAQTLRHYGYLRFDACVADFPEKDCPVVVSAGNSELSLQLRLP GQQLREGSFRVTRMRCWRVTSSVPLPSGSTSSPGRGRGEVRLELAFEYLMSKDRLQWVTITSPQAIMMSICLQSMVDELMVKKSGGS IRKMLRRRVGGTLRRSDSQQAVKSPPLLESPDATRESMVKLSSKLSAVSLRGIGSPSTDASASDVAGNFAFEGIGDEDL

206	> His-TEV-MBP-SNX17$_{N459A+F462A}$ MGSSHHHHHHSSGENLYFQGMIEEGKLVIWINGDKGYNGLAEVGKKFEKDTGIKVTVEHPDKLEEKFPQVAATGDGPDIIFWAHDR FGGYAQSGLLAEITPDKAFQDKLYPFTWDAVRYNGKLIAYPIAVEALSLIYNKDLLPNPPKTWEEIPALDKELKAKGKSALMFNLQEP YFTWPLIAADGGYAFKYENGKYDIKDVGVDNAGAKAGLTFLVDLIKNKHMNADTDYSIAEAAFNKGETAMTINGPWAWSNIDTSK VNYGVTVLPTFKGQPSKPFVGVLSAGINAASPNKELAKEFLENYLLTDEGLEAVNKDKPLGAVALKSYEEELAKDPRIAATMENAQK GEIMPNIPQMSAFWYAVRTAVINAASGRQTVDEALKDAQTNSSSMHFSIPETESRSGDSGGSAYVAYNIHVNGVLHCRVRYSQLLGL HEQLRKEYGANVLPAFPPKKLFSLTPAEVEQRREQLEKYMQAVRQDPLLGSSETFNSFLRRAQQETQQVPTEEVSLEVLLSNGQKVL VNVLTSDQTEDVLEAVAAKLDLPDDLIGYFSLFLVREKEDGAFSFVRKLQEFELPYVSVTSLRSQEYKIVLRKSYWDSAYDDDVMEN RVGLNLLYAQTVSDIERGWILVTKEQHRQLKSLQEKVSKKEFLRLAQTLRHYGYLRFDACVADFPEKDCPVVVSAGNSELSLQLRLP GQQLREGSFRVTRMRCWRVTSSVPLPSGSTSSPGRGRGEVRLELAFEYLMSKDRLQWVTITSPQAIMMSICLQSMVDELMVKKSGGS IRKMLRRRVGGTLRRSDSQQAVKSPPLLESPDATRESMVKLSSKLSAVSLRGIGSPSTDASASDVHGAFAAEGIGDEDL
238	> His-Sumo3-EGFP-SNX17$_{R36A+Y37A}$ MGSSHHHHHHSSGLVPRGSHMNDHINLKVAGQDGSVVQFKIKRHTPLSKLMKAYCERQGLSMRQIRFRFDGQPINETDTPAQLEM EDEDTIDVFQQQTGGSVSKGEELFTGVVPILVELDGDVNGHKFSVSGEGEGDATYGKLTLKFICTTGKLPVPWPTLVTTLTYGVQCFS RYPDHMKQHDFFKSAMPEGYVQERTIFFKDDGNYKTRAEVKFEGDTLVNRIELKGIDFKEDGNILGHKLEYNYNSHNVYIMADKQK NGIKVNFKIRHNIEDGSVQLADHYQQNTPIGDGPVLLPDNHYLSTQSALSKDPNEKRDHMVLLEFVTAAGITLGMDELYKGGGGSM HFSIPETESRSGDSGGSAYVAYNIHVNGVLHCRVAASQLLGLHEQLRKEYGANVLPAFPPKKLFSLTPAEVEQRREQLEKYMQAVRQ DPLLGSSETFNSFLRRAQQETQQVPTEEVSLEVLLSNGQKVLVNVLTSDQTEDVLEAVAAKLDLPDDLIGYFSLFLVREKEDGAFSFV RKLQEFELPYVSVTSLRSQEYKIVLRKSYWDSAYDDDVMENRVGLNLLYAQTVSDIERGWILVTKEQHRQLKSLQEKVSKKEFLRLA QTLRHYGYLRFDACVADFPEKDCPVVVSAGNSELSLQLRLPGQQLREGSFRVTRMRCWRVTSSVPLPSGSTSSPGRGRGEVRLELAF EYLMSKDRLQWVTITSPQAIMMSICLQSMVDELMVKKSGGSIRKMLRRRVGGTLRRSDSQQAVKSPPLLESPDATRESMVKLSSKLS AVSLRGIGSPSTDASASDVHGNFAFEGIGDEDL
248	> His-Sumo3-EGFP-SNX17$_{K431LSSK:AAAAA}$ MGSSHHHHHHSSGLVPRGSHMNDHINLKVAGQDGSVVQFKIKRHTPLSKLMKAYCERQGLSMRQIRFRFDGQPINETDTPAQLEM EDEDTIDVFQQQTGGSVSKGEELFTGVVPILVELDGDVNGHKFSVSGEGEGDATYGKLTLKFICTTGKLPVPWPTLVTTLTYGVQCFS RYPDHMKQHDFFKSAMPEGYVQERTIFFKDDGNYKTRAEVKFEGDTLVNRIELKGIDFKEDGNILGHKLEYNYNSHNVYIMADKQK NGIKVNFKIRHNIEDGSVQLADHYQQNTPIGDGPVLLPDNHYLSTQSALSKDPNEKRDHMVLLEFVTAAGITLGMDELYKGGGGSM HFSIPETESRSGDSGGSAYVAYNIHVNGVLHCRVRYSQLLGLHEQLRKEYGANVLPAFPPKKLFSLTPAEVEQRREQLEKYMQAVRQ DPLLGSSETFNSFLRRAQQETQQVPTEEVSLEVLLSNGQKVLVNVLTSDQTEDVLEAVAAKLDLPDDLIGYFSLFLVREKEDGAFSFV RKLQEFELPYVSVTSLRSQEYKIVLRKSYWDSAYDDDVMENRVGLNLLYAQTVSDIERGWILVTKEQHRQLKSLQEKVSKKEFLRLA QTLRHYGYLRFDACVADFPEKDCPVVVSAGNSELSLQLRLPGQQLREGSFRVTRMRCWRVTSSVPLPSGSTSSPGRGRGEVRLELAF EYLMSKDRLQWVTITSPQAIMMSICLQSMVDELMVKKSGGSIRKMLRRRVGGTLRRSDSQQAVKSPPLLESPDATRESMVAAAAAL SAVSLRGIGSPSTDASASDVHGNFAFEGIGDEDL
250	> His-Sumo3-EGFP-SNX17$_{7-470}$ MGSSHHHHHHSSGLVPRGSHMNDHINLKVAGQDGSVVQFKIKRHTPLSKLMKAYCERQGLSMRQIRFRFDGQPINETDTPAQLEM EDEDTIDVFQQQTGGSVSKGEELFTGVVPILVELDGDVNGHKFSVSGEGEGDATYGKLTLKFICTTGKLPVPWPTLVTTLTYGVQCFS RYPDHMKQHDFFKSAMPEGYVQERTIFFKDDGNYKTRAEVKFEGDTLVNRIELKGIDFKEDGNILGHKLEYNYNSHNVYIMADKQK NGIKVNFKIRHNIEDGSVQLADHYQQNTPIGDGPVLLPDNHYLSTQSALSKDPNEKRDHMVLLEFVTAAGITLGMDELYKGGGGSET ESRSGDSGGSAYVAYNIHVNGVLHCRVRYSQLLGLHEQLRKEYGANVLPAFPPKKLFSLTPAEVEQRREQLEKYMQAVRQDPLLGSS ETFNSFLRRAQQETQQVPTEEVSLEVLLSNGQKVLVNVLTSDQTEDVLEAVAAKLDLPDDLIGYFSLFLVREKEDGAFSFVRKLQEFE LPYVSVTSLRSQEYKIVLRKSYWDSAYDDDVMENRVGLNLLYAQTVSDIERGWILVTKEQHRQLKSLQEKVSKKEFLRLAQTLRHYG YLRFDACVADFPEKDCPVVVSAGNSELSLQLRLPGQQLREGSFRVTRMRCWRVTSSVPLPSGSTSSPGRGRGEVRLELAFEYLMSKD RLQWVTITSPQAIMMSICLQSMVDELMVKKSGGSIRKMLRRRVGGTLRRSDSQQAVKSPPLLESPDATRESMVKLSSKLSAVSLRGIG SPSTDASASDVHGNFAFEGIGDEDL
29	> His-Sumo3-SNX17$_{FERM-CT}$-TEV-L2$_{FBR}$ MGSSHHHHHHSSGLVPRGSHMNDHINLKVAGQDGSVVQFKIKRHTPLSKLMKAYCERQGLSMRQIRFRFDGQPINETDTPAQLEM EDEDTIDVFQQQTGGTQQVPTEEVSLEVLLSNGQKVLVNVLTSDQTEDVLEAVAAKLDLPDDLIGYFSLFLVREKEDGAFSFVRKLQE FELPYVSVTSLRSQEYKIVLRKSYWDSAYDDDVMENRVGLNLLYAQTVSDIERGWILVTKEQHRQLKSLQEKVSKKEFLRLAQTLRH YGYLRFDACVADFPEKDCPVVVSAGNSELSLQLRLPGQQLREGSFRVTRMRCWRVTSSVPLPSGSTSSPGRGRGEVRLELAFEYLMS KDRLQWVTITSPQAIMMSICLQSMVDELMVKKSGGSIRKMLRRRVGGTLRRSDSQQAVKSPPLLESPDATRESMVKLSSKLSAVSLR GIGSPSTDASASDVHGNFAFEGIGDEDLENLYFQGDPAFVTTPTKLITYDNPAYEGIDVDNTLYF
42	> His-Sumo3-SNX17$_{FERM-CT}$-TEV-APP$_{739-770}$ MGSSHHHHHHSSGLVPRGSHMNDHINLKVAGQDGSVVQFKIKRHTPLSKLMKAYCERQGLSMRQIRFRFDGQPINETDTPAQLEM EDEDTIDVFQQQTGGTQQVPTEEVSLEVLLSNGQKVLVNVLTSDQTEDVLEAVAAKLDLPDDLIGYFSLFLVREKEDGAFSFVRKLQE FELPYVSVTSLRSQEYKIVLRKSYWDSAYDDDVMENRVGLNLLYAQTVSDIERGWILVTKEQHRQLKSLQEKVSKKEFLRLAQTLRH YGYLRFDACVADFPEKDCPVVVSAGNSELSLQLRLPGQQLREGSFRVTRMRCWRVTSSVPLPSGSTSSPGRGRGEVRLELAFEYLMS KDRLQWVTITSPQAIMMSICLQSMVDELMVKKSGGSIRKMLRRRVGGTLRRSDSQQAVKSPPLLESPDATRESMVKLSSKLSAVSLR GIGSPSTDASASDVHGNFAFEGIGDEDLENLYFQGADAAVTPEERHLSKMQQNGYENPTYKFFEQMQN
181	> His-Sumo3-SNX17$_{FERM-CT\ (del406-442)}$ MGSSHHHHHHSSGLVPRGSHMNDHINLKVAGQDGSVVQFKIKRHTPLSKLMKAYCERQGLSMRQIRFRFDGQPINETDTPAQLEM EDEDTIDVFQQQTGGTQQVPTEEVSLEVLLSNGQKVLVNVLTSDQTEDVLEAVAAKLDLPDDLIGYFSLFLVREKEDGAFSFVRKLQE FELPYVSVTSLRSQEYKIVLRKSYWDSAYDDDVMENRVGLNLLYAQTVSDIERGWILVTKEQHRQLKSLQEKVSKKEFLRLAQTLRH

	YGYLRFDACVADFPEKDCPVVVSAGNSELSLQLRLPGQQLREGSFRVTRMRCWRVTSSVPLPSGSTSSPGRGRGEVRLELAFEYLMS KDRLQWVTITSPQAIMMSICLQSMVDELMVKKSGGSIRKMLRRRVGGTLRGIGSPSTDASASDVHGNFAFEGIGDEDL
146	> His-Sumo3-SNX17$_{109-388}$-TEV-L2$_{FBR}$ MGSSHHHHHHSSGLVPRGSHMNDHINLKVAGQDGSVVQFKIKRHTPLSKLMKAYCERQGLSMRQIRFRFDGQPINETDTPAQLEM EDEDTIDVFQQQTGGTQQVPTEEVSLEVLLSNGQKVLVNVLTSDQTEDVLEAVAAKLDLPDDLIGYFSLFLVREKEDGAFSFVRKLQE FELPYVSVTSLRSQEYKIVLRKSYWDSAYDDDVMENRVGLNLLYAQTVSDIERGWILVTKEQHRQLKSLQEKVSKKEFLRLAQTLRH YGYLRFDACVADFPEKDCPVVVSAGNSELSLQLRLPGQQLREGSFRVTRMRCWRVTSSVPLPSGSTSSPGRGRGEVRLELAFEYLMS KDRLQWVTITSPQAIMMSICLQSMVDELMVKKSENLYFQGDPAFVTTPTKLITYDNPAYEGIDVDNTLYF
20	> His-Sumo3-SNX31$_{FERM-CT}$ MGSSHHHHHHSSGLVPRGSHMNDHINLKVAGQDGSVVQFKIKRHTPLSKLMKAYCERQGLSMRQIRFRFDGQPINETDTPAQLEM EDEDTIDVFQQQTGGFDIATKKAYLDIFLPNEQSIRIEIITSDTAERVLEVVSHKIGLCRELLGYFGLFLIRFGKEGKLSVVKKLADFELP YVSLGSSEVENCKVGLRKWYMAPSLDSVLMDCRVAVDLLYMQAIQDIEKGWAKPTQAQRQKLEAFQKEDSQTKFLELAREVRHYG YLQLDPCTCDYPESGSGAVLSVGNNEISCCITLPDSQTQDIVFQMSRVKCWQVTFLGTLLDTDGPQRTLNQNLELRFQYSEDSCWQW FVIYTKQAFLLSSCLKKMISEKMVKLAAENTEMQIEVPEQSKSKKYHIQQSQQKDYSSFLSRKSKIKIAKDDCVFGNIKEEDL
18	> GST-TEV-LRP1$_{ICD}$ MGSSMSPILGYWKIKGLVQPTRLLLEYLEEKYEEHLYERDEGDKWRNKKFELGLEFPNLPYYIDGDVKLTQSMAIIRYIADKHNMLG GCPKERAEISMLEGAVLDIRYGVSRIAYSKDFETLKVDFLSKLPEMLKMFEDRLCHKTYLNGDHVTHPDFMLYDALDVVLYMDPMC LDAFPKLVCFKKRIEAIPQIDKYLKSSKYIAWPLQGWQATFGGGDHPPKSSGENLYFQGYKRRVQGAKGFQHQRMTNGAMNVEIGN PTYKMYEGGEPDDVGGLLDADFALDPDKPTNFTNPVYATLYMGGHGSRHSLASTDEKRELLGRGPEDEIGDPLA
275	>GST-TEV-LRP1$_{ICD-mut(N4470A+Y4473A)}$ MGSSMSPILGYWKIKGLVQPTRLLLEYLEEKYEEHLYERDEGDKWRNKKFELGLEFPNLPYYIDGDVKLTQSMAIIRYIADKHNMLG GCPKERAEISMLEGAVLDIRYGVSRIAYSKDFETLKVDFLSKLPEMLKMFEDRLCHKTYLNGDHVTHPDFMLYDALDVVLYMDPMC LDAFPKLVCFKKRIEAIPQIDKYLKSSKYIAWPLQGWQATFGGGDHPPKSSGENLYFQGYKRRVQGAKGFQHQRMTNGAMNVEIGA PTAKMYEGGEPDDVGGLLDADFALDPDKPTNFTNPVYATLYMGGHGSRHSLASTDEKRELLGRGPEDEIGDPLA
173	> MBP-TEV-His$_{10}$-LRP1$_{ICD}$ MSYYMIEEGKLVIWINGDKGYNGLAEVGKKFEKDTGIKVTVEHPDKLEEKFPQVAATGDGPDIIFWAHDRFGGYAQSGLLAEITPDK AFQDKLYPFTWDAVRYNGKLIAYPIAVEALSLIYNKDLLPNPPKTWEEIPALDKELKAKGKSALMFNLQEPYFTWPLIAADGGYAFK YENGKYDIKDVGVDNAGAKAGLTFLVDLIKNKHMNADTDYSIAEAAFNKGETAMTINGPWAWSNIDTSKVNYGVTVLPTFKGQPS KPFVGVLSAGINAASPNKELAKEFLENYLLTDEGLEAVNKDKPLGAVALKSYEEELAKDPRIAATMENAQKGEIMPNIPQMSAFWYA VRTAVINAASGRQTVDEALKDAQTNSSSNNNNNNNNNLGSSGENLYFQGHHHHHHHHHHYKRRVQGAKGFQHQRMTNGAMN VEIGNPTYKMYEGGEPDDVGGLLDADFALDPDKPTNFTNPVYATLYMGGHGSRHSLASTDEKRELLGRGPEDEIGDPLA
49	> GST-TEV-APP$_{ICD}$ MGSSMSPILGYWKIKGLVQPTRLLLEYLEEKYEEHLYERDEGDKWRNKKFELGLEFPNLPYYIDGDVKLTQSMAIIRYIADKHNMLG GCPKERAEISMLEGAVLDIRYGVSRIAYSKDFETLKVDFLSKLPEMLKMFEDRLCHKTYLNGDHVTHPDFMLYDALDVVLYMDPMC LDAFPKLVCFKKRIEAIPQIDKYLKSSKYIAWPLQGWQATFGGGDHPPKSSGENLYFQGKKKQYTSIHHGVVEVDAAVTPEERHLSK MQQNGYENPTYKFFEQMQN
168	> GST-TEV-ITGB1$_{ICD}$ MGSSMSPILGYWKIKGLVQPTRLLLEYLEEKYEEHLYERDEGDKWRNKKFELGLEFPNLPYYIDGDVKLTQSMAIIRYIADKHNMLG GCPKERAEISMLEGAVLDIRYGVSRIAYSKDFETLKVDFLSKLPEMLKMFEDRLCHKTYLNGDHVTHPDFMLYDALDVVLYMDPMC LDAFPKLVCFKKRIEAIPQIDKYLKSSKYIAWPLQGWQATFGGGDHPPKSSGENLYFQGKLLMIIHDRREFAKFEKEKMNAKWDTGE NPIYKSAVTTVVNPKYEGK
28	> GST-TEV-L2$_{FBR}$ MGSSMSPILGYWKIKGLVQPTRLLLEYLEEKYEEHLYERDEGDKWRNKKFELGLEFPNLPYYIDGDVKLTQSMAIIRYIADKHNMLG GCPKERAEISMLEGAVLDIRYGVSRIAYSKDFETLKVDFLSKLPEMLKMFEDRLCHKTYLNGDHVTHPDFMLYDALDVVLYMDPMC LDAFPKLVCFKKRIEAIPQIDKYLKSSKYIAWPLQGWQATFGGGDHPPKSSGENLYFQGDPAFVTTPTKLITYDNPAYEGIDVDNTLY F
276	>GST-TEV-L2$_{FBR-mut(N254A+Y257A)}$ MGSSMSPILGYWKIKGLVQPTRLLLEYLEEKYEEHLYERDEGDKWRNKKFELGLEFPNLPYYIDGDVKLTQSMAIIRYIADKHNMLG GCPKERAEISMLEGAVLDIRYGVSRIAYSKDFETLKVDFLSKLPEMLKMFEDRLCHKTYLNGDHVTHPDFMLYDALDVVLYMDPMC LDAFPKLVCFKKRIEAIPQIDKYLKSSKYIAWPLQGWQATFGGGDHPPKSSGENLYFQGDPAFVTTPTKLITYDAPAAEGIDVDNTLY F
131	> GST-HRV3C-His$_{10}$-L2$_{FBR}$ MSPILGYWKIKGLVQPTRLLLEYLEEKYEEHLYERDEGDKWRNKKFELGLEFPNLPYYIDGDVKLTQSMAIIRYIADKHNMLGGCPK ERAEISMLEGAVLDIRYGVSRIAYSKDFETLKVDFLSKLPEMLKMFEDRLCHKTYLNGDHVTHPDFMLYDALDVVLYMDPMCLDAF PKLVCFKKRIEAIPQIDKYLKSSKYIAWPLQGWQATFGGGDHPPKSSGLEVLFQGPHHHHHHHHHHDPAFVTTPTKLITYDNPAYEG IDVDNTLYF
85	> His-TEV-VPS35L-Twin-Strep-TEV-VPS26C-VPS29 MGSSHHHHHHSSGENLYFQGMAVFPWHSRNRNYKAEFASCRLEAVPLEFGDYHPLKPITVTESKTKKVNRKGSTSSTSSSSSSVVD PLSSVLDGTDPLSMFAATADPAALAAAMDSSRRKRDRDDNSVVGSDFEPWTNKRGEILARYTTTEKLSINLFMGSEKGKAGTATLA MSEKVRTRLEELDDFEEGSQKELLNLTQQDYVNRIEELNQSLKDAWASDQKVKALKIVIQCSKLLSDTSVIQFYPSKFVLITDILDTFG KLVYERIFSMCVDSRSVLPDHFSPENANDTAKETCLNWFFKIASIRELIPRFYVEASILKCNKFLSKTGISECLPRLTCMIRGIGDPLVSV

	YARAYLCRVGMEVAPHLKETLNKNFFDFLLTFKQIHGDTVQNQLVVQGVELPSYLPLYPPAMDWIFQCISYHAPEALLTEMMERCK KLGNNALLLNSVMSAFRAEFIATRSMDFIGMIKECDESGFPKHLLFRSLGLNLALADPPESDRLQILNEAWKVITKLKNPQDYINCAE VWVEYTCKHFTKREVNTVLADVIKHMTPDRAFEDSYPQLQLIIKKVIAHFHDFSVLFSVEKFLPFLDMFQKESVRVEVCKCIMDAFIK HQQEPTKDPVILNALLHVCKTMHDSVNALTLEDEKRMLSYLINGFIKMVSFGRDFEQQLSFYVESRSMFCNLEPVLVQLIHSVNRLA METRKVMKGNHSRKTAAFVRACVAYCFITIPSLAGIFTRLNLYLHSGQVALANQCLSQADAFFKAAISLVPEVPKMINIDGKMRPSES FLLEFLCNFFSTLLIVPDHPEHGVLFLVRELLNVIQDYTWEDNSDEKIRIYTCVLHLLSAMSQETYLYHIDKVDSNDSLYGGDSKFLAE NNKLCETVMAQILEHLKTLAKDEALKRQSSLGLSFFNSILAHGDLRNNKLNQLSVNLWHLAQRHGCADTRTMVKTLEYIKKQSKQP DMTHLTELALRLPLQTRT MASWSHPQFEKGGGSGGGSGGSAWSHPQFEKSSGENLYFQGMGTALDIKIKRANKVYHAGEVLSGVVVISSKDSVQHQGVSLTMEG TVNLQLSAKSVGVFEAFYNSVKPIQIINSTIEMVKPGKFPSGKTEIPFEFPLHLKGNKVLYETYHGVFVNIQYTLRCDMKRSLLAKDLT KTCEFIVHSAPQKGKFTPSPVDFTITPETLQNVKERALLPKFLLRGHLNSTNCVITQPLTGELVVESSEAAIRSVELQLVRVETCGCAE GYARDATEIQNIQIADGDVCRGLSVPIYMVFPRLFTCPTLETTNFKVEFEVNIVVLLHPDHLITENFPLKLCRI MLVLVLGDLHIPHRCNSLPAKFKKLLVPGKIQHILCTGNLCTKESYDYLKTLAGDVHIVRGDFDENLNYPEQKVVTVGQFKIGLIHGH QVIPWGDMASLALLQRQFDVDILISGHTHKFEAFEHENKFYINPGSATGAYNALETNIIPSFVLMDIQASTVVTYVYQLIGDDVKVERI EYKKP
122	> His-TEV-VPS35L-Twin-Strep-TEV-VPS26C-GST-HRV3C-VPS29 MGSSHHHHHHSSGENLYFQGMAVFPWHSRNRNYKAEFASCRLEAVPLEFGDYHPLKPITVTESKTKKVNRKGSTSSTSSSSSSSVVD PLSSVLDGTDPLSMFAATADPAALAAAMDSSRRKRDRDDNSVVGSDFEPWTNKRGEILARYTTTEKLSINLFMGSEKGKAGTATLA MSEKVRTRLEELDDFEEGSQKELLNLTQQDYVNRIEELNQSLKDAWASDQKVKALKIVIQCSKLLSDTSVIQFYPSKFVLITDILDTFG KLVYERIFSMCVDSRSVLPDHFSPENANDTAKETCLNWFFKIASIRELIPRFYVEASILKCNKFLSKTGISECLPRLTCMIRGIGDPLVSV YARAYLCRVGMEVAPHLKETLNKNFFDFLLTFKQIHGDTVQNQLVVQGVELPSYLPLYPPAMDWIFQCISYHAPEALLTEMMERCK KLGNNALLLNSVMSAFRAEFIATRSMDFIGMIKECDESGFPKHLLFRSLGLNLALADPPESDRLQILNEAWKVITKLKNPQDYINCAE VWVEYTCKHFTKREVNTVLADVIKHMTPDRAFEDSYPQLQLIIKKVIAHFHDFSVLFSVEKFLPFLDMFQKESVRVEVCKCIMDAFIK HQQEPTKDPVILNALLHVCKTMHDSVNALTLEDEKRMLSYLINGFIKMVSFGRDFEQQLSFYVESRSMFCNLEPVLVQLIHSVNRLA METRKVMKGNHSRKTAAFVRACVAYCFITIPSLAGIFTRLNLYLHSGQVALANQCLSQADAFFKAAISLVPEVPKMINIDGKMRPSES FLLEFLCNFFSTLLIVPDHPEHGVLFLVRELLNVIQDYTWEDNSDEKIRIYTCVLHLLSAMSQETYLYHIDKVDSNDSLYGGDSKFLAE NNKLCETVMAQILEHLKTLAKDEALKRQSSLGLSFFNSILAHGDLRNNKLNQLSVNLWHLAQRHGCADTRTMVKTLEYIKKQSKQP DMTHLTELALRLPLQTRT MASWSHPQFEKGGGSGGGSGGSAWSHPQFEKSSGENLYFQGMGTALDIKIKRANKVYHAGEVLSGVVVISSKDSVQHQGVSLTMEG TVNLQLSAKSVGVFEAFYNSVKPIQIINSTIEMVKPGKFPSGKTEIPFEFPLHLKGNKVLYETYHGVFVNIQYTLRCDMKRSLLAKDLT KTCEFIVHSAPQKGKFTPSPVDFTITPETLQNVKERALLPKFLLRGHLNSTNCVITQPLTGELVVESSEAAIRSVELQLVRVETCGCAE GYARDATEIQNIQIADGDVCRGLSVPIYMVFPRLFTCPTLETTNFKVEFEVNIVVLLHPDHLITENFPLKLCRI MSPILGYWKIKGLVQPTRLLLEYLEEKYEEHLYERDEGDKWRNKKFELGLEFPNLPYYIDGDVKLTQSMAIIRYIADKHNMLGGCPK ERAEISMLEGAVLDIRYGVSRIAYSKDFETLKVDFLSKLPEMLKMFEDRLCHKTYLNGDHVTHPDFMLYDALDVVLYMDPMCLDAF PKLVCFKKRIEAIPQIDKYLKSSKYIAWPLQGWQATFGGGDHPPKSDLEVLFQGPMLVLVLGDLHIPHRCNSLPAKFKKLLVPGKIQH ILCTGNLCTKESYDYLKTLAGDVHIVRGDFDENLNYPEQKVVTVGQFKIGLIHGHQVIPWGDMASLALLQRQFDVDILISGHTHKFEA FEHENKFYINPGSATGAYNALETNIIPSFVLMDIQASTVVTYVYQLIGDDVKVERIEYKKP
164	> His-TEV-VPS35L-Twin-Strep-TEV-VPS26C-His-TEV-MBP-VPS29 MGSSHHHHHHSSGENLYFQGMAVFPWHSRNRNYKAEFASCRLEAVPLEFGDYHPLKPITVTESKTKKVNRKGSTSSTSSSSSSSVVD PLSSVLDGTDPLSMFAATADPAALAAAMDSSRRKRDRDDNSVVGSDFEPWTNKRGEILARYTTTEKLSINLFMGSEKGKAGTATLA MSEKVRTRLEELDDFEEGSQKELLNLTQQDYVNRIEELNQSLKDAWASDQKVKALKIVIQCSKLLSDTSVIQFYPSKFVLITDILDTFG KLVYERIFSMCVDSRSVLPDHFSPENANDTAKETCLNWFFKIASIRELIPRFYVEASILKCNKFLSKTGISECLPRLTCMIRGIGDPLVSV YARAYLCRVGMEVAPHLKETLNKNFFDFLLTFKQIHGDTVQNQLVVQGVELPSYLPLYPPAMDWIFQCISYHAPEALLTEMMERCK KLGNNALLLNSVMSAFRAEFIATRSMDFIGMIKECDESGFPKHLLFRSLGLNLALADPPESDRLQILNEAWKVITKLKNPQDYINCAE VWVEYTCKHFTKREVNTVLADVIKHMTPDRAFEDSYPQLQLIIKKVIAHFHDFSVLFSVEKFLPFLDMFQKESVRVEVCKCIMDAFIK HQQEPTKDPVILNALLHVCKTMHDSVNALTLEDEKRMLSYLINGFIKMVSFGRDFEQQLSFYVESRSMFCNLEPVLVQLIHSVNRLA METRKVMKGNHSRKTAAFVRACVAYCFITIPSLAGIFTRLNLYLHSGQVALANQCLSQADAFFKAAISLVPEVPKMINIDGKMRPSES FLLEFLCNFFSTLLIVPDHPEHGVLFLVRELLNVIQDYTWEDNSDEKIRIYTCVLHLLSAMSQETYLYHIDKVDSNDSLYGGDSKFLAE NNKLCETVMAQILEHLKTLAKDEALKRQSSLGLSFFNSILAHGDLRNNKLNQLSVNLWHLAQRHGCADTRTMVKTLEYIKKQSKQP DMTHLTELALRLPLQTRT MASWSHPQFEKGGGSGGGSGGSAWSHPQFEKSSGENLYFQGMGTALDIKIKRANKVYHAGEVLSGVVVISSKDSVQHQGVSLTMEG TVNLQLSAKSVGVFEAFYNSVKPIQIINSTIEMVKPGKFPSGKTEIPFEFPLHLKGNKVLYETYHGVFVNIQYTLRCDMKRSLLAKDLT KTCEFIVHSAPQKGKFTPSPVDFTITPETLQNVKERALLPKFLLRGHLNSTNCVITQPLTGELVVESSEAAIRSVELQLVRVETCGCAE GYARDATEIQNIQIADGDVCRGLSVPIYMVFPRLFTCPTLETTNFKVEFEVNIVVLLHPDHLITENFPLKLCRI MGSSHHHHHHSSGENLYFQGMIEEGKLVIWINGDKGYNGLAEVGKKFEKDTGIKVTVEHPDKLEEKFPQVAATGDGPDIIFWAHDR FGGYAQSGLLAEITPDKAFQDKLYPFTWDAVRYNGKLIAYPIAVEALSLIYNKDLLPNPPKTWEEIPALDKELKAKGKSALMFNLQEP YFTWPLIAADGGYAFKYENGKYDIKDVGVDNAGAKAGLTFLVDLIKNKHMNADTDYSIAEAAFNKGETAMTINGPWAWSNIDTSK VNYGVTVLPTFKGQPSKPFVGVLSAGINAASPNKELAKEFLENYLLTDEGLEAVNKDKPLGAVALKSYEEELAKDPRIAATMENAQK GEIMPNIPQMSAFWYAVRTAVINAASGRQTVDEALKDAQTNSSSMLVLVLGDLHIPHRCNSLPAKFKKLLVPGKIQHILCTGNLCTK ESYDYLKTLAGDVHIVRGDFDENLNYPEQKVVTVGQFKIGLIHGHQVIPWGDMASLALLQRQFDVDILISGHTHKFEAFEHENKFYIN PGSATGAYNALETNIIPSFVLMDIQASTVVTYVYQLIGDDVKVERIEYKKP
118	> His-TEV-VPS35L$_{110-963}$-Twin-Strep-TEV-VPS26C-VPS29

	MGSSHHHHHHSSGENLYFQGVGSDFEPWTNKRGEILARYTTTEKLSINLFMGSEKGKAGTATLAMSEKVRTRLEELDDFEEGSQKE LLNLTQQDYVNRIEELNQSLKDAWASDQKVKALKIVIQCSKLLSDTSVIQFYPSKFVLITDILDTFGKLVYERIFSMCVDSRSVLPDHFS PENANDTAKETCLNWFFKIASIRELIPRFYVEASILKCNKFLSKTGISECLPRLTCMIRGIGDPLVSVYARAYLCRVGMEVAPHLKETL NKNFFDFLLTFKQIHGDTVQNQLVVQGVELPSYLPLYPPAMDWIFQCISYHAPEALLTEMMERCKKLGNNALLLNSVMSAFRAEFIA TRSMDFIGMIKECDESGFPKHLLFRSLGLNLALADPPESDRLQILNEAWKVITKLKNPQDYINCAEVWVEYTCKHFTKREVNTVLAD VIKHMTPDRAFEDSYPQLQLIIKKVIAHFHDFSVLFSVEKFLPFLDMFQKESVRVEVCKCIMDAFIKHQQEPTKDPVILNALLHVCKT MHDSVNALTLEDEKRMLSYLINGFIKMVSFGRDFEQQLSFYVESRSMFCNLEPVLVQLIHSVNRLAMETRKVMKGNHSRKTAAFVR ACVAYCFITIPSLAGIFTRLNLYLHSGQVALANQCLSQADAFFKAAISLVPEVPKMINIDGKMRPSESFLLEFLCNFFSTLLIVPDHPEH GVLFLVRELLNVIQDYTWEDNSDEKIRIYTCVLHLLSAMSQETYLYHIDKVDSNDSLYGGDSKFLAENNKLCETVMAQILEHLKTLAK DEALKRQSSLGLSFFNSILAHGDLRNNKLNQLSVNLWHLAQRHGCADTRTMVKTLEYIKKQSKQPDMTHLTELALRLPLQTRT MASWSHPQFEKGGGSGGGSGGSAWSHPQFEKSSGENLYFQGMGTALDIKIKRANKVYHAGEVLSGVVVISSKDSVQHQGVSLTMEG TVNLQLSAKSVGVFEAFYNSVKPIQIINSTIEMVKPGKFPSGKTEIPFEFPLHLKGNKVLYETYHGVFVNIQYTLRCDMKRSLLAKDLT KTCEFIVHSAPQKGKFTPSPVDFTITPETLQNVKERALLPKFLLRGHLNSTNCVITQPLTGELVVESSEAAIRSVELQLVRVETCGCAE GYARDATEIQNIQIADGDVCRGLSVPIYMVFPRLFTCPTLETTNFKVEFEVNIVVLLHPDHLITENFPLKLCRI MLVLVLGDLHIPHRCNSLPAKFKKLLVPGKIQHILCTGNLCTKESYDYLKTLAGDVHIVRGDFDENLNYPEQKVVTVGQFKIGLIHGH QVIPWGDMASLALLQRQFDVDILISGHTHKFEAFEHENKFYINPGSATGAYNALETNIIPSFVLMDIQASTVVTYVYQLIGDDVKVERI EYKKP
116	> His-TEV-VPS35L$_{110-598}$-Twin-Strep-TEV-VPS26C-VPS29 MGSSHHHHHHSSGENLYFQGVGSDFEPWTNKRGEILARYTTTEKLSINLFMGSEKGKAGTATLAMSEKVRTRLEELDDFEEGSQKE LLNLTQQDYVNRIEELNQSLKDAWASDQKVKALKIVIQCSKLLSDTSVIQFYPSKFVLITDILDTFGKLVYERIFSMCVDSRSVLPDHFS PENANDTAKETCLNWFFKIASIRELIPRFYVEASILKCNKFLSKTGISECLPRLTCMIRGIGDPLVSVYARAYLCRVGMEVAPHLKETL NKNFFDFLLTFKQIHGDTVQNQLVVQGVELPSYLPLYPPAMDWIFQCISYHAPEALLTEMMERCKKLGNNALLLNSVMSAFRAEFIA TRSMDFIGMIKECDESGFPKHLLFRSLGLNLALADPPESDRLQILNEAWKVITKLKNPQDYINCAEVWVEYTCKHFTKREVNTVLAD VIKHMTPDRAFEDSYPQLQLIIKKVIAHFHDFSVLFSVEKFLPFLDMFQKESVRVEVCKCIMDAFIKHQQ MASWSHPQFEKGGGSGGGSGGSAWSHPQFEKSSGENLYFQGMGTALDIKIKRANKVYHAGEVLSGVVVISSKDSVQHQGVSLTMEG TVNLQLSAKSVGVFEAFYNSVKPIQIINSTIEMVKPGKFPSGKTEIPFEFPLHLKGNKVLYETYHGVFVNIQYTLRCDMKRSLLAKDLT KTCEFIVHSAPQKGKFTPSPVDFTITPETLQNVKERALLPKFLLRGHLNSTNCVITQPLTGELVVESSEAAIRSVELQLVRVETCGCAE GYARDATEIQNIQIADGDVCRGLSVPIYMVFPRLFTCPTLETTNFKVEFEVNIVVLLHPDHLITENFPLKLCRI MLVLVLGDLHIPHRCNSLPAKFKKLLVPGKIQHILCTGNLCTKESYDYLKTLAGDVHIVRGDFDENLNYPEQKVVTVGQFKIGLIHGH QVIPWGDMASLALLQRQFDVDILISGHTHKFEAFEHENKFYINPGSATGAYNALETNIIPSFVLMDIQASTVVTYVYQLIGDDVKVERI EYKKP
138	> His-TEV-VPS35L$_{1-598}$-Twin-Strep-TEV-VPS26C-VPS29 MGSSHHHHHHSSGENLYFQGMAVFPWHSRNRNYKAEFASCRLEAVPLEFGDYHPLKPITVTESKTKKVNRKGSTSSTSSSSSSVVD PLSSVLDGTDPLSMFAATADPAALAAAMDSSRRKRDRDDNSVVGSDFEPWTNKRGEILARYTTTEKLSINLFMGSEKGKAGTATLA MSEKVRTRLEELDDFEEGSQKELLNLTQQDYVNRIEELNQSLKDAWASDQKVKALKIVIQCSKLLSDTSVIQFYPSKFVLITDILDTFG KLVYERIFSMCVDSRSVLPDHFSPENANDTAKETCLNWFFKIASIRELIPRFYVEASILKCNKFLSKTGISECLPRLTCMIRGIGDPLVSV YARAYLCRVGMEVAPHLKETLNKNFFDFLLTFKQIHGDTVQNQLVVQGVELPSYLPLYPPAMDWIFQCISYHAPEALLTEMMERCK KLGNNALLLNSVMSAFRAEFIATRSMDFIGMIKECDESGFPKHLLFRSLGLNLALADPPESDRLQILNEAWKVITKLKNPQDYINCAE VWVEYTCKHFTKREVNTVLADVIKHMTPDRAFEDSYPQLQLIIKKVIAHFHDFSVLFSVEKFLPFLDMFQKESVRVEVCKCIMDAFIK HQQ MASWSHPQFEKGGGSGGGSGGSAWSHPQFEKSSGENLYFQGMGTALDIKIKRANKVYHAGEVLSGVVVISSKDSVQHQGVSLTMEG TVNLQLSAKSVGVFEAFYNSVKPIQIINSTIEMVKPGKFPSGKTEIPFEFPLHLKGNKVLYETYHGVFVNIQYTLRCDMKRSLLAKDLT KTCEFIVHSAPQKGKFTPSPVDFTITPETLQNVKERALLPKFLLRGHLNSTNCVITQPLTGELVVESSEAAIRSVELQLVRVETCGCAE GYARDATEIQNIQIADGDVCRGLSVPIYMVFPRLFTCPTLETTNFKVEFEVNIVVLLHPDHLITENFPLKLCRI MLVLVLGDLHIPHRCNSLPAKFKKLLVPGKIQHILCTGNLCTKESYDYLKTLAGDVHIVRGDFDENLNYPEQKVVTVGQFKIGLIHGH QVIPWGDMASLALLQRQFDVDILISGHTHKFEAFEHENKFYINPGSATGAYNALETNIIPSFVLMDIQASTVVTYVYQLIGDDVKVERI EYKKP
144	> His-TEV-VPS35L$_{1-436}$-Twin-Strep-TEV-VPS26C-VPS29 MGSSHHHHHHSSGENLYFQGMAVFPWHSRNRNYKAEFASCRLEAVPLEFGDYHPLKPITVTESKTKKVNRKGSTSSTSSSSSSVVD PLSSVLDGTDPLSMFAATADPAALAAAMDSSRRKRDRDDNSVVGSDFEPWTNKRGEILARYTTTEKLSINLFMGSEKGKAGTATLA MSEKVRTRLEELDDFEEGSQKELLNLTQQDYVNRIEELNQSLKDAWASDQKVKALKIVIQCSKLLSDTSVIQFYPSKFVLITDILDTFG KLVYERIFSMCVDSRSVLPDHFSPENANDTAKETCLNWFFKIASIRELIPRFYVEASILKCNKFLSKTGISECLPRLTCMIRGIGDPLVSV YARAYLCRVGMEVAPHLKETLNKNFFDFLLTFKQIHGDTVQNQLVVQGVELPSYLPLYPPAMDWIFQCISYHAPEALLTEMMERCK KLGNNALLLNSVMSAFR MASWSHPQFEKGGGSGGGSGGSAWSHPQFEKSSGENLYFQGMGTALDIKIKRANKVYHAGEVLSGVVVISSKDSVQHQGVSLTMEG TVNLQLSAKSVGVFEAFYNSVKPIQIINSTIEMVKPGKFPSGKTEIPFEFPLHLKGNKVLYETYHGVFVNIQYTLRCDMKRSLLAKDLT KTCEFIVHSAPQKGKFTPSPVDFTITPETLQNVKERALLPKFLLRGHLNSTNCVITQPLTGELVVESSEAAIRSVELQLVRVETCGCAE GYARDATEIQNIQIADGDVCRGLSVPIYMVFPRLFTCPTLETTNFKVEFEVNIVVLLHPDHLITENFPLKLCRI MLVLVLGDLHIPHRCNSLPAKFKKLLVPGKIQHILCTGNLCTKESYDYLKTLAGDVHIVRGDFDENLNYPEQKVVTVGQFKIGLIHGH QVIPWGDMASLALLQRQFDVDILISGHTHKFEAFEHENKFYINPGSATGAYNALETNIIPSFVLMDIQASTVVTYVYQLIGDDVKVERI EYKKP
151	> His-TEV-VPS35L-GST-HRV3C-VPS29

	MGSSHHHHHHSSGENLYFQGMAVFPWHSRNRNYKAEFASCRLEAVPLEFGDYHPLKPITVTESKTKKVNRKGSTSSTSSSSSSSVVD PLSSVLDGTDPLSMFAATADPAALAAAMDSSRRKRDRDDNSVVGSDFEPWTNKRGEILARYTTTEKLSINLFMGSEKGKAGTATLA MSEKVRTRLEELDDFEEGSQKELLNLTQQDYVNRIEELNQSLKDAWASDQKVKALKIVIQCSKLLSDTSVIQFYPSKFVLITDILDTFG KLVYERIFSMCVDSRSVLPDHFSPENANDTAKETCLNWFFKIASIRELIPRFYVEASILKCNKFLSKTGISECLPRLTCMIRGIGDPLVSV YARAYLCRVGMEVAPHLKETLNKNFFDFLLTFKQIHGDTVQNQLVVQGVELPSYLPLYPPAMDWIFQCISYHAPEALLTEMMERCK KLGNNALLLNSVMSAFRAEFIATRSMDFIGMIKECDESGFPKHLLFRSLGLNLALADPPESDRLQILNEAWKVITKLKNPQDYINCAE VWVEYTCKHFTKREVNTVLADVIKHMTPDRAFEDSYPQLQLIIKKVIAHFHDFSVLFSVEKFLPFLDMFQKESVRVEVCKCIMDAFIK HQQEPTKDPVILNALLHVCKTMHDSVNALTLEDEKRMLSYLINGFIKMVSFGRDFEQQLSFYVESRSMFCNLEPVLVQLIHSVNRLA METRKVMKGNHSRKTAAFVRACVAYCFITIPSLAGIFTRLNLYLHSGQVALANQCLSQADAFFKAAISLVPEVPKMINIDGKMRPSES FLLEFLCNFFSTLLIVPDHPEHGVLFLVRELLNVIQDYTWEDNSDEKIRIYTCVLHLLSAMSQETYLYHIDKVDSNDSLYGGDSKFLAE NNKLCETVMAQILEHLKTLAKDEALKRQSSLGLSFFNSILAHGDLRNNKLNQLSVNLWHLAQRHGCADTRTMVKTLEYIKKQSKQP DMTHLTELALRLPLQTRT MSPILGYWKIKGLVQPTRLLLEYLEEKYEEHLYERDEGDKWRNKKFELGLEFPNLPYYIDGDVKLTQSMAIIRYIADKHNMLGGCPK ERAEISMLEGAVLDIRYGVSRIAYSKDFETLKVDFLSKLPEMLKMFEDRLCHKTYLNGDHVTHPDFMLYDALDVVLYMDPMCLDAF PKLVCFKKRIEAIPQIDKYLKSSKYIAWPLQGWQATFGGGDHPPKSDLEVLFQGPMLVLVLGDLHIPHRCNSLPAKFKKLLVPGKIQH ILCTGNLCTKESYDYLKTLAGDVHIVRGDFDENLNYPEQKVVTVGQFKIGLIHGHQVIPWGDMASLALLQRQFDVDILISGHTHKFEA FEHENKFYINPGSATGAYNALETNIIPSFVLMDIQASTVVTYVYQLIGDDVKVERIEYKKP
231	> His-TEV-VPS35L$_{R248E+W280D}$-Twin-Strep-TEV-VPS26C-VPS29 MGSSHHHHHHSSGENLYFQGMAVFPWHSRNRNYKAEFASCRLEAVPLEFGDYHPLKPITVTESKTKKVNRKGSTSSTSSSSSSSVVD PLSSVLDGTDPLSMFAATADPAALAAAMDSSRRKRDRDDNSVVGSDFEPWTNKRGEILARYTTTEKLSINLFMGSEKGKAGTATLA MSEKVRTRLEELDDFEEGSQKELLNLTQQDYVNRIEELNQSLKDAWASDQKVKALKIVIQCSKLLSDTSVIQFYPSKFVLITDILDTFG KLVYEEIFSMCVDSRSVLPDHFSPENANDTAKETCLNDFFKIASIRELIPRFYVEASILKCNKFLSKTGISECLPRLTCMIRGIGDPLVSV YARAYLCRVGMEVAPHLKETLNKNFFDFLLTFKQIHGDTVQNQLVVQGVELPSYLPLYPPAMDWIFQCISYHAPEALLTEMMERCK KLGNNALLLNSVMSAFRAEFIATRSMDFIGMIKECDESGFPKHLLFRSLGLNLALADPPESDRLQILNEAWKVITKLKNPQDYINCAE VWVEYTCKHFTKREVNTVLADVIKHMTPDRAFEDSYPQLQLIIKKVIAHFHDFSVLFSVEKFLPFLDMFQKESVRVEVCKCIMDAFIK HQQEPTKDPVILNALLHVCKTMHDSVNALTLEDEKRMLSYLINGFIKMVSFGRDFEQQLSFYVESRSMFCNLEPVLVQLIHSVNRLA METRKVMKGNHSRKTAAFVRACVAYCFITIPSLAGIFTRLNLYLHSGQVALANQCLSQADAFFKAAISLVPEVPKMINIDGKMRPSES FLLEFLCNFFSTLLIVPDHPEHGVLFLVRELLNVIQDYTWEDNSDEKIRIYTCVLHLLSAMSQETYLYHIDKVDSNDSLYGGDSKFLAE NNKLCETVMAQILEHLKTLAKDEALKRQSSLGLSFFNSILAHGDLRNNKLNQLSVNLWHLAQRHGCADTRTMVKTLEYIKKQSKQP DMTHLTELALRLPLQTRT MASWSHPQFEKGGGSGGGSGGSAWSHPQFEKSSGENLYFQGMGTALDIKIKRANKVYHAGEVLSGVVVISSKDSVQHQGVSLTMEG TVNLQLSAKSVGVFEAFYNSVKPIQIINSTIEMVKPGKFPSGKTEIPFEFPLHLKGNKVLYETYHGVFVNIQYTLRCDMKRSLLAKDLT KTCEFIVHSAPQKGKFTPSPVDFTITPETLQNVKERALLPKFLLRGHLNSTNCVITQPLTGELVVESSEAAIRSVELQLVRVETCGCAE GYARDATEIQNIQIADGDVCRGLSVPIYMVFPRLFTCPTLETTNFKVEFEVNIVVLLHPDHLITENFPLKLCRI MLVLVLGDLHIPHRCNSLPAKFKKLLVPGKIQHILCTGNLCTKESYDYLKTLAGDVHIVRGDFDENLNYPEQKVVTVGQFKIGLIHGH QVIPWGDMASLALLQRQFDVDILISGHTHKFEAFEHENKFYINPGSATGAYNALETNIIPSFVLMDIQASTVVTYVYQLIGDDVKVERI EYKKP
232	> His-TEV-VPS35L$_{K157E+R161E}$-Twin-Strep-TEV-VPS26C-VPS29 MGSSHHHHHHSSGENLYFQGMAVFPWHSRNRNYKAEFASCRLEAVPLEFGDYHPLKPITVTESKTKKVNRKGSTSSTSSSSSSSVVD PLSSVLDGTDPLSMFAATADPAALAAAMDSSRRKRDRDDNSVVGSDFEPWTNKRGEILARYTTTEKLSINLFMGSEKGKAGTATLA MSEEVRTELEELDDFEEGSQKELLNLTQQDYVNRIEELNQSLKDAWASDQKVKALKIVIQCSKLLSDTSVIQFYPSKFVLITDILDTFG KLVYERIFSMCVDSRSVLPDHFSPENANDTAKETCLNWFFKIASIRELIPRFYVEASILKCNKFLSKTGISECLPRLTCMIRGIGDPLVSV YARAYLCRVGMEVAPHLKETLNKNFFDFLLTFKQIHGDTVQNQLVVQGVELPSYLPLYPPAMDWIFQCISYHAPEALLTEMMERCK KLGNNALLLNSVMSAFRAEFIATRSMDFIGMIKECDESGFPKHLLFRSLGLNLALADPPESDRLQILNEAWKVITKLKNPQDYINCAE VWVEYTCKHFTKREVNTVLADVIKHMTPDRAFEDSYPQLQLIIKKVIAHFHDFSVLFSVEKFLPFLDMFQKESVRVEVCKCIMDAFIK HQQEPTKDPVILNALLHVCKTMHDSVNALTLEDEKRMLSYLINGFIKMVSFGRDFEQQLSFYVESRSMFCNLEPVLVQLIHSVNRLA METRKVMKGNHSRKTAAFVRACVAYCFITIPSLAGIFTRLNLYLHSGQVALANQCLSQADAFFKAAISLVPEVPKMINIDGKMRPSES FLLEFLCNFFSTLLIVPDHPEHGVLFLVRELLNVIQDYTWEDNSDEKIRIYTCVLHLLSAMSQETYLYHIDKVDSNDSLYGGDSKFLAE NNKLCETVMAQILEHLKTLAKDEALKRQSSLGLSFFNSILAHGDLRNNKLNQLSVNLWHLAQRHGCADTRTMVKTLEYIKKQSKQP DMTHLTELALRLPLQTRT MASWSHPQFEKGGGSGGGSGGSAWSHPQFEKSSGENLYFQGMGTALDIKIKRANKVYHAGEVLSGVVVISSKDSVQHQGVSLTMEG TVNLQLSAKSVGVFEAFYNSVKPIQIINSTIEMVKPGKFPSGKTEIPFEFPLHLKGNKVLYETYHGVFVNIQYTLRCDMKRSLLAKDLT KTCEFIVHSAPQKGKFTPSPVDFTITPETLQNVKERALLPKFLLRGHLNSTNCVITQPLTGELVVESSEAAIRSVELQLVRVETCGCAE GYARDATEIQNIQIADGDVCRGLSVPIYMVFPRLFTCPTLETTNFKVEFEVNIVVLLHPDHLITENFPLKLCRI MLVLVLGDLHIPHRCNSLPAKFKKLLVPGKIQHILCTGNLCTKESYDYLKTLAGDVHIVRGDFDENLNYPEQKVVTVGQFKIGLIHGH QVIPWGDMASLALLQRQFDVDILISGHTHKFEAFEHENKFYINPGSATGAYNALETNIIPSFVLMDIQASTVVTYVYQLIGDDVKVERI EYKKP
120	> His-TEV-VPS35L-Twin-Strep-TEV-VPS26C-VPS29-mKate2 MGSSHHHHHHSSGENLYFQGMAVFPWHSRNRNYKAEFASCRLEAVPLEFGDYHPLKPITVTESKTKKVNRKGSTSSTSSSSSSSVVD PLSSVLDGTDPLSMFAATADPAALAAAMDSSRRKRDRDDNSVVGSDFEPWTNKRGEILARYTTTEKLSINLFMGSEKGKAGTATLA MSEKVRTRLEELDDFEEGSQKELLNLTQQDYVNRIEELNQSLKDAWASDQKVKALKIVIQCSKLLSDTSVIQFYPSKFVLITDILDTFG KLVYERIFSMCVDSRSVLPDHFSPENANDTAKETCLNWFFKIASIRELIPRFYVEASILKCNKFLSKTGISECLPRLTCMIRGIGDPLVSV YARAYLCRVGMEVAPHLKETLNKNFFDFLLTFKQIHGDTVQNQLVVQGVELPSYLPLYPPAMDWIFQCISYHAPEALLTEMMERCK

	KLGNNALLLNSVMSAFRAEFIATRSMDFIGMIKECDESGFPKHLLFRSLGLNLALADPPESDRLQILNEAWKVITKLKNPQDYINCAE VWVEYTCKHFTKREVNTVLADVIKHMTPDRAFEDSYPQLQLIIKKVIAHFHDFSVLFSVEKFLPFLDMFQKESVRVEVCKCIMDAFIK HQQEPTKDPVILNALLHVCKTMHDSVNALTLEDEKRMLSYLINGFIKMVSFGRDFEQQLSFYVESRSMFCNLEPVLVQLIHSVNRLA METRKVMKGNHSRKTAAFVRACVAYCFITIPSLAGIFTRLNLYLHSGQVALANQCLSQADAFFKAAISLVPEVPKMINIDGKMRPSES FLLEFLCNFFSTLLIVPDHPEHGVLFLVRELLNVIQDYTWEDNSDEKIRIYTCVLHLLSAMSQETYLYHIDKVDSNDSLYGGDSKFLAE NNKLCETVMAQILEHLKTLAKDEALKRQSSLGLSFFNSILAHGDLRNNKLNQLSVNLWHLAQRHGCADTRTMVKTLEYIKKQSKQP DMTHLTELALRLPLQTRT MASWSHPQFEKGGGSGGGSGGSAWSHPQFEKSSGENLYFQGMGTALDIKIKRANKVYHAGEVLSGVVVISSKDSVQHQGVSLTMEG TVNLQLSAKSVGVFEAFYNSVKPIQIINSTIEMVKPGKFPSGKTEIPFEFPLHLKGNKVLYETYHGVFVNIQYTLRCDMKRSLLAKDLT KTCEFIVHSAPQKGKFTPSPVDFTITPETLQNVKERALLPKFLLRGHLNSTNCVITQPLTGELVVESSEAAIRSVELQLVRVETCGCAE GYARDATEIQNIQIADGDVCRGLSVPIYMVFPRLFTCPTLETTNFKVEFEVNIVVLLHPDHLITENFPLKLCRI MLVLVLGDLHIPHRCNSLPAKFKKLLVPGKIQHILCTGNLCTKESYDYLKTLAGDVHIVRGDFDENLNYPEQKVVTVGQFKIGLIHGH QVIPWGDMASLALLQRQFDVDILISGHTHKFEAFEHENKFYINPGSATGAYNALETNIIPSFVLMDIQASTVVTYVYQLIGDDVKVERI EYKKPGGGGSSMVSELIKENMHMKLYMEGTVNNHHFKCTSEGEGKPYEGTQTMRIKAVEGGPLPFAFDILATSFMYGSKTFINHTQ GIPDFFKQSFPEGFTWERVTTYEDGGVLTATQDTSLQDGCLIYNVKIRGVNFPSNGPVMQKKTLGWEASTETLYPADGGLEGRADM ALKLVGGGHLICNLKTTYRSKKPAKNLKMPGVYYVDRRLERIKEADKETYVEQHEVAVARYCDLPSKLGHR
101	> His-NusA-His-HRV3C-DENND10 MGSSHHHHHHSSMNKEILAVVEAVSNEKALPREKIFEALESALATATKKKYEQEIDVRVQIDRKSGDFDTFRRWLVVDEVTQPTKEI TLEAARYEDESLNLGDYVEDQIESVTFDRITTQTAKQVIVQKVREAERAMVVDQFREHEGEIITGVVKKVNRDNISLDLGNNAEAVIL REDMLPRENFRPGDRVRGVLYSVRPEARGAQLFVTRSKPEMLIELFRIEVPEIGEEVIEIKAAARDPGSRAKIAVKTNDKRIDPVGACV GMRGARVQAVSTELGGERIDIVLWDDNPAQFVINAMAPADVASIVVDEDKHTMDIAVEAGNLAQAIGRNGQNVRLASQLSGWELN VMTVDDLQAKHQAEAHAAIDTFTKYLDIDEDFATVLVEEGFSTLEELAYVPMKELLEIEGLDEPTVEALRERAKNALATIAQAQEES LGDNKPADDLLNLEGVDRDLAFKLAARGVCTLEDLAEQGIDDLADIEGLTDEKAGALIMAARNICWFGDEATSGSGHHHHHHSAAL EVLFQGPMAAAEVADTQLMLGVGLIEKDTNGEVLWVWCYPSTTATLRNLLLRKCCLTDENKLLHPFVFGQYRRTWFYITTIEVPDS SILKKVTHFSIVLTAKDFNPEKYAAFTRILCRMYLKHGSPVKMMESYIAVLTKGICQSEENGSFLSKDFDARKAYLAGSIKDIVSQFGM ETVILHTALMLKKRIVVYHPKIEAVQEFTRTLPALVWHRQDWTILHSYVHLNADELEALQMCTGYVAGFVDLEVSNRPDLYDVFVN LAESEITIAPLAKEAMAMGKLHKEMGQLIVQSAEDPEKSESHVIQDIALKTREIFTNLAPFSEVSADGEKRVLNLEALKQKRFPPATE NFLYHLAAAEQMLKI
8	> His-TEV MGSSHHHHHHGGGESLFKGPRDYNPISSTICHLTNESDGHTTSLYGIGFGPFIITNKHLFRRNNGTLVVQSLHGVFKVKNTTTLQQHL IDGRDMIIIRMPKDFPPFPQKLKFREPQREERICLVTTNFQTKSMSSMVSDTSCTFPSGDGIFWKHWIQTKDGQCGSPLVSTRDGFIV GIHSASNFTNTNNYFTSVPKNFMELLTNQEAQQWVSGWRLNADSVLWGGHKVFMVKPEEPFQPVKEATQLMNELVYSQ
9	> His-Senp2 MGSSHHHHHHSSGLVPRGSHMASDLLELTEDMEKEISNALGHGPQDEILSSAFKLRITRGDIQTLKNYHWLNDEVINFYMNLLVER NKKQGYPALHVFSTFFYPKLKSGGYQAVKRWTKGVNLFEQEIILVPIHRKVHWSLVVIDLRKKCLKYLDSMGQKGHRICEILLQYLQD ESKTKRNSDLNLLEWTHHSMKPHEIPQQLNGSDCGMFTCKYADYISRDKPITFTQHQMPLFRKKMVWEILHQQLL
10	> GST-PreScission MSPILGYWKIKGLVQPTRLLLEYLEEKYEEHLYERDEGDKWRNKKFELGLEFPNLPYYIDGDVKLTQSMAIIRYIADKHNMLGGCPK ERAEISMLEGAVLDIRYGVSRIAYSKDFETLKVDFLSKLPEMLKMFEDRLCHKTYLNGDHVTHPDFMLYDALDVVLYMDPMCLDAF PKLVCFKKRIEAIPQIDKYLKSSKYIAWPLQGWQATFGGGDHPPKSDLVPRGSPEVPRGPNTEFALSLLRKNIMTITTSKGEFTGLGIH DRVCVIPTHAQPGDDVLVNGQKIRVKDKYKLVDPENINLELTVLTLDRNEKFRDIRGFISEDLEGVDATLVVHSNNFTNTILEVGPVT MAGLINLSSTPTNRMIRYDYATKTGQCGGVLCATGKIFGIHVGGNGRQGFSAQLKKQYFVEKQ

Table 13. SAXS data of DENND10.

	DENND10
Data collection parameters	
Instrument	B21 (Diamond Light Source, United Kingdom)
Buffer	50 mM Tris pH 7.5, 200 mM NaCl, 1 mM TCEP
Beam size at sample (mm)	1.10 x 0.24
Wavelength (Å)	0.954
q range ($Å^{-1}$)	0.0045 - 0.34
Exposure Time (s/frame)	3.000
Exposure Temperature (ºC)	15.000
Concentration used in gel filtration chromatography (mg/ml)	5.0
Structural Parameters	
Forward scattering intensity *[I*(0)] (from Guinier)	0.021
Forward scattering intensity [*I*(0)] [from *P*(r)]	0.021
R_g (Å) [from Guinier)	24.330
R_g (Å) [from *P*(r)]	24.620
D_{max} (Å)	92.00
Porod Volume estimate ($Å^3$) [from *P*(r)]	79,885.402
Porod Volume estimate corrected ($Å^3$) [from *P*(r)]	50,287.801
c^2 [from *P*(r)]	1.053
Total estimate [from *P*(r)]	0.816
Molecular weight determination (kDa)	
Theoretical molecular weight	40.667
From volume of correlation (V_c)	37.562
From Bayesian assessment [credibility interval], probability	39.350 [46.5,40.65], 97.9
From Shape&Size assessment	40.084
From Porod volume assessment	41.739
Software employed	
Data processing	BioXSTAS RAW 2.2.1
Ab initio (analysis)	ATSAS-3.2.0
Validation, averaging and final refinement	GASBOR
3D structure prediction	AlphaFold2
Computation of model intensities	CRYSOL
3D graphics representations	UCSF ChimeraX

Chapter 4: RESULTS

4.1. Characterization of the structural organization of the Retriever complex

4.1.1. Purification of VPS26C, VPS29 and VPS35L proteins

To characterize the structure of the Retriever complex, the initial focus was placed on purifying its individual subunits and the complete complex. This crucial step was undertaken to facilitate subsequent structural studies, enabling the acquisition of high-quality samples for further analysis, including crystallography and cryo-electron microscopy. By isolating each component, a better understanding of their interactions and how they assemble to form the functional complex was sought.

The Retriever complex subunits VPS26C and VPS29 were overexpressed in bacteria and purified by affinity chromatography (using a His-tag for VPS26C and a GST-tag for VPS29), followed by removal of the affinity tags, ion exchange chromatography, and gel filtration chromatography (**Figure 10**).

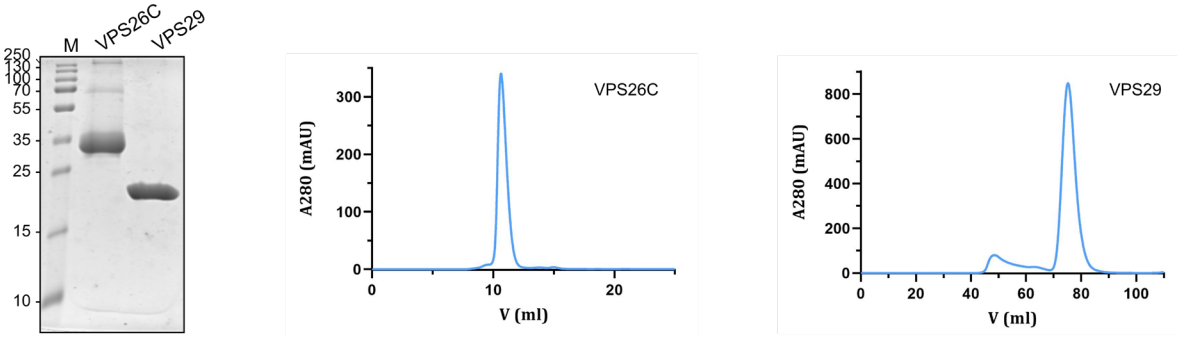

Figure 10. Purification of VPS26C and VPS29 subunits. VPS26C (33.1 kDa), and VPS29 (20.8 kDa) were successfully overexpressed and purified, as indicated by a single peak in the gel filtration chromatogram and confirmed in the corresponding SDS-PAGE gel. *M*, protein marker.

By contrast, despite numerous attempts, the VPS35L subunit could not be purified using bacteria as the expression system. To improve VPS35L solubility, several genetically modified bacterial strains designed for enhanced human protein expression, such as BL21(DE3) pLysS, Rosetta, C41, C43, and Origami, were tested, along with different protein tags (His-Sumo3, GST, Strep, His-MBP, His-TRX, His-Zbasic). Nevertheless, soluble protein was not obtained. Additionally, several VPS35L truncation constructs were tested (**Figure 11A,B**), with the goal of mapping the interacting regions of VPS35L fragments with the other subunits of the complex and potentially performing crystallization trials, but no satisfactory results were achieved (**Figure 11C**). A synthetic *VPS35L* gene with codons optimized for bacterial expression was also ordered, but bacterial overexpression of VPS35L continued to fail. The protein was only observed in the insoluble fraction after cell lysis, likely because it requires specific chaperons or post-translational

modifications that bacteria cannot provide. Lastly, we attempted overexpression of VPS35L in insect cells, which can offer advantages over bacterial cells for expressing human proteins, as insect cells provide post-translational modifications, such as glycosylation and protein folding machinery, that are more similar to those in human cells. The strains used were Sf21 and HighFive™. However, no soluble protein was obtained from these trials either. Therefore, we conclude that VPS35L cannot be purified alone, either in bacteria or insect cells, as it is unstable in the absence of the other complex subunits.

In the previuosly mentioned VPS35L truncation analysis, we removed the first 109 residues based on the structural predictions from the Robetta server (Baek et al., 2021), which indicated that this region is disordered. The remaining residues (110-963) were predicted to form HEAT-repeats, composed of repetitive arrays of short amphiphilic α-helices. We dissected the protein into two major regions based on its homology to Retromer's crystallized VPS35 domains: the N-terminal region, which is responsible for VPS26 binding in Retromer (residues 110-578 or 110-598; differing by an α-helix), and the C-terminal region (residues 579-963 or 599-963), which corresponds to the VPS35-VPS29 binding region. Of all the constructs, only VPS35L$_{1-169}$ and VPS35L$_{1-222}$ were soluble, but this small region of the protein precipitated after tag removal, so purification could not be accomplished (**Figure 11C**).

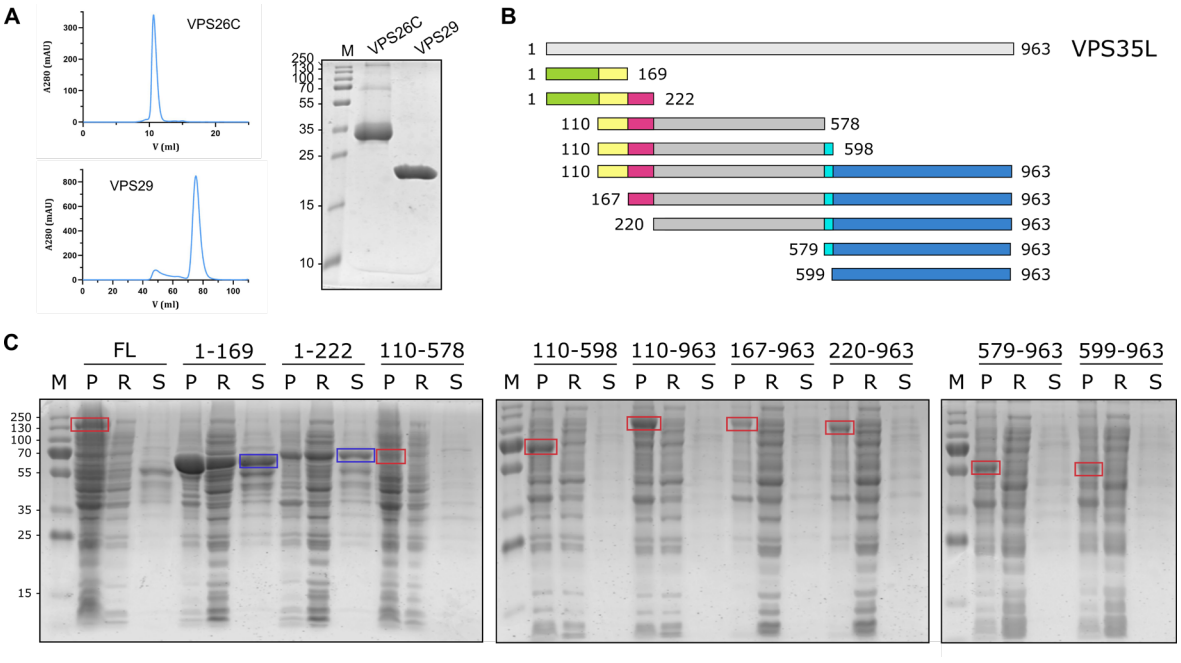

Figure 11. Purification of VPS35L constructs. (**A**) VPS35L structural model obtained using Robetta server, shown in cartoon representation. The colors in the structure correspond to the following: green represents disordered regions; yellow and magenta indicate α-helices with varying degrees of disorder; gray represents the region equivalent to the crystallized N-terminus from VPS35; cyan shows intermediate α-helices between domains; and blue represents the region equivalent to the C-terminal region of VPS35. (**B**) VPS35L was

dissected into different regions to remove potentially disordered regions, with the same coloring scheme as in A. (**C**) Purification tests of the constructs. The tested constructs include: His-MBP-TEV-VPS35L$_{FL}$ (154.2 kDa), His-MBP-TEV-VPS35L$_{1-169}$ (63.2 kDa), His-MBP-TEV-VPS35L$_{1-222}$ (69.2 kDa), His-TrxA-TEV-VPS35L$_{110-578}$ (68.2 kDa), His-TrxA-TEV-VPS35L$_{110-598}$ (70.5 kDa), His-TrxA-TEV-VPS35L$_{110-963}$ (112.1 kDa), His-TrxA-TEV-VPS35L$_{167-963}$ (105.8 kDa), His-TrxA-TEV-VPS35L$_{220-963}$ (99.7 kDa), His-TrxA-TEV-VPS35L$_{579-963}$ (58.3 kDa), His-TrxA-TEV-VPS35L$_{599-963}$ (56.0 kDa). *M*, protein marker; *P*, pellet; *S*, supernatant; *R*, resin; *FL*, full-length.

4.1.2. Purification of the Retriever complex

Since the VPS35L protein requires the binding of the other Retriever subunits for proper folding, attempts to co-express VPS35L with VPS26C or VPS29 in bacteria were performed. However, while soluble VPS29 or VPS26C were obtained, VPS35L either was not overexpressed or remained in the insoluble fraction. Therefore, overexpression and purification trials of the entire Retriever complex (VPS26C, VPS35L and VPS29) were conducted in insect cells. This strategy was successful, resulting in the purification of the human Retriever complex as a stable assembly of all three proteins in a 1:1:1 stoichiometry (**Figure 12A**). This result indicates that the association of VPS35L with either VPS26C or VPS29 is necessary to maintain the structural integrity of VPS35L in solution. One litre of HighFive^{TM} insect cells was infected with a baculovirus encoding all three proteins (Twin-Strep-TEV-VPS26C, VPS29 and His-TEV-VPS35L). Cells were harvested, lysed, and the cleared lysates were purified by affinity chromatography (using His- and Twin-Strep-tags), followed by removal of the affinity tags with TEV protease, reverse affinity chromatography (with Ni-INDIGO resin), and gel filtration on a Superdex 200 size-exclusion column. Gel filtration chromatography revealed two distinct peaks: the first corresponding to a dimer of Retriever (a minor population) and the second to a monomer of Retriever (the major population). This dual oligomeric state is also observed in the Retromer complex (Lucas et al., 2016). Additionally, Retriever was purified with a GST tag for GST pull-down assays (**Figure 12B**). The yield of Retriever purification is approximately 2 mg per liter of culture.

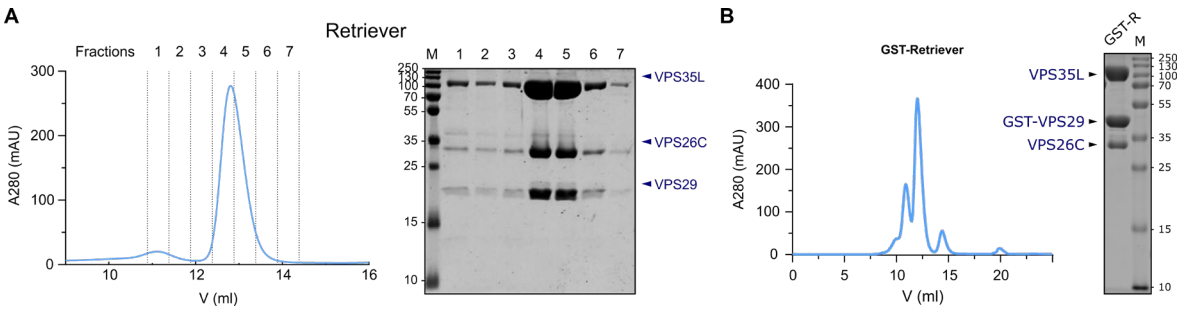

Figure 12. Purification of Retriever complex. (**A**) Purification of the VPS35L:VPS26C:VPS29 complex. The three proteins comprising the complex are visualized on an SDS-PAGE gel. The Superdex 200 Increase 10/300 gel filtration chromatogram shows two peaks, representing the dimeric form (first peak) and to the monomeric form (second peak) of the complex, both containing all three proteins. (**B**) Purification of the Retriever complex with GST tag. The first peak of the chromatogram corresponds to a dimer of the GST-Retriever complex, present in a higher proportion compared to the purification of Retriever alone (**A**). This increased proportion could be attributed to the inherent tendency of GST to dimerize. VPS35L (109.6 kDa), VPS26C (33.1 kDa), VPS29 (20.9 kDa), GST-VPS29 (47.1 kDa). *M*, Protein marker; *R*, Retriever.

4.1.3. Study of Retriever subunits interactions

To investigate the interactions among Retriever subunits and determine if they resemble those within the Retromer complex, the interaction between the two Retriever subunits that can be purified individually, VPS26C and VPS29, was first analysed. As expected, based on their similarity to Retromer and the predicted structural model of the complex, no interaction was observed in gel filtration analysis (**Figure 13**). This result suggests that complex formation is mediated by VPS35L, which likely acts as the anchor point between VPS26C and VPS29.

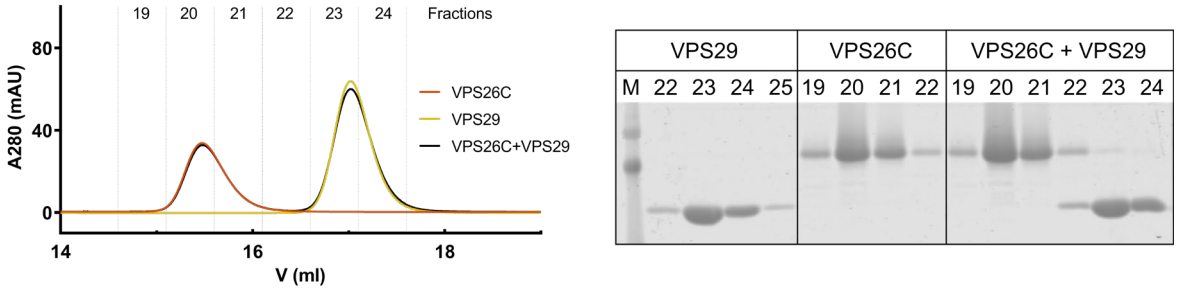

Figure 13. Analysis of the interaction between VPS26C and VPS29. Samples of 100 µM VPS26C, 100 µM VPS29, and a mixture of 100 µM VPS26C + 100 µM VPS29 were analyzed by gel filtration chromatography in Superdex 200 Increase 10/300. VPS26C precipitates during sample preparation when boiled, resulting in a diffuse band on the SDS-PAGE gel. *M*, Protein marker.

Further analysis of subunit interactions could not be performed because isolated VPS35L could not be purified. Therefore, to investigate the Retriever assembly mechanism purifying specific VPS35L truncation constructs were purified in combination with VPS26C and VPS29. The isolation of stable complexes allowed us to map the interacting regions of the subunits (**Figure 14A,B**). All VPS35L fragments tested ($VPS35L_{1-436}$, $VPS35L_{1-598}$, $VPS35L_{110-598}$, and $VPS35L_{110-963}$) showed binding to VPS26C, indicating that the VPS26C-binding region in VPS35L is restricted to residues 110-436. However, VPS29 was not retained in any of the constructs except for the full-length protein.

Deletion of either the first 110 residues or the last 365 residues abolished VPS29 binding. These results indicate that stable VPS29 binding to VPS35L differs from that in Retromer, where VPS29 only interacts with the C-terminal region of VPS35. In contrast, VPS35L contains two cooperative regions to bind VPS29: one within the first 110 residues and another between residues 598-963 (**Figure 14C**).

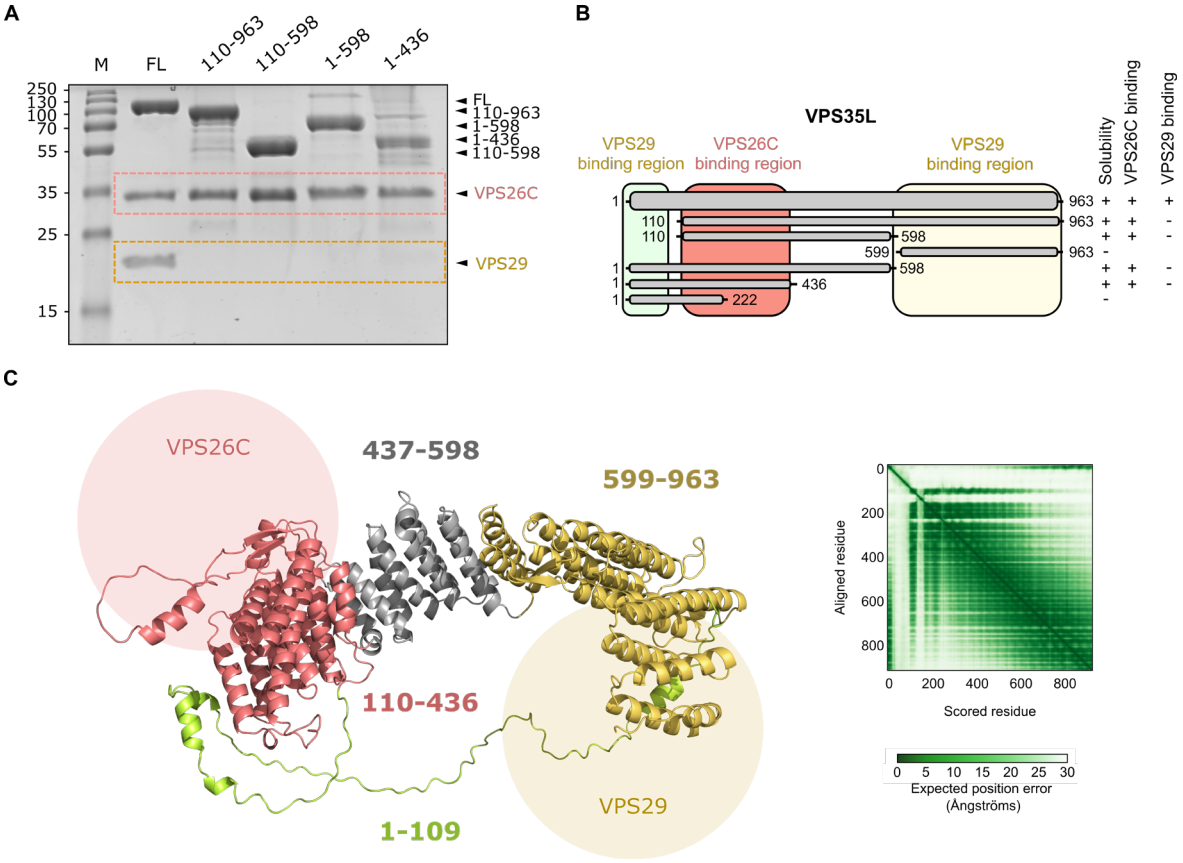

Figure 14. Analysis of the interactions between the Retriever subunits. (**A**) Coomassie-stained SDS-PAGE gel showing the purified Retriever complex using various VPS35L truncations. VPS35L (109.6 kDa), $VPS35L_{110-963}$ (97.8 kDa), $VPS35L_{1-598}$ (68.0 kDa), $VPS35L_{1-436}$ (49.1 kDa), $VPS35L_{110-598}$ (58.4 kDa), VPS26C (33.1 kDa), VPS29 (20.8 kDa). *M*, Protein marker; *FL*, Full length. (**B**) Schematic diagram illustrating the regions of VPS35L that bind to VPS26C and VPS29 as determined experimentally. (**C**) VPS35L structural model obtained from the AlphaFold2 (AF2) server, with regions of interest highlighted: the VPS26C binding region (residues 110-436) is shown in red, while the VPS29 binding regions (residues 599-963 and residues 1-109) are depicted in yellow and green, respectively. The Predicted Aligned Error (PAE) plot of the AF2 model is also shown.

The AlphaFold model of the Retriever complex suggests that the first 10 residues of VPS35L interact with its C-terminal region explaining that the N-terminal and C-terminal regions of VPS35L are in proximity and cover the VPS29 binding surface. Interestingly, this structural feature is likely conserved across known VPS35L orthologs, as VPS35L AlphaFold models for *Mus musculus*,

Gallus gallus, *Danio rerio*, *Drosophila melanogaster,* and *Nematostella vectensis* also display this intramolecular interaction (**Figure 15**). Among the available protein structure prediction softwares, AlphaFold AI system was used in this thesis due to its proven higher accuracy (Jumper et al., 2021).

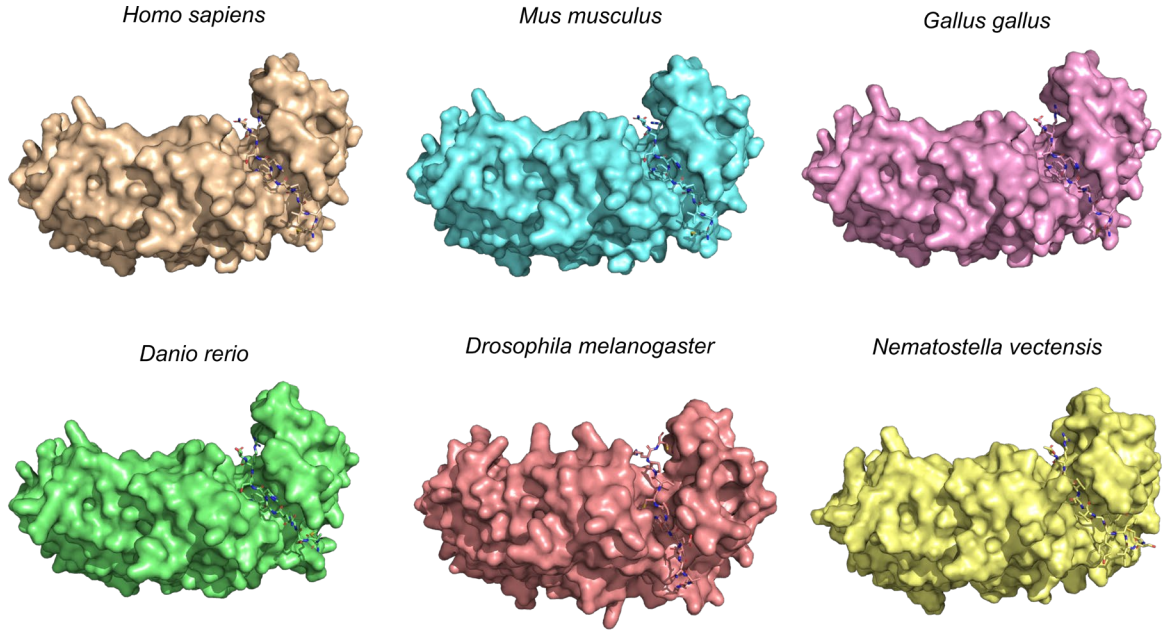

Figure 15. Structural conservation of VPS35L models in different species. Comparison of VPS35L models from different species demonstrates that the first 10 residues (shown as sticks) consistently interact with the C-terminal region of VPS35L (shown as surface) across all species, supporting a conserved binding mechanism.

4.1.4. Crystallization of the Retriever complex and the VPS26C subunit

To elucidate the molecular details of the Retriever complex, X-ray crystallography was used. X-ray crystallography is a powerful analytical technique widely used in structural biology to determine the atomic and molecular structure of a crystal. The process involves directing X-ray beams at a crystallized sample, which diffract the X-rays into specific patterns. By analyzing these diffraction patterns, detailed three-dimensional models of the structure of molecules can be constructed. This technique has been instrumental in elucidating the structures of complex biological macromolecules, thereby providing valuable insights into their function and interactions.

To grow into a protein crystal suitable for X-ray crystallography, the protein must be highly pure to ensure that it is homogeneous and free of contaminants, and it should be stable and properly folded. The crystallization process itself requires finding the right conditions, including appropriate temperature, pH, and concentration of the protein and precipitating agents. The formation of crystals often depends on the ability of the protein to self-associate into a regular, repeating lattice structure.

Achieving these conditions often involves extensive screening of various conditions and careful optimization.

At the time I attempted to achieve this objective, the atomic structure of the Retriever complex was still unknown. Rod-shaped crystals of the complex were obtained using the JCSG-plus™ HT-96 Crystal Screen (Molecular Dimensions) (**Figure 16A,B**). Although the reproduction of these crystals was successful, their quality only slightly improved after extensive refinement trials (**Figure 16C,D**). X-ray diffraction was performed on the crystals at the ALBA synchrotron, but the diffraction quality was too low to solve the structure.

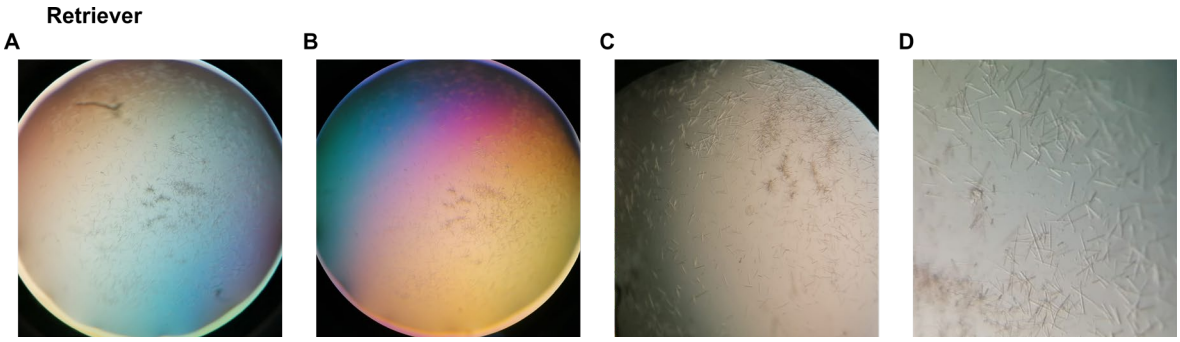

Figure 16. Protein crystals of the Retriever complex. (**A-D**) Various images of the rod-shaped crystals of the Retriever complex. Crystals were grown using two different protein-to-precipitant ratios, where 0.5 µl of the protein complex at either at 3 mg/ml or 5 mg/ml was mixed with either 0.5 or 1 µl of precipitant. The Retriever complex was prepared in a buffer composed by 25 mM Hepes pH 7.5, 300 mM NaCl, and 1 mM TCEP, supplemented with 10% glycerol. The initial screening condition used was 1.1 M sodium malonate dibasic monohydrate, 0.1 M Hepes pH 7.0, and 0.5% v/v Jeffamine® ED-2003 from the JCSG-plus™ HT-96 Crystal Screen (Molecular Dimensions). Based on this initial condition, increasing the pH to 7.5 and the Jeffamine® ED-2003 concentration to 0.8% produced the best crystals, with a protein concentration of 5 mg/ml (**C** and **D**).

Additional protein crystallization attempts were made with individual subunits of the complex. Since VPS35L could not be purified in isolation and the structure of VPS29 was already known from Retromer studies (PDB ID: 1W24, from Wang et al., 2005, and PDB ID: 2R17, from Hierro et al., 2007), the most promising candidate for crystallization was VPS26C. Circular quasi-crystals of VPS26C, (**Figure 18A**) were successfully grown using the Stura Footprint Screen™ + MacroSol™ HT-96 (Molecular Dimensions).

Quasi-crystals typically exhibit a more complex, aperiodic atomic arrangement, meaning they do not exhibit the same kind of repeating structure over long distances, though they still show some order (Hargittai, 2010). As a result, they are likely to exhibit weaker diffraction patterns because their atomic structure lacks the regular periodicity found in typical crystals. For this reason, attempts to improve these circular quasi-crystals of VPS26C to obtain more highly ordered, "more refractive"

crystals were undertaken. However, neither changes in protein-to-precipitant ratios nor alterations in the concentrations of the screening condition components induced any significant shape changes in the crystals.

In an attempt to improve protein stability and solubility, which are known to be key factors in increasing the success rate of crystal formation (Vedadi et al., 2006), various compounds that could potentially stabilize our proteins of interest were investigated. For this purpose, a temperature-based assay, called Thermal Shift Assay, developed by Pantoliano *et al.* to determine melting temperatures (Tm) was carried out (Pantoliano et al., 2001). The technique detects changes in the Tm, which corresponds to the temperature at which half of the sample protein is denatured. This thermal scanning method revealed certain compounds that increased the melting temperature of VPS26C by at least 1 ºC, such as 100 mM and 200 mM lithium sulphate, 6% glycerol, 3.5% meso-erythritol, 4% xylitol, 1.5%, 3%, and 6% D-glucose, 6% sucrose, 5% D-trehalose, and 2% and 4% PEG 400 (**Figure 17**). Specifically, 200 mM lithium sulphate and 3% D-glucose increased the melting temperature by more than 2 ºC.

Interestingly, the data showed that although increasing the concentration of a beneficial compound generally has a proportional effect on thermal stability (i.e., the greater the concentration, the higher the Tm), some compounds exhibited a threshold effect. Beyond this threshold, the compound became detrimental. For example, 3% D-glucose had a more positive effect on Tm than either 1.5% or 6%, and while 4% PEG 400 was beneficial, 8% PEG 400 no longer had a stabilizing effect on VPS26C.

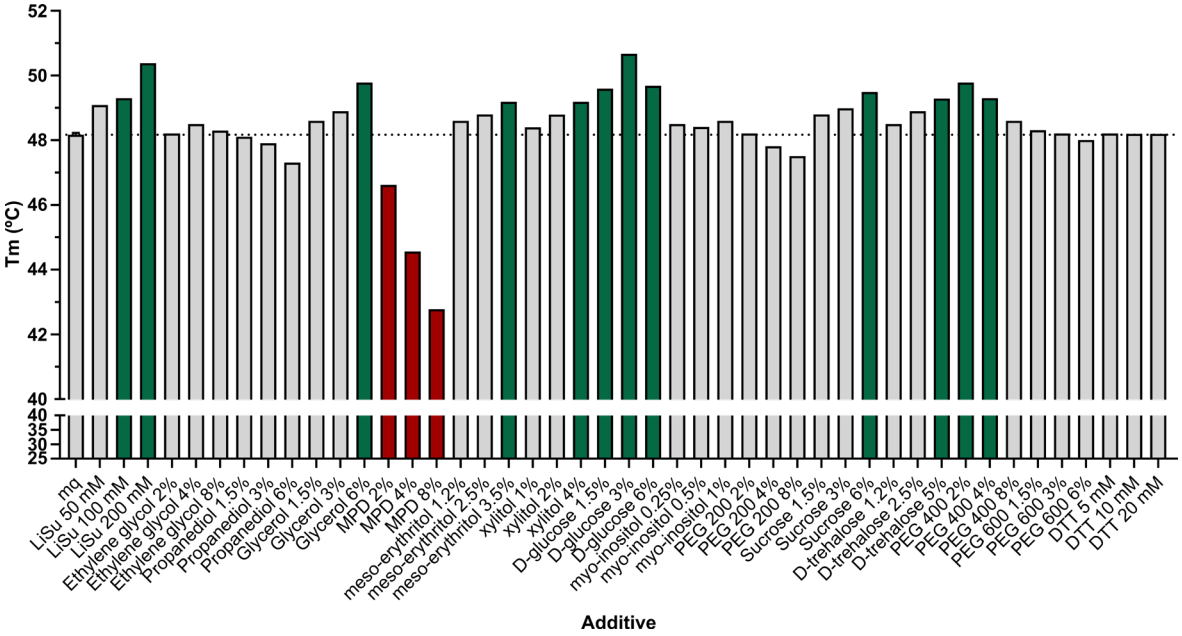

Figure 17. Effect of different compounds on the thermal stability of VPS26C. The graph shows the melting temperature of VPS26C obtained from melting curves after supplementation with various additives. The final

concentration of each additive in the protein sample is indicated. The starting temperature was set to 25 ºC, each step was increased by 0.5 ºC, while fluorescence was monitored in real time using a qPCR machine. The control condition (mq) was replicated three times. Conditions that show an increase in Tm of at least 1 ºC are highlighted in green, those where the Tm worsened by ≤ 1 ºC are marked in red, and conditions that resulted in no change in temperature (within 1 unit) are colored grey. mq, Milli-Q water; *LiSu*, lithium sulphate; *MPD*, 2-Methyl-2,4-pentanediol; *PEG*, Polyethylene glycol; *DTT*, Dithiothreitol.

Using the initial screening condition that induced VPS26C quasi-crystal growth, a refinement plate was prepared by adding each of the potential protein stabilizers analyzed in the temperature-based assay. Several additives facilitated crystal formation: 50 mM lithium sulphate, 8% ethylene glycol, 3% propanediol, 2% and 4% PEG 200, 1.5% sucrose, 1.2% and 2.5% D-trehalose, and 1.5%, 3%, and 6% PEG 600. While some of these compounds that promoted crystal growth were shown to increase the thermal stability of VPS26C (**Figure 17**), others did not appear to be beneficial. Although several additives, such as 50 mM lithium sulphate (**Figure 18B,C**) or 3% propanediol (**Figure 18D**), led to an increase in crystal size, these quasi-crystals did not diffract, and efforts to alter their shape were unsuccessful.

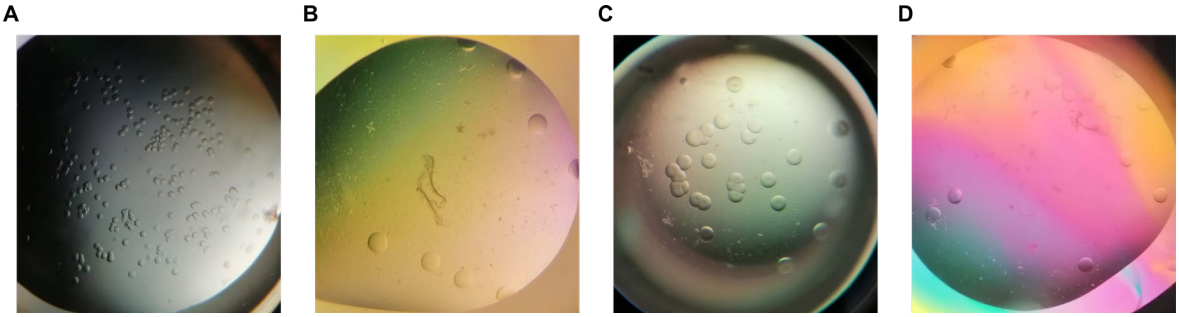

Figure 18. Protein crystals of the VPS26C subunit. (**A-D**) Images of VPS26C spherulites. The concentration of VPS26C was 5.3 mg/ml or 6.3 mg/ml, and the buffer was 25 mM Hepes pH 7.5, 150 mM NaCl, and 1 mM TCEP. Crystals were grown in 15% PEG 4000 and 0.2 M imidazole malate pH 7.0, using the Stura Footprint Screen™ + MacroSol™ HT-96 (Molecular Dimensions). The addition of 50 mM lithium sulphate (**B** and **C**), or propanediol (**D**) slightly improved crystal quality, as indicated by the increased crystal size, compared to when no additive was added (**A**).

4.1.5. Structural resolution of Retriever complex by cryo-electron microscopy (cryo-EM)

As obtaining the 3D-structure of Retriever by X-ray crystallography proved to be challenging and required a substantial amount of protein, an alternative approach, cryo-electron microscopy, was pursued. Cryo-electron microscopy is a powerful imaging technique that allows for the high-resolution visualization of biological macromolecules and complexes in their native states. By rapidly freezing samples to cryogenic temperatures, cryo-EM preserves their structural integrity and minimizes radiation damage, enabling detailed observation of their three-dimensional structures. The technique involves collecting a series of two-dimensional projection images from different angles and then reconstructing these images into a three-dimensional model using advanced computational algorithms. Cryo-EM has revolutionized structural biology by providing insights into the architecture of complex biological systems, including proteins, nucleic acids, and virus particles, with unprecedented clarity (Carroni & Saibil, 2016).

In this technique, the vitrification process is crucial for preserving the sample in a near-native, unstained state at cryogenic temperatures. Optimizing vitrification involves several parameters to consider for achieving high-quality specimen preparation: sample concentration, grid type, blotting conditions, and temperature and humidity control. Preliminary vitrification tests with Retriever samples at various concentrations determined that the optimal concentration was 1.5 µM. Quantifoil Holey Carbon R2/2 Mesh 300 copper grids were glow-discharged for 40 seconds at 8.6 mA before applying 4 µl of the protein sample. The grids were then plunge-frozen in liquid ethane using a Vitrobot System, with a chamber humidity of 75-85% at 16°C. The sample was incubated on the grids for 15 seconds before the grids were blotted for 2 seconds.

With the assistance of our collaborators at the Electron Microscopy Platform at CIC bioGUNE (Basque Country, Spain), we collected a dataset of micrographs and performed preliminary 2D classification of the Retriever complex. In this process, 22,971 particles were classified into 30 different classes, and 15,134 particles from 5 classes were selected for further analysis. After 4 consecutive rounds of 2D classification, 9 classes were chosen for 3D classification. An initial 3D model was generated from the last set of 2D selected particles using Relion (Zivanov et al., 2018). However, due to the flexibility of the complex and its multiple conformations, additional particles were required to produce more robust classes (**Figure 19A-C**).

Additionally, grids of the Retriever complex with an MBP tag on VPS29 were prepared at 2 µM, resulting in micrographs with enhanced contrast (**Figure 19D**). This increase in contrast significantly improved the signal-to-noise ratio, which is crucial for image processing (Palovcak et

al., 2020). The micrographs were of sufficient quality to apply for access to the Titan Krios cryo-electron microscope at Diamond Light Source (Didcot, United Kingdom).

While this thesis was in progress, the structure of the Retriever complex solved by cryo-electron microscopy was published by three different groups, at both low (Healy et al., 2023 and Laulumaa et al., 2024) and high resolution (Boesch et al., 2024). Additionally, the structure of VPS29:VPS35L$_{peptide}$ was solved by X-ray crystallography at 1.35 Å resolution (PDB ID: 8ESE) (Healy et al., 2023). These studies faced issues with preferential orientation and required numerous attempts to improve the quality of the micrographs. As a result, we decided to discontinue our cryo-electron microscopy studies of the Retriever complex.

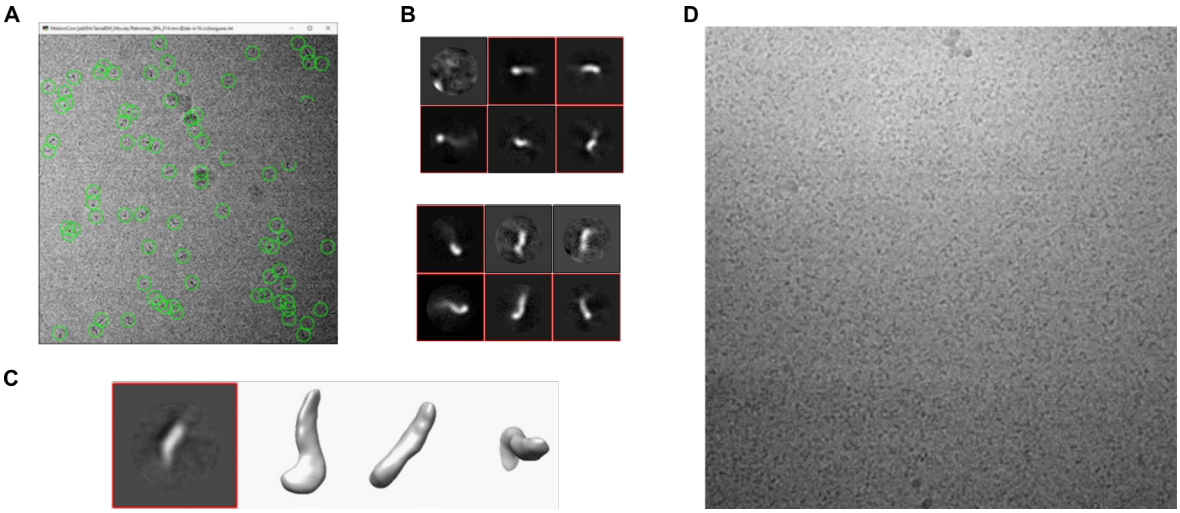

Figure 19. Single-particle analysis of the Retriever complex. (**A**) A representative electron micrograph showing particle picking from grids containing the Retriever complex, collected at the Electron Microscopy Platform at CIC bioGUNE. (**B**) Alignment and classification of different particle classes, with 9 selected for subsequent 3D classification. (**C**) An initial 3D model of the complex created from selected 2D particles. (**D**) A representative electron micrograph of the Retriever-MBP complex at 2 µM concentration.

As solving the atomic structure of the full-length Retriever complex was unsuccessful, we employed AlphaFold2-Multimer (AF2) to generate structural models of the entire Retriever complex (VPS26C:VPS35L:VPS29) (**Figure 20A**). The predicted model exhibits high overall confidence values, as indicated by the pLDDT (predicted local distance difference test) values. The first 113 residues of VPS35L show the lowest values, probably due to the high flexibility of this region. Additionally, residues 137 to 176, which compose a β-hairpin featuring a long turn that includes an α-helix, also display low pLDDT values. This region will be further examined in section 4.3. Alongside pLDDT values, PAE matrices play a significant role in interpreting structural models, as they provide valuable insights into the confidence level of the predictions. While PAE values are generally high, indicating that the positioning of each subunit relative to the others is likely correct,

there is a notable lack of confidence in the predicted position of the middle region of VPS35L concerning the remaining portions of the protein and other subunits of the complex. VPS35L is composed of HEAT repeats that confer high flexibility, allowing the protein to undergo significant conformational changes, which explains the variability in its relative positioning.

Additionally, the model aligns with our experimental data (**Figure 20B,C**): VPS26C is positioned within the N-terminal region of VPS35L, while VPS29 is located in a pocket formed by both the C-terminus and a loop comprised of the first 110 residues of VPS35L. The robustness of the predicted model enabled its use in subsequent structural analysis with high consistency. When the structure of the Retriever complex was experimentally solved at high resolution by Boesch *et al.* and Laulumaa *et al.* (Boesch et al., 2024; Laulumaa et al., 2024), a comparison of the three structures revealed significant similarity, despite of a slightly difference in the VPS26C position relative to VPS35L, confirming the high accuracy of the *in silico* model (**Figure 20D**). The model from Boesch *et al.* lacks the flexible linker region of the N-terminus in VPS35L that connects with the C-terminal domain.

Moreover, a sequence conservation analysis of the Retriever complex revealed that residues on the interacting surfaces are highly conserved across homologous proteins for the three subunits: VPS26C, VPS35L, and VPS29 (**Figure 21**). This analysis was performed using the ConSurf server (Yariv et al., 2023), which maps conservation scores onto the three-dimensional structure, providing more informative insights than sequence-based analysis alone. The analysis incorporated the sequence alignment of human VPS35L orthologs. Sequence conservation can highlight functionally important residues but is often intertwined with signals for maintaining structural stability (Cagiada et al., 2023). The high evolutionary conservation of these interfaces is likely crucial for functionality (i.e., interaction with other subunits of the complex) and contributes to the preservation of structural stability, as the three proteins demonstrate greater stability upon complex formation.

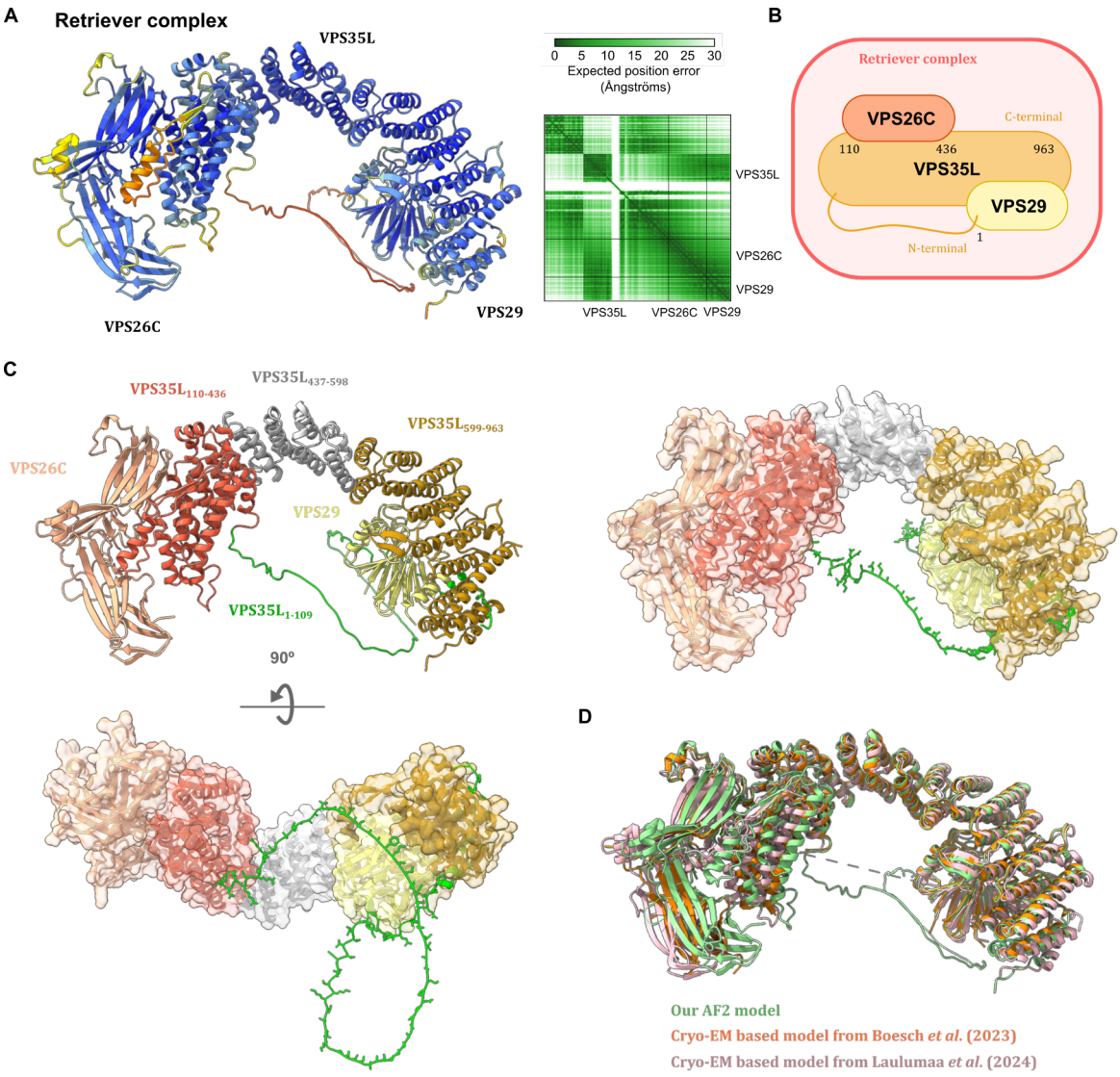

Figure 20. Model of the Retriever complex assembly. (**A**) Our AF2 model of the Retriever complex, colored according to the pLDDT confidence score (blue, very high confidence pLDDT ≥ 90; cyan, high confidence 70 ≤ pLDDT < 90; yellow, low confidence 50 ≤ pLDDT < 70; orange, very low confidence pLDDT < 50). The graph displays the corresponding PAE plot. *PAE*, predicted aligned error. (**B**) Diagram summarizing the interacting regions of the Retriever complex based on our experimental data. (**C**) AF2 model of the Retriever complex with experimentally observed interaction regions highlighted. The interaction region of VPS35L with VPS26C ($VPS35L_{110-436}$) is shown in red, the C-terminal interaction region of VPS35L with VPS29 ($VPS35L_{599-963}$) in dark yellow, and the N-terminal ($VPS35L_{1-109}$) in green, all depicted in cartoon representation. (Model Archive ID: ma-3cag5 (Boesch et al., 2024). In the first model, all subunits are represented in cartoon format, while in the following models, for clarity, VPS26C, VPS29, and $VPS35L_{111-963}$ are shown as ribbon diagrams with a transparent surface, while $VPS35L_{1-110}$ is displayed in stick representation. (**D**) Structural comparison between our AF2 model used for further experiments (in green), the AF2 model based on cryo-EM data from Boesch *et al.* (Boesch et al., 2024) (in orange), and the model from Laulumaa *et al.* (Laulumaa et al., 2024) (in pink). The models are highly similar, with the main core of each subunit in the same position and only subtle differences in the more mobile regions. Structural images were generated using ChimeraX.

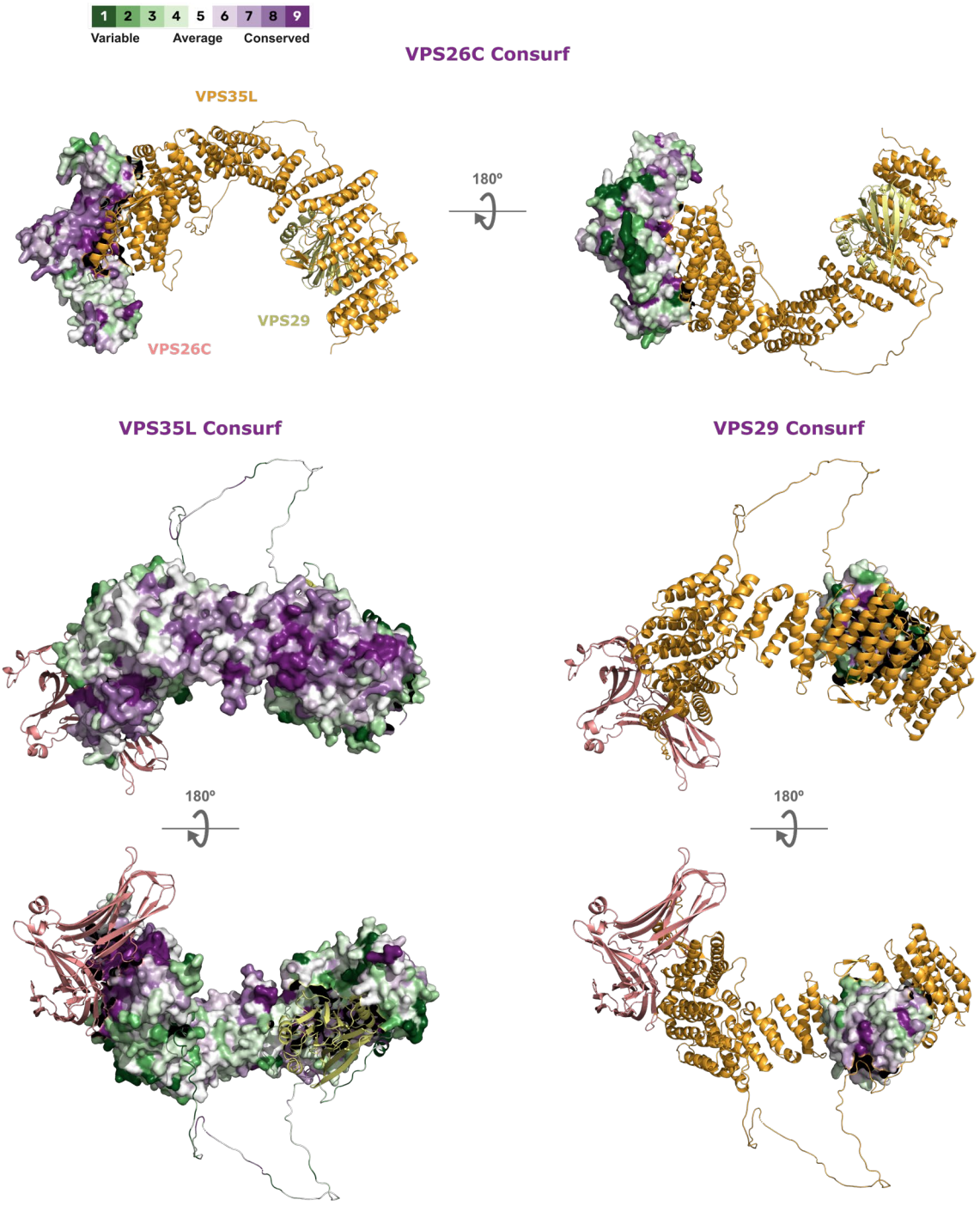

Figure 21. ConSurf analysis of the interacting regions between the Retriever subunits. The conservation of VPS26C, VPS35L and VPS29 is shown in surface representation, except for the flexible region of VPS35L (1-109), which is displayed as cartoon. Conservation scores were calculated using the ConSurf server (Yariv et al., 2023). The score values are represented by the colors indicated in the color key. The Retriever model was obtained using AF2.

4.2. Study of the cargo recognition by SNX17

The sorting nexin family, specifically members SNX17 and SNX31, play a crucial role in the cellular process of recognizing and binding cargos that are destined for recycling via the Retriever pathway (McNally et al., 2017). This pathway is essential for maintaining cellular homeostasis by ensuring that key membrane proteins are returned to the plasma membrane or other cellular compartments, rather than being degraded in the lysosome. The sorting nexins SNX17 and SNX31 act as cargo receptors, identifying specific proteins marked for recycling and facilitating their transport through endosomal compartments. In consequence, understanding the precise molecular mechanisms underlying how sorting nexins interact with their cargo proteins is of great importance. The binding interactions are highly selective, and this specificity is vital for ensuring the correct delivery of proteins to their appropriate destinations. Investigating these interactions at a structural and biochemical level can provide deeper insights into the regulation of the Retriever pathway. For this reason, protein-cargo interaction assays to determine binding affinity, as well as X-ray crystallography trials to solve the structure, were performed in this work.

4.2.1. Purification of cargo and SNX17 constructs

To achieve Aim 2, a series of cargo and SNX17 constructs were created. Constructs containing our cargos of interest were generated. The selected cargos included the low-density lipoprotein receptor-related protein L1 (LRP1), amyloid precursor protein (APP), ß-1 integrin (ITGB1) and human papillomavirus type 16 (HPV16) capsid protein L2 (L2), all of which have been previously identified as SNX17 cargos (Bergant Marušič et al., 2012; Farfán et al., 2013; J. Lee et al., 2008; Steinberg et al., 2012). The FERM binding motif (NPxY) of the transmembrane proteins LRP1, APP and ITGB1 is located within the intracellular domain (ICD) at distances of 26, 37, and 29 residues from the plasma membrane, respectively. The capsid protein L2 of the HPV16 virus also exhibits characteristics of a transmembrane protein. It crosses the endosomal membrane thanks to a positively charged cell-penetrating peptide located at the C-terminus of the protein (P. Zhang et al., 2018), and a predicted alpha helical structure at the N-terminus can function as a transmembrane domain (Bronnimann et al., 2013). Moreover, L2 features an NPxY motif arranged in the central region of the protein spanning residues 254-257 (Bergant & Banks, 2013) (**Figure 22**).

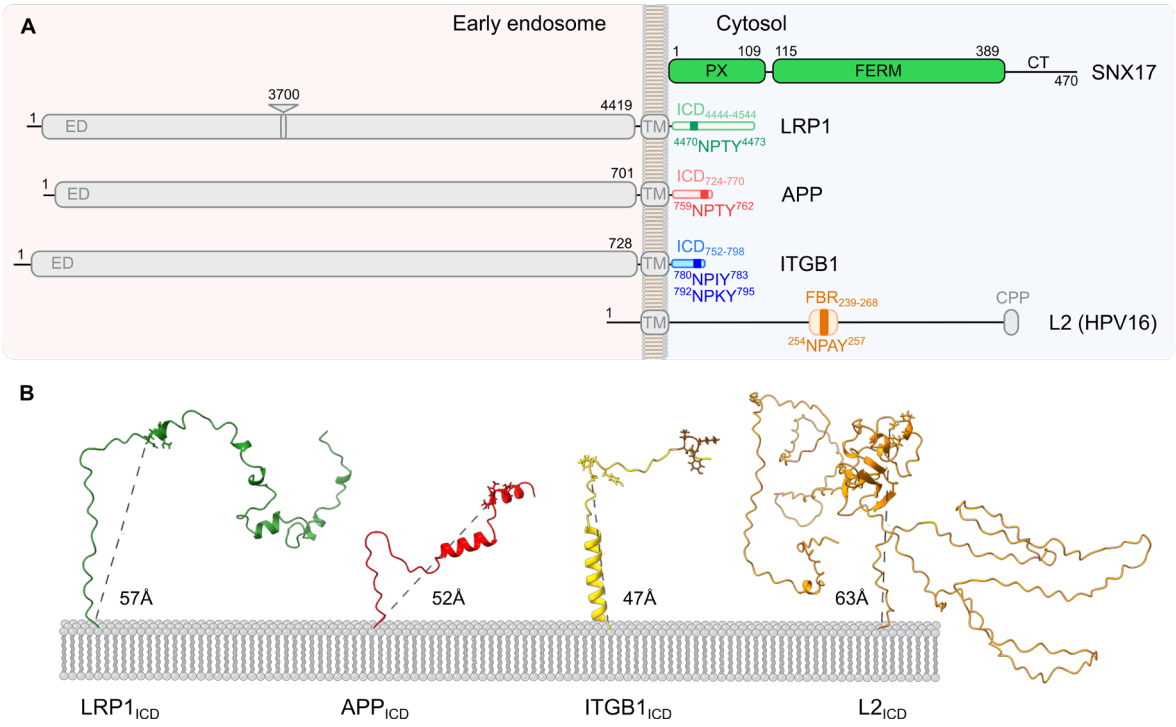

Figure 22. Diagram and representation of the AF2 model of the cargos studied in this thesis. (**A**) Schematic representation of the domains from SNX17 and the cargos studied in this thesis. The recycling signaling motif NPxY is highlighted in the diagram. The intracellular domain (ICD) of the physiological cargos and the FERM binding region (FBR) of the L2 protein, which were fused with GST for pull-down assays, are also highlighted. The length of the proteins is scaled according to their respective number of amino acids, except for LRP1, where the depicted triangle corresponds to the missing sequence of 3700 amino acids. *CT*, C-terminal domain; *ED*, extracellular domain; *TM*, transmembrane domain; *CPP*, cell penetrating peptide. (**B**) Representation of the AF2 model of the intracellular domain of the cargos within the membrane. The NPxY motif from each cargo is displayed as sticks, and the distance between the motif and the membrane is indicated. The proximal NPxY motif from ITGB1 is colored yellow, and the distal NPxY motif is colored brown. Structural images of cargo models were generated using ChimeraX.

GST-tagged cargos were generated and used for pull-down analyses (**Figure 23**). GST fusion proteins encompassing the full intracellular domains (ICD) of the cargos of interest were used. These included $LRP1_{ICD}$ (residues 4444-4544), APP_{ICD} (residues 724-770), and $ITGB1_{ICD}$ (residues 752-798). For the L2 capsid protein, we selected 30 residues around the NPxY motif (residues 239-268) and named this sequence the FERM binding region (FBR). Purified MBP and purified GST were used as negative controls for amylose-based and GST-based pull-downs, respectively.

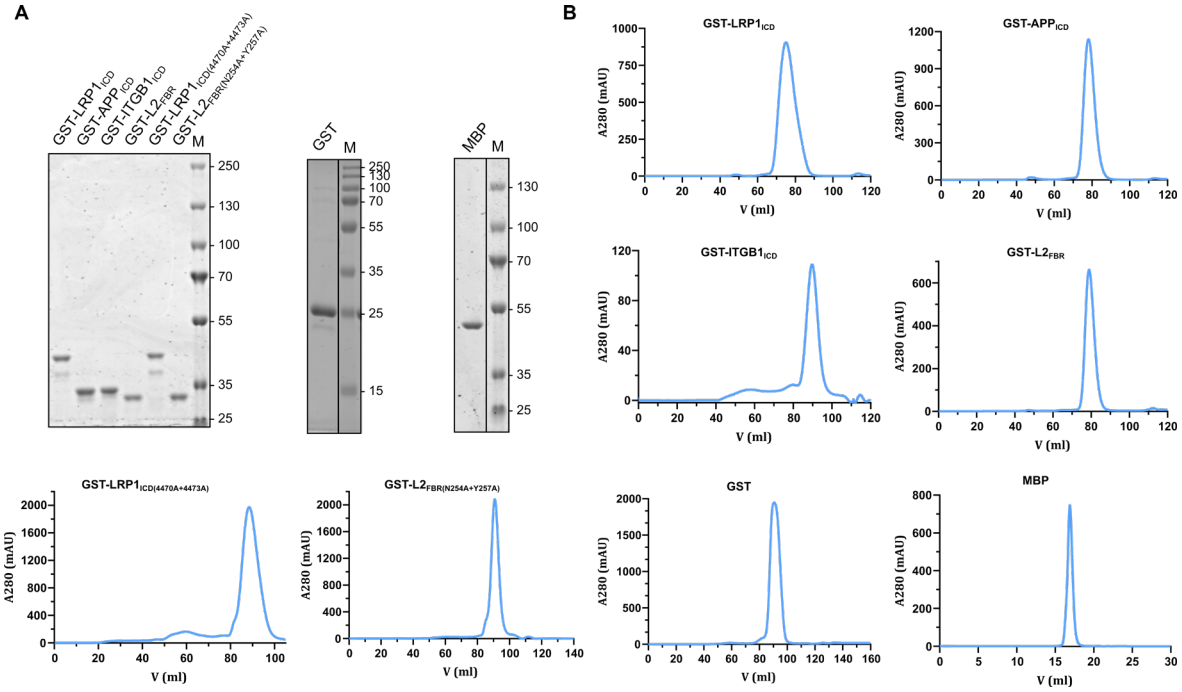

Figure 23. Purification of cargo constructs, GST, and MBP. (**A**) SDS-PAGE gel with Coomassie staining showing the purified cargo proteins and the proteins used as negative controls in protein-protein interaction assays; GST and MBP. The lanes separated by a line indicate that the wells of interest were not adjacent on the original gel. GST-LRP1$_{ICD}$ (37.6 kDa), GST-APP$_{ICD}$ (32.5 kDa), GST-ITGB1$_{ICD}$ (32.1 kDa), GST-L2$_{FBR}$ (30.0 kDa), GST-LRP1$_{ICD(4470A+4473A)}$ (37.8 kDa), GST-L2$_{FBR(N254A+Y257A)}$ (29.8 kDa), GST (26.5kDa), MBP (41.0 kDa). *M*, Protein marker. (**B**) Gel filtration chromatograms of the purified proteins shown in (**A**).

Additionally, a series of SNX17 constructs were created (**Figure 24**). SNX17$_{PX}$, SNX17$_{FERM-CT}$ and full-length SNX17 constructs were generated. The PX domain of SNX17 responsible for binding to phosphatidylinositol 3-phosphate, spans residues 1-108. The FERM domain, which mediates cargo binding, comprises the region 115-389, while the unstructured C-terminal region includes residues 390-470 (**Figure 22A**). Additionally, a construct with a disordered loop deleted, SNX17$_{FERM-CT(del406-442)}$, was generated.

Full-length SNX17 showed low solubility and stability. For this reason, SNX17 was also purified with an N-terminal MBP tag (MBP-SNX17) and used in certain experiments that require high protein concentrations. MBP tag was chosen, as it is a well-known highly soluble partner that usually enhances the solubility and promotes the proper folding of the recombinant protein it is fused to (Kapust & Waugh, 1999). Mutants of SNX17 were also tagged with MBP and used for structural and functional validation of the critical interacting regions through pull-down assays, fluorescence anisotropy, and fluorescence microscopy using GUV-based assays. The solubility and purification yield of the SNX17 mutants were identical to those of the wild-type (WT) proteins, indicating that the mutations do not significantly disrupt their structure.

Finally, several constructs, including SNX17$_{FERM-CT}$-TEV-L2$_{FBR}$, SNX17$_{FERM-CT}$-TEV-APP$_{739-770}$, and SNX17$_{109-388}$-L2$_{FBR}$, were produced for crystallization purposes (**Figure 24**). These constructs are composed of fusion proteins (SNX17 with the cargos of interest) in which the linker TEV was not removed.

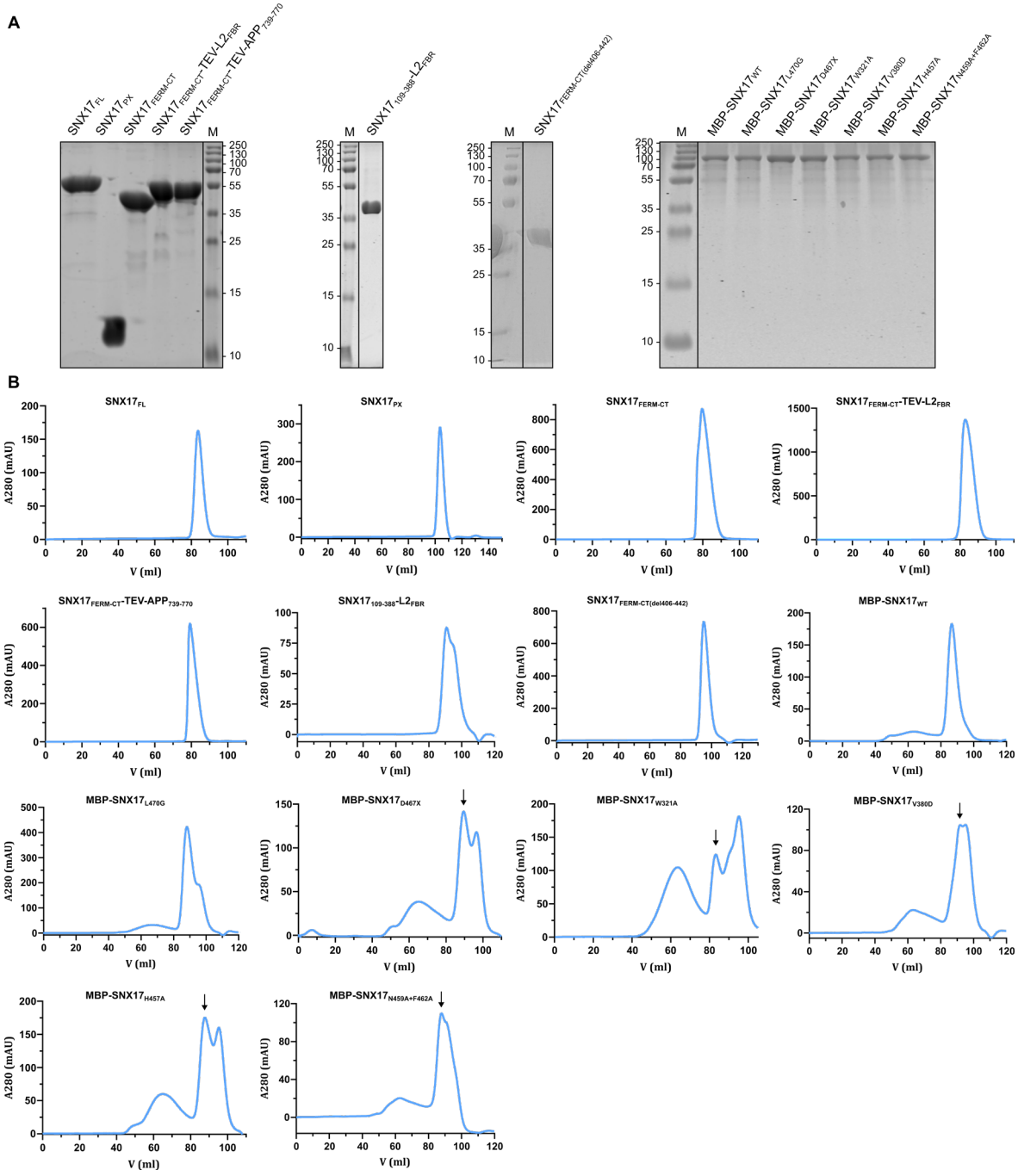

Figure 24. Purification of SNX17 constructs. (**A**) SDS-PAGE gel with Coomassie staining showing the purified proteins SNX17 used in the experiments described in this thesis. The lanes separated by a line indicate that the wells of interest were not adjacent on the original gel. SNX17$_{FL}$ (52.9 kDa), SNX17$_{PX}$ (12.3 kDa), SNX17$_{FERM-CT}$ (40.3 kDa), SNX17$_{FERM-CT}$-TEV-L2$_{FBR}$ (44.8 kDa), SNX17$_{FERM-CT}$-TEV-APP$_{739-770}$ (45.3 kDa), SNX17$_{109-388}$-L2$_{FBR}$ (36.2 kDa), SNX17$_{FERM-CT(del406-442)}$ (36.6 kDa), MBP-SNX17$_{WT}$ (93.5 kDa), MBP-

$SNX17_{L470G}$ (93.5 kDa), MBP-$SNX17_{D467X}$ (93.1 kDa), MBP-$SNX17_{W321A}$ (93.4 kDa), MBP-$SNX17_{V380D}$ (93.5 kDa), MBP-$SNX17_{H457A}$ (95.7 kDa), MBP-$SNX17_{N459A+F462A}$ (93.4 kDa). The graphs displaying various peaks are due to protein aggregation, degradation, or tag cleavage, with the peak corresponding to the purified protein indicated by an arrow. *M*, Protein marker. (**B**) Gel filtration chromatograms of the purified proteins shown in (**A**).

4.2.2. Structural model of SNX17

In order to gain insights into the function and mechanism of action of SNX17, a structural prediction of the protein was firstly obtained using AF2 (**Figure 25**).

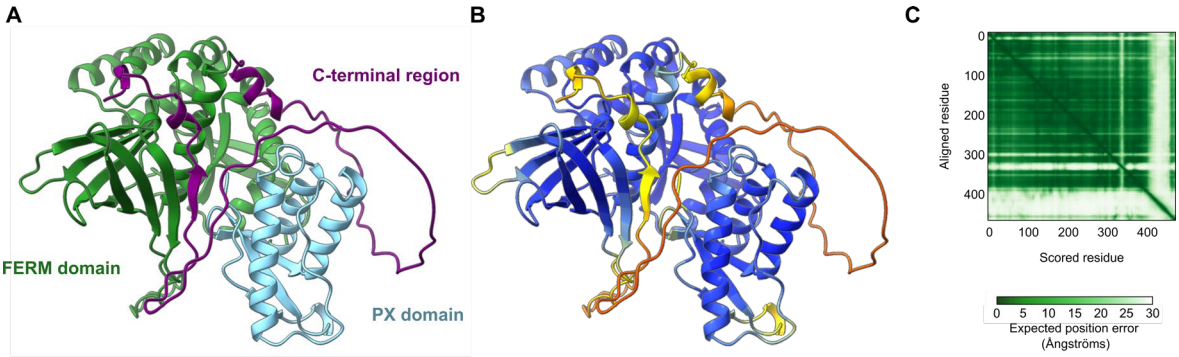

Figure 25. Structural prediction of SNX17 using AF2. (**A**) SNX17 model colored by domains, with the PX domain in blue, the FERM domain in green, and the C-terminal region in purple. (**B**) SNX17 model colored according to the pLDDT confidence score (blue, very high confidence pLDDT ≥ 90; cyan, high confidence 70 ≤ pLDDT < 90; yellow, low confidence 50 ≤ pLDDT < 70; orange, very low confidence pLDDT < 50). (**C**) The graph displays the corresponding PAE plot. *PAE*, predicted aligned error.

To confirm that MBP-SNX17 protein was correctly folded and that the mutations did not affect protein conformation or stability, the purified proteins were analyzed using circular dichroism (CD). MBP-SNX17 exhibited an α-helix-like curvature, characterized by negative bands at 222 nm and 208 nm. However, the two characteristic peaks were not well-defined, giving the spectrum a resemblance to a β-sheet conformation as well, indicated by the presence of a negative band at 218 nm (**Figure 26**). This suggests that the proteins contain both α-helixes and β-sheets (Greenfield, 2006). This agrees with the AF2 model, that predicts the presence of α-helixes and β-sheets in both domains. All the MBP-SNX17 mutants exhibited a CD spectrum similar to that of the wild-type protein. BeStSel webserver (Micsonai et al., 2022) identified a similar percentage of α-helixes (ranging from 5% to 11%), and β-stands (ranging from 27% to 35%), indicating that their secondary structural characteristics are preserved. Therefore, we can infer that any differential activity observed experimentally is due to the mutations themselves and not to incorrect protein folding.

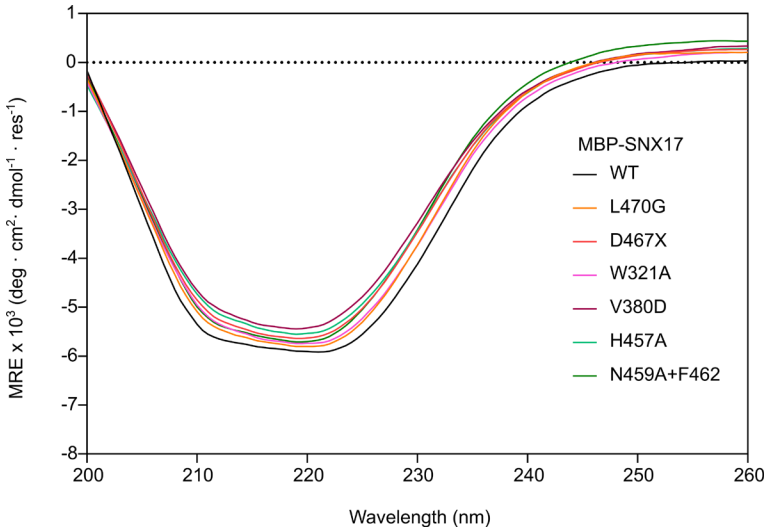

Figure 26. Conformational properties of MBP-SNX17 and its mutants. Far-UV CD spectra of WT MBP-SNX17 and the mutants used in this thesis. *MRE*, mean residual ellipticity.

4.2.3. Quantification of SNX17-cargos binding affinities

Initially, the binding affinity between $SNX17_{FERM-CT}$ and different cargos was characterized. The FERM domain of SNX17 contains the region responsible for binding proteins that includes the NPxY or NxxY motif. To determine the dissociation constants (K_Ds), fluorescence anisotropy assays with the $SNX17_{FERM-CT}$ protein and 5-FAM-labeled peptides was performed. These peptides span 14 residues covering the FERM (NPxY) binding motif, including $LRP1_{14-mer}$ (residues 4464-4477), APP_{14-mer} (residues 753-766), $ITGB1_{P-14-mer}$ (residues 774-787), $ITGB1_{D-13-mer}$ (residues 786-798), and $L2_{14-mer}$ (residues 248-261) (**Figure 27A**). A peptide spanning residues 1044-1057 from the vascular endothelial growth factor receptor 1 or VEGFR1 ($VEGFR1_{1044-1057}$) was also tested because it was suggested to be a cargo of SNX17 and contained an NPxY motif (Ghai et al., 2013b). All the cargos showed no binding affinity for the negative control protein BSA (**Figure 27B**). $SNX17_{FERM-CT}$ exhibited high affinity for L2 (K_D = 0.6 µM) and LRP1 (K_D = 2.2 µM), and moderate affinity for APP (K_D = 19 µM). We tested two potential SNX17 binding sites located in the cytoplasmic region of ITGB1, both containing the NPxY motif. The site closest to the transmembrane region ($ITGB1_P$) (K_D = 72 µM) displayed higher affinity than the more distal one ($ITGB1_D$) (K_D = 125 µM) (**Figure 27C**). Our K_D values align with previously reported ITC-derived K_Ds for SNX17 interaction with a 15-mer APP peptide (K_D= 22-33 µM) (Ghai et al., 2011, 2013b). It is of noted that the NPxY-containing peptide $VEGFR1_{14-mer}$ does not exhibit binding affinity to $SNX17_{FERM-CT}$. VEGFR1 has been suggested to be a cargo of SNX17 in the literature, but in our experiments no binding was observed. These results indicate that L2 can outcompete the binding of the physiological cargos due to its higher binding affinity for SNX17.

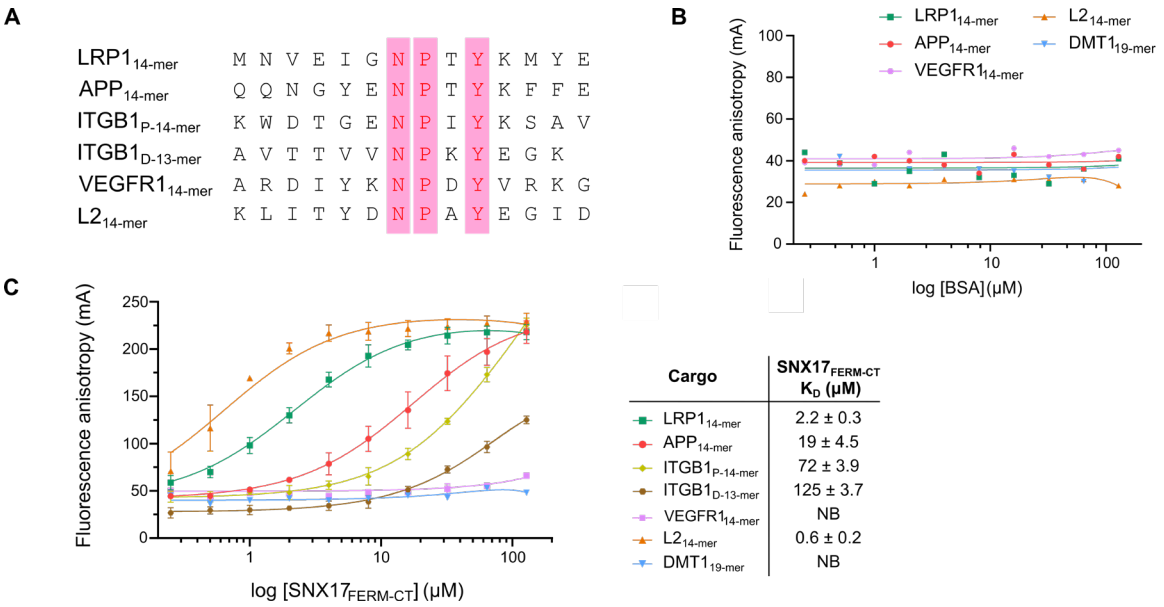

Figure 27. Characterization of cargo recognition by SNX17. (**A**) Alignment of the sequences of cargo peptides used in fluorescence anisotropy assays. The conserved NPxY motif is highlighted with pink bars. (**B**) Analysis of cargo binding affinity to BSA to detect potential non-specific binding (n = 1). The color legend for the peptides is shown in C. (**C**) Fluorescence anisotropy assays were performed to study the interaction of $SNX17_{FERM-CT}$, with the peptides outlined in panel A. The peptides were labeled with the fluorescent reagent 5-FAM at the N-terminus. The data points on the graph represent the mean ± standard deviation (SD) across three technical replicates, with the line representing the fit to the data. The dissociation constants values are presented in the accompanying table. The Retromer-dependent cargo DMT1 was used as a negative control (Tabuchi et al., 2010). *NB*, no detectable binding.

In addition, full-length MBP-tagged SNX17 was tested for interaction with FAM-$L2_{14-mer}$ by fluorescence anisotropy assay (**Figure 28A**), and a comparable K_D to $SNX17_{FERM-CT}$ was obtained. Moreover, the PX domain of SNX17 showed no binding affinity for any of the cargos, as expected (**Figure 28B**). Thus, we can conclude that the FERM domain alone is sufficient for cargo binding.

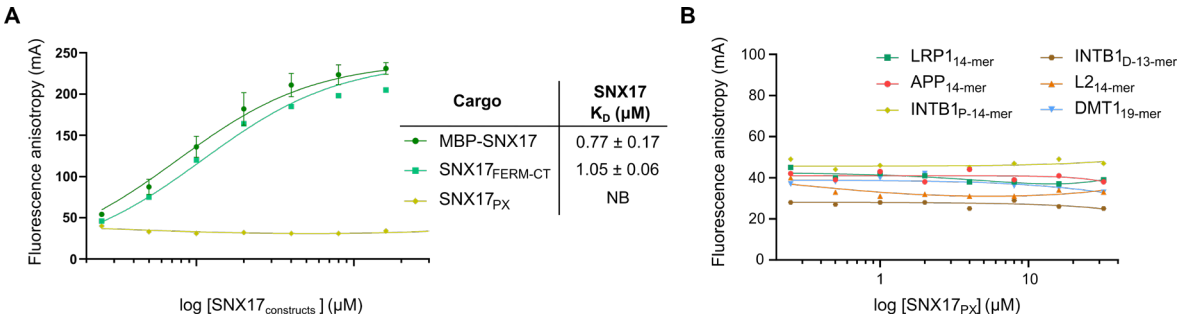

Figure 28. Analysis of full-length SNX17 and $SNX17_{PX}$ on cargo binding by fluorescence anisotropy. (**A**) Comparison of the binding affinity for FAM-L2 between full-length MBP-SNX17, $SNX17_{FERM-CT}$, and $SNX17_{PX}$ (n = 2 for MBP-SNX17 and $SNX17_{FERM-CT}$, and n = 1 for $SNX17_{PX}$). (**B**) Examination of the binding potential of the $SNX17_{PX}$ domain for all the cargos of interest (n = 1).

4.2.4. Crystallization of SNX17$_{FERM-CT}$ and SNX17 $_{FERM-CT}$-cargo complexes

Several crystal structures of SNX17 have been determined so far: two structures of the PX domain (PDB ID: 3LUI, from Ghai et al., 2011, and 3FOG) and two structures of the FERM domain, one complexed with the cargo P-selectin (PDB ID: 4GXB, from Ghai et al., 2013) and one with the cargo KRIT1 (PDB ID: 4TKN, from Stiegler et al., 2014). However, the FERM domain only extend up to residue 389, while the region that interacts with Retriever was suggested to comprise residues at the C-terminus (McNally et al., 2017). Therefore, the putative Retriever-binding region remains unresolved. To address this, crystallization trials were conducted to determine the structure of the FERM domain in conjunction with the C-terminal tail. Additionally, SNX17 complexed with various cargos was subjected to crystallization, as solving these structures could facilitate comparisons with the two previously crystallized cargos (P-selectin and KRIT1) and provide detailed insights into the mechanism of recognition. This may also help explain the differences in binding affinities observed for different cargos.

Initial crystallization trials of SNX17, including its C-terminal region, were conducted using full-length SNX17 (SNX17$_{FL}$) without any tags. However, the protein could not be concentrated beyond 2 mg/ml due to its high tendency to precipitate. A thermal scan of SNX17 revealed improved protein stability with the addition of 6% glycerol, 4% xylitol, and 5% D-trehalose, as indicated by an increase in the Tm of more than 1 ºC (**Figure 29**). Consequently, glycerol was incorporated into the protein buffer for subsequent refinement plates. Despite these adjustments, the issue of limited protein concentration remained.

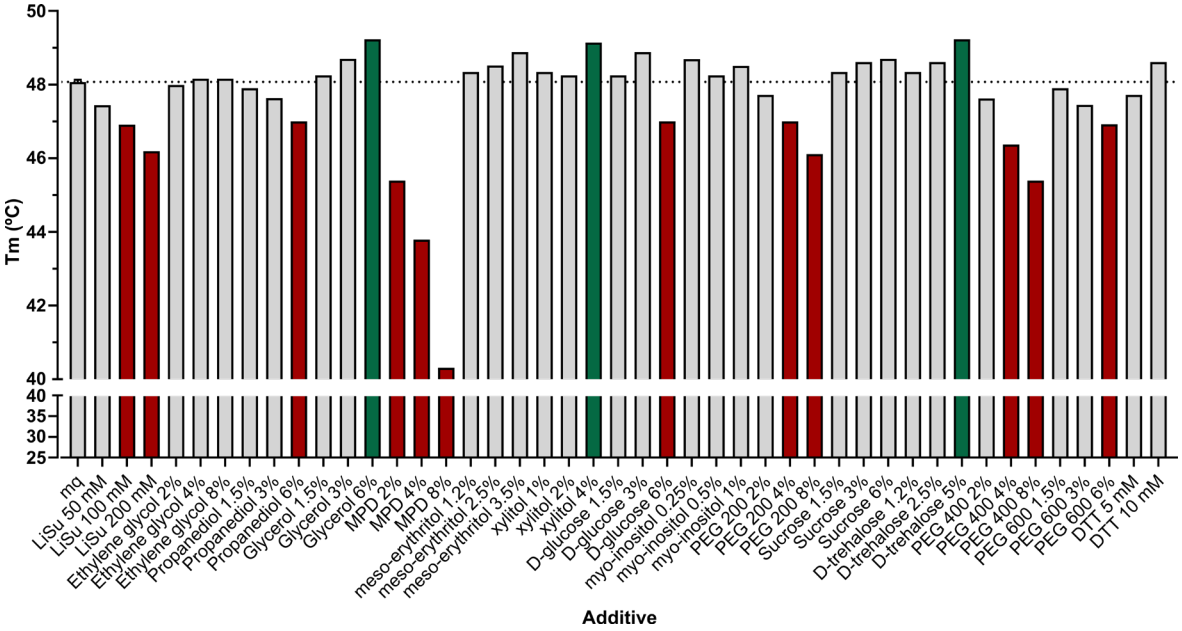

Figure 29. Effect of various compounds on the thermal stability of SNX17$_{FL}$. The graph illustrates the melting temperature (Tm) of SNX17$_{FL}$, as derived from melting curves after the addition of various additives.

The control condition (mq) was repeated three times. Conditions that show an increase in Tm of at least 1 ºC are highlighted in green, those where the Tm dropped by 1 ºC or more are marked in red, and conditions with minimal temperature variations (within 1 ºC) are shown in grey. *mq*, Milli-Q water; *LiSu*, lithium sulphate; *MPD*, 2-Methyl-2,4-pentanediol; *PEG*, Polyethylene glycol; *DTT*, Dithiothreitol.

On the other hand, the $SNX17_{FERM-CT}$ construct, which also includes the region of interest, demonstrated significantly greater stability and solubility compared to $SNX17_{FL.}$ This resulted in higher yield of purified protein, and the concentration could be increased to 16 mg/ml. Therefore, further efforts were focused on this construct. Crystals of the $SNX17_{FERM-CT}$ construct were successfully grown using the Stura Footprint Screen™ + MacroSol™ HT-96 (Molecular Dimensions) (**Figure 30A**). Refinement plates were prepared by adjusting the concentration of the initial screening condition and incubating $SNX17_{\mathbf{FERM-CT}}$ with the peptides $APP_{14\text{-mer}}$, $LRP1_{14\text{-mer}}$, or $L2_{14\text{-mer}}$ at different ratios in various drops, which successfully led to the reproduction of crystals (**Figure 30B,C**). Consequently, glycerol was incorporated into the protein buffer for subsequent refinement plates.

Crystals with the highest quality were harvested and transferred into cryoprotectant solutions containing 15-25% ethylene glycol or 15-25% glycerol. The crystals were flash-frozen in liquid nitrogen, and X-ray diffraction data were collected using an X-ray beam from beamline BL13-XALOC at the ALBA Synchrotron (Barcelona, Spain). However, the crystals only diffracted at a low resolution (8 Å), preventing the structure from being solved (**Figure 30D**).

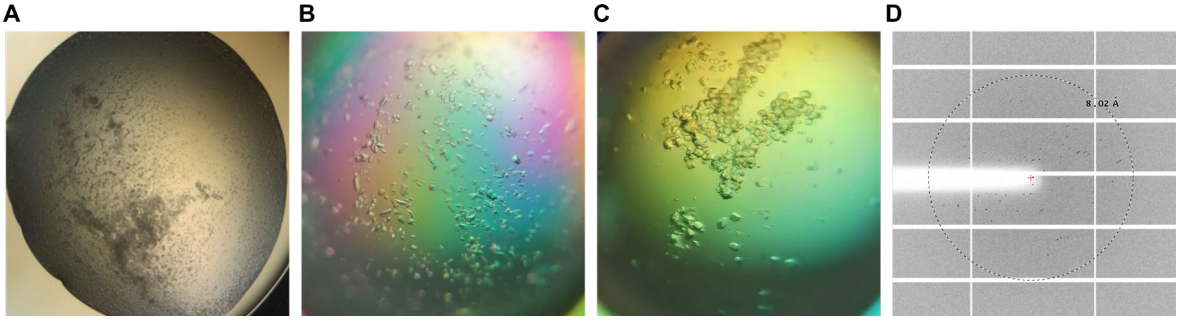

Figure 30. Crystallization trials of $SNX17_{\mathbf{FERM-CT}}$. Images of some of the crystals of $SNX17_{FERM-CT}$ grown using as precipitant 0.6-2.0 M ammonium sulfate and 0.15 M sodium citrate pH 5.5-6.5, with $SNX17_{FERM-CT}$ at concentrations ranging from 10 to 15 mg/ml in a buffer composed by 25 mM Hepes pH 7.5, 150 mM NaCl, and 1 mM TCEP, complemented with glycerol at 10%. (**A**) Crystals grown in the initial crystal screening condition B1 from Stura Footprint Screen™ + MacroSol™ HT-96 (Molecular Dimensions), composed by 0.75 M ammonium sulfate and 0.15 M sodium citrate pH 5.5. (**B**) Improvement of the crystals in 0.7 M ammonium sulfate and 0.15 M sodium citrate pH 5.5, with $SNX17_{FERM-CT}$ at 10.1 mg/ml (250 µM) with a protein-to-precipitant ratio of 1:1. (**C**) Crystals in 1.1 M ammonium sulfate and 0.15 M sodium citrate pH 6.0, with $SNX17_{FERM-CT}$ at 10.1 mg/ml (250 µM) and $LRP1_{14\text{-mer}}$ at 0.5 mg/ml (275 µM) in protein-to-precipitant ratio of

2:1. (**D**) Image of the diffraction pattern obtained in ALBA Synchrotron. The maximum resolution achieved from diffraction was 8.02 Å, which was insufficient for solving the structure.

Additionally, refinement plates based on conditions reported for the crystal structure of $SNX17_{FERM}$ with P-selectin$_{735-768}$ (PDB ID: 4GXB, Ghai et al., 2013) were prepared using a solution of 0.1 M sodium acetate, 0.2 M magnesium chloride and 15% PEG 4000 at pH 5.5. Despite the formation of some pseudo-crystals, high-quality crystals were not obtained. Moreover, crystallization trials of SNX17-cargo chimeras ($SNX17_{FERM-CT}$-TEV-$L2_{FBR}$ and $SNX17_{FERM-CT}$-TEV-$APP_{739-770}$) were performed. The rationale was that covalently linking interacting partners might facilitate complex assembly and increase protein stability (Kobe et al., 2015). Additionally, the chimera could promote conformational homogeneity, by locking the protein into a specific conformation, thereby improving the likelihood of obtaining well-ordered crystals. Unfortunately, no crystals were obtained. In the case of $SNX17_{FERM-CT}$-TEV-$L2_{FBR}$, the protein was subjected to a thermal scan assay. Although it exhibited greater Tm in the absence of additives (Tm = 58.6 ºC) compared to $SNX17_{FL}$ (Tm = 48.1 ºC, **Figure 29**), indicating a greater stability of this construct, none of the additives tested improved its stability (**Figure 31**).

Interestingly, while compounds such as glycerol, xylitol, and D-trehalose improved the thermal stability of all three proteins analyzed - VPS26C (**Figure 17**, section 4.1.4.), $SNX17_{FL}$ (**Figure 29**), and $SNX17_{FERM-CT}$-$L2_{FBR}$ (**Figure 31**) - other compounds showed protein-specific effects. For instance, lithium sulfate enhanced VPS26C stability but negatively impacted the stability of SNX17 and SNX17-L2.

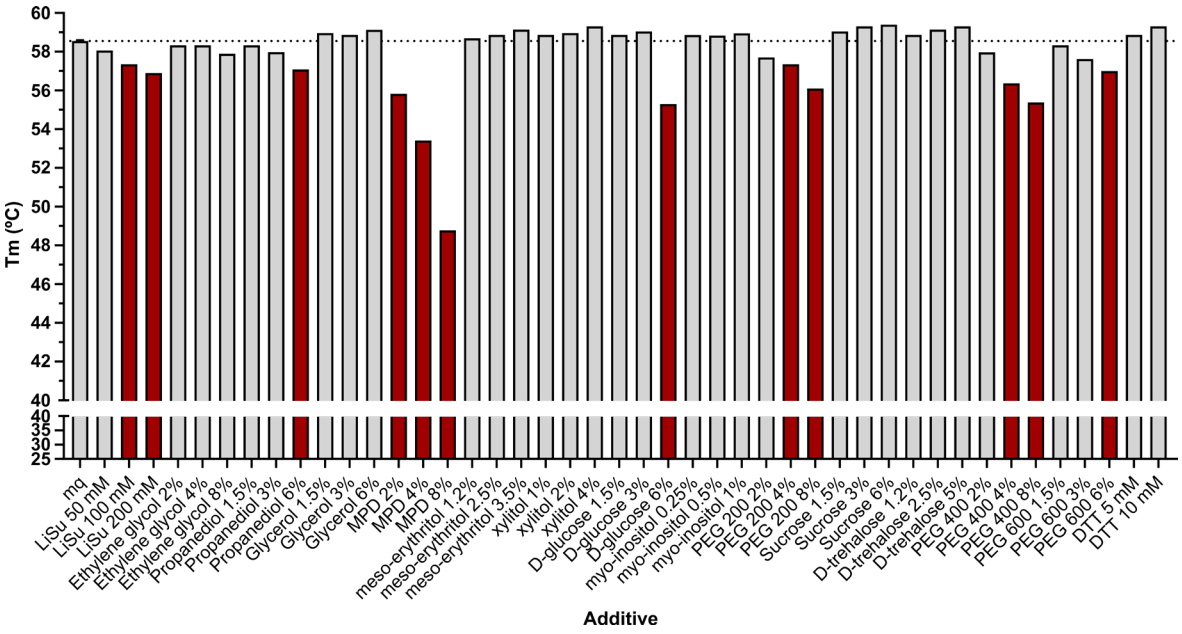

Figure 31. Effect of different compounds on the thermal stability of $SNX17_{FERM-CT}$-TEV-$L2_{FBR}$. The graph displays the Tm of $SNX17_{FERM-CT}$-TEV-$L2_{FBR}$ as determined from melting curves following the addition of

various additives (with n = 3 for the control condition). Conditions where the melting temperature decreased by 1 ºC or more are highlighted in red, while conditions with negligible temperature changes (within 1 ºC) are shown in grey. *mq*, Milli-Q water; *LiSu*, lithium sulphate; *MPD*, 2-Methyl-2,4-pentanediol; *PEG*, Polyethylene glycol; *DTT*, Dithiothreitol.

We suspected that the flexibility of the C-terminal region of the protein was hindering the growth of well-diffracting crystals. Consequently, a new construct containing $SNX17_{FERM\text{-}CT(del406\text{-}442)}$ was tested. This construct was designed to mitigate potential instability caused by the disordered loop in the deleted residues. Crystals were grown under the same conditions as those for the $SNX17_{FERM\text{-}CT}$ construct, and further refinement was attempted to enhance crystal quality (**Figure 32**). We found that reducing the concentration of ammonium sulfate significantly improved the crystals. However, despite these improvements, good-quality X-ray diffraction could not be achieved.

To address this issue, another construct containing $SNX17_{109\text{-}388}$-$L2_{FBR}$ was produced. The removal of the entire C-terminal loop along with the presence of the cargo was expected to favor protein crystallization. However, this chimeric protein could not be concentrated above 2 mg/ml, and crystals were not obtained.

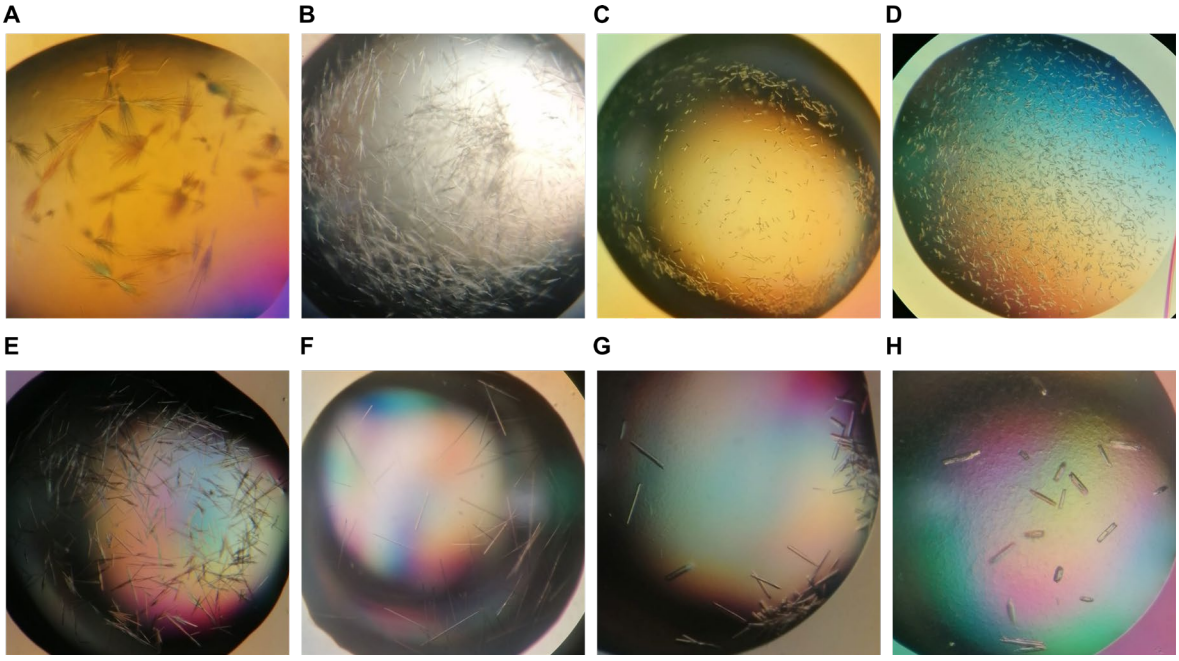

Figure 32. Crystallization trials of $SNX17_{FERM\text{-}CT(del406\text{-}442)}$. In all crystallization conditions, $SNX17_{FERM\text{-}CT(del406\text{-}442)}$ at 10 mg/ml (270 µM) was pre-incubated with $HPV_{14\text{-}mer}$ at 1.3 mg/ml (810 µM), and seed stock diluted 1/100 (**A**). The buffer used contained 25 mM Hepes pH 7.5, 300 mM NaCl, and 1 mM TCEP (**C, D, F, G**), with the addition of 10% glycerol (**A, B, E, F**). Crystals were grown in in varying concentrations of ammonium sulfate and 0.15 M sodium citrate, with different pH values, as follows: (**A**) 1.1 M ammonium sulfate, pH 5.5, with a 1:1 protein-to-precipitant ratio; (**B**) 1 M ammonium sulfate, pH 5.5, 1:1 ratio; (**C**) 0.75

M ammonium sulfate, pH 6.0, 1:2 ratio; (**D**) 0.75 M ammonium sulfate, pH 6.0, 2:1 ratio; (**E**) 0.75 M ammonium sulfate, pH 5.5, 1:1 ratio; (**F**) 0.6 M ammonium sulfate, pH 5.5, 1:2 ratio; (**G**) 0.6 M ammonium sulfate, pH 5.5, 1:1 ratio; and (**H**) 0.65 M ammonium sulfate, pH 5.5, 2:1 ratio.

4.2.5. Study of the SNX17-cargo interface by molecular dynamics

Our results indicate that the NPxY motif in cargos is not the only contributor to SNX17 binding, as all the cargos contain this motif but exhibit varying binding affinities. In fact, one of the NPxY-containing peptides, VEGFR1, shows no binding capacity to SNX17 (**Figure 27C**, section 4.2.3.). This indicates that additional specificity determinants beyond the NPxY motif are involved in the interaction.

To identify the residues in the cargos that significantly contribute to their interaction with SNX17, a computational approach was initially employed. AlphaFold3 (AF3) was used to generate structural models of the SNX17-cargo complex, using the 14-mer or 13-mer sequences that were used for fluorescence anisotropy assays of the L2, LRP1, APP, INTβ1 and VEGFR1 peptides (**Figure 33**). All the cargos were positioned at the same location, and a β-sheet formed by residues 2-6 was modelled for all of them, except for INTβ1$_P$. This β-sheet was modeled in an anti-parallel orientation relative to the β-sheet of SNX17, which is formed by residues 318-326. The positions of all the cargos show moderate pLDDT (predicted local distance difference test) values, with VEGFR1 exhibiting the lowest values. Additionally, the positions of all the cargo peptides relative to SNX17 are well-supported by the PAE matrices.

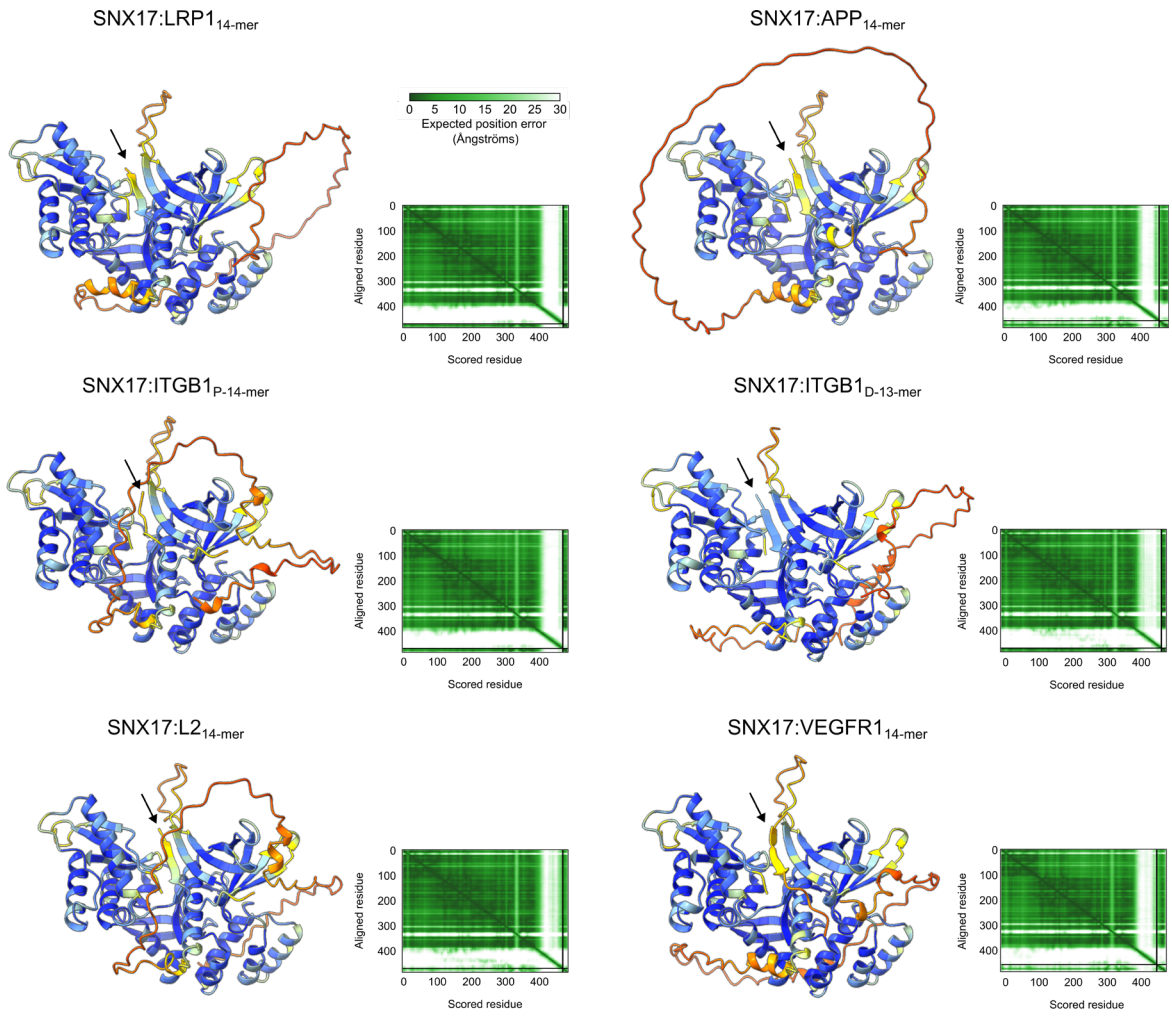

Figure 33. Structural predictions of SNX17:cargo complexes using AF3. Complexes formed by SNX17 with $LRP1_{14\text{-mer}}$, $APP_{14\text{-mer}}$, $INT\beta1_{P\text{-}14\text{-mer}}$, $INT\beta1_{D\text{-}13\text{-mer}}$, $VEGFR1_{14\text{-mer}}$, or $L2_{14\text{-mer}}$ the peptides were modelled using AF3. The models are colored according to the pLDDT confidence score as in **Figure 25**. The graphs display the corresponding PAE plots. Arrows indicate the structure of the cargo peptides. *PAE*, predicted aligned error.

As previously mentioned, VEGFR1 does not exhibit binding affinity to SNX17. This lack of binding might be attributed to the electrostatic characteristics of VEGFR1 compared to the other cargos. $VEGFR1_{14\text{-mer}}$ is relatively basic, with a pI of 9.53, whereas the other cargos are more acidic, with pI values ranging from 4.03 to 6.07. This discrepancy suggests that electrostatic forces crucial for binding to SNX17 may be absent in VEGFR1.

Indeed, an analysis of the electrostatic potential of SNX17 reveals that the cargo-binding pocket features two distinct regions: an acidic region that interacts with basic residues in the cargos, and a basic region that interacts with acidic residues from the cargos (**Figure 34**). While the basic electrostatic potential of the initial residues is common across all cargos, VEGFR1 lacks the acidic potential found in the last residues of the other cargos and instead contains two positively charged

residues, R1055 and K1056. Therefore, the presence of the NPxY motif alone does not ensure SNX17 binding. The surrounding residues and the electrostatic environment are critical for the interaction.

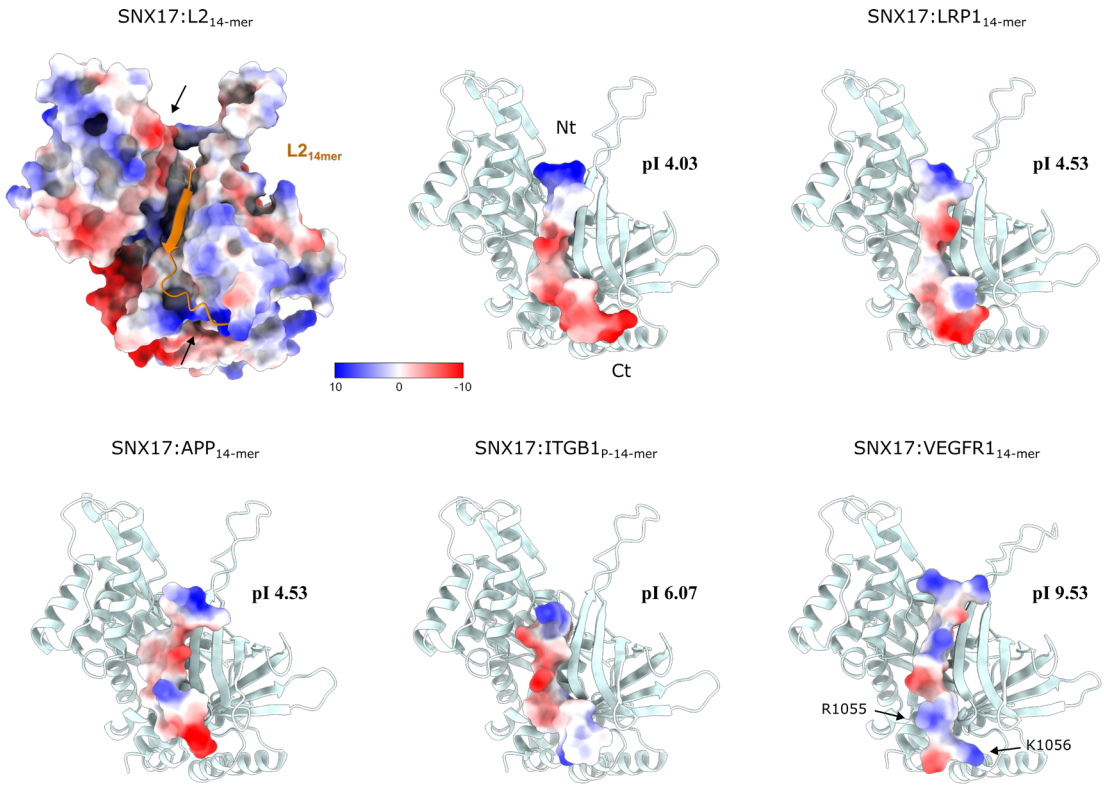

Figure 34. Study of the electrostatic potential of SNX17 and its cargo peptides. The first model displays the electrostatic characteristics of SNX17 in surface representation, with the 14-mer peptide L2 shown in cartoon (in orange). The circles highlight the acidic region in the upper part and the basic region in the lower part of the SNX17 binding pocket. The C-terminal region (residues 390-470) of SNX17 is omitted in all models to enhance the visualization of the binding pocket. Subsequent models show SNX17 in cartoon and the cargo peptides in surface representation. Electrostatic potentials are visualized using ChimeraX with Coulombic Surface Coloring, where electronegative values are represented in red (up to -10 kcal/(mol·e)) and electropositive values in blue (up to 10 kcal/(mol·e)), as indicated by the color key.

To gain deeper insights into SNX17-cargo interactions, a computational alanine mutagenesis screen was performed using the resEnergy tool from the pyDock web server (Romero-Durana et al., 2020). This tool calculates the energetic contribution of each residue to the interaction at the surface level. The difference in the energy between the wild-type *cargo:SNX17* interaction and the mutant *cargo:SNX17* interaction, known as ΔΔG, was calculated, to quantify the energetic contribution of each residue to the binding affinity (**Figure 35A**). Positive ΔΔG values indicate that the mutated residue contributes significantly to binding. The residues within the NPxY motif were not taken into consideration in this analysis since they are present in all cargos and do not account

for the specific binding affinity variations among them. Negative ΔΔG values for certain residues suggest that their alanine mutation of these residues may stabilize the complex or introduce favorable interactions. The screen identified three key amino acids in the L2 sequence with significant energetic contributions to the interaction with SNX17, as indicated by highly positive ΔΔG values: Y252, E258 and D261 (**Figure 35B,C**). The highly positive ΔΔG values observed for the Y757A mutation in APP and the W775A mutation in ITGB1$_P$ are likely due to the loss of crucial aromatic interactions with a hydrophobic pocket in SNX17.

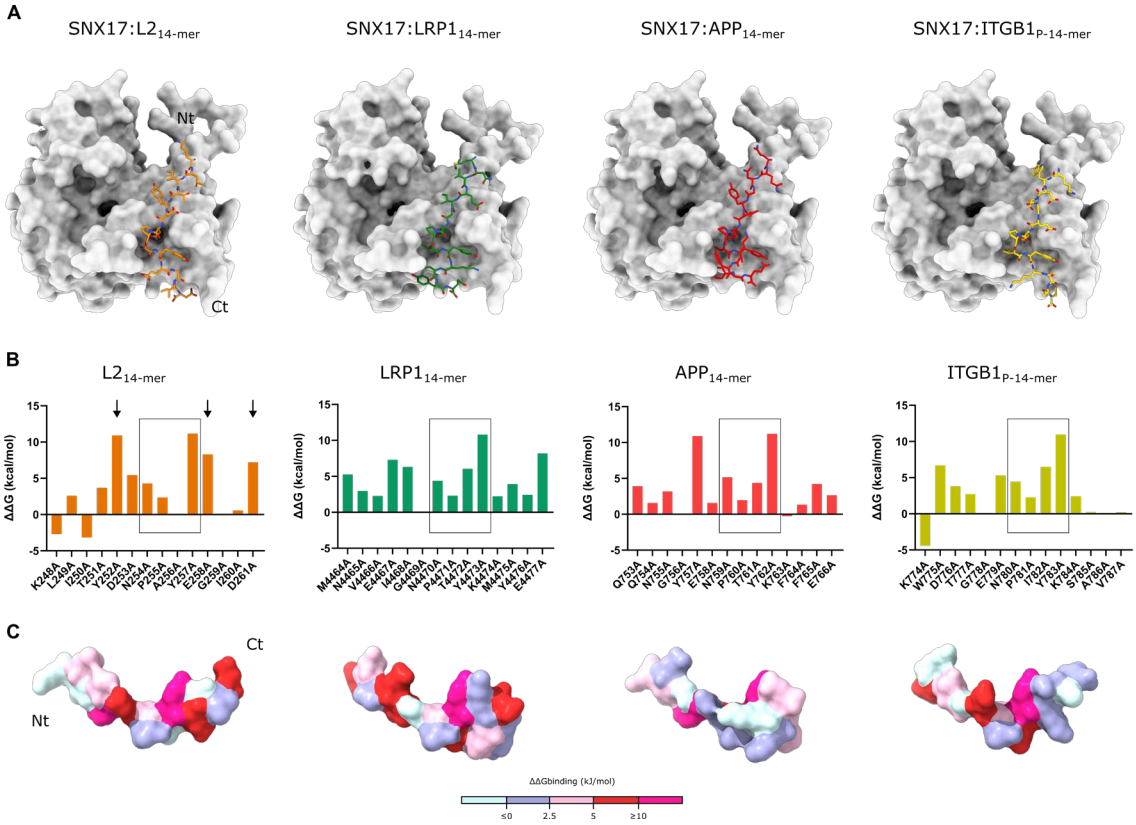

Figure 35. Molecular interactions at the interface of SNX17 with the cargos L2, LRP1, APP and ITGB1. (**A**) Comparison of the interacting residues from the peptides of L2, LRP1, APP and ITGB1 (shown as sticks) with the surface of SNX17 (in light grey). The models of SNX17:L2$_{14\text{-mer}}$, SNX17:LRP1$_{14\text{-mer}}$, SNX17:APP$_{14\text{-mer}}$ and SNX17:ITGB1$_{14\text{-mer}}$ were obtained with AF3. The structural images were generated using ChimeraX for better visualization of the binding pocket the PX domain (residues 1-109) and the C-terminal region (residues 390-470) of SNX17 were removed in all models. (**B**) Analysis of the energetic contribution of each residue to the *ligand:receptor* interaction between SNX17 and the cargos of interest, calculated by computational alanine-scanning mutagenesis using the resEnergy tool from the pyDock web server (Romero-Durana et al., 2020). Positive ΔΔG values indicate that the mutated residue contributes significantly to binding. The rectangles highlight the conserved NPxY motif, which is present in all SNX17 cargos. Arrows in the L2 graph indicate the amino acids with the highest energetic contribution: Y252, E258 and D261. (**C**) The cargo surface is displayed and colored with an intensity gradient, as indicated in the figure legend, based on the

change in binding free energy. This change is estimated as the difference between the binding ΔG of the wild-type and the alanine-mutated complex ($\Delta\Delta G = \Delta G_{wild\text{-}type} - \Delta G_{ALA}$).

Additionally, ΔΔG values from the alanine mutagenesis scanning were dissected into the three energetic parameters that are considered in the scoring, which are electrostatics, desolvation and van der Waals forces (**Figure 36**).

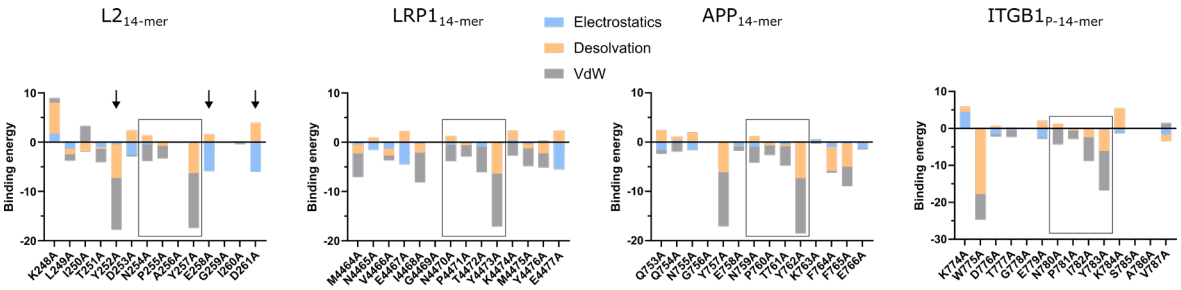

Figure 36. Interactions at the interface between SNX17 and its cargo proteins, including L2, LRP1, APP, and ITGB1, split into the three energy terms. The graphs represent the binding energy (in arbitrary units) of each residue, where the energetic parameters components are electrostatics, desolvation, and van der Waals forces. In the L2 graph, arrows highlight the amino acids that contribute the most energetically: Y252, E258, and D261. *VdW*, van der Waals forces.

In the structural model of SNX17:$L2_{14\text{-}mer}$ (**Figure 37**), Y252 forms hydrogen bonds with the main chain of SNX17, but not with its side chain. Additionally, Van der Waals forces may occur between Y252 and W321 in SNX17, as suggested by theoretical molecular docking binding energy of Y252 (-10.5) (**Figure 36**). This indicates that Van der Waals forces likely contribute to the interaction between Y252 and SNX17.

E258 forms a salt bridge with K387 in SNX17, a strong electrostatic interaction not present in other cargos. According to the *in silico* model, the distance between the nitrogen atom of the amino group in K387 (NZ) and the oxygen atom of the carboxyl group of E258 (OE1) is 2.8Å, which qualifies as a salt bridge, given that it is less than the 4Å threshold (Barlow & Thornton, 1983).

Similarly, the oxygen atom of the carboxyl group in the acidic residue D261 (OD1) interacts with the nitrogen atom of the amino group in R317 (NH2) at a distance of less than 4Å, indicating a salt bridge interaction.

In conclusion, through *in silico* structural and energetic modeling, we have identified three amino acids in L2 - Y252, E258 and D261 - that may be responsible for the higher binding affinity of this cargo to SNX17 compared to others. The residues in SNX17 that appear to interact with these L2 amino acids are W321, K387, and R317. Notably, these three residues of SNX17 have been highlighted in the sequence for showing the highest contributions to the interface, which is consistent

with observations from the structural model. These residues exhibit high ΔΔG values (ΔΔG of R317A = 7.9 kcal/mol, ΔΔG of W321A = 7.0 kcal/mol, and ΔΔG of K387A = 6.4 kcal/mol).

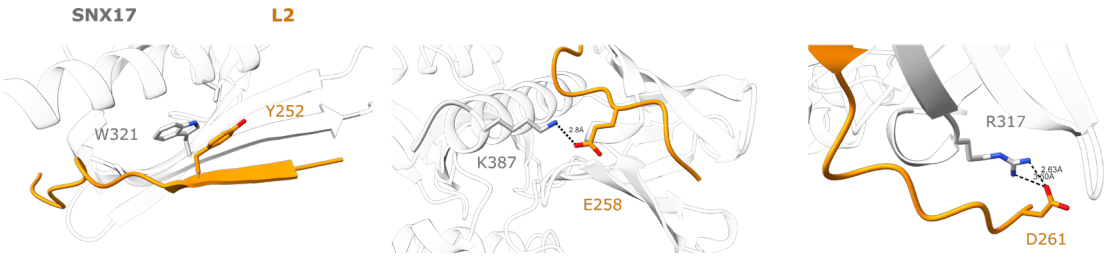

Figure 37. Structural details of the binding interface between L2 and SNX17. The primary interacting residues based on the computational alanine mutagenesis screen are displayed as sticks. SNX17 is colored in light grey, and L2 is colored in orange. Dashed lines indicate salt bridges, with annotated distances between interacting atoms.

4.2.6. Study of the SNX17-L2 interface through mutational analysis

Since L2 has been shown to exhibit a significantly higher binding affinity compared to other cargo proteins, understanding the molecular mechanisms governing the interaction between SNX17 and L2 could provide valuable insights into how SNX17 recognizes and processes different cargos. Therefore, SNX17-L2 interface was further studied to uncover potential differences in cargo sorting, since the interactions may be distinct or more specialized.

After analyzing the binding surface of the SNX17-L2 complex through mutational alanine scanning, the residues that provided a particularly large energetic contribution to the interaction were selected for experimental validation, and the following mutants were designed: $L2_{E258A}$, $L2_{D261A}$ and $L2_{Y252A}$.

In addition to the results of the *in silico* mutagenesis analysis, other properties of these residues provided further evidence of their contribution to a tighter binding (**Figure 38A**). E258 in L2 provides a negatively charged residue, whereas the other analyzed cargos have a positively charged lysine at this position (with the exception of the cargo $ITGB1_D$). D261 is the terminal residue of the peptide and is absent in $ITGB1_D$, the cargo with the lowest binding affinity. Y252 was selected for mutational analysis based on previous literature showing that a construct with the FTNPVY sequence from LRP1 exhibited stronger binding than its wild-type counterpart, the IGNPTY motif (Farfán et al., 2013). It was proposed that phenylalanine mediates a stronger interaction with SNX17 compared to isoleucine, and that the flanking regions contribute to a better environment for the presentation of this motif. Since tyrosine and phenylalanine are structurally similar, it was hypothesized that Y252 might have a similar effect on the interaction. Notably, tyrosine is unique to L2, except for APP.

Additionally, a mutant of APP was designed: APP_{K763E}. Since E258 in L2 appears to be one of the most critical residues for tight binding because of its contribution to the charge, and APP contains a lysine at this position, which has the opposite charge, substituting this lysine with the glutamic acid present in L2 could potentially enhance binding affinity. This mutant is intended to phenocopy L2 activity.

The binding of the L2 and APP mutated peptides fused with 5-FAM to $SNX17_{FERM-CT}$ was analyzed by fluorescence anisotropy and compared to their wild-type counterparts (**Figure 38B**). The $L2_{D261A}$ mutant did not significantly affect binding affinity to SNX17, whereas $L2_{E258A}$ and $L2_{Y252A}$ displayed a pronounced decrease in affinity compared to $L2_{WT}$, with reductions of approximately 9-fold and 22-fold, respectively (K_D for $L2_{E258A}$ = 3.79 µM and K_D for $L2_{Y252A}$ = 9.42 µM, compared to K_D = 0.43 µM for $L2_{WT}$). Additionally, APP_{K763E} showed a 1.8-fold increase in affinity (K_D = 20.5 µM), compared to the wild-type (K_D = 37.3 µM). The contributions of Y252 and E258 to the high binding affinity that L2 exhibits for SNX17 have been experimentally validated through biochemical binding assays. These experiments confirmed that both residues play critical roles in stabilizing the interaction between L2 and SNX17. The *in silico* mutagenesis analysis predicted these effects with high accuracy, as evidenced by a strong correlation between the predicted ΔΔG values and the experimental results.

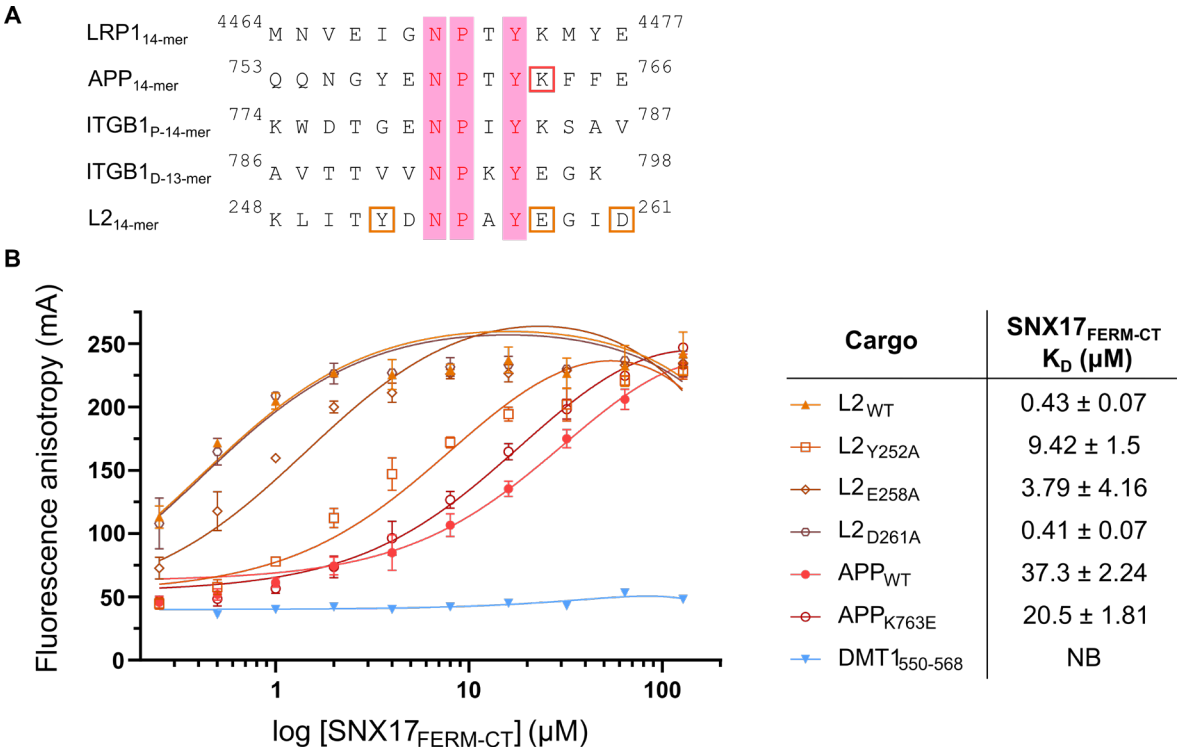

Figure 38. Alignment of the sequences of the analyzed cargo peptides and fluorescence anisotropy assays measuring the interaction between $SNX17_{FERM-CT}$ and 5-FAM-labeled peptides of wild-type and mutant forms of L2 and APP. (**A**) The conserved NPxY motif is highlighted with pink bars. Residues targeted in

mutagenesis studies are marked with red squares for APP and orange squares for L2. (**B**) 5-FAM-labeled peptides were added at a final concentration of 0.05 μM. DMT1 cargo was used as a negative control. Data points represent the mean ± SD of three independent experiments. The table presents the dissociation constants (K_D) for each peptide. *NB*, no detectable binding.

4.3. Characterization of the Retriever-SNX17 complex

4.3.1. Characterization and *in vitro* validation of Retriever association to SNX17 and the role of the cargo in this interaction

SNX17 interaction with cargo triggers Retriever recruitment

It has been suggested that SNX17 interact with Retriever, as previous studies using co-immunoprecipitation assays of cellular extracts provided preliminary insights into the involvement of the C-terminus of SNX17 in its association with Retriever through the VPS26C subunit (McNally et al., 2017). However, other researchers have reported an inability to detect such an interaction between SNX17 and Retriever in solution (Healy et al., 2022). Therefore, no direct *in vitro* reconstitution data are available.

To investigate the interaction between Retriever and SNX17, we first tested whether the Retriever subunit VPS26C directly interacts with $SNX17_{FERM-CT}$ using gel filtration chromatography (**Figure 39A**), but no direct interaction was detected. We then conducted additional interaction assays to confirm this result. Isothermal titration calorimetry (ITC), a more sensitive technique capable of detecting low-affinity interactions, was used to analyze the interaction between $SNX17_{FERM-CT}$ and VPS26C at the Biophysics Unit (UPV-EHU, CSIC). However, no significant heat release was observed, since the heat release observed was equivalent to the negative control for the titration of $SNX17_{FERM-CT}$ in buffer (**Figure 39B**). Additionally, a GST-based pull-down assay was conducted to evaluate the binding of VPS26C to $SNX17_{FL}$, $SNX17_{FERM}$ and the GST-L2 cargo (**Figure 39C**). However, VPS26C was not retained under any of these conditions. Moreover, VPS26C binding was analyzed in the presence of MBP-SNX17 using GST-based pull-down assays (**Figure 39D**), where GST-L2 was attached to the resin. MBP-SNX17 was retained in the resin, whereas VPS26C was not. This result further corroborated the lack of binding affinity between VPS26C and SNX17.

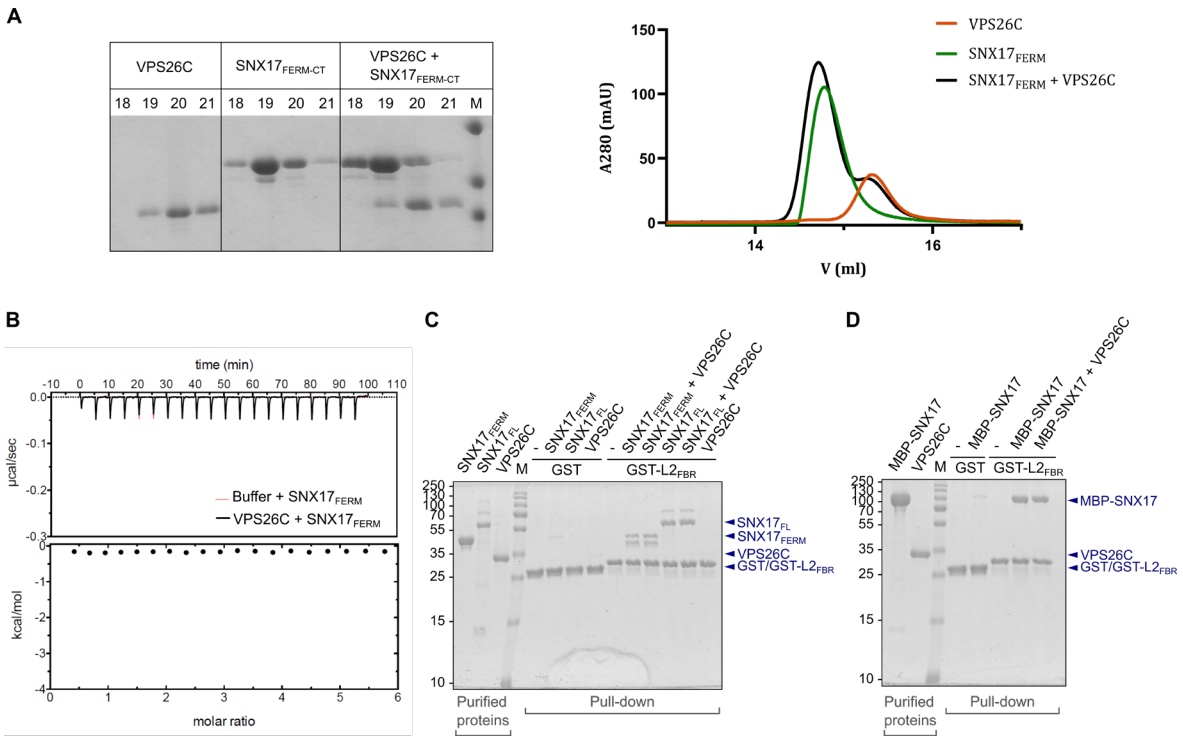

Figure 39. Analysis of the interaction between VPS26C and SNX17. (**A**) Gel filtration chromatography of 100 µM VPS26C with 100 µM SNX17$_{FERM-CT}$. The presence of two separate absorbance peaks indicates no direct interaction between the proteins. *M*, Protein marker. (**B**) ITC assay of 30 µM VPS26C and 300 µM SNX17$_{FERM-CT}$. No significant interaction was detected, with values comparable to the negative control. (**C, D**) VPS26C was incubated with SNX17$_{FL}$, SNX17$_{FERM}$ (**C**) or MBP-SNX17$_{FL}$ (**D**) in the presence of GST-L2$_{FBR}$ in GST pull-down assays. Non-fused GST protein was used as a negative control. Purified proteins and pull-down samples were separated by SDS-PAGE and visualized by Coomassie Blue staining.

These results suggest that for Retriever binding to SNX17 the presence of the entire Retriever complex or the cargo may be required. Cargo association to SNX17 could induce conformational changes and thereby increase binding affinity. Notably, certain proteins involved in intracellular trafficking, such as the motor proteins dynein (Xiang & Qiu, 2020) and myosin (Hirano et al., 2011) are activated through cargo binding. In addition, studies on the Retromer complex, which shares functional and structural similarities with Retriever, have shown that the binding of SNX3 with Retromer is dependent on the presence of cargo (Lucas et al., 2016). For this reason, we decided to explore whether the interaction between SNX17 and Retriever is also cargo-dependent.

To investigate the contribution of cargo to the interaction between SNX17 and Retriever we employed pull-down assays. Since the MBP-tagged SNX17 construct was capable of efficiently binding to the cargo (**Figure 39D**), we assumed that the tag does not affect protein activity. Therefore, the MBP-SNX17 construct was used in subsequent experiments, as this tag enhances the stability and solubility of SNX17. MBP-SNX17 was immobilized on amylose beads and incubated with Retriever in the presence or absence of various cargo proteins. In these experiments, GST fusion

proteins encompassing the full intracellular domains of the previously studied cargos were used. These included $LRP1_{ICD}$ (residues 4444-4544), APP_{ICD} (residues 724-770), and $ITGB1_{ICD}$ (residues 752-798). For the L2 capsid protein, we selected 30 residues around the NPxY motif (residues 239-268) and named this sequence the FERM binding region (FBR) (**Figure 22A**, section 4.2.1.). In the absence of cargo, only a modest amount of Retriever was retained. However, a significant increase in Retriever binding was observed when SNX17 was pre-incubated with the endogenous cargo $LRP1_{ICD}$ or the viral protein $L2_{FBR}$ (**Figure 40A**). No significant interaction was detected in the presence of APP_{ICD} or $ITGB1_{ICD}$, likely due to their low affinity for SNX17 (**Figure 27C**, section 4.2.3.). This enhanced binding of Retriever to SNX17 is attributed to the interaction of the cargos with SNX17 rather than with Retriever, as no direct interaction between the Retriever complex and the cargos was observed in GST pull-downs (**Figure 40B**).

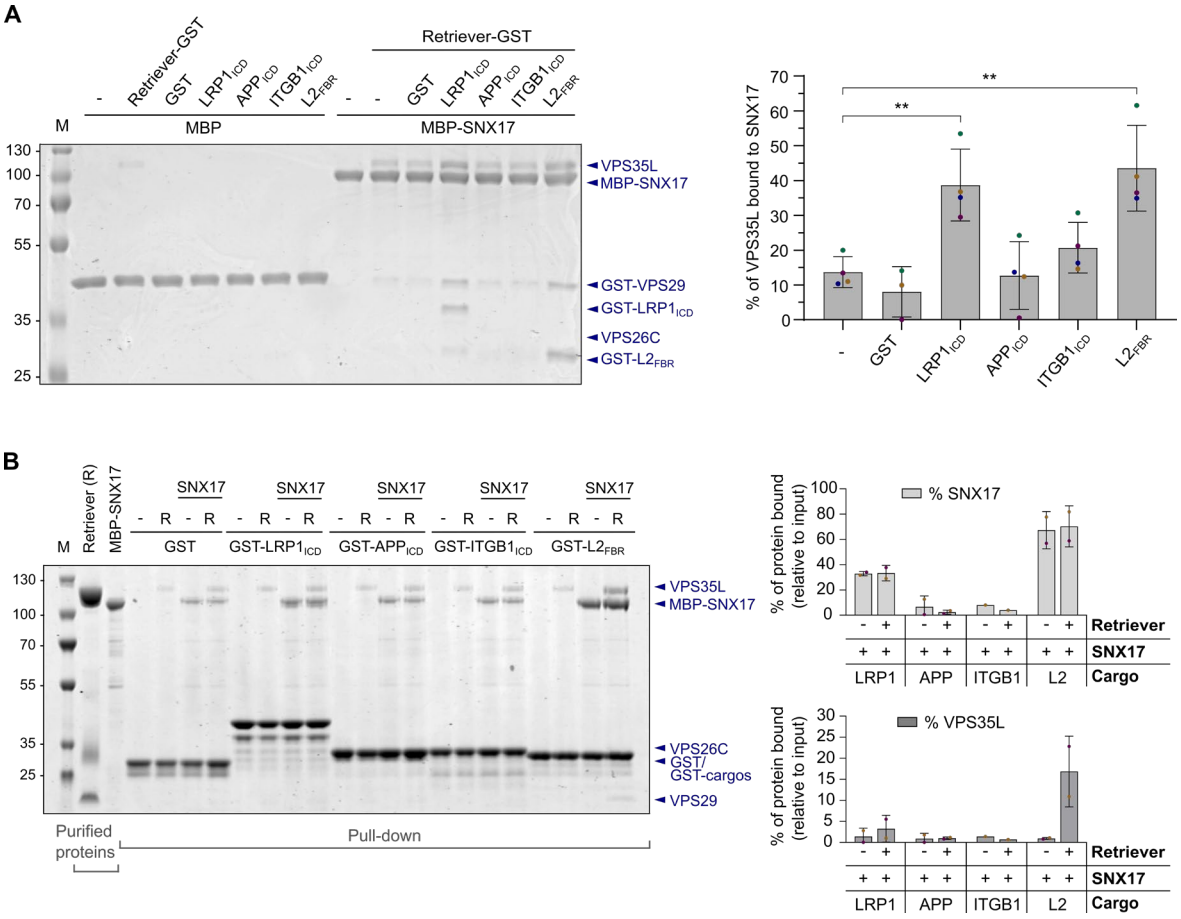

Figure 40. SNX17 interaction with cargo triggers Retriever recruitment. (**A**) The interaction of the Retriever complex with MBP-SNX17 was evaluated in the presence and absence of the cargos $LRP1_{ICD}$, APP_{ICD}, $ITGB1_{ICD}$, and $L2_{FBR}$, each fused with GST, in MBP pull-down assays. Non-fused MBP protein was used as a negative control. Proteins were visualized by Coomassie Blue staining. The right panel shows the quantification of the Retriever binding to SNX17. Quantification was carried out using ImageJ, measuring VPS35L as a representative band of the Retriever complex. The ratio of the VPS35L pull-down band to the MBP-SNX17 band was calculated in each lane, assuming a one-to-one binding stoichiometry. Non-specific

binding of VPS35L to MBP was subtracted from the VPS35L band intensities. The results are expressed as mean ± SD (n = 4 technical replicates). Statistical analysis was performed using unpaired Student's t-test, with cargo vs. without cargo. ** p = 0.004. M, protein marker. (**B**) The Retriever complex was incubated with MBP-SNX17 in the presence of GST-LRP1$_{ICD}$, GST-APP$_{ICD}$, GST-ITGB1$_{ICD}$, and GST-L2$_{FBR}$ in GST pull-down assays. Non-fused GST protein was used as a negative control. Purified proteins and pull-down samples were separated by SDS-PAGE and visualized by Coomassie Blue staining (a representative gel shown). The right panel presents the densitometry-based quantification of the amount of SNX17 or Retriever retained in the cargo-GST pull-down assays. VPS35L was used as a representative band of the Retriever complex. The band intensities of SNX17 and VPS35L were normalized to the GST or GST-cargo band intensity. Non-specific binding to GST was subtracted. The percentage of SNX17 or VPS35L binding to GST-cargos was calculated as the ratio of the pull-down protein to the input protein (lanes 2 and 3). Values represent mean ± SD of two independent experiments. *M*, protein marker; *R*, Retriever.

Furthermore, mutating the NPxY motif to APxA in LRP1 and L2 abolished their binding to SNX17, and no significant increase in Retriever retention was observed in MBP-SNX17 pull-downs with these mutants (**Figure 41**). Given their high binding affinity to SNX17, LRP1 and L2 were chosen for further *in vitro* characterization of the cargo-SNX17-Retriever complexes. Despite L2 being a viral cargo, it is predicted to bind to the same SNX17 pocket as cellular cargos (Bergant et al., 2017; Bergant Marušič et al., 2012).

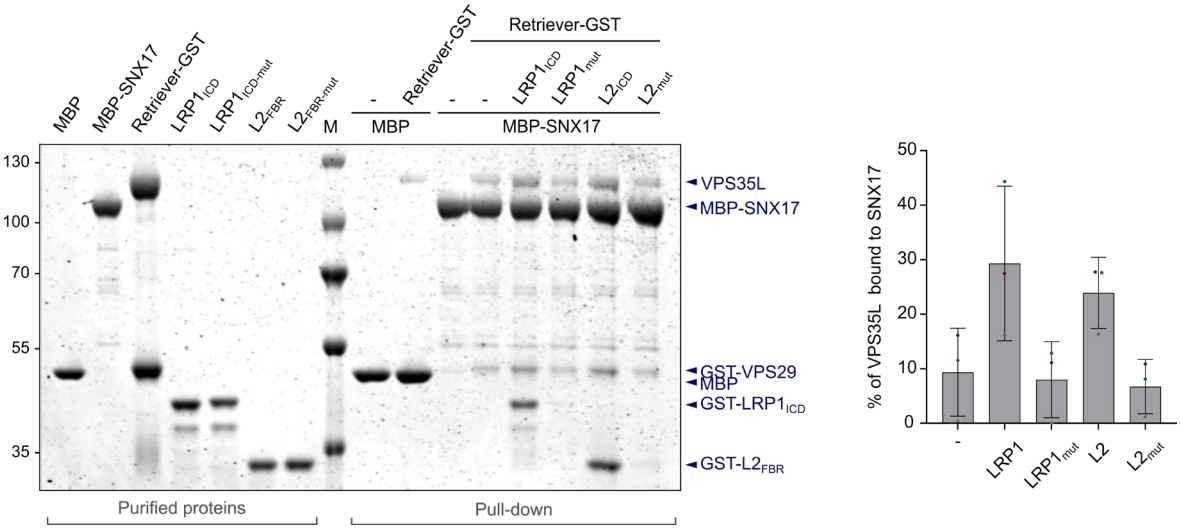

Figure 41. The NPxY motif of the cargo is crucial for SNX17 binding and subsequent Retriever recruitment. (**C**) The effect of mutating the conserved NPxY motif to APxA in LRP1 and L2 on the cargo-dependent Retriever-SNX17 interaction. Coomassie-stained SDS-PAGE gel of pull-down assays with MBP-SNX17 and Retriever in the presence of GST-LRP1$_{ICD}$, GST-LRP1$_{ICD-mut}$ (N4470A+Y4473A), GST-L2$_{FBR}$, and GST-L2$_{FBR-mut}$ (N254A+Y257A). Retriever binding to MBP-SNX17 was quantified as described in panel A. Values represent mean ± SD of three independent experiments. *M*, protein marker; *R*, Retriever.

The effect of ionic strength on the cargo-mediated interaction between SNX17 and Retriever was also examined. At low salt concentrations (50 mM NaCl), a strong interaction was observed even in the absence of cargo, likely due to non-physiological interactions between oppositely charged regions. However, increasing the salt concentration to physiological levels (150 mM) significantly reduced the binding of Retriever to SNX17 in the absence of cargo, with a more pronounced effect at 300 mM NaCl (**Figure 42**). Based on these observations, subsequent *in vitro* assays were conducted at a salt concentration of 200-300 mM NaCl, which is closer to physiological conditions and optimal for our studies.

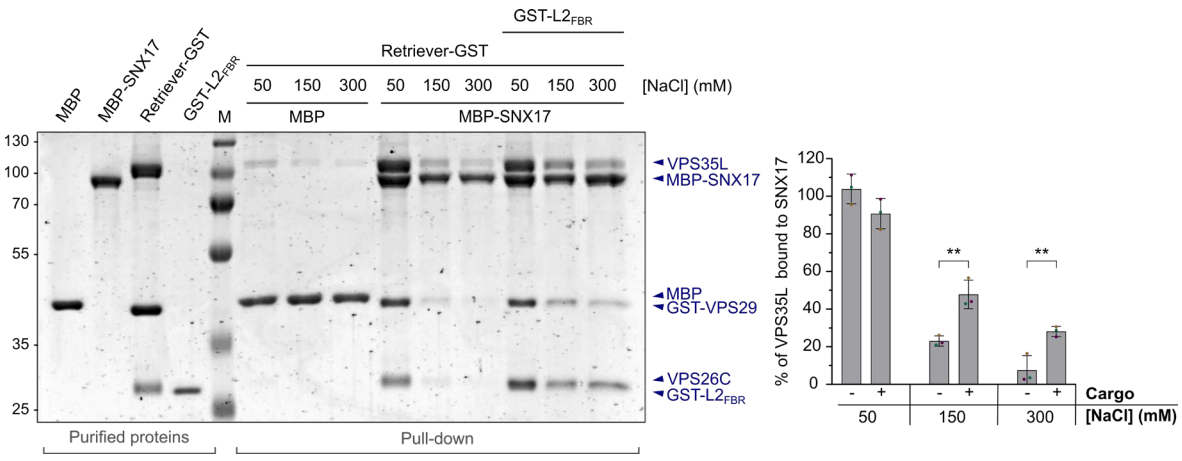

Figure 42. MBP pull-down assays to examine the impact of salt concentration on the SNX17-Retriever interaction in the presence or absence of cargo. The Coomassie-stained SDS-PAGE gel shown is a representative image of three technical replicates. MBP was included as a control for non-specific binding. Retriever binding to MBP-SNX17 was quantified as described in **Figure 41**. Statistical analysis was performed using unpaired Student's t-test, with cargo vs. without cargo, under the three different salt conditions. ** $p \leq 0.01$. *M*, protein marker; *R*, Retriever.

The C-terminal end of SNX17 contacts the VPS35L/VPS26C interface

To delineate the interaction region between SNX17 and Retriever, we employed AF2-multimer to generate models of their assembly. We predicted the structure of the entire Retriever complex with SNX17 (**Figure 43A**), and the structure of the Retriever subunits VPS26C:VPS35L$_{110-598}$ in complex with either the last 18 residues of SNX17 (SNX17$_{CT-18}$) (**Figure 43B**), or with full-length SNX17 and the cargo peptide L2$_{17-mer}$ (residues 245-261) (**Figure 44**). All the generated structural models consistently showed that the C-terminal tail of SNX17 binds to a groove at the VPS26C-VPS35L interface making several polar and hydrophobic contacts with residues along the groove. These SNX17 residues are trapped by a VPS35L β-hairpin featuring a long turn that includes an α-helix (amino acids 135-178). We named this structural motif the hinge region since we speculate that the β-strands act as a molecular hinge, conferring dynamic adaptability to the residues between the β-strands. Notably, this hinge region is absent in the Retriever structure determined by cryo-EM (Boesch et al., 2024) and is characterized by low pLDDT (predicted local distance difference test) scores in the AF2-multimer models (**Figures 43** and **44**), suggesting that it exhibits flexibility in solution. Such flexibility likely facilitates the insertion of the SNX17 C-terminus into the space framed by the hinge region and the VPS26C-VPS35L interface. The precise position of the hinge region varies across the AF2 models of the different constructs analyzed. In the SNX17$_{CT-18}$:VPS26C:VPS35L$_{110-598}$ model, it is located in the most closed position, supported by salt bridges between specific residues of VPS35L and SNX17 (**Figure 43B**). The position of SNX17 last 12 residues at the VPS26C-VPS35L interface is well supported by high pLDDT) scores in the SNX17$_{CT-18}$:VPS26C:VPS35L$_{110-598}$ model (pLDDT > 90 for the last 4 residues, and 73 < pLDDT < 90 for residues 459-465) (**Figure 43B**). Furthermore, the PAE (Predicted Aligned Error) plots of the three Retriever-SNX17 complexes analyzed demonstrate a high level of confidence in the relative position of the last 18 residues of SNX17 with respect to the Retriever subunits. Additionally, sequence conservation analysis with ConSurf highlights the evolutionary conservation of the Retriever binding residues within SNX17, which reinforces the role of this sequence in Retriever interaction (**Figure 44**). In the SNX17:VPS26C:VPS35L$_{110-598}$:L2$_{17-mer}$ model, an additional SNX17 binding interface is identified involving the VPS26C surface at the apex of the two β-sandwich domains, and the SNX17 FERM F1 and F2 regions. This interaction was observed in eight of the ten models generated by AF2 (**Figure 44**), and the contact residues are evolutionarily conserved across human orthologs, including the early Metazoan *Nematostella vectensis* (**Figures 45**, **46** and **47**).

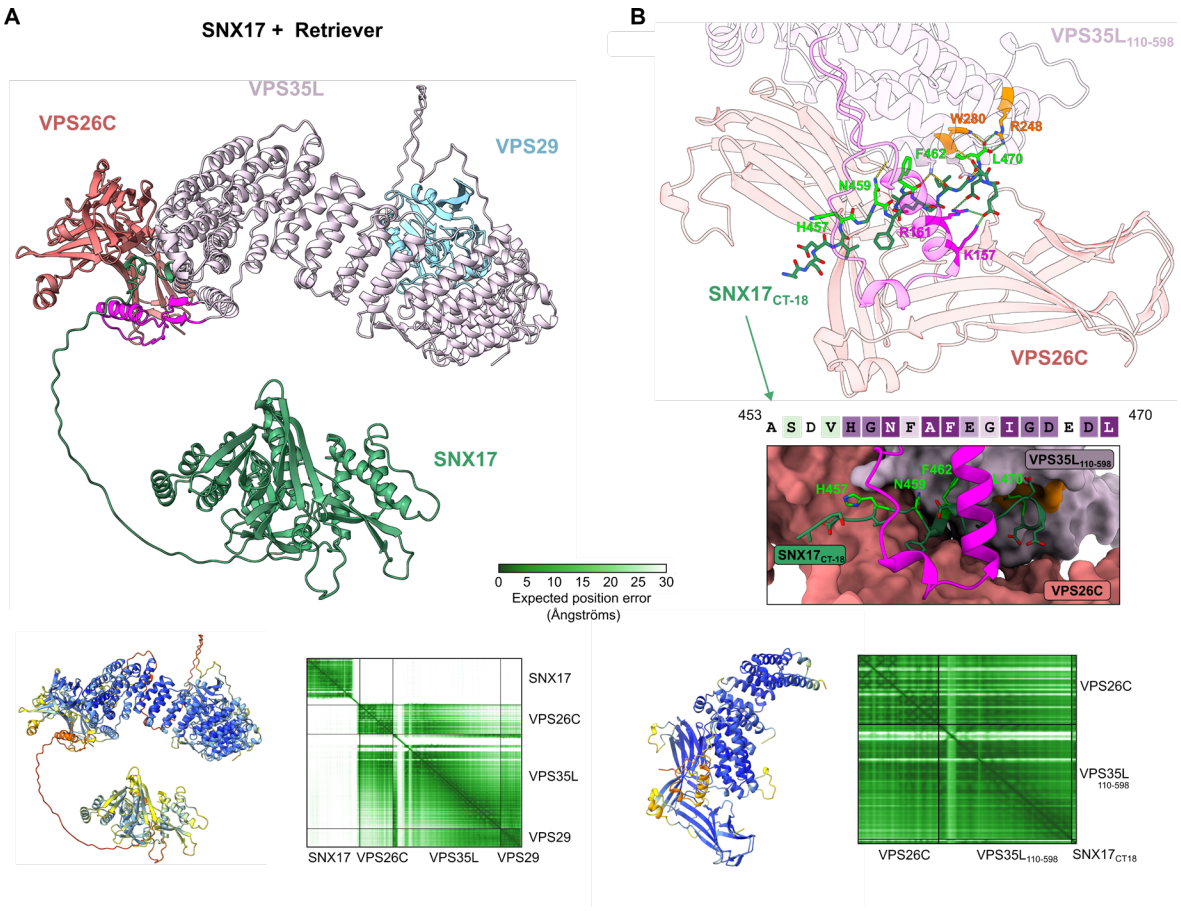

Figure 43. AlphaFold2-multimer predictions of Retriever-SNX17 interactions. (**A**) Cartoon representation of the AF2 model of the SNX17:Retriever complex. VPS26C is colored in red, VPS35L in light pink, SNX17 in green, and the hinge region of VPS35L (residues 135-178) is colored in magenta. In the second representation, the model is colored according to the pLDDT confidence score (blue, very high confidence pLDDT ≥ 90; cyan, high confidence 70 ≤ pLDDT < 90; yellow, low confidence 50 ≤ pLDDT < 70; orange, very low confidence pLDDT < 50). The graph at the bottom displays the corresponding PAE plot. (**B**) Top panel: Detailed view of the SNX17$_{CT-18}$ interaction with the VPS35L-VPS26C interface in the AF2 model of the complex SNX17$_{CT-18}$:VPS26C:VPS35L$_{110-598}$. Proteins are color-coded as in panel A. Residues involved in H-bonds (yellow dashed lines), salt bridges (green dashed lines), and those mutated in this thesis are shown as sticks. The mutated residues are highlighted with a different color: SNX17 residues with light green, residues of the VPS35L C-terminal binding pocket in orange, and residues of the VPS35L hinge region in magenta. Middle panel: The sequence of SNX17$_{CT-18}$ colored according to sequence conservation calculated with the ConSurf server using green-through-purple scale, corresponding to variable (grade 1) through conserved (grade 9) positions. Zoomed-in-view of the binding surface of SNX17$_{CT-18}$ is shown, with SNX17 residues displayed as cartoon and sticks, and the hinge region of VPS35L (residues 135-178) in magenta. Mutated residues are colored as in the top panel. Bottom panel: Cartoon representation of SNX17$_{CT-18}$:VPS26C:VPS35L$_{110-598}$ model, colored according to the pLDDT confidence score as in A, and the corresponding PAE plot. Structural models were visualized with ChimeraX. *PAE*, predicted aligned error.

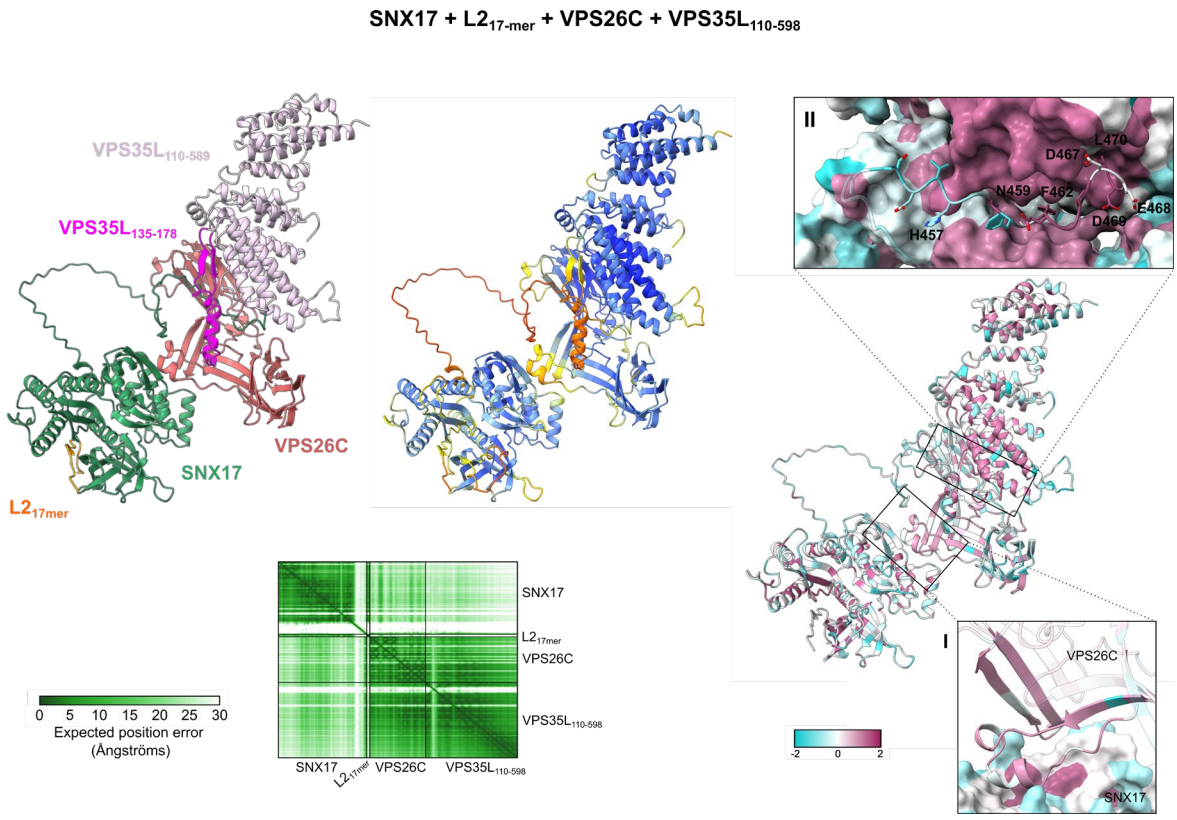

Figure 44. AF2 model of SNX17:L2$_{17\text{-mer}}$:VPS26C:VPS35L$_{110\text{-}598}$. Cartoon representations of AF2-multimer predicted structure of SNX17:L2$_{17\text{-mer}}$:VPS26C:VPS35L$_{110\text{-}598}$. On the first representation, SNX17 colored is colored green, L2 orange, VPS26C red and VPS35L$_{110\text{-}598}$ pink. The hinge region (VPS35L$_{135\text{-}178}$) is highlighted in magenta. In the second representation, the model is colored according to the pLDDT confidence score, following the same color key as in **Figure 43**. The graph at the bottom displays the corresponding PAE plot. In the third representation, the model is colored according to the evolutionary conservation calculated by AL2CO (Pei & Grishin, 2001) implemented in ChimeraX using the alignments of SNX17 (**Figure 45**), VPS26C (**Figure 46**) and VPS35L (**Figure 47**), with blue-to-purple color scale indicating variable-to-conserved positions. Zoomed-in view I focused on the interaction interface between VPS26C (in cartoon) and SNX17 (as surface). Zoomed-in view II shows the conservation of the SNX17$_{CT\text{-}18}$ binding pocket, with SNX17 residues as sticks, and VPS26C and VPS35L$_{110\text{-}598}$ as surface. The orientation is the same as in **Figure 43B.** To facilitate visualization of the binding pocket, the residues 135-178 of VPS35L were omitted. *PAE*, predicted aligned error.

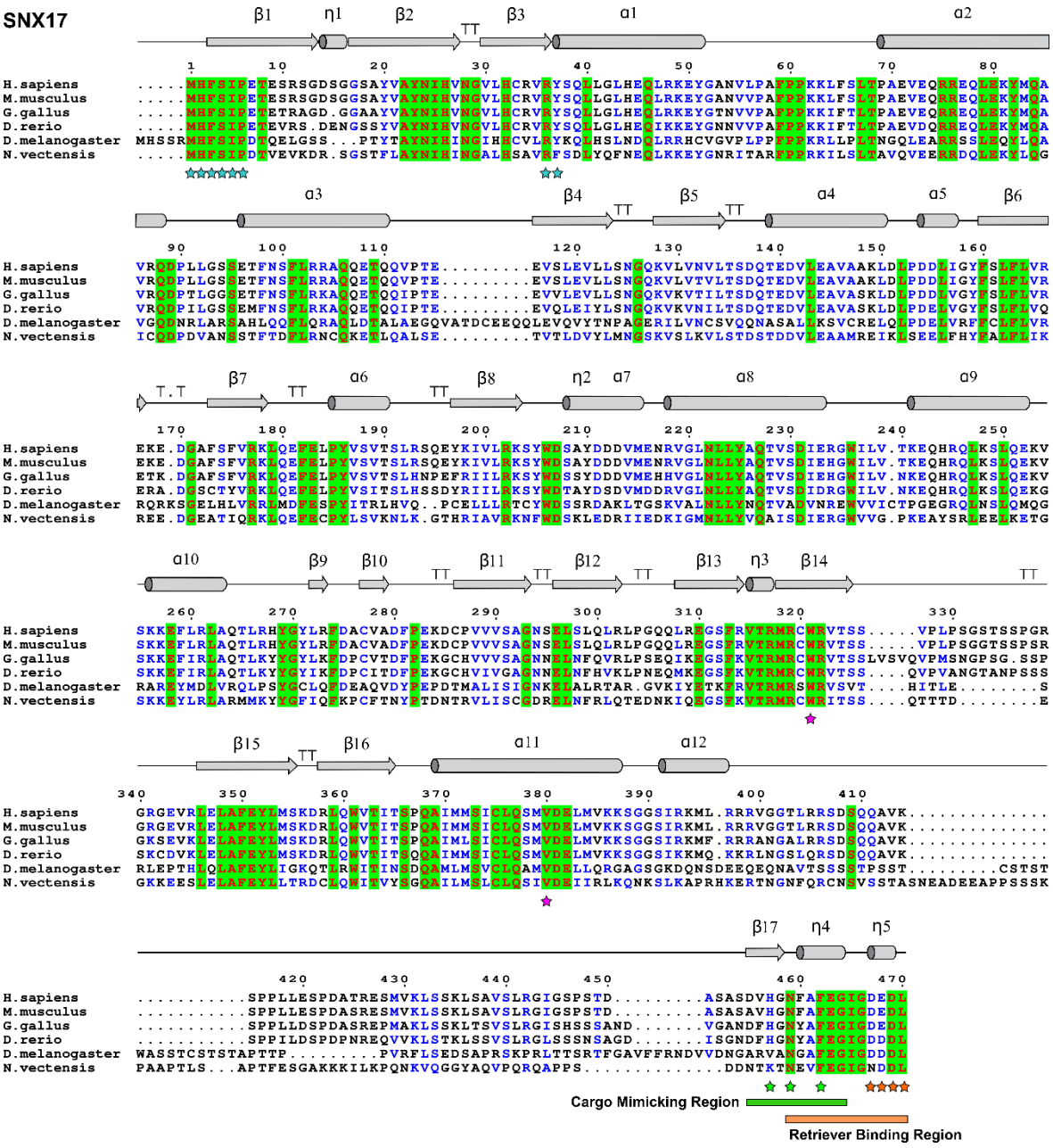

Figure 45. Conservation of contact residues across SNX17 orthologs. Structure-based sequence alignment of human SNX17 and orthologs generated with the PROMALS3D server and plotted with ESPript 3. The UniProt accession numbers of the AF2 models used in the sequence alignment are as follows: *Homo sapiens* (Q15036), *Mus musculus* (Q8BVL3), *Gallus gallus* (A0A1D5NVF3), *Danio rerio* (Q5RID7), *Drosophila melanogaster* (Q9VL28), and *Nematostella vectensis* (A7SGL2). The numbering of the residues and secondary structure annotations refer to SNX17 from *Homo sapiens*. α refers to alpha-helices and η to 3_{10} helices (both represented as cylinders). β refers to beta-strands (represented as arrows) and TT to strict β-turns. Invariant residues are colored red on a green background, and conserved residues are in blue. Mutated residues implicated in membrane binding are marked with blue starts, mutated residues involved in the autoinhibition mechanism are marked with purple stars (for the cargo-binding pocket) or green stars (for the cargo-mimicking region), and mutated residues critical for Retriever binding are marked with orange stars.

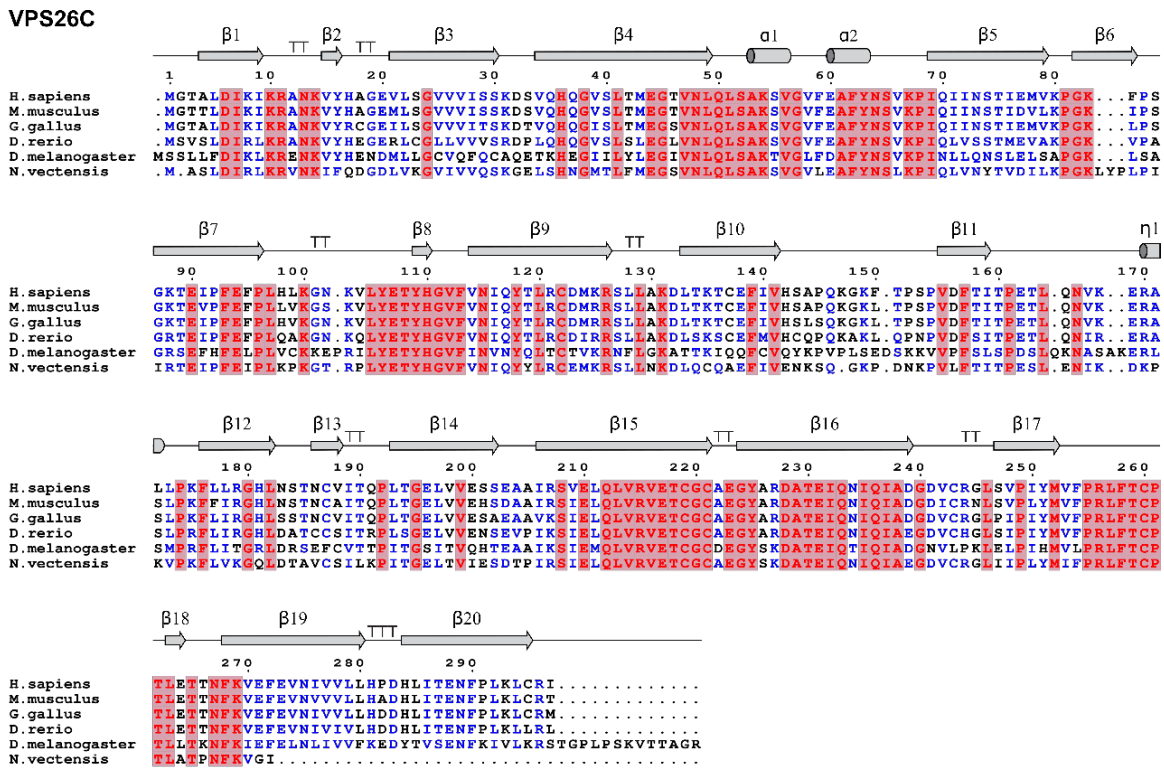

Figure 46. Conservation of contact residues across VPS26C orthologs. Structure-based sequence alignment of human VPS26C and orthologs. The alignment was generated as detailed in **Figure 45**. The color code is the same as in **Figure 45**, except for invariant residues, which are highlighted with a red background. The residue numbering and the secondary structure elements shown above the alignment correspond to human VPS26C. The UniProt accession numbers of the AF2 models used in the alignment are as follows: *Homo sapiens* (O14972), *Mus musculus* (O35075), *Gallus gallus* (E1BSI1), *Danio rerio* (Q6DHL2), *Drosophila melanogaster* (Q9VPC3), and *Nematostella vectensis* (A7S8I4).

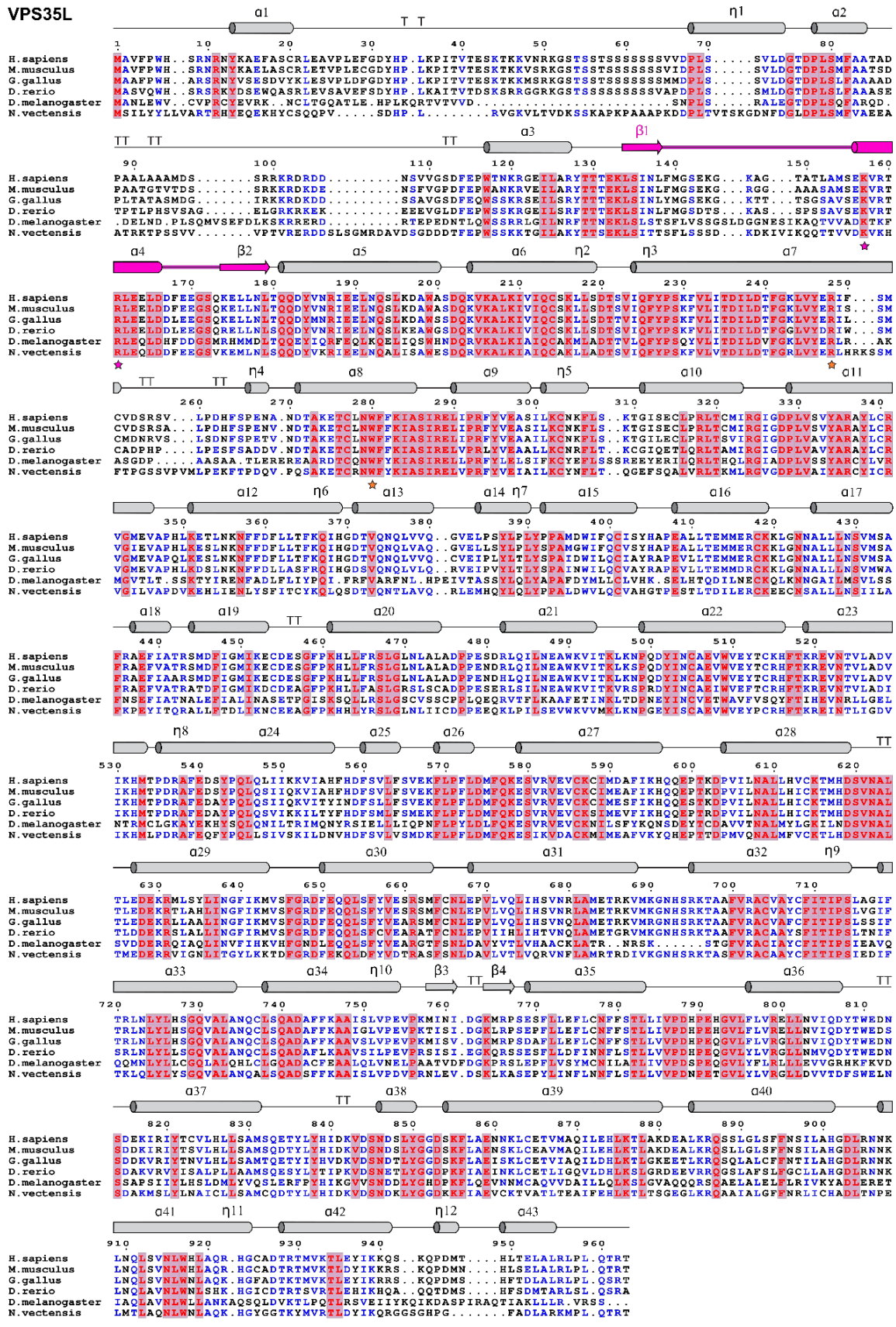

Figure 47. Conservation of contact residues across VPS35L orthologs. Structure-based sequence alignment of human VPS35L with its orthologs. The alignment generation process and the color-coding scheme are the same as those described in **Figure 45**, except for invariant residues, which are highlighted with a pink

background. The residue numbering and the secondary structure elements shown above the alignment correspond to human VPS35L. The UniProt accession numbers of the AF2 models used in the alignment are as follows: *Homo sapiens* (Q7Z3J2), *Mus musculus* (Q8BWQ6), *Gallus gallus* (A0A1D5PY39), *Danio rerio* (A4VCH4), *Drosophila melanogaster* (Q9VHM2), and *Nematostella vectensis* (XP_048575353). AF2 models were downloaded from the AlphaFold Protein Structure Database, with the exception of the model for *Nematostella vectensis*, which was obtained using ColabFold. The secondary structure elements of the hinge region are colored in magenta. Residues mutated in this work located in the SNX17 L470 binding pocket are marked with orange stars (R248 and W280), and those within the hinge region are marked with magenta stars (K157 and R161).

To validate the predicted interaction region between Retriever and SNX17 bound to cargo, various SNX17 constructs were initially assessed. As expected, the PX domain of SNX17 did not bind the cargo and does not interact with Retriever (**Figure 48**). The pull-down assays confirmed that the interaction domain resides in the FERM-CT region, since this construct ($SNX17_{FERM\text{-}CT}$) exhibited comparable Retriever recruitment as the full-length protein ($SNX17_{FL}$).

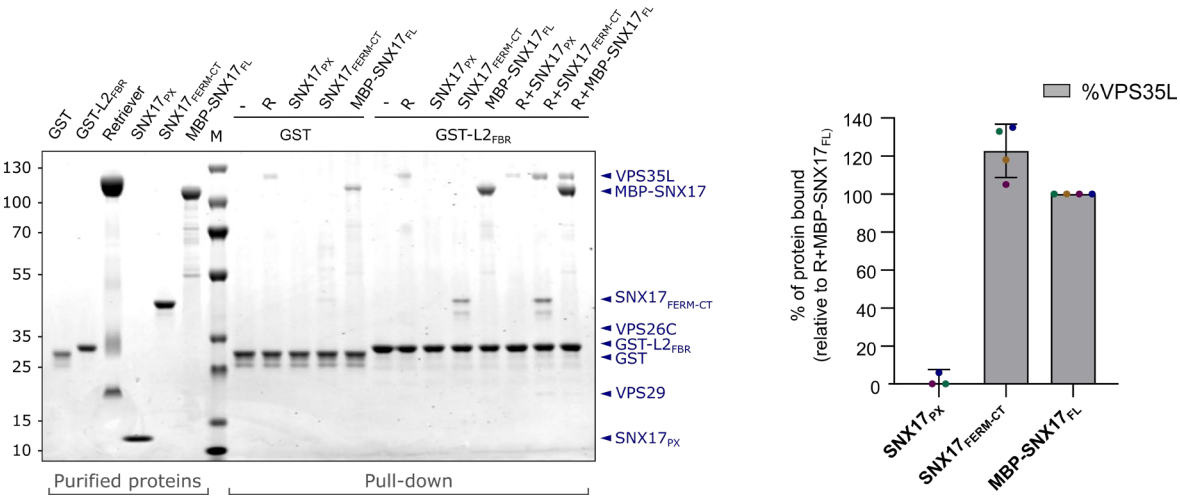

Figure 48. The FERM-CT domain of SNX17 is sufficient for Retriever recruitment. GST pull-down assays to map the region of SNX17 that interacts with Retriever. GST-$L2_{FBR}$ was incubated with $SNX17_{PX}$, $SNX17_{FERM\text{-}CT}$ and MBP-$SNX17_{FL}$. Non-fused GST protein was used as a negative control. Samples were loaded onto an SDS-PAGE gel and stained with Coomassie Blue. Densitometry-based quantification was carried out with ImageJ, measuring VPS35L as a representative band of the Retriever complex. The band intensities of VPS35L were normalized to the GST or GST-cargo band intensity. Non-specific binding to GST was subtracted. The percentage of VPS35L bound in the presence of MBP-$SNX17_{FL}$ and GST-$L2_{FBR}$ was set to 100%, and the values for the other conditions were calculated relative to this. Values represent mean ± SD based on four technical replicates. *M*, protein marker; *R*, Retriever.

Previous studies performed using immunoprecipitation techniques with cell lysates (McNally et al., 2017) have provided preliminary insights into the involvement of the C-terminus of SNX17 in its association with Retriever. However, no direct *in vitro* reconstitution was available. Therefore,

we purified and tested two previously examined SNX17 mutants: a truncation of the terminal four residues (D467X) and the substitution of the last leucine with glycine (L470G) (McNally et al., 2017). The deletion mutant displayed a slight reduction in binding affinity for the cargos LRP1 and L2 (**Figure 49A**) in fluorescence anisotropy assays, but no change was observed with the point mutation L470G. These results indicate that the cargo binding is not compromised with the studied mutations, as expected because the cargo-binding pocket is not disrupted. However, these SNX17 mutants failed to pull-down the Retriever complex, in the absence or presence of cargo (**Figure 49B**).

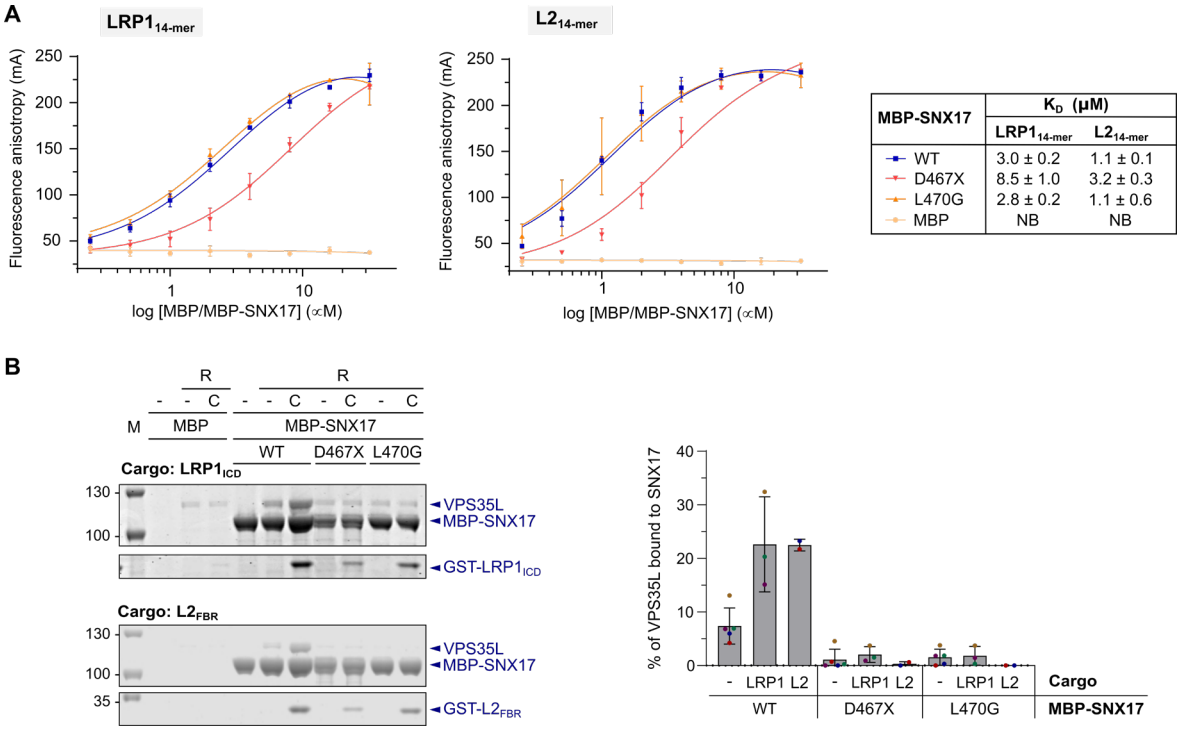

Figure 49. The C-terminal end of SNX17 contacts the Retriever complex. (**A**) Effect of SNX17 mutants of the Retriever-binding region on cargo binding affinity. Fluorescence anisotropy binding curves of 5-FAM-labeled LRP1$_{14\text{-mer}}$ or L2$_{14\text{-mer}}$ peptide titrated with indicated SNX17 mutants. Data points are the mean ± SD of two biological replicates, with MBP-SNX17 and its mutants obtained from two independent protein purifications. The estimated K_D ± SD of each mutant is listed in the right panel. MBP is used as negative control. (**B**) Analysis of the interaction between Retriever and SNX17 mutants in the presence and absence of the cargos LRP1 or L2**.** MBP pull-down assays were performed with wild-type MBP-SNX17 or indicated mutants, Retriever, GST-LRP1$_{ICD}$ or GST-L2$_{FBR}$. Non-fused MBP protein was used as a negative control. Samples were loaded onto an SDS-PAGE gel and stained with Coomassie Blue. Quantification was carried out as detailed in **Figure 40A**. The graph represents the mean ± SD of technical replicates (LRP1: n = 3; L2: n=2). *M*, protein marker; *R*, Retriever; *C*, cargo; *WT*, wild-type.

In the AF2-multimer models, SNX17 C-terminal residue L470 establishes a hydrophobic interaction with VPS35L W280, and its carboxyl group forms a salt bridge with VPS35L residue R248 (**Figure 43B**). Our results prove that this interaction is a key determinant for the stability of the Retriever-SNX17 complex. Since the relevant Retriever-binding region resides in the C-terminal part of SNX17, the binding ability of a peptide encompassing the final 18 residues of SNX17 ($SNX17_{CT-18}$) was tested in fluorescence anisotropy binding assays (**Figure 50**). Our analysis unveils a discernible binding affinity of the $SNX17_{CT-18}$ peptide toward the Retriever complex, characterized by a K_D of 5.7 µM. Additionally, the Retriever-binding region was mapped using different Retriever complex configurations. $SNX17_{CT-18}$ displayed a comparable affinity for full-length Retriever and VPS26C-$VPS35L_{110-598}$ (K_D = 5.3 µM). In contrast, no discernible binding was detected with VPS26C or VPS29, and only a very weak interaction was observed with VPS35L-VPS29. These results are consistent with the AF2-multimer models of the interaction surface between SNX17 and Retriever. To further validate the predicted Retriever-SNX17 interface, two Retriever mutants were tested with point mutations in the VPS35L subunit. Given that our AF models indicate that VPS26C interacts with the SNX17 C-terminus solely through main-chain mediated interactions, we did not conduct site-directed mutagenesis of VPS26C residues. The first pair of mutations, R248E+W280D, were designed to disrupt the interaction of VPS35L with L470 residue of SNX17. The second pair of mutations, K157E+R161E, disrupts the salt bridges involving amino acids K157 and R161 situated within the VPS35L hinge region and their counterparts in SNX17 (residues E468 and D469, respectively) (**Figure 43B**). The solubility and purification yield of the Retriever mutants were the same as those of the WT proteins, suggesting that the mutations do not significantly affect their structural integrity. Remarkably, Retriever with VPS35L(R248E+W280D) failed to interact with the $SNX17_{CT-18}$ peptide, and Retriever with VPS35L(K157E+R161E) displayed a pronounced 5-fold decrease in binding affinity (K_D = 30 µM) (**Figure 50**). Therefore, these mutagenesis results validate the predicted interaction cavity in Retriever for SNX17 binding.

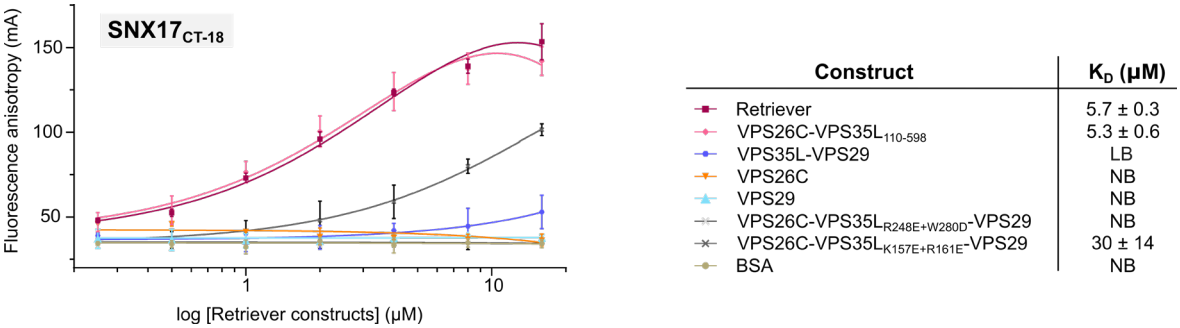

Figure 50. Mapping the interaction between SNX17 and the Retriever complex. Fluorescence anisotropy assays measuring direct interaction between 5-FAM-labeled $SNX17_{CT-18}$ peptide and the indicated Retriever constructs to delimit the SNX17 binding region in Retriever. BSA protein was used as a negative control. Data

points are the mean ± SD of two technical replicates. Bottom panel: K_D values ± SD calculated using GraphPad Prism, unless too weak to be determined. *NB*, no detectable binding; *LB*, low binding (poor fit quality).

It should be noted that the AF2-multimer model of the SNX17:$L2_{17\text{-mer}}$:VPS26C:$VPS35L_{110\text{-}598}$ complex (**Figure 44**, panel I) suggests an additional SNX17-VPS26C interface, involving the FERM F1 and F2 regions of SNX17. However, no interaction between SNX17 and VPS26C was detected in our experiments (**Figure 39**). We suggest that the strong affinity of the C-terminal tail of SNX17 for the VPS26C-VPS35L interface entraps Retriever and facilitates the predicted, possibly weaker, interaction between SNX17 and VPS26C, thereby drawing Retriever towards the membrane.

4.3.2. Characterization and validation of SNX17 autoinhibition mechanism for Retriever binding *in vitro*

SNX17 autoinhibition mechanism for Retriever binding in the absence of cargo

We then embarked on deciphering the molecular mechanism that controls SNX17 activation via cargo binding, a process that facilitates the binding of the Retriever complex.

As previously mentioned in section 4.2.4, published structures of SNX17 are available, but none of them feature the CT region, which is predicted to be disordered. Despite extensive x-ray crystallization trials, I was unsuccessful in solving the structure (**Figure 30**). However, the AF2 model of SNX17 (UniProt Q15036) includes the CT region, consisting of an extensive unstructured loop, three short α-helices, and a β-strand (**Figure 25**, section 4.2.2. and **Figure 51A**). Interestingly, the predicted β-strand and the subsequent α-helix (residues 455-464) are located within the cargo-binding pocket, precisely where the P-selectin and the KRIT1 peptide bind in the structures determined by X-ray crystallography (**Figure 51B**). Moreover, the sequence alignment of the terminal 18 residues of SNX17 with the FERM binding motif of LRP1 and L2 shows that the NxxY binding motif is partially conserved in SNX17, with is a phenylalanine replacing the tyrosine (**Figure 51**). These observations led us to designate this sequence as the cargo-mimicking region. The structural prediction for this particular region has moderate confidence, with pLDDT scores ranging from 57 to 71 (**Figure 51C**). However, this sequence exhibits significant conservation across the orthologs of human SNX17 (**Figure 45**). Consistently, in all the AF2 models of SNX17 orthologs we examined, the equivalent residues occupy the cargo-binding pocket and their PAE values indicate high confidence of this intramolecular interaction (**Figure 52**). We then compared the AF2 model of SNX17 with the model of SNX17:$L2_{FBR}$, and observed that the $L2_{FBR}$ is correctly modeled bound to the cargo binding groove. Remarkably, the association with cargo causes a shift of the CT domain, leading to a pronounced conformational change in this region, characterized by the emergence of a highly flexible and unfolded loop comprising the Retriever-binding region at the C-terminus (**Figure**

51B). Such conformational change was consistently observed across all AF2 models of SNX17 when complexed with each cargo examined in this work (**Figure 53**).

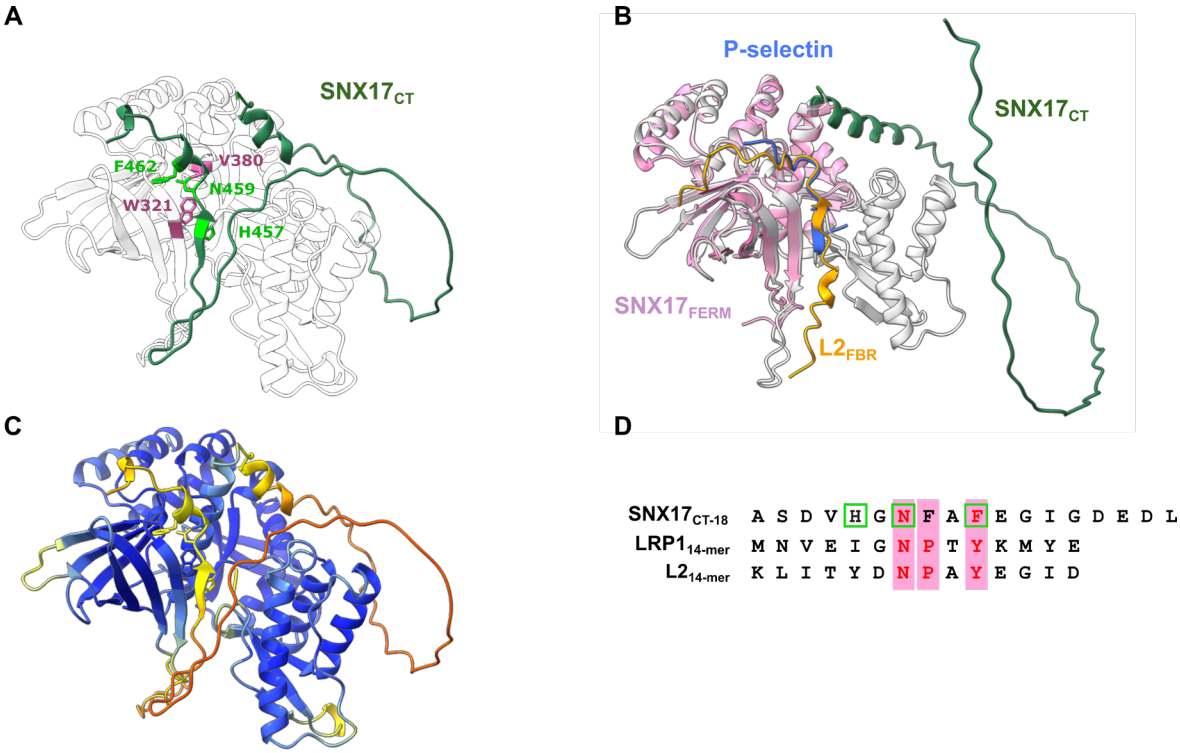

Figure 51. Structures of SNX17 in the presence and absence of cargo, and sequence alignment of the CT-18 region. (**A**) SNX17 residues involved in the autoinhibition mechanism. The CT region of SNX17 (residues 389 to 470) is depicted in dark green. Key amino acids are highlighted with sticks; W321 and V390 residues belong to the cargo-binding pocket (pink), whereas H457, N459, and F462 residues are part of the cargo-mimicking region (light green). (**B**) Alignment of the $SNX17_{FERM}$:P-selectin crystal structure (PDB ID: 4GXB) with the SNX17-$L2_{FBR}$ AF2 model. SNX17 (grey) aligns with $SNX17_{FERM}$ (pink), and the $L2_{FBR}$ peptide (orange) occupies the same position in the cargo-binding pocket as the P-selectin peptide (blue). In the presence of L2 cargo, the CT region of SNX17 (green) is positioned distantly from the cargo- binding pocket, thus making the CT region accessible for potential interactions with other proteins. (**C**) Cartoon representation of the AF2 model for human SNX17 (UniProt Q15036), colored by pLDDT confidence score. The prediction confidence color-coding is the same as **Figure 43**. (**D**) Sequence alignment of $SNX17_{CT-18}$ with the FERM binding motifs of LRP1 and L2. Residues targeted in mutagenesis studies are marked with green squares.

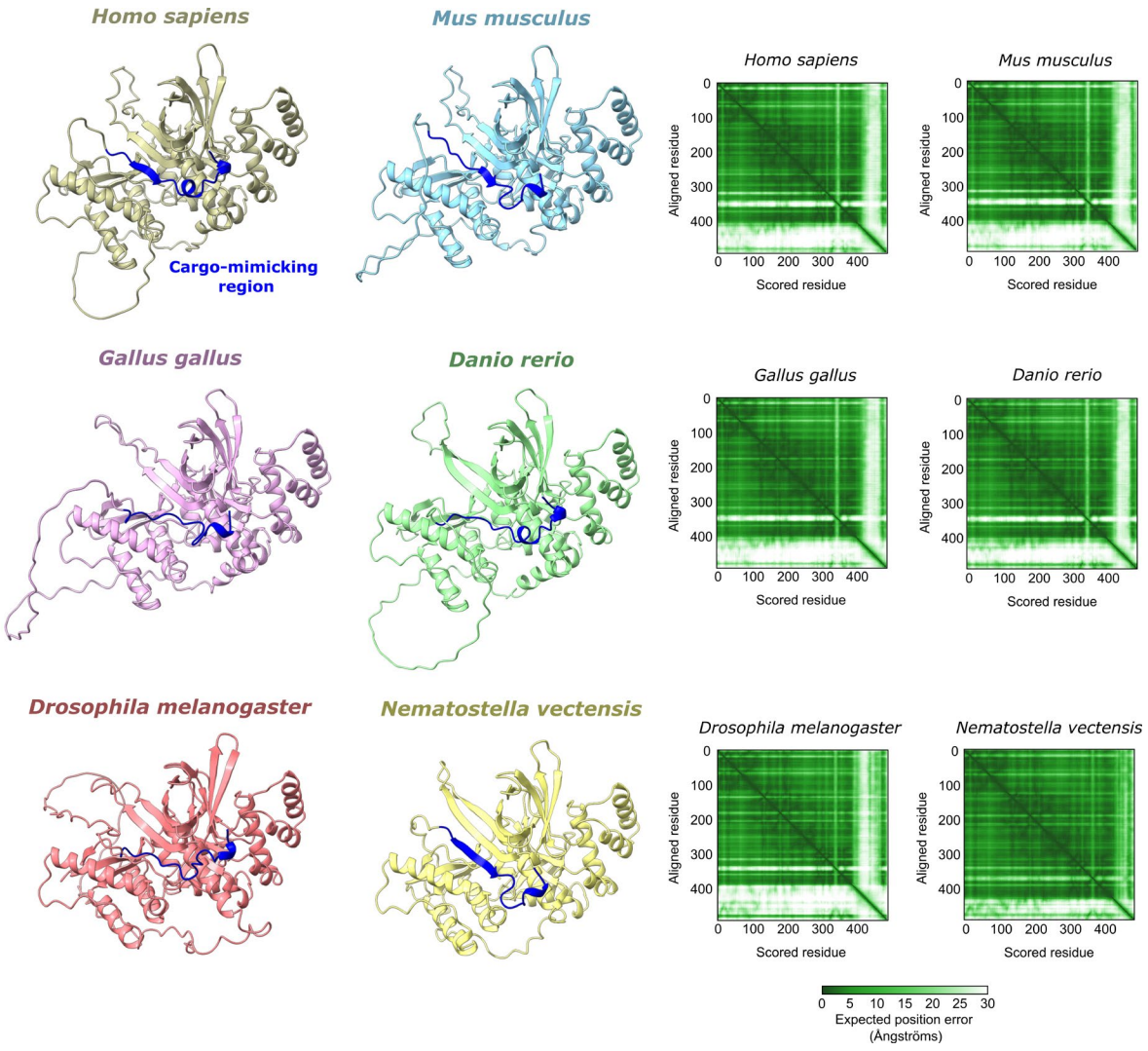

Figure 52. Conservation of the autoinhibitory mechanism across SNX17 orthologs. AF2 models of human SNX17 and orthologs with the corresponding PAE plots. The cargo-mimicking region (from 453 to 470 in the human sequence) is highlighted in dark blue. Models were downloaded from the AlphaFold Protein Structure Database, with the exception of the *Nematostella vectensis* model, which was obtained using ColabFold. The UniProt accession numbers for these proteins are detailed in **Figure 45**.

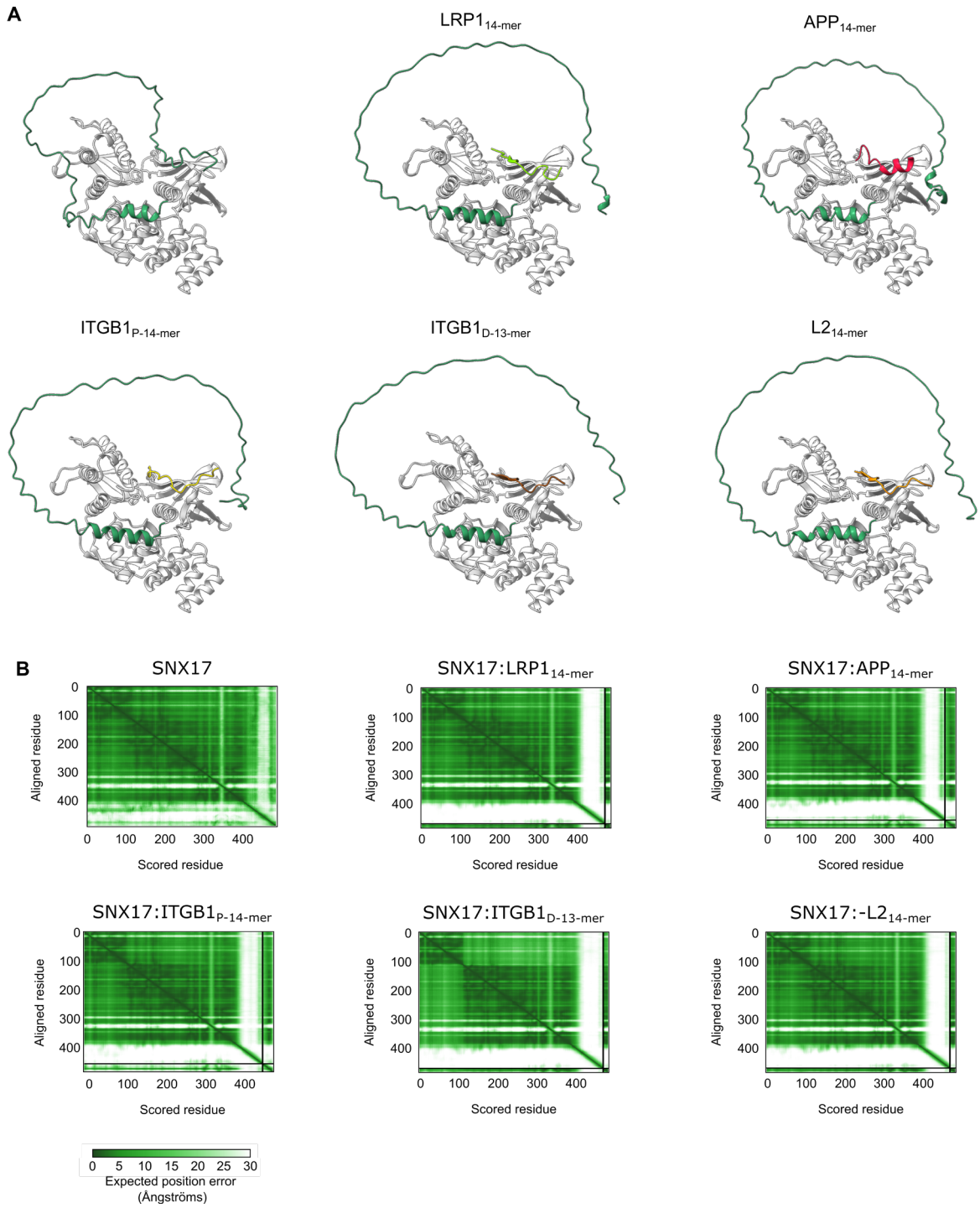

Figure 53. Assessment of the disruption of SNX17 autoinhibited conformation through cargo binding using AF2-multimer modeling. (**A**) AF2-multimer prediction of the complex between SNX17 (grey) and the cargo peptides used in fluorescence anisotropy assays: $LRP1_{14\text{-mer}}$ (light green), $APP_{14\text{-mer}}$ (red), $ITG\beta1_{P\text{-}14\text{-mer}}$ (yellow), $ITG\beta1_{D\text{-}13\text{-mer}}$ (brown), and $L2_{14\text{-mer}}$ (orange). Note the displacement of the CT region (green) of SNX17 when cargo peptides are present. (**B**) PAE plots of the models shown in A.

Based on these observations, we suggest the following autoinhibition mechanism: (i) in the absence of cargo, SNX17 exhibits minimal affinity for Retriever, since the cargo-mimicking region is bound to the cargo binding groove, rendering the overlapping Retriever-binding region poorly accessible; (ii) cargo binding disrupts this inhibitory arrangement, thus liberating the Retriever-binding region; and (iii) the CT domain, which spans 80 amino acids (from 390 to 470), serves as a dynamic hook that captures the Retriever complex and brings it closer to the endosomal surface (**Figure 54**).

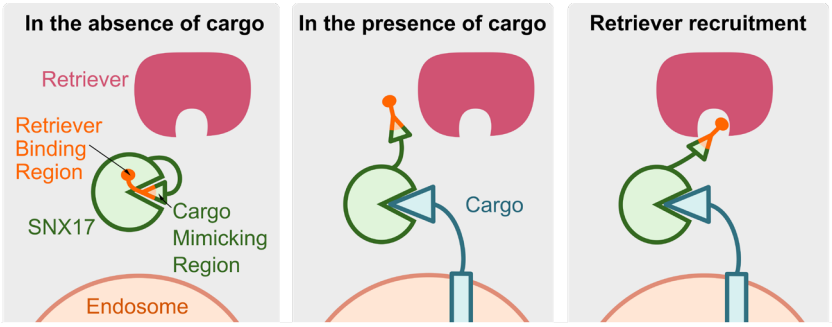

Figure 54. Diagram illustrating the potential autoinhibition mechanism of SNX17. In the absence of cargo, SNX17 exhibits minimal affinity for Retriever, because the cargo-mimicking region (depicted as a triangle) is bound to the cargo-binding pocket rendering the Retriever-binding region poorly accessible (left scene). Cargo binding displaces the inhibitory cargo-mimicking region from the pocket, freeing the Retriever-binding region (middle scene) and facilitating its association with Retriever (right scene). The Retriever-binding region and the cargo-mimicking region partially overlap.

To experimentally validate this proposed autoinhibition mechanism, we introduced specific mutations in the SNX17 residues shown in **Figure 51A**. Mutations W321A and V380D in the SNX17 cargo-binding pocket were introduced to perturb the interaction of the CT region, affecting both autoinhibition and cargo interaction. Additionally, we introduced the mutations H457A and N459A+F462A in the cargo-mimicking region to target only the autoinhibition mechanism. Fluorescence anisotropy assays confirmed that the W321A and V380D mutations effectively prevent cargo binding. In fact, the V380D mutation completely abolished binding, while the W321A mutation strongly reduced the binding affinity to the LRP1 and L2 peptides (**Figure 55**). In contrast, the N459A+F462A mutation enhanced binding affinity for both cargos by approximately two-fold, supporting the proposed role of these residues in mimicking cargo. This mutation likely frees the cargo-binding pocket, thereby increasing the affinity for cargos. On the other hand, the H457A mutation had no significant effect on binding affinity, suggesting a less critical role in the autoinhibition mechanism. To further study the proposed autoinhibition mechanism, we evaluated whether the $SNX17_{CT\text{-}18}$ peptide covering the C-terminal 18 amino acids of SNX17 along with the NxxF motif engages in autointeraction with SNX17 within its cargo-binding pocket. Fluorescence anisotropy assays confirmed that the $SNX17_{CT\text{-}18}$ peptide can bind to SNX17, with low affinity, as

expected due to competition with the internal binding of SNX17. Notably, the N459A+F462A mutation significantly enhanced binding affinity, while the W321A and V380D mutations prevented this interaction (**Figure 55**). These findings indicate that the last 18 residues of SNX17 occupy the cargo binding site, thus validating the structural model of SNX17 elucidated by AF2 and supporting the proposed autoinhibitory conformation.

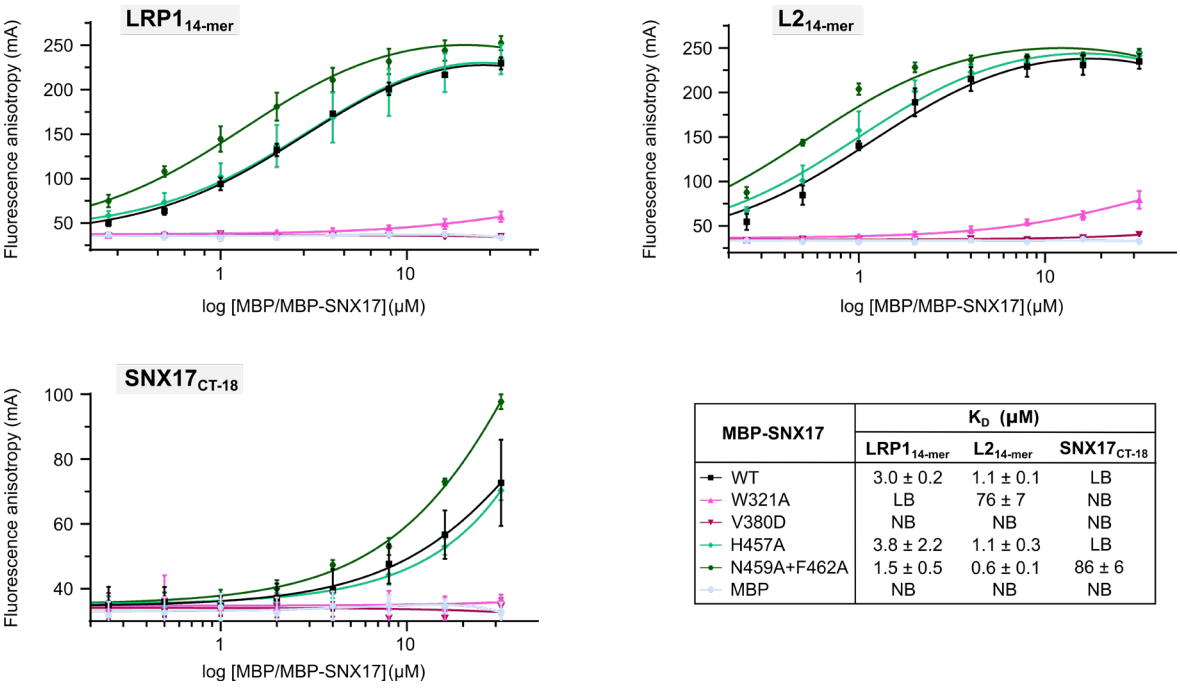

MBP-SNX17	K_D (μM)		
	$LRP1_{14\text{-mer}}$	$L2_{14\text{-mer}}$	$SNX17_{CT\text{-}18}$
WT	3.0 ± 0.2	1.1 ± 0.1	LB
W321A	LB	76 ± 7	NB
V380D	NB	NB	NB
H457A	3.8 ± 2.2	1.1 ± 0.3	LB
N459A+F462A	1.5 ± 0.5	0.6 ± 0.1	86 ± 6
MBP	NB	NB	NB

Figure 55. Fluorescence anisotropy assays to validate the autoinhibition mechanism of SNX17. Fluorescence anisotropy binding curves upon titration of indicated SNX17 mutants to 5-FAM-labeled $LRP1_{14\text{-mer}}$, $L2_{14\text{-mer}}$ or $SNX17_{CT\text{-}18}$ peptide to validate the autoinhibition mechanism. K_D values ± SD were determined from the binding curves plotted in the graphs. These values are based on three technical replicates for MBP and three biological replicates for MBP-SNX17 and its mutants, obtained from three distinct protein purifications. MBP protein was used as a negative control. *NB*, no detectable binding; *LB*, low binding (poor fit quality).

To directly evaluate whether the autoinhibition of SNX17 modulates its ability to recruit the Retriever complex, we conducted pull-down assays with the purified SNX17 mutants to examine their interaction with Retriever under cargo-present or cargo-absent conditions (**Figure 56**). The results showed that mutations W321A, V380D, and H457A significantly increased the binding of SNX17 to Retriever in the absence of cargo. This suggests that disrupting the autoinhibition process renders the CT region of SNX17 accessible, bypassing the need for cargo-induced release. In contrast, the SNX17 N459A+F462A mutant did not show enhanced binding to Retriever, regardless of cargo presence or absence. These residues are involved in the interaction with the VPS26C-VPS35L interface according to the AF2-multimer models (**Figure 43B** and **Figure 44**, panel II).

Therefore, while the CT region is expected to be released from autoinhibition, the alteration of key residues critical for Retriever interaction hampers its recruitment.

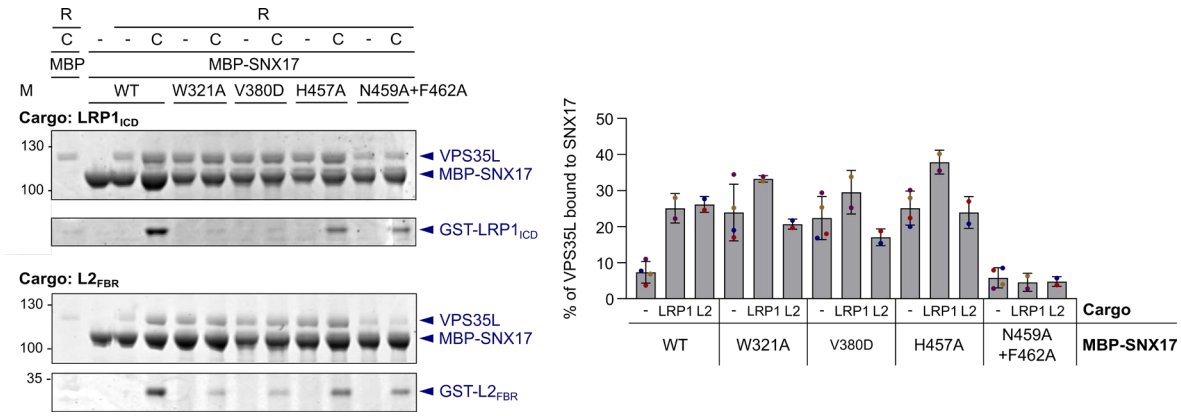

Figure 56. SNX17 autoinhibition mechanism for Retriever binding in the absence of cargo. Purified Retriever complex was incubated with the indicated MBP-SNX17 mutants in the presence or absence of GST-$LRP1_{ICD}$ or GST-$L2_{FBR}$ in MBP pull-down assays. Non-fused MBP protein was used as a negative control. Quantification of the Coomassie stained SDS-PAGE gel was carried out in ImageJ, measuring VPS35L as a representative band of the Retriever complex. The level of Retriever binding to MBP-SNX17 was quantified as described in **Figure 40A**. Values represent mean ± SD (n = 2 biological replicates, with MBP-SNX17 and its mutants obtained from two independent protein purifications). *M*, protein marker; *R*, Retriever; *C*, cargo; *WT*, wild-type.

Altogether, these results support the proposed autoinhibition state of SNX17 for Retriever association, which is unlocked through cargo binding (**Figure 54**). This mechanism explains the previously reported data, which demonstrated that the binding of cargo to SNX17 enhances its ability to recruit the Retriever complex.

4.3.3. Cryo-EM of the Retriever-SNX17-cargo complex

Solving the structure of the Retriever complex together with SNX17 and the cargo by cryo-electron microscopy would enable us to visualize the proteins within the complex at near-atomic resolution, enhancing our understanding of their interactions and functional dynamics. We successfully isolated a stable complex of Retriever, SNX17 and the cargo $L2_{FBR}$ using gel filtration chromatography (**Figure 57**).

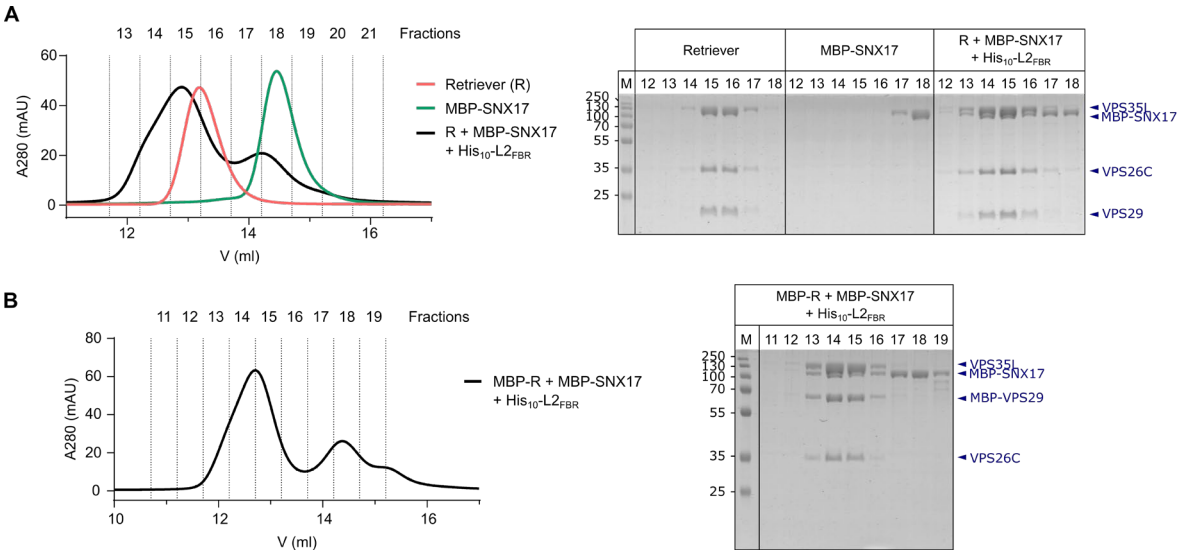

Figure 57. Isolation of the Retriever-SNX17-$L2_{FBR}$ complex by gel filtration chromatography. Gel filtration chromatography was performed using a Superdex 200 Increase 10/300 column and the following samples: (1) 20 µM Retriever, (2) 20 µM MBP-SNX17, and (3) a mixture of 20 µM Retriever, 20 µM MBP-SNX17 and 40 µM His_{10}-$L2_{FBR}$ (**A**), or a mixture of 20 µM MBP-Retriever, 25 µM MBP-SNX17 and 50 µM His_{10}-$L2_{FBR}$ (**B**). Fractions 13 and 14 contain a co-elution of the complex Retriever-MBP-SNX17-His_{10}-$L2_{FBR}$ (**A**) or the complex MBP- Retriever-MBP-SNX17-His_{10}-$L2_{FBR}$ (**B**). Note that $L2_{FBR}$ is not visible on the SDS-PAGE gel due to its low molecular mass. *M*, Protein marker.

Preliminary cryo-electron microscopy studies were carried out to analyze the complex formed by MBP-Retriever, MBP-SNX17, and $L2_{FBR}$. The cryo-EM sample was prepared by concentrating the first fraction (F13) of the co-elution from gel filtration chromatography (**Figure 57B**) to 1.3 µM, using the same glow-discharging and vitrification conditions outlined in section 4.1.5 (**Figure 19**). Quantifoil Holey Carbon R2/2 Mesh 300 copper grids were glow-discharged at 8.6 mA for 40 seconds before 4 µl of the protein sample was applied. The grids were rapidly frozen in liquid ethane using a Vitrobot system, maintained at 75-85% humidity and 16°C. After incubating the sample on the grids for 15 seconds, the grids were blotted for 2 seconds.

Grids were prepared with an optimal concentration of 1.3 µM and sent to the Electron Bio-Imaging Centre (eBIC) at Diamond Light Source (Didcot, United Kingdom). Data were collected on a Titan Krios IV microscope equipped with a Gatan K3 camera (**Figure 58A-C**). Super-resolution

movies (50 frames) were recorded with a 2-second exposure time, a total dose of 52.7 e−/Å^2, and a pixel size of 0.829 Å/px at the specimen level. A total of 17,552 images were acquired.

After extensive data processing by our collaborators at CIC bioGUNE, a final density map was obtained at a resolution of 7.58 Å. The map revealed significant flexibility in the Retriever complex, as evidenced by considerable heterogeneity between particles. The observed curvature of the complex aligned with predictions made by AlphaFold2 modeling (**Figure 58D**). Notably, MBP-SNX17 was not visible in the density map. This absence of SNX17 could be attributed to two factors: either SNX17 dissociated from the complex during sample preparation, or SNX17 is present but adopts varying orientations in each particle due to the high flexibility of its C-terminal tail, making it difficult to resolve in a single density map.

The AF2 model of the Retriever:SNX17 complex (**Figure 43** and **44**), it is observed that the Retriever-interacting region of SNX17 has the lowest pLDDT values, indicating high flexibility. Additionally, the PAE plot shows low confidence in the relative positioning between SNX17 and Retriever, with a reliable conformation for individual subunits but less certainty regarding the packing of the complex. Consequently, the variable positioning of SNX17 relative to Retriever across particles likely contributed to its absence in the cryo-EM density map. While the C-terminal tail of SNX17 is likely bound to Retriever, it may not be visible due to the low resolution of the data.

Based on these results, extensive improvements are required to resolve the structure of the entire Retriever:SNX17 complex by cryo-electron microscopy. The sample needs to be optimized to enhance both its quality and homogeneity, and a significantly greater number of particles must be obtained for reliable structural analysis. Unfortunately, these objectives could not be accomplished within the timeframe of this thesis.

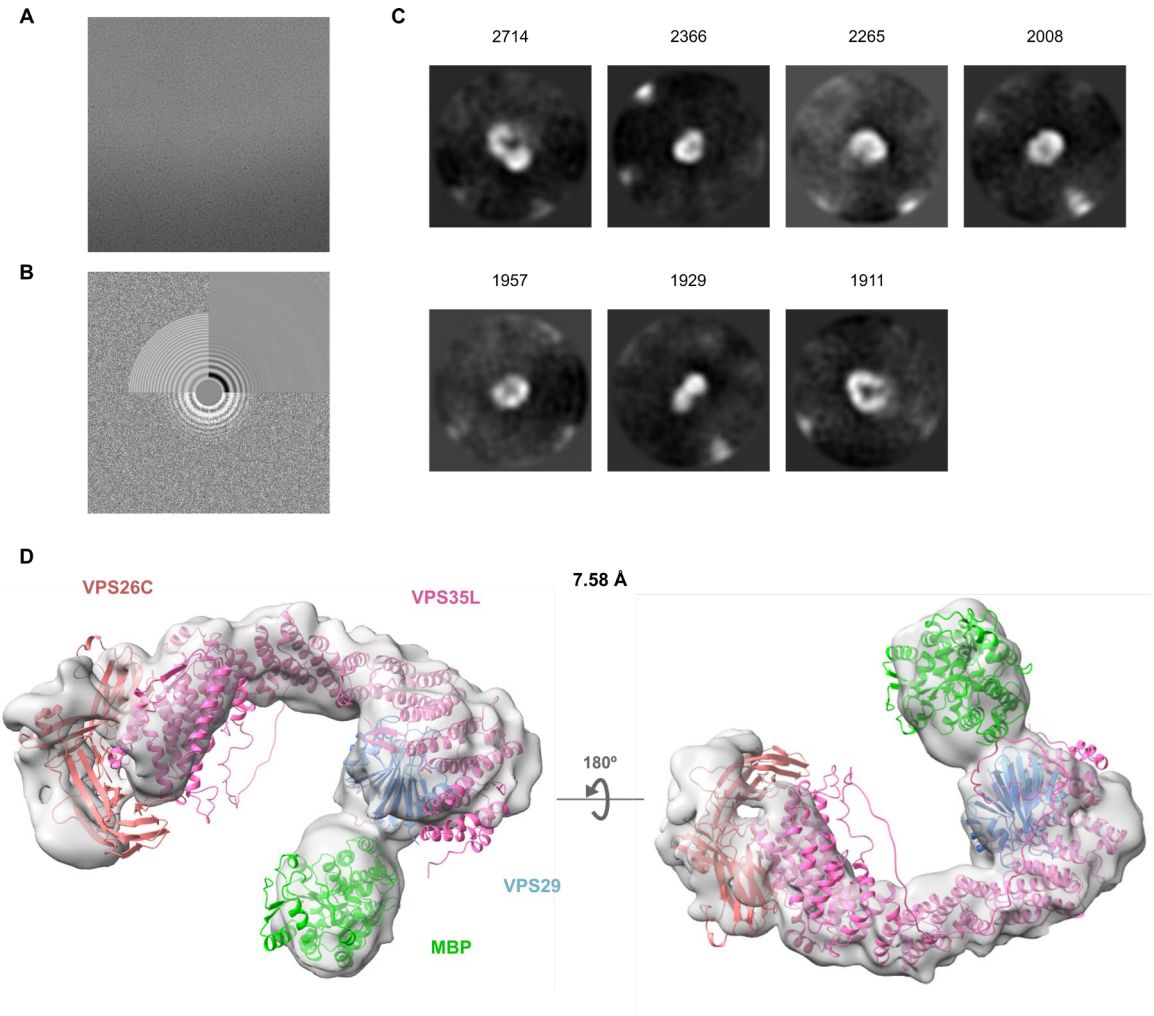

Figure 58. Structure of Retriever complex obtained by cryo-electron microscopy coupled with the AlphaFold2 model. (**A**) A representative image of the collected micrographs showing individual particle projections. (**B**) Power spectra of the image shown in (**A**) and the estimated contrast transfer function (CTF) which matches the Thon ring oscillations. (**C**) Some of the most significant 2D classifications sorted by automatic processing, with the number of particles detected for each class. (**D**) Retriever complex density map obtained by cryo-EM coupled with the AlphaFold2 model. The MBP tag in VPS29 improved contrast and facilitated subunit localization. The model lacks the density corresponding to SNX17.

4.4. Study of membrane association of SNX17 and the Retriever complex

The mechanism of Retriever recruitment to endosomal membranes was an unresolved question in the field. It was unclear whether Retriever possessed intrinsic membrane-binding capabilities or if it relied solely on interactions with other components. Additionally, it was uncertain whether the cargo-dependent activation mechanism observed in solution for SNX17 could also apply in the membrane environment. Understanding these dynamics is crucial for unraveling the intricate process involved in protein recycling and trafficking through the endosomal system.

4.4.1. Purification of GFP-SNX17 constructs and mKate2-Retriever complex

For visualization of the proteins of interest by fluorescence microscopy, the Retriever complex was tagged with the mKate2 fluorescent protein, while SNX17 was tagged with green fluorescent protein (GFP) (**Figure 59**). Additionally, three GFP-tagged SNX17 mutants were constructed and used for functional validation of key interacting regions related to membrane binding: GFP-SNX17$_{R36A+Y37A}$, GFP-SNX17$_{K431LSSK:AAAA}$, and GFP-SNX17$_{7-470}$.

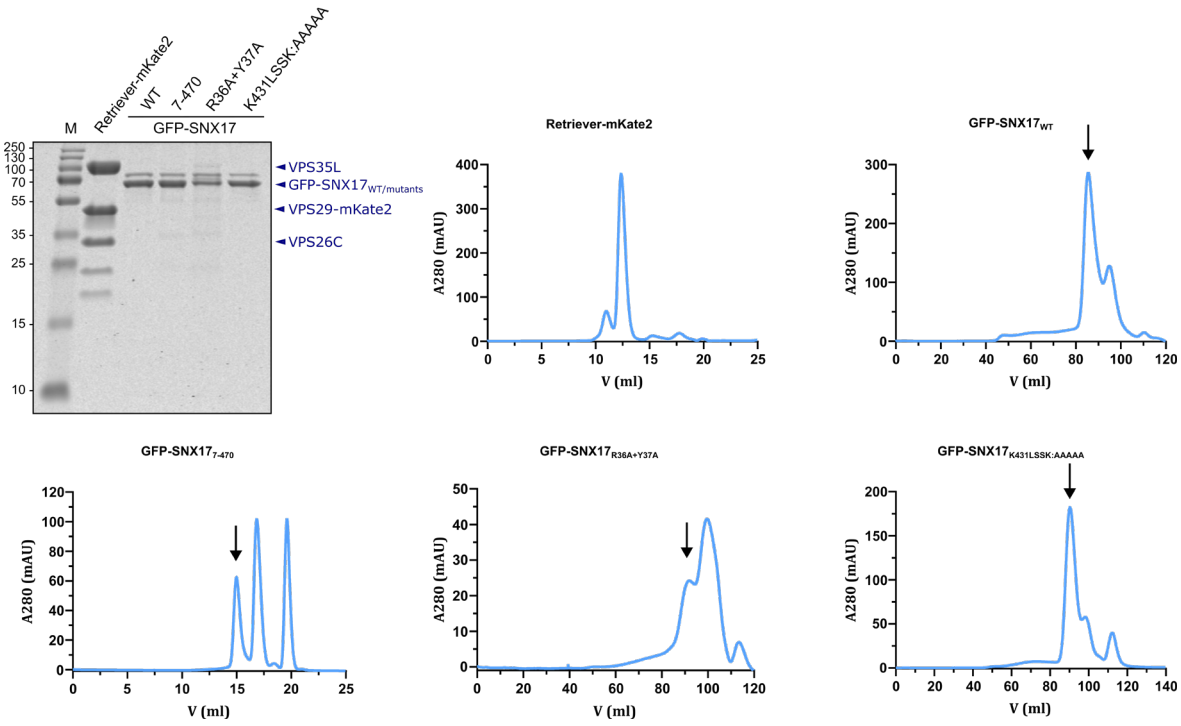

Figure 59. Purification of GFP-SNX17$_{WT}$, GFP-SNX17$_{mutants}$, and Retriever-mKate2. SDS-PAGE gel stained with Coomassie and gel filtration chromatograms showing the purified proteins used in the results section. The two additional bands observed in the Retriever-mKate2 purification correspond to protein degradation. In the wild-type SNX17 and its mutants, the higher molecular mass band corresponds to His-Sumo3-GFP-SNX17$_{WT/mutants}$, with theoretical molecular masses ranging between 90.7 and 91.4 kDa, as not all the protein was properly cleaved. The graphs showing various peaks are attributed to protein degradation or tag cleavage, with an arrow highlighting the peak corresponding to the purified protein. VPS35L (109.6 kDa),

VPS29-mKate (47.0 kDa), VPS26C (33.1 kDa), GFP-SNX17$_{WT}$ (80.1 kDa), GFP-SNX17$_{7-470}$ (79.4 kDa), GFP-SNX17$_{R36A+Y37A}$ (79.9 kDa), GFP-SNX17$_{K431LSSK:AAAAA}$ (79.9 kDa). *M*, Protein marker.

To ensure that the GFP tag does not interfere with protein activity, we evaluated the binding of GFP-SNX17 to the cargo L2 using a pull-down assay (**Figure 60**). GFP-SNX17 was efficiently retained by His$_{10}$-L2$_{FBR}$ previously attached to Ni-Indigo agarose beads, indicating that the GFP tag does not affect SNX17 binding affinity for cargo. The result is comparable to that of untagged SNX17, suggesting that GFP-SNX17 is functionally equivalent to SNX17.

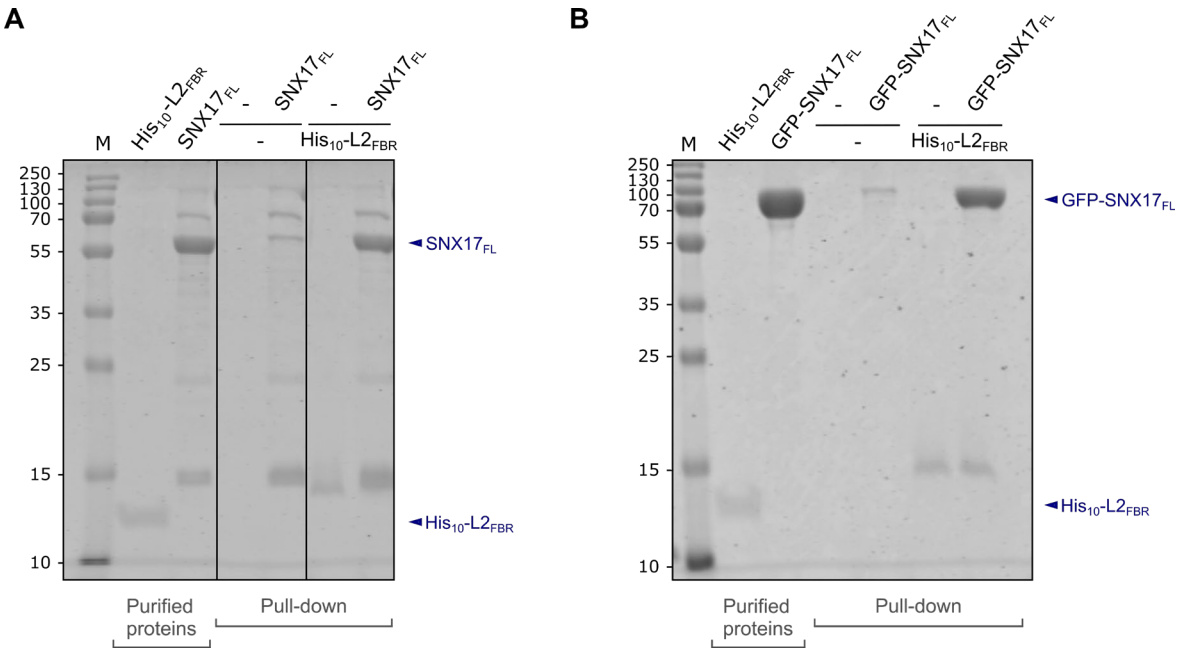

Figure 60. Pull-down assays analyzing the cargo-binding capacity of SNX17 and GFP-SNX17. His$_{10}$-L2$_{FBR}$ was incubated with untagged SNX17$_{FL}$ (**A**) or GFP-SNX17$_{FL}$ (**B**) in Ni-Indigo pull-down assays. Ni-Indigo agarose beads alone were used as a negative control. Purified proteins and pull-down samples were separated by SDS-PAGE and visualized by Coomassie Blue staining. *M*, protein marker; *FL*, full-length; *FBR*, FERM-Binding Region.

Additionally, circular dichroism analysis revealed that the secondary structure and folding of GFP-SNX17 mutants are comparable to those of wild-type GFP-SNX17, demonstrating that the assayed mutations do not perturb protein structure (**Figure 61**).

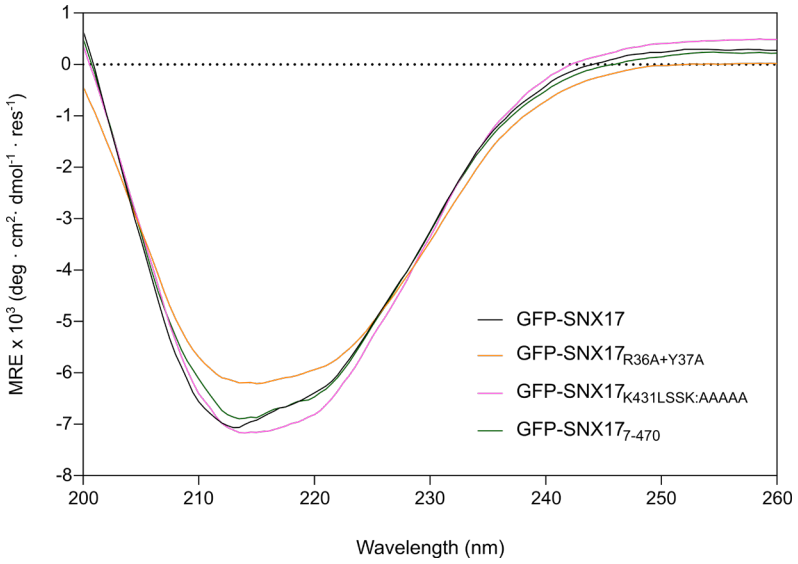

Figure 61. Conformational properties of GFP-SNX17 wild-type and mutants. Far-UV CD spectra of WT GFP-SNX17 and its mutants. The CD spectra were normalized by the area under the curve, using the WT protein values as a reference. *MRE*, mean residual ellipticity.

4.4.2. Giant Unilamellar Vesicles (GUVs) as a membrane model

SNX17 interaction with vesicles triggers Retriever recruitment

Lipid distribution plays a key role in the specific recruitment of trafficking proteins to distinct membrane compartments via PIP-specific lipid-binding domains. Specifically, early endosomes, where the recycling pathway initiates, are characterized by the presence of phosphatidylinositol 3-phosphate (PI3P) (Elkin et al., 2016). To mimic physiological conditions, we performed membrane-binding studies of Retriever using artificial vesicles containing PI3P, which is recognized by the PX domain of SNX17 (Chandra et al., 2019).

Initially, we used giant unilamellar vesicles (GUVs), which have diameters of 1–30 µm and offer the advantage of being easily imaged by microscopy. A small fraction of a far blue fluorophore (Marina Blue™ DHPE) was incorporated into the lipid mixture, allowing membrane detection via confocal fluorescence microscopy. As outlined above, we purified SNX17, fused to GFP, and Retriever, fused to mKate2, both of which could be detected in separate fluorescence channels. When GFP-SNX17 was incubated with the labeled GUVs, we observed the protein bound over their entire surface. In contrast, when mKate2-Retriever was incubated with GUVs, no protein was detected bound to the GUV membranes, indicating that Retriever lacks PI3P-binding ability. Interestingly, the incorporation of GFP-SNX17 into the protein mixture efficiently led to mKate2-Retriever recruitment to the GUV membranes, even in the absence of cargo. Strikingly, adding the cargo His_{10}-

$L2_{FBR}$ to this protein mixture did not notably increase Retriever binding to SNX17 on the GUV membranes (**Figure 62A**).

Additionally, a time-lapse microscopy experiment confirmed that Retriever is recruited to membranes only in the presence of SNX17. In this experiment, mKate2-Retriever was preincubated with GUVs, and no membrane binding was observed at time 0, prior to SNX17 addition. However, the addition of GFP-SNX17 at time 1 induced the recruitment of Retriever to the membranes, which became detectable by time 5 (corresponding to 4 minutes after SNX17 addition) (**Figure 62B**).

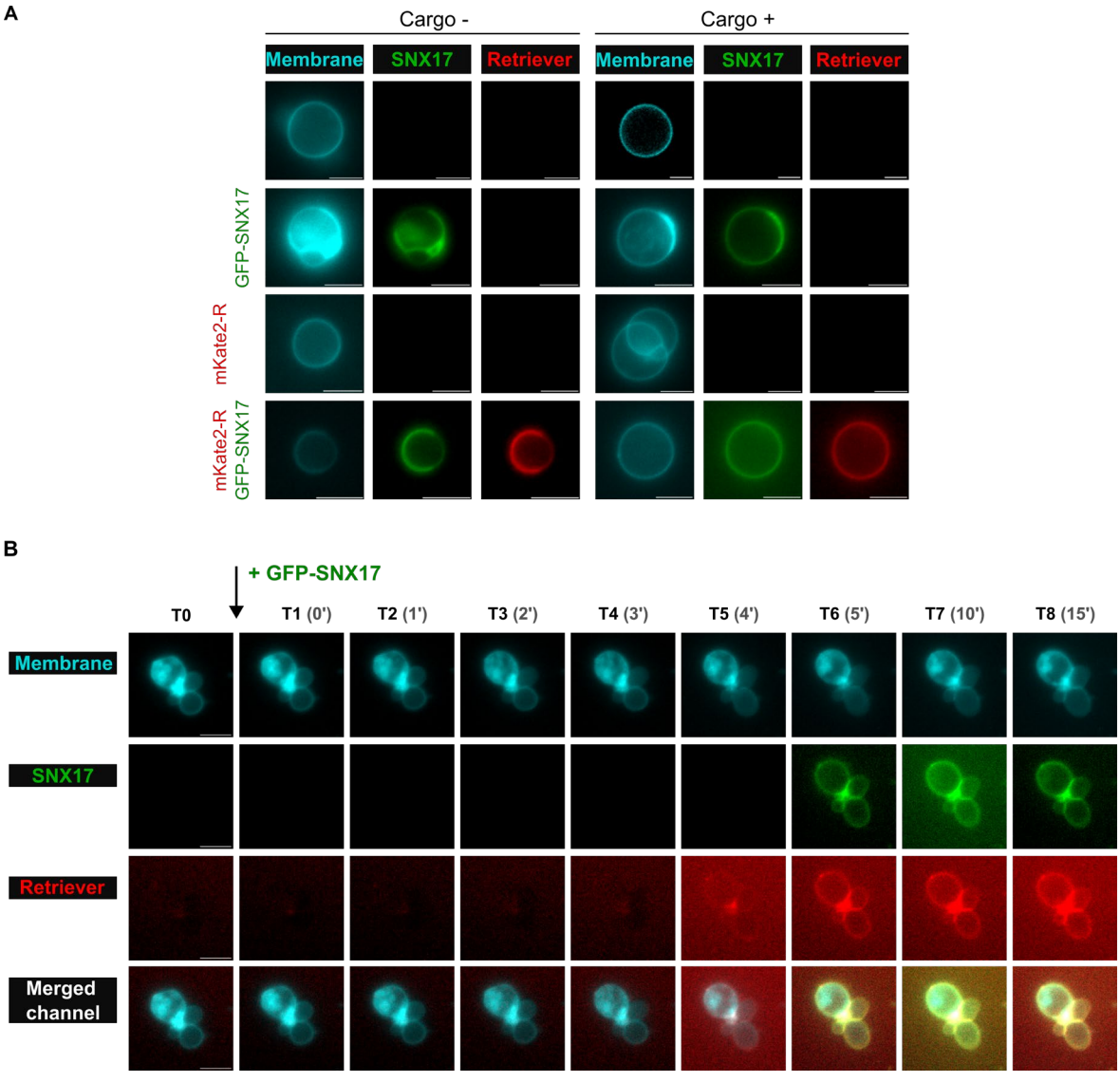

Figure 62. Assessment of the membrane-binding potential of Retriever and SNX17 *in vitro*. (**A**) Confocal fluorescence imaging of GUVs incubated with mKate2-Retriever (red), GFP-SNX17 (green), or both, in the presence and absence of His_{10}-$L2_{FBR}$. GUV membranes were stained with the Marina Blue DHPE lipid dye (cyan). Scale bar, 5 µm. (**B**) Time-lapse experiment showing the effect of adding SNX17 to a pre-incubated mixture of Retriever and GUVs. The initial condition contains GUVs and mKate2-Retriever at 2 µM. After capturing an image at time 0 (T0), GFP-SNX17 was added at 2 µM, an image was taken (T1), and subsequently

further images were taken at 1-minute intervals for 5 minutes, followed by additional images every 5 minutes over the next 10 minutes. The merged channel displays the superimposed images of the three individual channels. Scale bar, 5 µm.

We propose that membrane association induces a conformational change in SNX17 similar to the one triggered by cargo binding. The observed activation of SNX17, which leads to Retriever recruitment upon membrane binding, is likely due to a conformational change in the SNX17 C-terminal region. Membrane association through the PX domain probably triggers this conformational change, allowing the C-tail to interact with and capture Retriever (**Figure 63**).

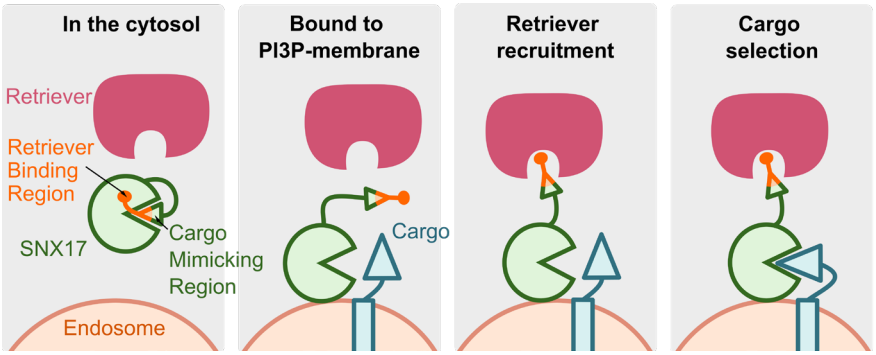

Figure 63. Proposed mechanism for Retriever recruitment via SNX17 on the membrane. In the absence of endosomal membrane and cargo, the CT region of SNX17 interacts with itself, masking the Retriever-binding motif and resulting in negligible affinity for Retriever. Upon membrane attachment, the CT region of SNX17 disengages from the cargo-binding pocket and becomes exposed, thereby releasing the Retriever-binding region located at the C-terminal end. This conformational change facilitates both Retriever recruitment and cargo binding, promoting the assembly of the recycling machinery.

To support the proposed mechanism, we evaluated previously studied SNX17 mutants of the Retriever-binding motif ($SNX17_{D467X}$ and $SNX17_{L470G}$) within a membrane-binding context (**Figure 64**). Both mutants failed to recruit Retriever to membranes, demonstrating that the GUV-based assay recreates the Retriever-SNX17 binding mode observed in solution, mediated through the C-terminal end of SNX17. We also assessed the SNX17 mutants associated with the autoinhibition mechanism, including $SNX17_{W321A}$, $SNX17_{V380D}$, $SNX17_{H457A}$ and $SNX17_{N459A+F462A}$. The first three mutants behaved identically to wild-type SNX17 successfully recruiting Retriever to the membrane surface. This indicates that these mutations do not affect SNX17 membrane binding or Retriever association. The $SNX17_{N459A+F462A}$ mutant, however, failed to recruit Retriever to the vesicle membrane because the residues involved in Retriever binding are compromised, as previously confirmed by pull-down assays (**Figure 56**, section 4.3.2.).

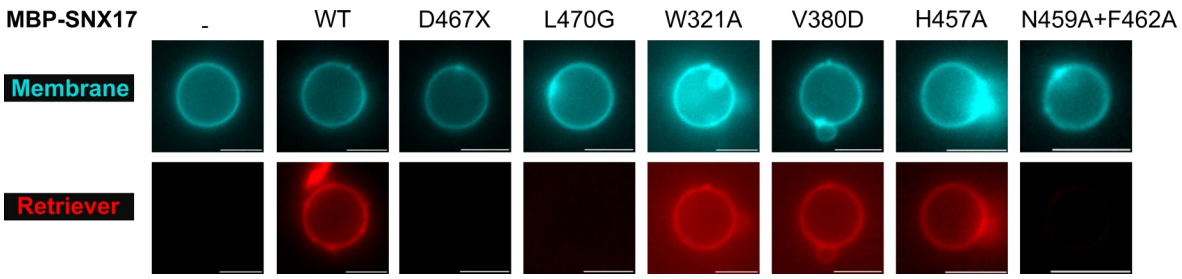

Figure 64. Assessment of SNX17 mutants' ability to recruit Retriever in a GUV model. GUVs were incubated with Retriever-mKate2 (red) and either MBP-SNX17$_{WT}$ or MBP-SNX17$_{mutants}$. GUV membranes were stained with Marina Blue DHPE lipid dye (shown in cyan). Scale bar, 5 μm.

Our findings suggest that SNX17 binds to Retriever in a manner consistent with the interactions observed in solution. However, in the presence of membranes, SNX17 is already in an "ON" state, bypassing the "OFF" state observed in solution in the absence of cargo. We propose that the autoinhibition mechanism of SNX17 may be disrupted either by cargo binding or membrane association. Nonetheless, the precise molecular mechanism by which SNX17 releases its C-terminal tail and recruits Retriever in the presence of membranes remains unknown.

To better understand this activation mechanism of SNX17, we first designed a mutant that interrupts PI3P binding. As previously described, the PX domain is the region of SNX17 responsible for membrane binding. Despite relatively low overall sequence homology, PX domains all share the same core fold, consisting of three antiparallel β-strands (β1-β3), followed by three α-helices (α1–α3). An extended sequence traverses the protein between helices α1 and α2, known as the PPK loop, which contains a conserved ΨPxxPxK motif (Ψ = large aliphatic amino acids V, I, L, and M). The side chains of residues from the β3 strand, α1 helix, and PPK loop collectively form a binding pocket for the headgroup of the lipid PI3P (Chandra et al., 2019). Notably, a mutation in the RRY motif of SNX3 (SNX3$_{R69RY:AAA}$), or even a replacement of the last residue with alanine, abolished the interaction of this sorting nexin with PI3P (Xu et al., 2001). This RRY motif is conserved in most PX domains and is localized in the end of the β3 (**Figure 65A**). Basic binding sites facilitate the interaction with the two negatively charged phosphate groups of PI3P (Cheever et al., 2001). A structural comparison between the crystal structure of Grd19p (the SNX3 yeast orthologue, PDB ID: 1OCS, from Zhou et al., 2003) and the AF3 model of SNX17 allowed us to identify the motif ^{35}VRY^{37} in SNX17 as the equivalent region for PI3P binding (**Figure 65B**). Thus, the residues R36 and Y37 in SNX17 are expected to be crucial for the association of SNX17 with membranes. For this reason, the SNX17$_{R36A+Y37A}$ mutant was designed.

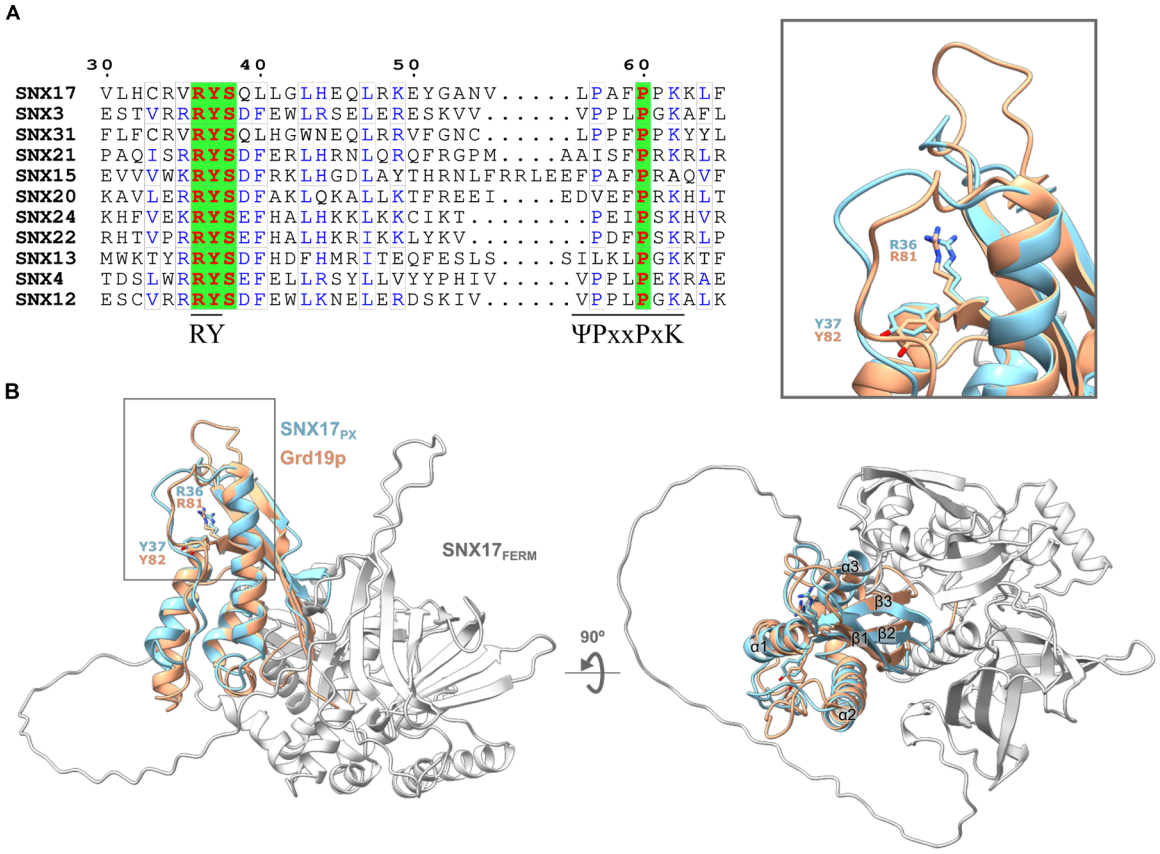

Figure 65. Sequence alignment of multiple SNXs, and structural alignment of SNX17 with the yeast orthologue of SNX3. (**A**) Multiple sequence alignment of human SNX family members, generated using the PROMALS3D server and visualized with ESPript 3. The conserved RRY and ΨPxxPxK motifs are highlighted. Residue numbering corresponds to SNX17, and only the region spanning residues 30-65 is shown. (**B**) Structural alignment between SNX17 and the yeast orthologue of SNX3, Grd19p. Grd19p (PDB ID: 1OCS) is colored orange, while the PX domain of SNX17 is blue, and its FERM domain is light grey. Key residues R36 and Y37 of SNX17, along with R81 and Y82 of Grd19p, are shown as sticks. The conserved core fold, comprising β1-β3 and α1–α3, is annotated. The inset provides a zoomed view of the RY motif critical for PI3P binding.

Additionally, the SNX17 structural model was further analyzed to identify regions potentially involved in liberating the Retriever-binding motif in the presence of membranes. Three regions were identified as potential candidates for SNX17 activation: ^{1}MHFSIP^{6}, ^{431}KLSSK^{435} and ^{467}DEDL^{470} (**Figure 66A**). The first region, ^{1}MHFSIP^{6}, consists of the first six residues at the N-terminus of SNX17. These residues are highly conserved and located near the cargo-binding pocket, suggesting a potential role in membrane association and/or the autoinhibition process (**Figure 45**). The second region is a cluster of basic residues, ^{431}KLSSK^{435} that may interact with the negatively charged membrane, inducing a conformational change that releases the C-terminal tail.

The third potentially relevant region was selected after examining acidic regions that might promote a conformational change in the protein upon PI3P association to avoid the consequent membrane proximity. Notably, a motif of negatively charged residues was identified, that comprises the last four residues of the C-terminus; ^{467}DEDL^{470}. This motif is positioned in contact with the basic region of the cargo-binding pocket, which would favor the interaction between these regions (**Figure 66B**). We hypothesize that the acidic nature of the C-terminal tail could play a role in turning off the protein's autoinhibition mechanism upon PI3P binding. The resulting repulsion from the membrane due to this acidic tail could lead to its release, making it to be exposed and active for Retriever binding. Unfortunately, mutating this region is not feasible, as it is precisely the motif that is interacting with Retriever. Therefore, we would not be able to determine whether the observed lack of binding is due to disruption of the membrane repulsion mechanism or a compromise in the interaction with Retriever.

Based on this structural analysis, three SNX17 mutants were constructed and purified: (1) GFP-SNX17$_{R36A+Y37A}$, designed to disrupt PI3P binding, (2) GFP-SNX17$_{K431LSSK:AAAA,}$ a mutant with five basic residues replaced by alanine, and (3) GFP-SNX17$_{7-470,}$ a deletion of the first six residues. The GFP-SNX17$_{R36A+Y37A}$ mutant is expected to disrupt membrane association due to the loss of PI3P binding, thereby abolishing SNX17's ability to recruit Retriever. In contrast, the two remaining mutants, GFP-SNX17$_{K431LSSK:AAAA}$ and GFP-SNX17$_{7-470}$, are anticipated to still bind to the membrane since the PI3P-binding residues remain intact. However, these mutants may not induce the conformational change necessary for Retriever recruitment, as the C-terminus may no longer be released from the cargo-binding pocket.

The ability of these mutants to recruit Retriever in the presence of membranes was analyzed by fluorescence microscopy using GUVs (**Figure 66C**). As predicted, GFP-SNX17$_{R36A+Y37A}$ did not associate with the membranes or recruit Retriever. R36 and Y37 from SNX17 are, therefore, critical residues for PI3P binding, and a lack of PI3P interaction impairs both membrane association and subsequent Retriever recruitment. In contrast, GFP-SNX17$_{K431LSSK:AAAA}$ mutant bound the GUV membrane and induced Retriever recruitment, indicating that the ^{431}KLSSK^{435} basic region does not appear to induce a conformational change in the membrane environment that releases the C-terminal tail of the protein. Interestingly, the deletion of the first six residues in GFP-SNX17$_{7-470}$ disrupted membrane binding, and consequently, Retriever was not recruited. Since the deletion disrupted membrane binding, we cannot determine whether the protein's autoinhibition state is maintained. This finding suggests that the first six residues of SNX17 are necessary for membrane binding, which has not been previously described in the literature.

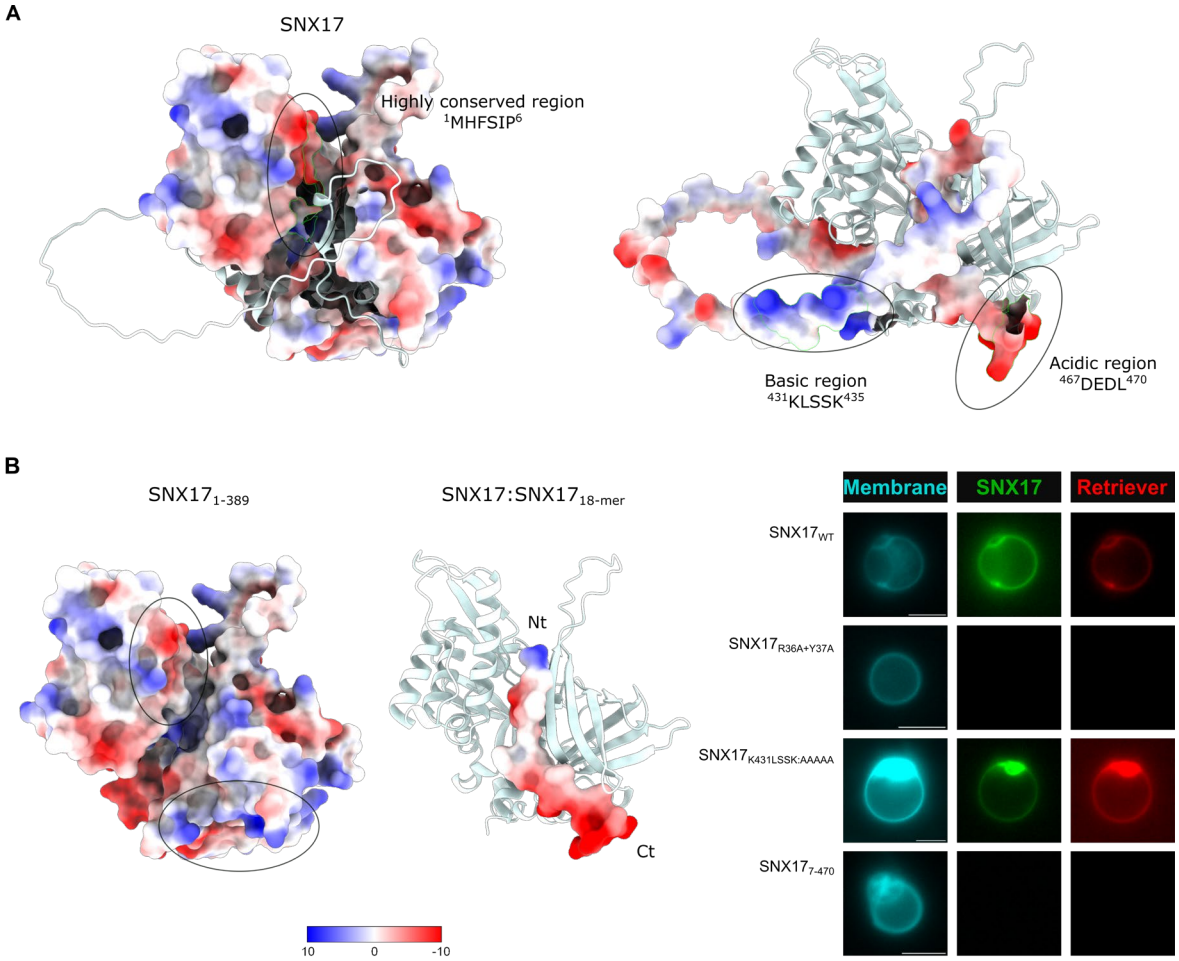

Figure 66. Structural models of SNX17 and the effect of GFP-SNX17$_{R36A+Y37A}$, GFP-SNX17$_{K431LSSK:AAAA}$ and GFP-SNX17$_{7-470}$ mutants on Retriever recruitment in GUVs assays. (**A**) Structural model of SNX17 from AF3. On the left, SNX17$_{1-389}$ is colored by electrostatic potential in surface view, and the C-terminal tail (region 390-470), is displayed in cartoon. On the right, SNX17$_{1-389}$ is displayed in cartoon and SNX17$_{390-470}$ is colored by electrostatic potential. The three potentially relevant regions, ^{1}MHFSIP^{6}, ^{431}KLSSK^{435} and ^{467}DEDL^{470}, are highlighted with black circles. (**B**) On the left, SNX17 is colored by electrostatic potential with the C-terminal region removed for better visualization of the binding pocket. Black circles indicate the acidic region in the upper part and the basic region in the lower part of the binding pocket. On the right, the model of SNX17$_{1-389}$ is displayed in cartoon in complex with SNX17$_{18-mer}$, which is colored by electrostatic potential. The SNX17$_{18-mer}$ electrostatic characteristics resemble those of its cargos, except for the last four residues, which are notably acidic. This suggests that the tail may move away from the negatively charged membrane. Images were created using ChimeraX, with Coulombic Surface Coloring representing electrostatic potential in kcal/(mol·e) units. Electronegativity is shown from -10 (red) to electropositivity of 10 (blue) on the color key. (**C**) Evaluation of the ability of SNX17 mutants to recruit Retriever in GUVs. GUVs were incubated with Retriever-mKate2 (red) and GFP-SNX17$_{WT/mutants}$ (green). Membranes were stained with Marina Blue DHPE lipid dye (cyan). Scale bar, 5 µm.

4.4.3. Co-sedimentation assay to study the recruitment of SNX17 and Retriever

Given our skepticism regarding the absence of cargo dependency observed in the GUV assays, we conducted liposome co-sedimentation assays with the assistance of Iván Méndez Guzmán. This method allows for quantifying protein-membrane binding affinities. Proteins and large unilamellar vesicles (LUVs) containing PI3P were incubated together and then centrifuged. The liposome-bound proteins were concentrated in the pellet fraction after centrifugation.

SNX17 alone bound efficiently to PI3P containing liposomes (64 ± 17%), while only a small amount of Retriever sedimented with liposomes (8.3 ± 2.8%), similar to the amount sedimented without liposomes (6.0 ± 5.4%). Therefore, we considered this binding to be nonspecific, likely due to protein aggregation during the assay. Interestingly, and in great accordance with the GUVs binding results described earlier, Retriever sedimentation levels with LUVs increased significantly in the presence of SNX17 (22 ± 7.0%) (**Figure 67A**). The addition of the cargo LRP1 to the protein mixture did not yield a statistically significant increase in liposome sedimentation for either SNX17 or Retriever. However, a significant increase in Retriever recruitment to liposomes was observed when SNX17 was preincubated with the cargo LRP1 (32 ± 7.0%) (**Figure 67A**). These results suggest that, in a membrane context, as observed in solution, the presence of cargo can further enhance Retriever recruitment. This observation could not be determined using fluorescence microscopy assays, as it is not a quantitative technique (**Figure 62**). Our co-sedimentation results indicate that SNX17 binding to PI3P-containing LUVs allows Retriever binding to SNX17 in the absence of cargo, consistent with the GUV imaging data.

Additionally, to corroborate that these observations are due to the binding of SNX17 to the PI3P lipid, as it has been suggested in the literature (Chandra et al., 2019), we performed co-sedimentation experiments, excluding this lipid from the liposome composition. As expected, liposomes deficient in PIPs failed to recruit SNX17 and/or Retriever (**Figure 67B**).

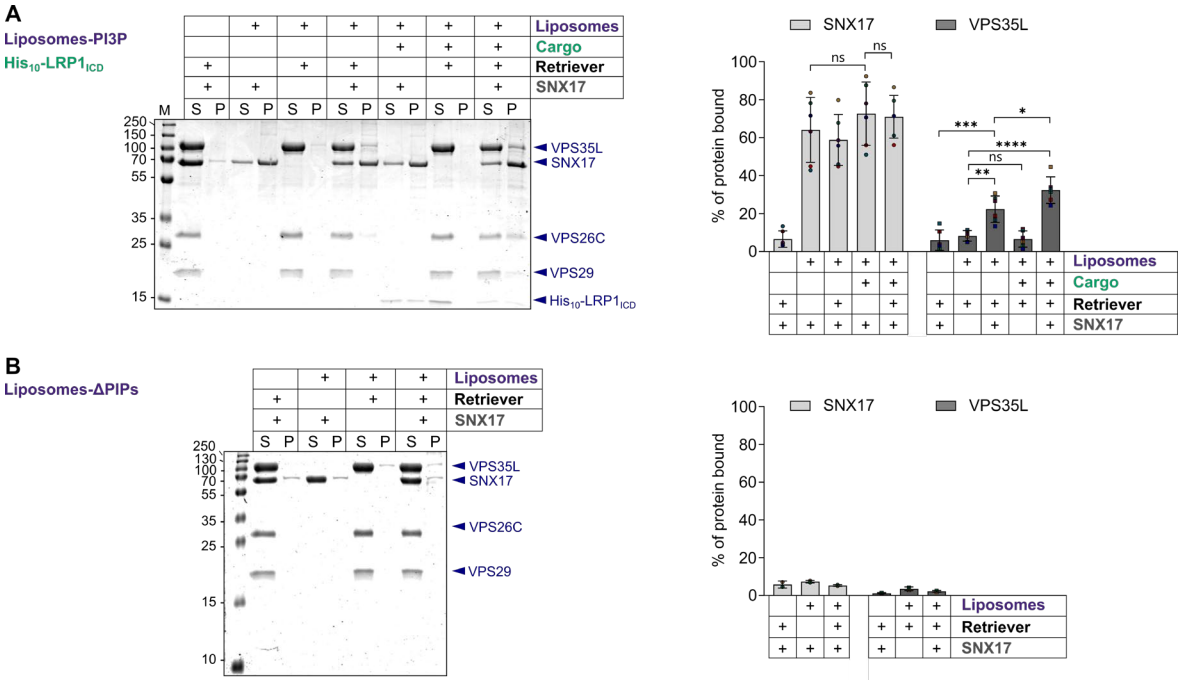

Figure 67. Co-sedimentation assays to analyze the effect of the cargo and the effect of PI3P lipid. (**A**) PI3P-containing liposomes were incubated with His-Sumo3-SNX17, Retriever, and/or His_{10}-$LRP1_{ICD}$, at 2:2:4 µM ratio. (**B**) Liposome membranes lacking PI3P were incubated with His-Sumo3-SNX17, and Retriever, at 2:2:4 µM ratio. 15 µl of each incubation sample was loaded onto an SDS-PAGE gel for separation of the soluble (supernatant, S) and co-sedimented (pellet, P) fractions. After Coomassie staining, densitometry-based quantification of the individual bands was performed. The binding of SNX17 and Retriever to liposomes was quantified as the percentage of total protein bound to the pellet under each condition, with VPS35L serving as a representative band of the Retriever complex. The values in the graph (bottom panel) represent the mean ± SD of six (**A**), or two (**B**) technical replicates. Statistical significance was tested using one-way ANOVA followed by Tukey's test for multiple comparisons. *p = 0.03, **p < 0.004, ***p < 0.0003, ****p = 0.0000006, *ns*, not significant.

4.5. Characterization of SNX31

While SNX17 has been extensively studied, its paralog SNX31 remains poorly characterized. SNX17 appears to be more relevant than SNX31, as evidenced by its ubiquitous expression across all tissues, whereas SNX31 exhibits a more restricted expression pattern, being primarily found in the urinary bladder and expressed at very low levels in other tissues. For these reasons, the primary focus of this thesis was directed towards SNX17. However, a series of experiments were conducted to gain deeper insights into the properties and behavior of SNX31.

4.5.1. Purification of SNX31

Similar to SNX17, SNX31 contains a PX domain responsible for binding PI3P, comprising residues 1-109, a FERM domain that mediates cargo binding, spanning residues 112-384, and a C-terminal region covering residues 385-440. SNX17 and SNX31 share 43% sequence identity, with the main difference being the length of their C-terminal regions, as SNX31 is 25 residues shorter than SNX17 (**Figure 68A,B**).

While the purification of SNX17 was challenging, purifying SNX31 proved to be even more difficult, yielding very low amounts of soluble protein. Nevertheless, the purification of the His-Sumo3-SNX31$_{FERM-CT}$ construct (residues 110-440), which was codon optimized for bacterial expression, was moderately successful (**Figure 68C**).

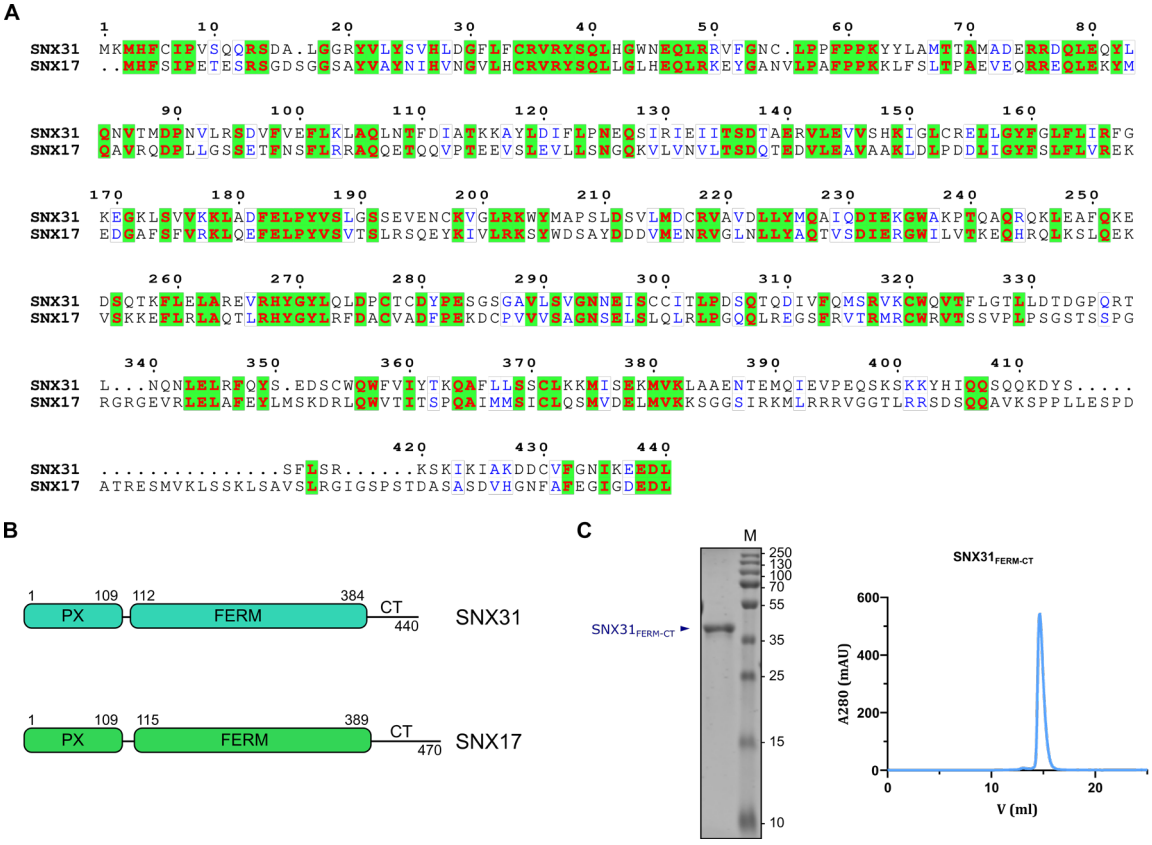

Figure 68. Sequence alignment and diagram of SNX31 and SNX17, and purification of SNX31$_{FERM-CT}$. (**A**) Sequence alignment of human SNX17 and SNX31. Invariant residues are colored red on a green background, and similar residues are in blue. (**B**) Schematic representation of the domains from SNX31 and SNX17. *CT*, C-terminal domain. (**C**) SDS-PAGE gel with Coomassie staining showing the purified SNX31$_{FERM-CT}$ used in the following experiments, and the corresponding gel filtration chromatogram. SNX31$_{FERM-CT}$ (38.0 kDa). *M*, Protein marker.

4.5.2. Structural model of SNX31

The architecture of SNX31 resembles that of SNX17. SNX31 contains a PX domain, which interacts with PI3P in membranes (Vieira et al., 2014), and a FERM domain, which recognizes the NPxY recycling signal of cargos (Ghai et al., 2011). A structural prediction of SNX31 was obtained using AF2 (**Figure 69**). Similar to SNX17, the overall structure shows high pLDDT values, with the C-terminal region exhibiting both the lowest confidence values and the highest PAE plot values. In addition, this region is characterized by a lack of secondary structures elements, a feature that appears to be conserved across species (**Figure 70**).

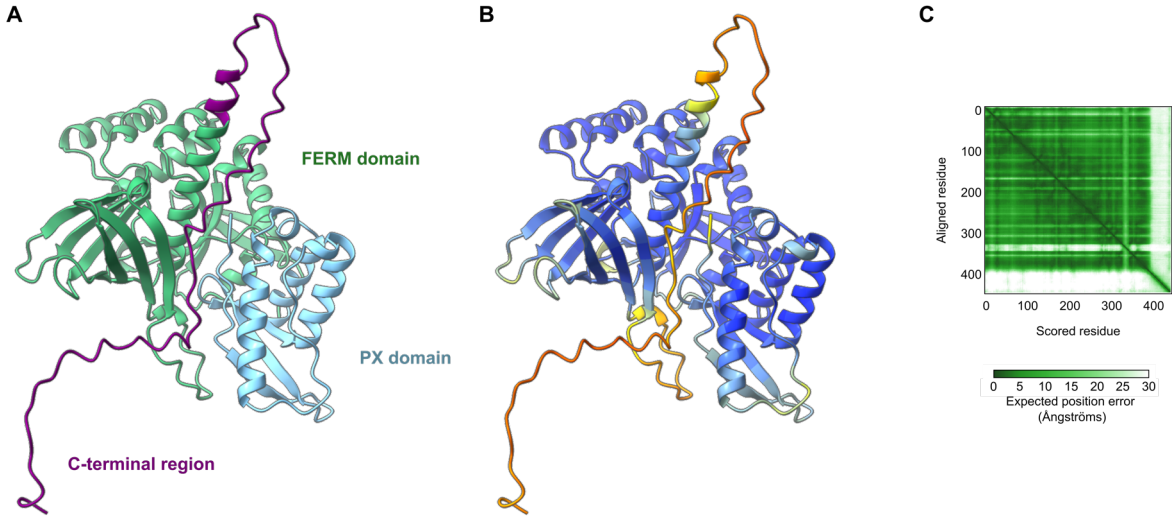

Figure 69. Structural prediction of SNX31 using AF2. (**A**) SNX31 model colored by domains, with the PX domain in blue, the FERM domain in light green, and the C-terminal region in purple, with a similar orientation than SNX17 model in **Figure 25**, section 4.2.2. (**B**) SNX31 model colored according to the pLDDT confidence score (blue, very high confidence pLDDT ≥ 90; cyan, high confidence 70 ≤ pLDDT < 90; yellow, low confidence 50 ≤ pLDDT < 70; orange, very low confidence pLDDT < 50). (**C**) The graph shows the corresponding PAE plot. *PAE*, predicted aligned error.

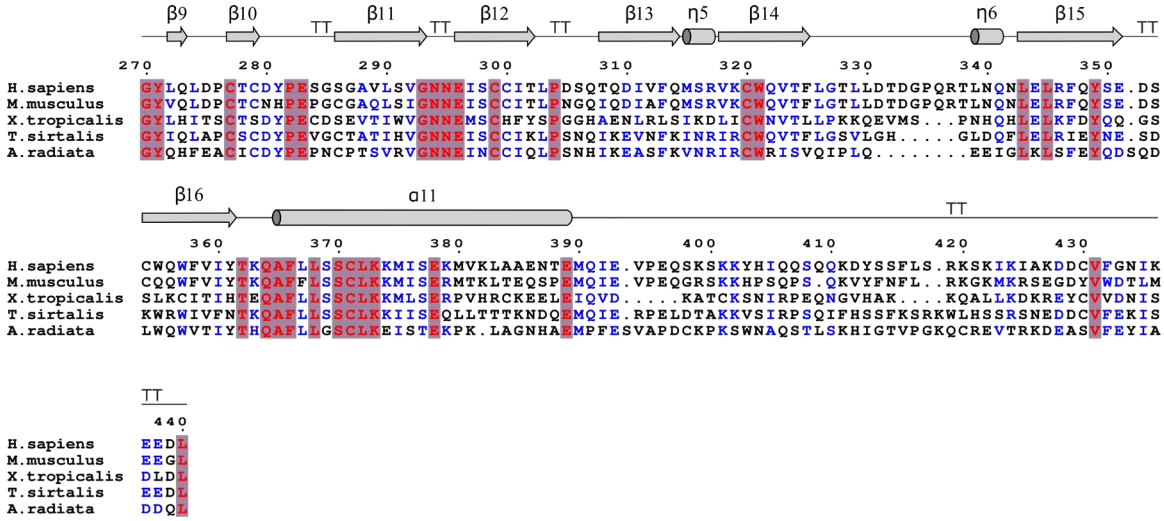

Figure 70. Sequence alignment of the F3 module from the FERM domain and the CT region across SNX31 orthologs. Structure-based sequence alignment of human SNX31 and orthologs generated with the PROMALS3D server and plotted with ESPript 3. The UniProt accession numbers of the AF2 models used in the sequence alignment are as follows: *Homo sapiens* (Q8N9S9), *Mus musculus* (Q6P8Y7), *Xenopus tropicalis* (Q28HD5), *Thamnophis sirtalis* (A0A6I9X7U5), and *Amblyraja radiata* (XP_032874833.1). The numbering of residues and secondary structures corresponds to SNX31 from *Homo sapiens*. α indicates alpha-helices and η represents 3_{10} helices, both shown as cylinders. β denotes beta-strands, depicted as arrows, and TT stands for strict β-turns. Invariant residues are highlighted in red with a purple background, while conserved residues are shown in blue.

Although the sequence identity between SNX17 and SNX31 is moderate, the predicted structure generated using AF show significant similarity, with the main differences observed in the C-terminal region (**Figure 71**).

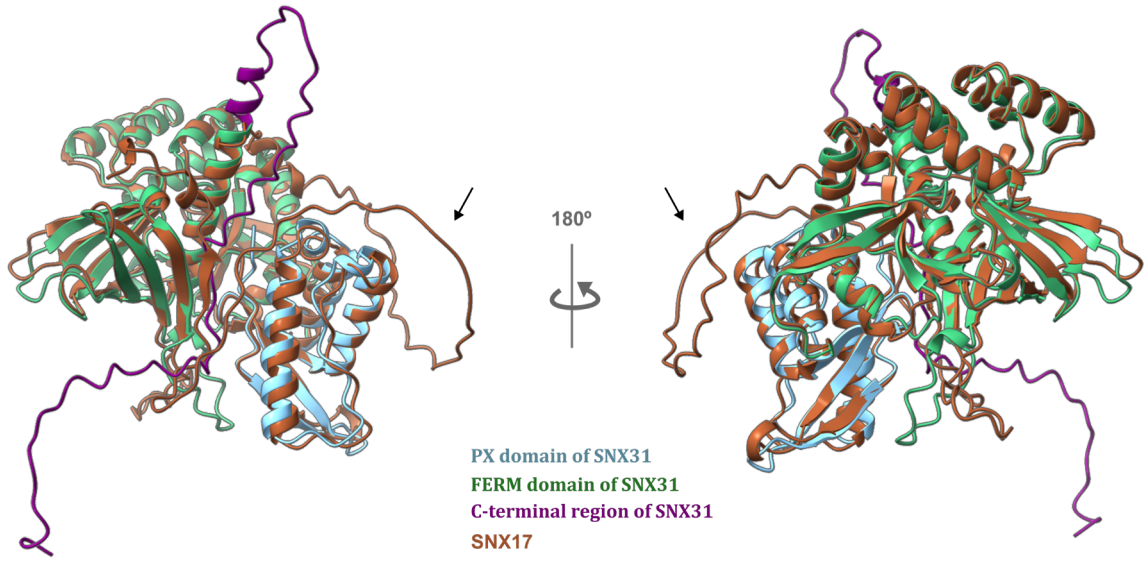

Figure 71. Structural comparison between SNX17 and SNX31. The SNX31 model colored by domains, with the PX domain in blue and the FERM domain in light green, while SNX17 is shown in brown. The extra loop present in SNX17 is highlighted with arrows.

4.5.3. Quantification of SNX31-cargos binding affinities

Like SNX17, SNX31 contains a FERM domain, which has been associated with the Retriever complex (McNally et al., 2017), and has demonstrated binding capability to numerous NPxY-containing transmembrane proteins through a peptide array screen (Ghai et al., 2013b). Therefore, the mechanism of interaction of SNX31 with the Retriever complex could be similar to that of SNX17, as well as its involvement in recycling specific cargo.

Therefore, the binding affinity of SNX31 to our cargos of interest - APP, LRP1, INTβ1, and VEGFR1 - was evaluated through fluorescence anisotropy assays (**Figure 72**). SNX31 demonstrated binding to LRP1 and L2, like SNX17; however, notable differences in the binding affinity characteristics were observed. While the dissociation constant (K_D) for $SNX17_{FERM-CT}$ binding to L2 is 0.60 μM (**Figure 27C**, section 4.2.3.), the K_D for $SNX31_{FERM-CT}$ is notably higher, 58.2 μM. Additionally, $SNX31_{FERM-CT}$ exhibits a low binding affinity to LRP1 (K_D = 167 μM) compared to SNX17 (K_D = 2.2 μM). Furthermore, in addition to differences in binding affinity, there are also variations in cargo specificity: none of the ITGB1 FERM binding motifs bind to SNX31, whereas they do bind to SNX17, and binding to APP is almost undetectable. In conclusion, although SNX31 shares some functional similarities with SNX17, such as a higher binding affinity for L2 compared to cellular cargos it exhibits distinct cargo-binding preferences and significantly different affinities.

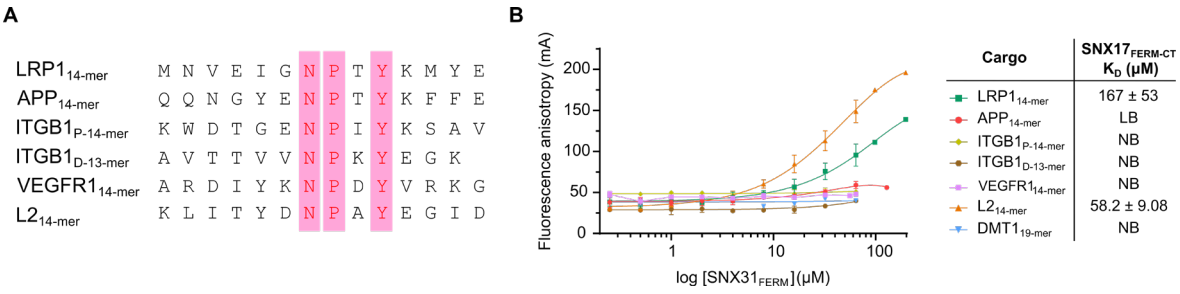

Figure 72. Fluorescence anisotropy assay to analyze the interactions between SNX31 and various cargos. (**A**) Alignment of the sequences of cargo peptides used in panel B. The conserved NPxY motif is highlighted with pink bars. (**B**) Fluorescence anisotropy assays were performed to study the interaction of $SNX31_{FERM-CT}$, with the peptides outlined in panel A. The peptides were labeled with the fluorescent reagent 5-FAM at the N-terminus. Dissociation constants values are presented in the accompanying table (n = 3 for $L2_{14-mer}$, $LRP1_{14-mer}$, and APP_{14-mer}, and n = 2 for the rest of the cargos). The Retromer-dependent cargo DMT1 was used as a negative control. *NB*, no detectable binding; *LB*, low binding (poor fit quality).

4.5.4. Crystallization of SNX31$_{FERM-CT}$

Understanding the structural differences between SNX17 and SNX31 could provide insights into the key interactions responsible for their differential cargo affinities. Therefore, we pursued the structural determination of SNX31. Currently, no crystal structures of this protein are available. Crystallization trials for SNX31$_{FERM-CT}$ were conducted using various screening kits, including Hampton Research Crystal Screen 1 and 2, AmSO4 Suite, Morpheus™, and MIDAS*plus*™. The protein was prepared at concentrations of 10 mg/ml and 5.3 mg/ml in a buffer composed of 25 mM Hepes pH 7.5, 300 mM NaCl, and 1 mM TCEP, with a protein-to-precipitant ratio of 1:1. Despite these efforts, no crystals were obtained under any of the conditions. The condition that successfully produced SNX17$_{FERM-CT}$ crystals (0.6 - 1.6 M ammonium sulfate and 0.15 M sodium citrate pH 5.5 - 6.5) was also tested but yielded no crystals.

4.5.5. Assessment of Retriever association to SNX31

Similar to SNX17, the C-terminal region of SNX31 is hypothesized to interact with the Retriever complex via the VPS26C subunit (McNally et al., 2017). To determine whether this interaction is direct, the Retriever subunit VPS26C was incubated with SNX31$_{FERM}$-CT and the mixture analyzed by gel filtration chromatography (**Figure 73**). However, as observed with SNX17 (**Figure 39**, section 4.3.1.), no direct interaction was detected.

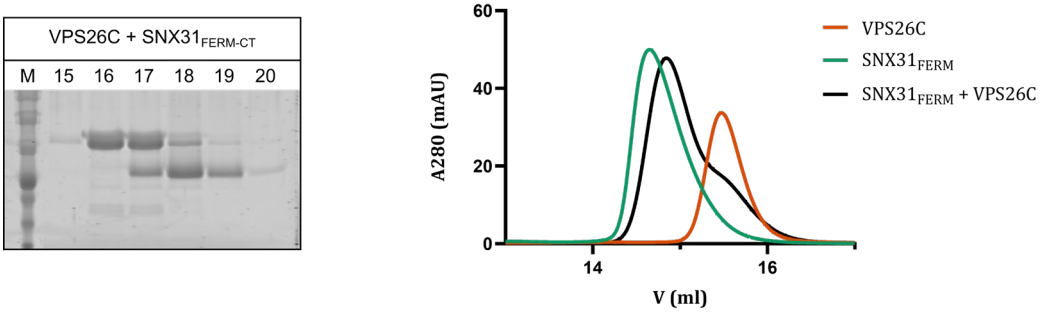

Figure 73. Analysis of the interaction between VPS26C and SNX31$_{FERM-CT}$. Samples of 100 µM VPS26C, 100 µM SNX31$_{FERM-CT}$, and a mixture of 100 µM VPS26C + 100 µM SNX31$_{FERM-CT}$ were analyzed by gel filtration chromatography in Superdex 200 Increase 10/300. The presence of two separate absorbance peaks indicates no direct interaction between both proteins.

This result suggests that, like SNX17, the presence of a cargo may be necessary to activate SNX31, enabling its interaction with the Retriever complex. In the absence of cargo, SNX31 might remain in an inactive or autoinhibited state, preventing efficient binding to Retriever. However, none of the cargos analyzed in this study exhibited high binding affinity to SNX31, making it difficult to

determine whether they can effectively overcome or disrupt this potential autoinhibition mechanism of the protein. This lack of high-affinity binding complicates the assessment of whether these cargos could serve as triggers for SNX31 activation and subsequent engagement with the Retriever complex. Consequently, the question of how SNX31 is regulated at the molecular level remains unanswered.

The structural predictions of SNX31 by AlphaFold2 reveal that, similar to SNX17, the C-terminal region of the protein occupies the cargo-binding pocket. However, in the case of SNX31, the motif interacting with the pocket does not consist of the last four amino acids (residues 437-440); instead, it is formed by a sequence located in a more proximal region to the FERM domain, spanning residues 410 to 420. AlphaFold-Multimer structural models of SNX31 complexes with L2 and LRP1 show a displacement of this C-terminal region from the pocket (**Figure 74**), comparable to the displacement observed in SNX17.

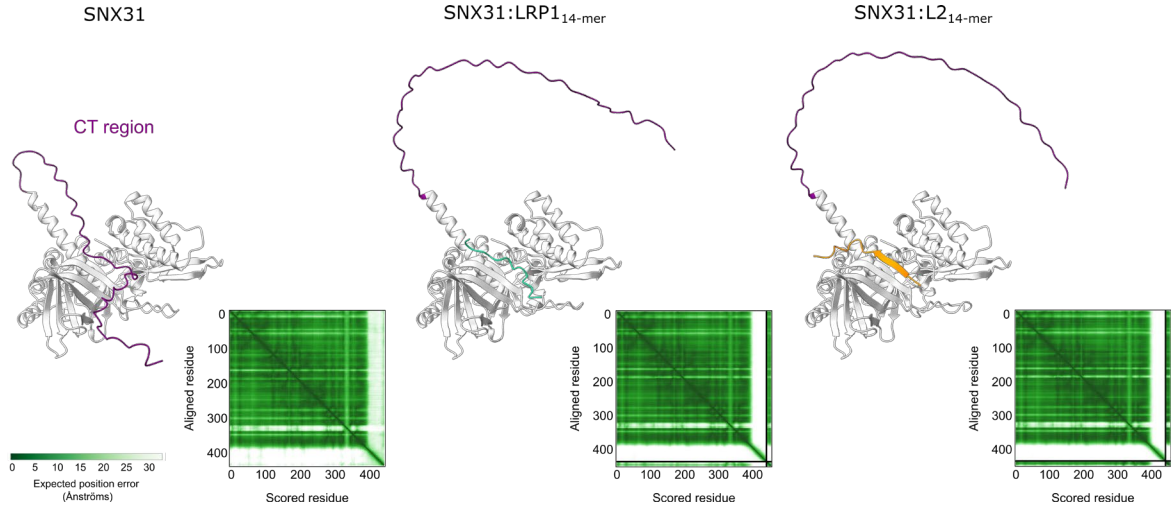

Figure 74. Evaluation of SNX31 autoinhibition disruption using AF2-multimer modeling. AlphaFold2 prediction models of SNX31 (light grey) are shown alone or in complex with the cargo peptides used in fluorescence anisotropy assays that exhibited highest binding affinity: LRP1$_{14\text{-mer}}$ (green) and L2$_{14\text{-mer}}$ (yellow). The C-terminal region of SNX31 is highlighted in purple. Note the displacement of the CT region when cargos are present. PAE plots for each model are included. Structure figures were generated with ChimeraX.

Additionally, the structural arrangement of SNX31 appears to be evolutionarily conserved, as all AlphaFold models from the species analyzed - *Homo sapiens*, *Mus musculus*, *Xenopus tropicalis*, *Thamnophis sirtalis*, and *Amblyraja radiata* - show the C-terminal region positioned within the cargo-binding pocket (**Figure 75**).

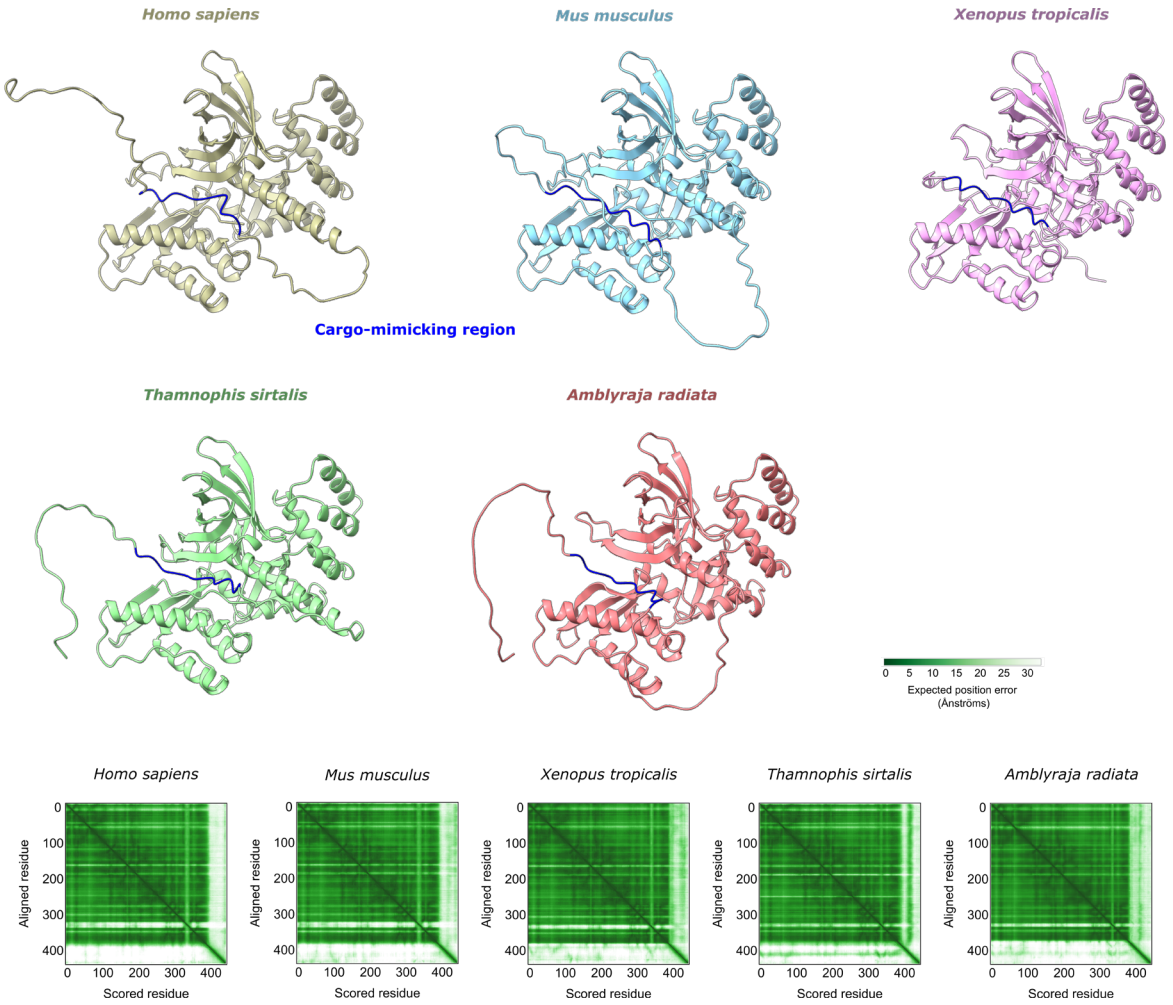

Figure 75. Conservation of the autoinhibitory mechanism across SNX31 orthologs. Models of human SNX31 and its orthologs generated by AF2, along with their respective PAE plots, are presented. The cargo-mimicking region, spanning residues 410 to 420 in the human sequence, is highlighted in dark blue. All models were sourced from the AlphaFold Protein Structure Database, except for *Amblyraja radiata* model, which was obtained using ColabFold. The UniProt accession numbers for these proteins are listed in **Figure 70**.

In conclusion, the C-tail of SNX31 appears to occupy the cargo-binding pocket, but through a different region than SNX17. As a result, the last four residues, which are thought to mediate interaction with Retriever (McNally et al., 2017), do not engage with the pocket. For this reason, it remains unclear whether the potential autoinhibition mechanism blocks Retriever interaction until cargo binding occurs or if this autoinhibition may be preventing interactions with other proteins. To determine whether SNX31 exhibits an autoinhibition mechanism similar to SNX17, or whether the pocket-interaction region corresponds to the area modeled by AF, two sequences of 18 residues from SNX31 were selected: one homologous to the region in SNX17 that binds to Retriever, referred to as SNX31$_D$ (distal from the FERM domain, residues 423 - 440), and another predicted to bind to the cargo-binding pocket in the AF2 model, referred to as SNX31$_P$ (proximal to the FERM domain, residues 409 - 426).

SNX31 in complex with both peptides, SNX31$_D$ and SNX31$_P$, was modeled using AF2. Both peptides were positioned within the cargo-binding pocket in 4 out of the 5 models for SNX31$_P$ and in all 5 models for SNX31$_D$. Although the predicted models of both peptides are associated with low pLDDT values, the expected position errors (PAE plot values) indicating the localization of SNX31 relative to both peptides are relatively low, particularly for the residues in the binding pocket. The only exception is the C-terminal region, which is expected to have high error values due to its disordered nature (**Figure 76A,B**). Notably, neither region exhibited resemblance to the characteristic NPxY motif (**Figure 76C**), which was found to be essential in SNX17 for binding to the cargo-binding pocket and triggering the autoinhibition mechanism.

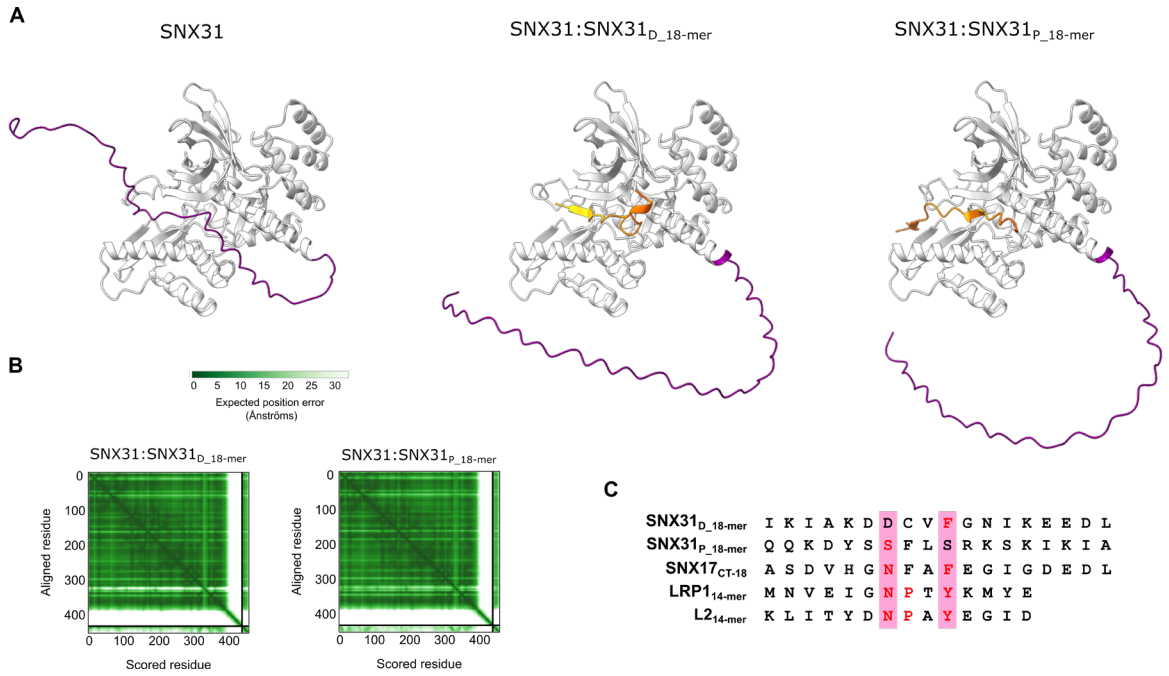

Figure 76. Sequence alignment and structural models of SNX31 with SNX31$_D$ and SNX31$_P$ to analyze potential self-interaction behavior of SNX31. (**A**) The highest-scoring structural model of SNX31, SNX31 with SNX31$_{D_18\text{-}mer}$, and SNX31 with SNX31$_{P_18\text{-}mer}$, generated using AF3, are displayed. SNX31 is oriented similarly to **Figure 75**. The C-terminal region of full-length SNX31 is shown in purple, while the SNX31$_{D_18\text{-}mer}$ and SNX31$_{P_18\text{-}mer}$ peptides are colored according to their pLDDT confidence scores (blue, very high confidence pLDDT ≥ 90; cyan, high confidence 70 ≤ pLDDT < 90; yellow, low confidence 50 ≤ pLDDT < 70; orange, very low confidence pLDDT < 50). Note the displacement of the CT region when either of the peptides are present. (**B**) PAE plots for SNX31:SNX31$_{D_18\text{-}mer}$ and SNX31:SNX31$_{P_18\text{-}mer}$. (**C**) Sequence alignment of SNX31$_{D_18\text{-}mer}$ and SNX31$_{P_18\text{-}mer}$ with SNX17$_{CT\text{-}18}$, LRP1, and L2.

In order to determine whether either of the two peptides interacts with the cargo-binding pocket, their binding affinity to SNX31 was analyzed using fluorescence anisotropy (**Figure 77A,B**). $SNX31_D$ demonstrated some binding capacity to $SNX31_{FERM-CT}$, but the affinity was too low to determine a dissociation constant. In contrast, $SNX31_P$ did not show any discernible binding. More sensitive techniques or higher peptide concentrations would be necessary to confirm whether SNX31 can effectively bind to $SNX31_P$.

Additionally, to assess whether SNX17 and SNX31 C-terminal regions are interchangeable, the ability of SNX31 to bind to $SNX17_{18-mer}$ was tested (**Figure 77B**), as well as the binding capacity of SNX17 to interact with $SNX31_{D\_18-mer}$ and $SNX31_{P\_18-mer}$ (**Figure 77C**). SNX31 did not exhibit binding to $SNX17_{18-mer}$, while SNX17 showed the expected interaction with $SNX17_{18-mer}$, but failed to bind to either $SNX31_{D\_18-mer}$ or $SNX31_{P\_18-mer}$. This indicates that the C-terminal regions are not interchangeable.

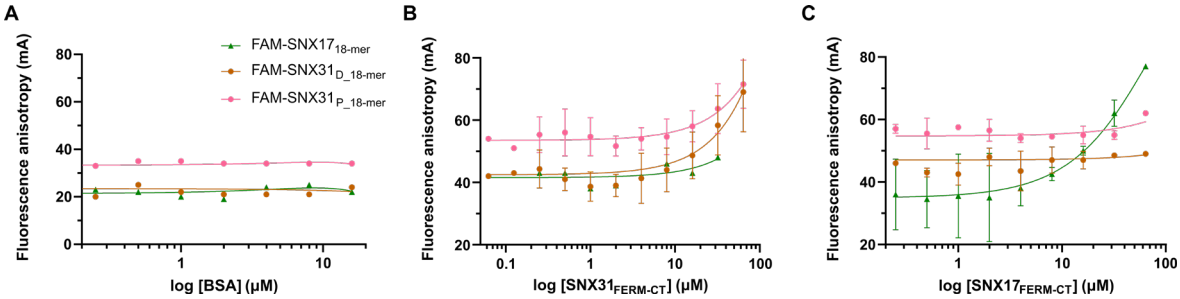

Figure 77. Fluorescence anisotropy assays to assess SNX31 self-interaction. (**A**) Analysis of cargo binding affinity to BSA to detect potential non-specific binding (n = 1). (**B**) Fluorescence anisotropy binding curves were generated by titrating $SNX31_{FERM-CT}$ against 5-FAM-labeled $SNX31_{D\_18-mer}$ (n=3), $SNX31_{P\_18-mer}$ (n=3), and $SNX17_{18-mer}$ (n=1) peptides. The binding curves are shown in the graphs. The dissociation constant for the $SNX31_{D\_18-mer}$ interaction was too high to be accurately measured. (**C**) Fluorescence anisotropy binding curves were generated for $SNX17_{FERM-CT}$ titrated against $SNX31_{D\_18-mer}$, $SNX31_{P\_18-mer}$, and $SNX17_{18-mer}$ peptides, labeled with 5-FAM. The curves are based on two replicates for each peptide. The K_D for the $SNX17_{18-mer}$ interaction was too high to be determined.

Finally, the interacting capability of SNX31 with the Retriever complex was assessed. It was hypothesized that the distal region of SNX31 would be responsible for binding to Retriever (McNally et al., 2017); however, experimental evidence for this direct interaction has not been available so far. The two SNX31 peptides, $SNX31_D$ and $SNX31_P$, were analyzed by fluorescence anisotropy to evaluate their binding to Retriever (**Figure 78**). Although the binding affinity of Retriever to SNX17 was higher (K_D = 5.7 µM), Retriever also showed the ability to bind to $SNX31_D$ (K_D = 28.8 µM), while no binding to $SNX31_P$ was detected. Therefore, the interacting region of SNX31 with Retriever appears to be comparable to that of SNX17, but with lower binding affinity.

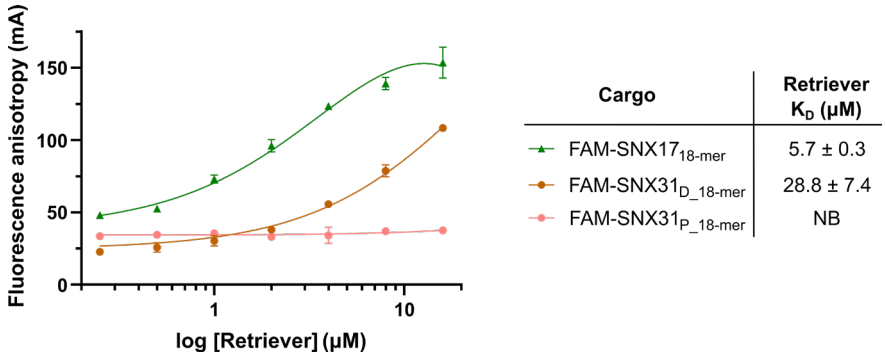

Cargo	Retriever K_D (µM)
FAM-SNX17$_{18\text{-mer}}$	5.7 ± 0.3
FAM-SNX31$_{D_18\text{-mer}}$	28.8 ± 7.4
FAM-SNX31$_{P_18\text{-mer}}$	NB

Figure 78. The C-terminal end of SNX31 contacts the Retriever complex. Fluorescence anisotropy assays measuring the direct interaction between the Retriever complex and 5-FAM-labeled SNX17$_{CT\text{-}18}$, SNX31$_{D_18\text{-}mer}$, and SNX31$_{P_18\text{-}mer}$ peptides. Data points represent the mean ± SD of three replicates for SNX31$_{D_18\text{-}mer}$ and two technical replicates for SNX31$_{P_18\text{-}mer}$ and for SNX17$_{CT\text{-}18}$. The K_D values ± SD were calculated using GraphPad Prism. *NB*, no detectable binding.

A structural model of the Retriever:SNX31$_{18\text{-}mer}$ complex was generated using AF3-Multimer (**Figure 79**). The model suggests that the C-terminal tail of SNX31 interacts with the VPS26C-VPS35L interface, forming contacts with several residues along the groove. The last 13 residues of the SNX31 peptide exhibit the highest pLDDT scores, and the PAE plot demonstrates a high level of confidence in the positioning of the last 18 residues of SNX31 relative to the Retriever subunits. Consequently, the structural model generated by AlphaFold suggests that the C-tail of SNX31 binds to the Retriever complex, a finding that has been further supported by our experimental data.

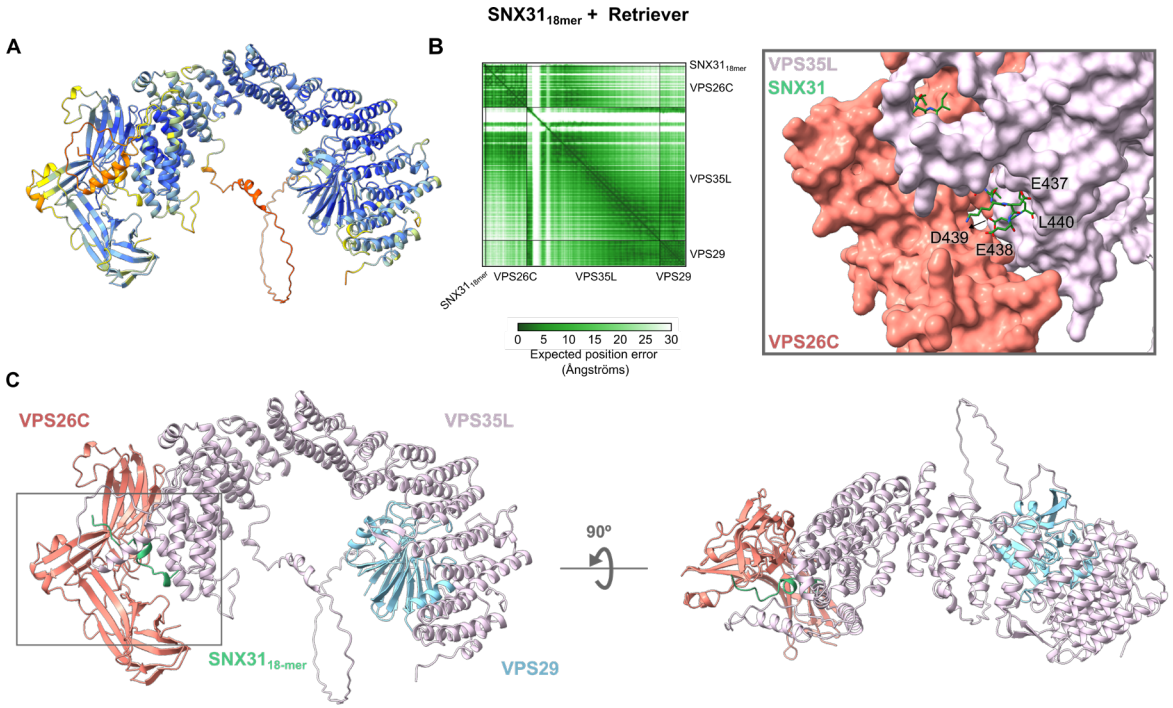

Figure 79. AlphaFold3-multimer predictions of Retriever-SNX31 interactions. (**A**) Cartoon representation of the AF2 model of the Retriever:$SNX31_{18\text{-}mer}$ complex, colored by pLDDT confidence score (blue, very high confidence pLDDT ≥ 90; cyan, high confidence 70 ≤ pLDDT < 90; yellow, low confidence 50 ≤ pLDDT < 70; orange, very low confidence pLDDT < 50). (**B**) PAE plot of the model. (**C**) Model of the complex, colored by subunits: VPS26C in red, VPS35L in light pink, and SNX31 in green. The inset provides a zoomed view of SNX31 interacting regions, showing VPS26C and VPS35L in surface view and $SNX31_{18\text{-}mer}$ in stick representation. The last four residues of SNX31 are annotated. Structural models were generated using ChimeraX. *PAE*, predicted aligned error.

4.6. Characterization of DENND10, a potential Retriever partner involved in intracellular trafficking

Finally, the analysis of another protein, DENND10, was of particular interest in this thesis, as it has been identified as a partner of the Retriever complex by co-immunoprecipitation assays (Singla et al., 2019). However, the exact role in the recycling pathway remains unknown. Additionally, the structure of DENND10 remained unresolved until recently.

DENND10 is primarily characterized by the presence of a DENN (differentially expressed in normal and neoplastic cells) domain (**Figure 80A**). This domain is known to function as a guanine nucleotide exchange factor (GEF) for Rab small GTPases. To determine whether DENND10 directly interacts with the Retriever complex, DENND10 was purified (**Figure 80B**), and its binding ability to Retriever was tested using a pull-down assay. However, no direct association was detected, as the small amount of protein retained in the presence of GST-Retriever was similar to that observed in the negative control (**Figure 80C**).

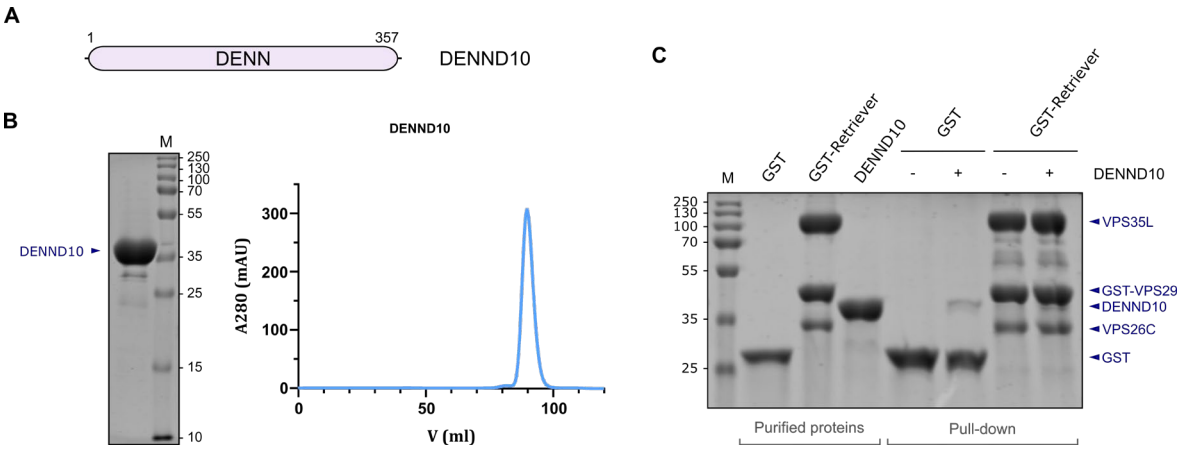

Figure 80. Diagram and purification of DENND10, and analysis of the interaction between Retriever and DENND10 by GST pull-down assay. (**A**) Schematic representation of DENND10, with the DENN domain highlighted. (**B**) SDS-PAGE gel with Coomassie staining showing the purified DENND10, along with the corresponding gel filtration chromatogram. DENND10 (40.7 kDa). *M,* Protein marker. (**C**) DENND10 was incubated with GST-Retriever in GST pull-down assays (n=1). Non-fused GST protein was used as a negative control. Purified proteins and pull-down samples were separated by SDS-PAGE and visualized by Coomassie Blue staining.

As structural characterization aids in understanding protein function, crystallization trials for DENND10 were carried out using several screening kits, including JCSG-*plus*™, Hampton Research Crystal Screens 1 and 2, ProPlex™, PACT *premier*™, PGA Eco, Stura Footprint Screen™ + MacroSol™, and MIDAS*plus*™. The protein was prepared at concentrations of 2.5 mg/ml and 5 mg/ml in a buffer containing 25 mM Hepes (pH 7.5), 150 mM NaCl, and 1 mM TCEP, or 50 mM Tris (pH 7.5), 200 mM NaCl, and 1mM TCEP, with a 1:1 ratio of protein to precipitant. Despite extensive efforts, no crystals formed under any of the tested conditions.

Since crystallization trials were unsuccessful, SEC-SAXS (size-exclusion chromatography coupled with small-angle X-ray scattering) was used as an alternative technique to gain insights into the structural dynamics and conformational flexibility of DENND10 in solution. The method combines size-exclusion chromatography with SAXS, allowing for the separation of heterogeneous mixtures while simultaneously collecting structural data on individual components as they elute from the column. As the separated species pass through the SAXS beam, scattering patterns are recorded, providing information on particle size, shape, and overall molecular architecture. DENND10 was concentrated to 5 mg/ml in a buffer composed of 50 mM Tris (pH 7.5), 200 mM NaCl, and 1 mM TCEP, and experimental SEC-SAXS data of DENND10 were collected at the B21 bioSAXS beamline at the Diamond Light Source synchrotron in Oxfordshire (**Figure 81**). Guinier analysis of the SAXS data showed linearity at low q, indicating that the sample was monodisperse, and demonstrated good quality for further analysis. Moreover, Porod analysis indicated that both DENND10 is monomeric at the concentrations employed (**Table 13**). The Kratky and the P(r) plot, displayed a marked Gaussian profile indicative of a compact conformation with limited flexibility (**Figure 81C,D**). The calculated scattering curves for the AF2 model (χ^2=1.08) aligned well with the experimental curve (**Figure 81E**) and docked properly into the corresponding *ab initio* SAXS envelope (**Figure 81F**). These results demonstrate that the AF2 model accurately represents the conformation of DENND10 in solution

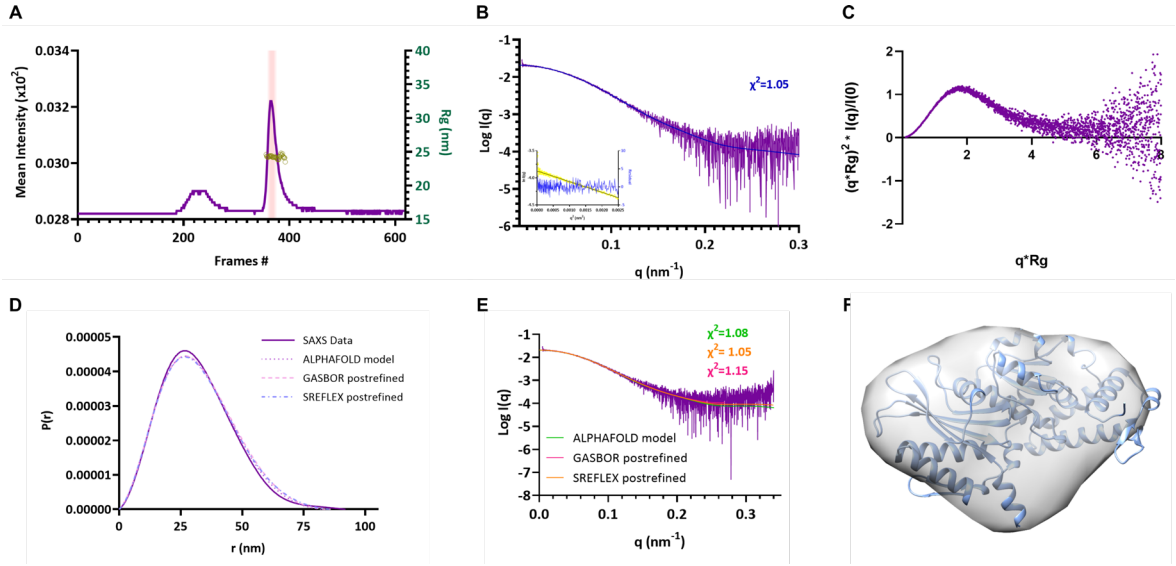

Figure 81. SEC-SAXS analysis of DENND10. (**A**) Profiles are plotted according to frame numbers. The frame range used for averaged data is highlighted. The radius of gyration is shown in yellow. (**B**) SAXS scattering profile overlaid with the fitting curve calculated by GNOM and the resultant $\chi 2$ fitting values of the experimental SAXS (purple and dark blue, respectively). The Guinier plot is shown in the inset with residuals in blue. (**C**) The *ab initio* model envelope (in transparent gray) superimposed with the AF2 protein model (in cartoon). The best-scoring *ab initio* bead model was selected using DAMMFILT and the envelope (in gray) was generated using the molmap function in UCSF Chimera.

The structure of DENND10 has been recently solved by cryo-EM (Laulumaa et al., 2024), and a comparison of this structure with the model generated using AF2 shows a high degree of similarity (**Figure 82**).

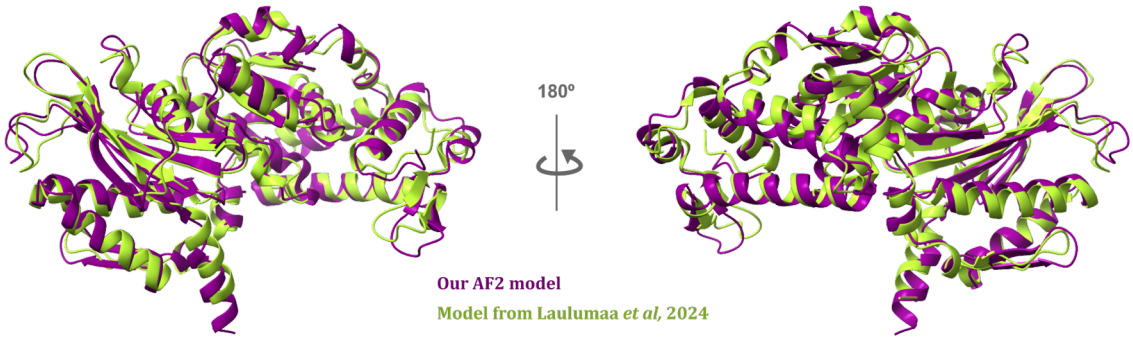

Figure 82. Structural alignment of DENND10 between the model obtained using AF2 and the cryo-EM model from Laulumaa *et al.* The AF2 model is shown in purple while the model based on cryo-EM data (PDB ID: 8P0V) is displayed in green.

Chapter 5: DISCUSSION

5.1. Characterization of the structural organization of the Retriever complex

In this work, the structural organization of the Retriever complex was investigated. By purifying specific VPS35L truncation constructs in combination with VPS26C and VPS29, we were able to map the critical interacting region of each subunit (**Figure 14**). VPS26C and VPS29 do not directly interact with each other; however, VPS35L interacts with both subunits through distinct and independent regions. The VPS26C-binding region in VPS35L is restricted to residues 110-436. Additionally, VPS35L contains two cooperative regions to bind VPS29: one within the first 110 residues and another between residues 598-963. Experimental validation of this observation was further supported by two research groups (Boesch et al., 2024; Healy et al., 2023) (**Figure 6**). The solved structure of the VPS29-VPS35L complex supports our observation that the initial residues of VPS35L are crucial for its interaction with VPS29, as deletion of the first 110 amino acids abolishes VPS35L-VPS29 interaction (Healy et al., 2023). Additionally, Boesch *et al*. demonstrated that the complete deletion of the "belt" sequence or even the first 100 amino acids of VPS35L, including the unstructured linker sequence, had no effect on the binding between VPS35L and VPS26C, which is consistent with our findings (Boesch et al., 2024).

Additionally, we have observed that although the Retriever complex forms a compact structure, the VPS35L subunit is composed of HEAT repeats, which confer significant flexibility to the protein. This flexibility is supported by structural predictions of the complex using AlphaFold, which show lower confidence values (via the PAE plot) in the positioning of various VPS35L repeats relative to the rest of the complex. This flexibility likely allows the protein to adopt different conformations when they interact with different binding partners or are exposed to external forces, which may be crucial for the assembly of the entire recycling machinery and for properly aligning the complex to the vesicle shape to carry out its function.

Furthermore, the oligomeric state of the Retriever complex was determined by gel filtration chromatography (**Figure 12**). When salt concentrations reached 300 mM, the major population of the complex consists of monomers of the trimer, while a small fraction forms dimer of trimers. A similar monomer-to-dimer ratio was also observed at NaCl concentrations closer to physiological salt levels (150mM). This differs from what has been observed in the Retromer complex, which tends to form dimers more readily (Lucas et al., 2016). This tendency toward oligomerization facilitates the formation of a helical structure that covers the tubule. Therefore, how the Retriever complex associates with the other components of the retrieval pathway and its contribution to tubule/vesicle formation remain open questions.

5.2. Study of the cargo recognition by SNX17

The association of SNX17 with our cargos of interest - LRP1, APP, ITGB1, VEGFR1, and L2 - has been explored. Using fluorescence anisotropy assays with the $SNX17_{FERM-CT}$ protein and 5-FAM-labeled peptides, the dissociation constants were determined (**Figure 27**), revealing several interesting observations.

First, we observed that the presence of an NPxY motif is not the sole requirement for SNX17 binding. Instead, additional specificity determinants beyond the NPxY motif seem to play a role in the interaction. This hypothesis has also been suggested by Farfán *et al.* (Farfán et al., 2013), and supported by Stockinger *et al*, who observed that the protein megalin, also known as LRP2, despite containing three NPxY motifs, does not interact with SNX17 (Stockinger, 2002). In our experiments, this hypothesis is further supported by the lack of binding affinity observed between the NPxY-containing $VEGFR1_{14-mer}$ peptide and SNX17.

Secondly, ITGB1, which contains two NPxY motifs in its cytoplasmic region - one located closer to the transmembrane region ($ITGB1_P$) and the other in a more distal region ($ITGB1_D$) - exhibited different affinities for SNX17. We found that $ITGB1_P$ has a higher binding affinity than $ITGB1_D$, with K_D values of 72 µM for $ITGB1_P$ and 125 µM for $ITGB1_D$. The peptide containing the proximal motif yielded a high affinity for SNX17, consistent with previous findings (Farfán et al., 2013). Notably, although earlier studies indicated that SNX17 associates with the ITGB1 distal NPxY motif (Böttcher et al., 2012; Steinberg et al., 2012), this work suggests that the membrane-proximal motif might play a more significant role than previously assumed.

Thirdly, it is important to note that the LRP1 cargo contains two distinct NPxY motifs. We focused exclusively on NPxY membrane-proximal motif (4470-4473) because previous experiments determined that only this motif, and not the membrane-distal motif (4504-4507), binds to SNX17 (Farfán et al., 2013). We observed a high affinity of the $LRP1_{14-mer}$ (residues 4464-4477), which contains the membrane-proximal NPxY motif, for SNX17 (K_D = 2.2 µM). However, Yong *et al.* reported that a 16-mer LRP1 peptide (4497-4512), which contains the membrane-distal NPxY motif, also exhibited high affinity for SNX17, with a K_D of 6 µM (Yong et al., 2021). Future studies could explore whether this second peptide similarly interacts with SNX17 in our experimental binding assay. While SNX17 can interact with proteins containing two NPxY motifs, such as in the case of LRP1 and integrins, it exhibits a higher affinity for the membrane-proximal NPxY motif. This preference may contribute to the regulation of SNX17's interactions with its cargo proteins. It has been reported that phosphorylation of the membrane-proximal NPxY motif of LRP1 reduces SNX17 binding (Betts et al., 2008), potentially influencing cargo recycling.

Fourthly, our analyses show that the cargos we examined bind to SNX17 with varying affinities, ranging from 2.2 μM to 125 M. This observation raises several questions: Why does each cargo have a different affinity? Is there a biological significance to this variation? One possibility is that cargos with higher affinity exist in fewer copies, requiring more rapid recycling. Alternatively, a higher proportion of these cargos may be required in the membrane compared to others.

Some of the cargos recycled by the SNX17-Retriever pathway have also been identified as cargos of the Retromer complex, such as APP. Interestingly, the affinity of SNX17 for this cargo is ten times lower than for LRP1 that is only recycled by the SNX17-Retriever pathway. Evolution may have developed redundant mechanisms to ensure that essential cargos are recycled by multiple pathways. This redundancy helps maintain the abundance of essential cargos at the plasma membrane, while modulating binding affinity may prevent excessive cargo accumulation at the plasma membrane. Further exploration of cargo recognition and its biological relevance is needed. For example, identifying all the cargos recycled by the Retriever pathway, analyzing their functional relationships and mapping common pathways could provide insights into potential roles in cancer and neurodegeneration. Dysregulated trafficking of growth factor receptors and adhesion proteins (such as integrins and cadherins) is a common hallmark in malignant cells (O'Sullivan & Lindsay, 2020). For instance, Rab25, an oncogene frequently amplified in breast and ovarian cancers, interacts directly with β1 integrin, driving invasive migration by directing α5β1 integrin and EGFR to the leading edge of ovarian cancer cells (Caswell et al., 2007).

Neuronal trafficking pathways are tightly regulated, with synaptic function being significantly altered in a short time frame due to changes in the levels of receptors, ion channels, and transporters. Protein trafficking is essential for numerous neuronal processes, including neurotransmitter release via exocytosis, the recycling of synaptic vesicle proteins, and the regulation of receptor signaling (Buckley et al 2000), underscoring the potential role of the Retriever pathway in preventing neurological disorders. For instance, neuronal recycling of APP has been shown to protect against Alzheimer's disease by diverting it away from the amyloidogenic pathway. Therefore, increasing the rate of APP recycling mediated by SNX17-Retriever could be a promising potential therapeutic target. Pharmacological chaperones, for example, could be used to enhance the stability of the SNX17-APP interaction, potentially increasing APP recycling rates. This strategy has already been explored for the Retromer complex by Mecozzi *et al.*, who designed a small molecule that stabilized Retromer levels and enhanced its function in neuronal cultures, leading to a reduction in APP levels within endosomes (Mecozzi et al., 2014). A similar approach could be applied to stabilize the Retriever-SNX17 interaction. Moreover, we have identified a mutation in the APP sequence (K763E) that increases SNX17 binding affinity (**Figure 38**). It is noteworthy that the overall effect on binding affinity is likely the result of a synergistic contribution from multiple residues. In this work, only

point mutations were analyzed, which may limit the observed impact on affinity. Future studies could explore multi-point mutations to gain a more comprehensive understanding of how the entire interaction surface of APP contributes to SNX17 binding.

Fifthly, we have observed that the L2 protein from HPV has the highest binding affinity to SNX17 (K_D = 2.2 μM) among all the studied cargos (**Figure 27C**). While the interaction between L2 and SNX17 had been previously described, the specific K_D for the SNX17-L2 interaction had not been determined. We also experimentally validated two critical residues for L2 binding to SNX17 (E258 and Y252), as alanine mutagenesis of these residues significantly reduced the binding affinity (**Figure 38**). This study shows that the central region of the HPV capsid protein L2 displays a remarkably high affinity for SNX17 and could outcompete the physiological cargos of SNX17. The L2-SNX17 interaction is essential for HPV infection, being necessary for optimal capsid disassembly and facilitating the viral escape from late endosomes (Bergant et al., 2017; Bergant Marušič et al., 2012). The role of the Retriever complex in HPV infection is still poorly understood. Two studies have shown that siRNA-mediated knockdown of Retriever reduces the infection efficiency of HPV16 pseudovirions (McNally et al., 2017; Pim et al., 2021). In addition, Retriever has been observed to colocalize with L2 in HeLa cells infected with HPV16 pseudovirions (Pim et al., 2021). Here, we confirm that the engagement of L2 with SNX17 efficiently recruits the Retriever complex, potentially facilitating HPV infection. Developing strategies to reduce viral binding affinity to the recycling pathway could have important clinical implications, as this could inhibit viral infection. Targeting the NPxY motif as a hotspot would likely result in too many side effects, given its ubiquity in cellular cargos. Instead, drugs that block the specific residues identified could significantly reduce the binding affinity of the virus, making it less effective in infection, without affecting physiological cargos.

Additionally, the virus itself might potentially be used as a vehicle for drug delivery to the nucleus. Many drugs fail due to degradation within the cell, particularly in the endosome, but L2 is already optimized for transport and possesses intrinsic properties that could be harnessed for this purpose. Viral-based delivery systems have already been explored in gene therapy and are becoming successful for their use in the clinic, such as retrovirus, adenovirus (types 2 and 5), adeno-associated virus, herpes virus, pox virus, human foamy virus (HFV), and lentivirus (Nayerossadat et al., 2012).

5.3. Characterization of the Retriever-SNX17 assembly

Retriever does not directly bind to cargo

We have observed that Retriever does not bind directly to the cargo, as evidenced by our experiments (**Figure 40B**). Instead, SNX17 is the only protein responsible for direct interaction with the cargo. This indicates that the cargo recognition mechanism within the Retriever complex is distinct from that of the Retromer complex. In the case of Retromer, the complex itself interacts directly with the cargo via VPS26, together with associated-SNX. In contrast, Retriever relies on SNX17 to mediate cargo recognition, acting as an intermediary between the cargo and the complex. This divergence in recognition strategies highlights functional differences between the two complexes.

Cargo binding to SNX17 triggers Retriever recruitment

We have determined that the binding of the cargo to SNX17 enhances Retriever recruitment (**Figure 40A**). A similar mechanism is required in the Retromer-SNX3 context. The crystal structure of the quaternary VPS35-VPS26-SNX3-DMT1 tail complex reveals that SNX3 binds at the interface between VPS35 and VPS26. Upon binding to SNX3, VPS26 undergoes a conformational change in its cargo-binding motif, which facilitates the recognition of the DMT1 cargo tail by both VPS26 and SNX3 (Lucas et al., 2016). Thus, the SNX3/Retromer complex serves two distinct functions: membrane association and cargo recognition. Consequently, the complete Retromer complex, together with SNX3 and the cargo, is necessary for the assembly of the recycling machinery (J. Wang et al., 2018).

In the Retromer-SNX27 system, a cooperativity mechanism also exists. The PDZ domain of SNX27 binds to both PDZ-binding motifs on the cargo and the Retromer subunit VPS26. Interaction with VPS26A significantly enhances the binding affinity of the SNX27 PDZ domain to PDZ-binding motifs, increasing it by an order of magnitude. This suggests a cooperative role in the process of cargo selection (Gallon et al., 2014).

However, the cargo recognition mechanisms in the Retromer complex differ from those in the Retriever pathway. In the Retromer context, SNX3 and Retromer must first interact to enable cargo recognition. In contrast, in the Retriever pathway, SNX must first interact with the cargo in order to promote Retriever complex recruitment.

This study demonstrates that the last 18 amino acids of SNX17 display a robust interaction with the VPS26C-VPS35L interface. Through mutational analysis based on AF2-modeling, we have identified two critical anchor points on VPS35L for SNX17 binding. The first is located in the VPS35L hinge region, involving residues K157 and R161, and the second in a pocket formed by R248E and W280 (**Figures 43B** and **50**). Variants of these VPS35L residues are present in the

COSMIC (Catalogue Of Somatic Mutations In Cancer) database. p.R161Q (associated with biliary tract cancer (Wardell et al., 2018)), p.R248G (associated with ovarian cancer (The Cancer Genome Atlas Research Network, 2011)), and p.W280L (associated with colorectal cancer) are predicted as probably damaging by PolyPhen2 (score ≥ 0.99) (Adzhubei et al., 2010)). Other cancer-associated mutations in VPS35L have been proven to disrupt Retriever complex formation and impair membrane protein homeostasis (Boesch et al., 2024). Further work will be required to evaluate the potential association between the disruption in Retriever recruitment by SNX17 to endosomes and cancer progression.

Ionic strength affects cargo-mediated SNX17-Retriever interactions

The effect of ionic strength on the cargo-mediated interaction between SNX17 and Retriever has been examined in this work (**Figure 42**). We observed that at low salt concentrations (50 mM NaCl), a strong interaction occurred even when the cargo was not present, likely due to non-physiological interactions between oppositely charged regions. In contrast, increasing the salt concentration to physiological levels (150 mM) significantly reduced the binding of Retriever to SNX17 in the absence of cargo, with a more pronounced effect at 300 mM NaCl. It is noteworthy that Boesch *et al.* recently reported a high level of interaction between Retriever and SNX17 in the absence of cargo (Boesch et al., 2024). However, their interaction assays were performed at low salt concentrations (50 mM), whereas we have observed that this interaction in the absence of the cargo is disrupted with increasing salt concentration.

SNX17 has an autoinhibition mechanism under cargo-absent conditions

This thesis has unexpectedly revealed that the C-terminal domain of SNX17 is involved in an evolutionary conserved intramolecular autoinhibitory interaction, a feature not previously described in sorting nexin proteins. We observed that cargo binding significantly enhances Retriever recruitment by SNX17. The autoinhibition of SNX17 that hampers Retriever binding in the absence of cargo is mediated by a physical interaction between the cargo-binding site and the C-terminal region of SNX17. We speculate that this mechanism prevents the assembly of the recycling machinery when there is no cargo to be recycled. In this way, autoinhibition may prevent Retriever-SNX17 complex aggregation in the cytosol, ensuring that the recycling machinery assembles only when SNX17 binds membrane proteins containing recycling signals and/or when recruited to endosomal membranes. Autoinhibition plays a crucial role in regulating the function of many proteins by preventing premature activation and ensuring that pathways respond only to specific signals (Trudeau et al., 2013). This mechanism has been described in various intracellular trafficking

proteins, such as cytoplasmic linker protein 170 (CLIP-170), a dimeric protein involved in regulating microtubule dynamics. The C-terminal zinc knuckle domain of CLIP-170 autoinhibits its CAP-Gly-1 and CAP-Gly-2 domains, preventing them from binding to microtubules or tubulin (Mishima et al., 2007). Another example is IST1 (Increased Sodium Tolerance-1), an ESCRT-III-related protein essential for cytokinesis, which binds to LIP5, VPS4, and CHMP1. Its autoinhibited state is maintained by an α-helix (α5) in the N-terminal domain, called the 'autoinhibitory helix', which packs perpendicularly against two other helices (α1 and α2), folding against the core to prevent higher-order interactions. In the inactive state, the ESCRT-III complex remains dispersed throughout the cytoplasm (Bajorek et al., 2009). Other intrinsically autoinhibited proteins include the WASP (Wiscott-Aldrich Syndrome Protein) family (Higgs & Pollard, 2001), cytoplasmic dynein-1 (Xiang & Qiu, 2020), and SHIP1 (Src homology 2 domain-containing inositol 5-phosphatase 1) (Waddell et al., 2023).

Activity inhibition of the functional domain of a protein can be achieved via allosteric mechanisms or direct occlusion of the active site. Reversal of inhibition often occurs through binding to activating partners, post-translational modifications, or proteolysis of the inhibitory module (Trudeau et al., 2013). In the context of SNX17, inhibition of the Retriever-binding motif happens via direct occlusion, as this region is positioned inside the cargo-binding pocket. In this way, SNX17 is constrained in a nonfunctional conformation. The inhibition is reversed upon cargo interaction, as the higher binding affinity of the cargo displaces the Retriever-binding motif, making it accessible for interaction with the Retriever complex. Autoinhibition mechanisms often involve regions with high flexibility, which facilitate the transition from an inhibited to an active state (Pufall & Graves, 2002). AlphaFold2-Multimer predicts that SNX17 has a highly flexible C-terminal domain, further supporting the presence of an autoinhibition mechanism. This autoinhibitory regulation is specific to particular protein activities, making it a potential target for therapeutic interventions (Pufall & Graves, 2002). Given that certain diseases have been linked to reduced levels of either the Retriever subunits VPS26C (Beetz et al., 2020) or VPS35L (Kato et al., 2019), the autoinhibitory domain of SNX17 could be a therapeutic target to promote Retriever recruitment and increase the stability of the SNX17-Retriever complex.

5.4. Membrane association of SNX17 and the Retriever complex

SNX17 binds to membranes but do not induce membrane deformation

In an attempt to recreate physiological conditions, fluorescence microscopy experiments in GUV model systems were performed, and showed that SNX17 can bind to membranes through its association with PI3P (**Figure 62**). However, no membrane deformation or invagination was observed upon SNX17 binding, as no tubules or smaller vesicles were formed. Thus, it remains unclear whether the Retriever recycling machinery is capable of deforming the membrane, and if so, what the underlying mechanism might be.

It is known that certain SNXs oligomerize through the dimerization of their BAR domains to induce membrane curvature. So far, SNX17 and SNX31 are the only SNX members associated with Retriever. Both SNXs tend to exist predominantly as monomers, although some oligomerization occurs, as suggested by their presence in multiple elution fractions in gel filtration chromatography, all in low quantities relative to the monomeric form (**Figure 24**). This observation, that the monomeric state is the predominant form, was previously reported (Czubayko et al., 2006). In line with their non-self-assembling behavior, neither SNX17 nor SNX31 has a defined BAR domain. However, while membrane curvature generation has typically been attributed to SNX-BAR adaptor proteins, Retromer's ability to transport a wide range of cargos is thought to rely on various adaptors, including those lacking membrane-bending BAR domains (Leneva et al., 2021). For example, SNX3 lacks a BAR domain, yet the Retromer:SNX3 complex promotes tubule formation. Retromer arches engage with SNX3 and the cargo to organize membrane contact points, forcing the bilayer into a tubular shape (Gopaldass et al., 2024).

We propose two possible scenarios for the membrane deformation process by the Retriever recycling machinery: a similar tubulation mechanism to that observed with SNX3 may apply to SNX17, or there may be additional Retriever-associated proteins, yet to be identified, with intrinsic membrane remodeling abilities that could be involved in membrane bending.

Membrane carriers typically adopt tubular or vesicular shapes. While the precise shape of the transport carriers potentially formed by the Retriever recycling machinery remains uncertain, we speculate that the most likely scenario involves the formation of tubular vesicles for several reasons. First, Retromer, which is closely related to Retriever, is known to induce the formation of tubulovesicles. Second, both Retromer and Retriever require the WASH complex, an actin-nucleating factor. While clathrin is characteristic of circular vesicles, actin is associated with tubular vesicles. Tubular carriers are believed to be advantageous for transporting large amounts of cargo over long distances, as multiple cargo molecules can be loaded into a single tubulovesicle and

transported simultaneously to the target membrane by a single microtubule-associated motor molecule (Polishchuk et al., 2009).

Membrane binding activates SNX17, inducing Retriever recruitment

In our endosome-mimicking system, membranes enriched with PI3P were capable of recruiting SNX17, followed by subsequent association of Retriever (**Figures 62** and **67**). This suggests that PI3P binding induces a conformational change in SNX17, similar to that produced by cargo binding. This change likely disengages the C-terminal region from the cargo-binding pocket, releasing the Retriever-binding region located at the C-terminus. This mechanism could act as a spatiotemporal control, ensuring that SNX17 is exclusively activated at endosomal membranes, facilitating Retriever recruitment. Similar activation mechanisms involving phospholipids have been described in other proteins, such as ERM (Ezrin, Radixin, and Moesin) proteins. ERM proteins serve as a link between the plasma membrane and the actin cytoskeleton. These proteins possess a FERM domain in their N-terminal region, which binds membrane proteins, and a C-terminal domain that binds F-actin. The two domains are held in an autoinhibited state by reciprocal intramolecular interactions. Activation occurs through phospholipid binding, with PIP2 shown to enhance ERM protein binding to the transmembrane protein CD44 via the FERM domain. A crystal structure of the radixin FERM domain complexed with IP3 (the head group of PIP2) suggests that phospholipid binding may allosterically disrupt these intramolecular interactions (Hamada, 2000). This disruption weakens the interaction between the FERM domain and the tail, exposing the actin-binding sites and activating the protein (Pearson et al., 2000).

Despite these insights, the precise molecular mechanism by which SNX17 releases its C-terminal tail and recruits Retriever in the presence of membranes remains unclear. Analyzing the AlphaFold model of SNX17, we identified an acidic region spanning residues T459-L470, which appears to be negatively charged, specially the last four residues (**Figure 65**). This region is responsible for recruiting the Retriever complex. We hypothesize that this negatively charged region prevents close membrane proximity, instead orienting this region away from the membrane, thereby making it accessible for interaction with Retriever. However, further experiments are necessary to validate this hypothesis. It is of noted that the presence of negatively charged residues within the PX domain, which contribute to naturally orienting this region away from the negatively charged membrane surface while simultaneously positioning the basic pole towards the phospholipid bilayer, has already been described in other SNX family members, such as SNX3 (Lenoir et al., 2018). Interestingly, some of the residues in SNX3 that are responsible for contributing to the negative charge are conserved in SNX17 and SNX31 (for instance, E73 in SNX17 and D73 in SNX31 are equivalent to E116 in SNX3, and E80 in SNX17 and E80 in SNX31 are equivalent to E123 in SNX3).

Therefore, negatively charged regions may play an important role in SNX17 activation, but experimental validation of this hypothesis has not yet been provided.

Molecular mechanism of Retriever recruitment to membranes

An outstanding question concerns the molecular mechanism behind the recruitment of Retriever to membranes. In the case of the Retromer complex, which lacks membrane-binding domains, membrane association occurs through interactions with SNX3 and the late endosomal/lysosomal Rab GTPase Rab7 (McNally & Cullen, 2018). Similarly, Retriever lacks predicted membrane-binding capacity and likely relies on protein–protein interactions for its recruitment to endosomes. Previous studies have suggested that Retriever recruitment to endosomes may be mediated by its association with the CCC complex, which itself is recruited by the WASH complex. However, conflicting reports exist: McNally *et al.* found that SNX17 depletion did not affect Retriever recruitment to membranes (McNally et al., 2017). Similarly, Giridharan *et al.* demonstrated that SNX17 and the WASH complex were insufficient to recruit Retriever or the CCC complex to endosomes (Giridharan et al., 2022).

In contrast, our *in vitro* studies provide evidence that SNX17 plays a crucial role in Retriever recruitment to membranes. We observed strong colocalization of Retriever with SNX17 bound to membranes of GUVs and LUVs carrying PI3P (**Figure 66**). Our data indicate that Retriever lacks inherent membrane-binding affinity, suggesting that SNX17 serves as an anchor for Retriever engagement on membranes. While there is good evidence that the CCC complex enhances Retriever recruitment, it is not essential for this process. Studies by Singla *et al.* observed an increased cytosolic staining of VPS35L following *COMMD3* or *CCDC93* deficiency, but it did not completely prevent endosomal recruitment of VPS35L (Singla et al., 2019). Boesch *et al.* also found that VPS35L variants, which disrupt CCC interaction, still retain endosomal localization in cellular studies (Boesch et al., 2024). Based on these findings, we propose that the interaction between SNX17 and Retriever might be sufficient for the recruitment of the Commander complex to endosomes and that CCC and WASH complexes act as reinforcement.

5.5. Characterization of SNX31

Even though SNX31 shares 43% sequence identity with SNX17, the structure of SNX31 has been suggested to closely resemble that of SNX17, and indeed, structural predictions show a comparable conformation. Both proteins feature PX and FERM domains of a similar length, and bind to NPxY-containing cargos through their cargo-binding pocket localized within the F3 module from the FERM domain. This suggests that their functions and mechanisms of action may also be similar. The ability of SNX17 and SNX31 to potentially recognize the same cargos could provide cells with alternative proteins capable of performing equivalent functions, acting as a protective mechanism. However, significant differences have been identified in this study. While the FERM domain of SNX17 exhibits strong binding affinity to the cargos LRP1 and L2 (**Figure 27B**), the FERM domain of SNX31 showed much lower affinity (**Figure 72**). Additionally, SNX31 demonstrates almost undetectable or completely undetectable binding to APP and ITGB1, respectively. This contradicts observations by Tseng *et al*., who reported that SNX31 can bind to the membrane-distal NPxY motif of integrin β1 tails in endosomes (Tseng et al., 2014).

Similar to SNX17, SNX31 displays a higher binding affinity for L2 compared to the cellular cargos studied, suggesting that the human papillomavirus may utilize this protein for its transport within the cell. However, SNX31 expression in mainly restricted to the urinary bladder (Tseng et al., 2014; Vieira et al., 2014; Habuka et al., 2015), with very low or absent expression in the skin based on the Human Protein Atlas (Uhlén et al., 2015), the primary tissue infected by HPV. While HPV predominantly infects epithelial cells in areas such as the genital, anal, and oral regions, it has also been linked to infections in the urinary tract, potentially causing lesions or growths, such as condylomas or papillomas, in the urethra and other parts of the urinary system (Barsegian & Kosova, 2023). Further investigation into the potential role of SNX31 in viral infections could be clinically relevant, as it could potentially serve as a drug target to inhibit HPV ability to replicate within host cells.

Regarding the expression profile of SNX31 in cellular tissues, differential expression levels of this protein have been observed in primary skin melanoma. Missense mutations in *SNX31* were reported in 7% of cases in a large-scale study on somatic mutations in melanoma (Hodis et al., 2012), while a 9.0% mutation frequency was noted in 46 primary mucosal melanomas in another study (Kim et al., 2017). Furthermore, mutations and copy number variations of *SNX31* were detected at a frequencies of 3.7% and 6%, respectively, in a separate skin melanoma dataset (Vanni et al., 2020). Somatic mutations in SNX31 have been identified throughout the entire protein, with several accumulated in the PX and FERM domains (Hodis et al., 2012) (**Figure 83**). One missense mutation is localized within the PX domain (E46K). While the R37 and Y38 residues, which could be responsible for PI3P binding in SNX31, based on similarities with the binding of SNX17 to PI3P,

are relatively distant from the mutated residue, it remains unknown whether this mutation could also affect the PI3P binding. Additionally, there is only one described mutation in the F3 lobe of the FERM domain (G327E). However, this mutation appears to be located far from the binding pocket in the structural prediction of the protein, suggesting it may not be relevant for cargo binding, though experimental validation is lacking. To date, no mutations affecting the C-terminal region of SNX31, which could be involved in Retriever binding, have been described. The reported mutations might impact interactions with other, yet unidentified proteins, or disrupt protein stability. Currently, it remains unclear how reduced SNX31 expression levels or mutations in its FERM domain influence melanoma pathology, and whether these changes result in abnormal cargo trafficking remains to be determined.

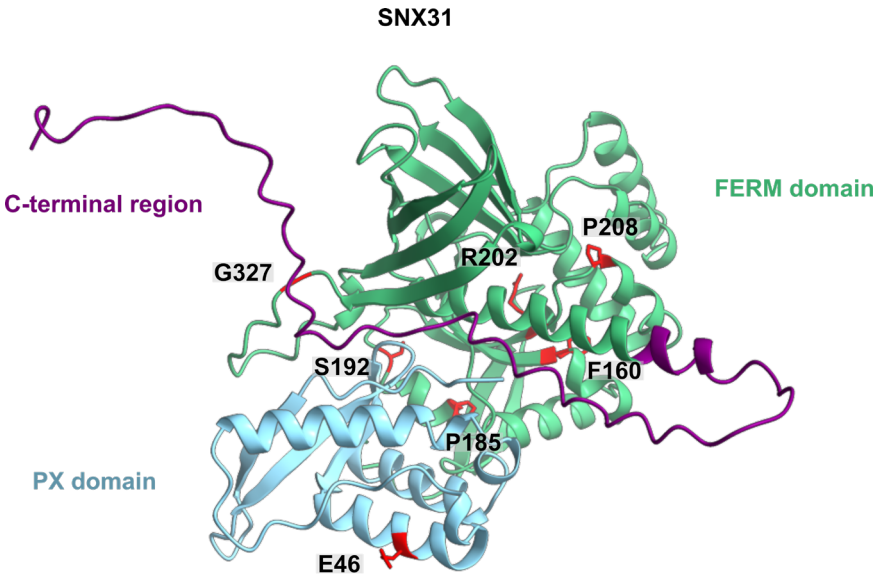

Figure 83. Structural model of SNX31 with cancer-related mutations highlighted. The structural model obtained using AF2 is colored in blue for the PX domain, green for the FERM domain, and purple for the C-terminal region. The residues that were found to be mutated in skin melanoma (Hodis et al., 2012) are highlighted in red and shown in sticks. The model is rotated 90º in relation with **Figure 69**.

Concerning the structural conformation of SNX31, our experimental results suggest that SNX31 may self-interact, potentially through its distal region of the CT-domain engaging with the cargo-binding pocket (**Figure 77B**). These findings differ from the predictions made by AlphaFold (**Figures 74** and **75**). The lack of sequence conservation between the distal region of SNX31 and its potential cargos (**Figure 76C**), along with limited experimental validation, leaves open the possibility of an autoinhibition mechanism for this protein.

We have established that the distal region of SNX31 directly interacts with the Retriever complex (**Figure 78**), which aligns with previous observations (McNally et al., 2017). However, it

remains uncertain whether cargo or membrane binding influences SNX31 interaction with the Retriever complex. Additionally, Retriever exhibits higher binding affinity of Retriever for SNX17 C-terminal region than for SNX31 C-terminal region, suggesting a preference for SNX17. Whether SNX31 requires additional interacting regions to enhance its affinity for Retriever or whether SNX31 has higher affinity for other recycling complexes remains unknown.

To further investigate SNX31 function, identifying a cargo with high-affinity binding for this protein would be beneficial, as it would help characterize its mechanism of action. A peptide array screen comprising multiple peptides derived from transmembrane proteins, which were incubated with SNX17 and SNX31 (Ghai et al., 2013b), revealed some promising cargos for SNX31. Considering that SNX31 is localized in the bladder, the NPxY-containing MET (mesenchymal-epithelial transition) protein could be a promising cargo candidate. The MET protein is a receptor tyrosine kinase that plays key roles in various cellular processes, including cell proliferation, survival, and motility. Dysregulation or mutations in the MET gene have been associated with various cancers and are often linked to tumor growth, metastasis, and poor prognosis. Thus, proper trafficking of the MET protein is crucial for tissue homeostasis and human health (Organ & Tsao, 2011). Specifically, mutations in *MET* gene are associated with hepatocellular carcinoma, various head and neck cancers, and papillary renal cell carcinoma. It would be very interesting to study the potential role of SNX31 in recycling MET and whether disruption of this trafficking has implications in cancer development.

In conclusion, SNX17 and SNX31, while structurally similar, they may target distinct groups of cargo proteins impacting on different cellular processes depending on the tissue type and cellular environment.

5.6. The role of DENND10

Although the DENND10 protein has been recognized as a component of the Retriever complex, its specific function within the recycling machinery remains unclear. In this work, no direct interaction of this protein with the Retriever complex was detected (**Figure 80C**). Indeed, recent studies have shown that DENND10 directly interacts with CCDC22 and CCDC93 subunits of the CCC complex, rather than with Retriever. CCDC22 and CCDC93 form a V-shaped coiled-coil dimer that is bridged by conserved elements in the DENN domain of DENND10 (**Figure 84**). These interactions have been validated using isothermal titration calorimetry (ITC), which determined a binding affinity of 28 ± 6 nM, and by isolating a stable trimer of DENND10 and the CCDC coiled-coil domains via size-exclusion chromatography (Healy et al., 2023). Additionally, Boesch *et al.* demonstrated that the point mutations W30D and Y32D in DENND10 completely abolish its binding to the CCDC22-CCDC93 complex (Boesch et al., 2024).

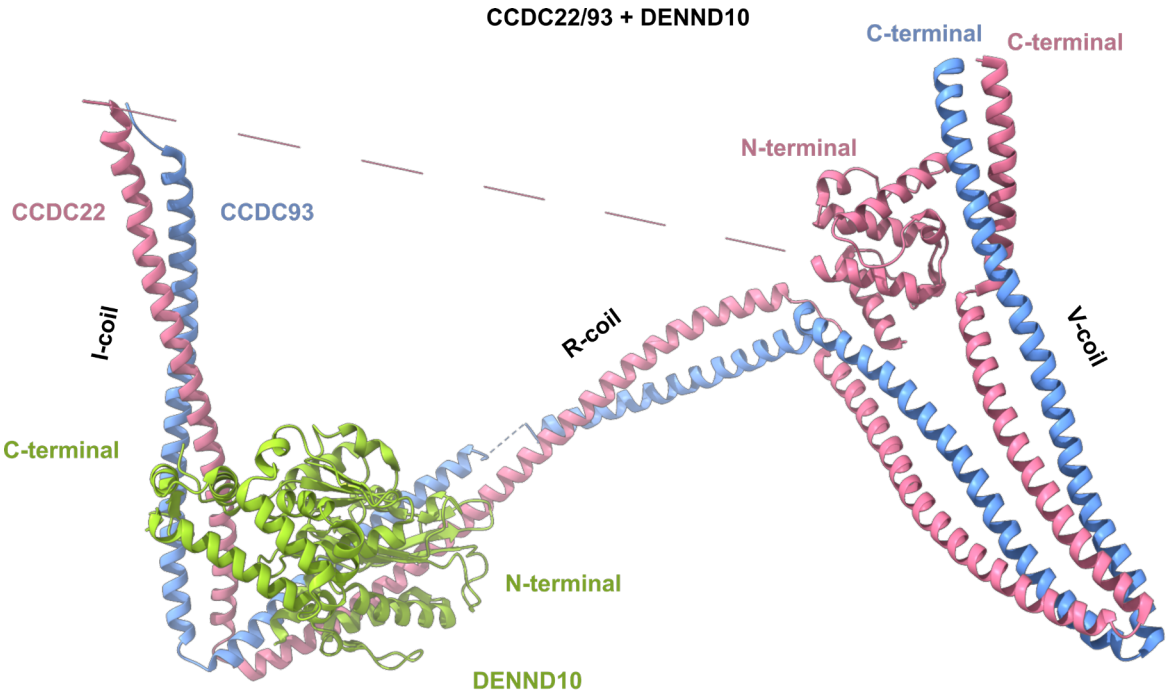

Figure 84. The structure of CCDC22, CCDC93, and DENND10. The structure of the coiled-coil region and the NTD of CCDC22 is colored pink, the coiled-coil regions of CCDC93 is colored blue, and DENND10 is colored green (PDB ID: 8P0V, Laulumaa et al., 2024). The primary interface features a hydrophobic core along the R-coil groove, complemented by a charged region on its C-terminal side.

While the mechanism of interaction of DENND10 with the Commander complex is beginning to be understood, its precise role remains a challenging question. Laulumaa *et al.* suggest that although the putative Rab-binding site of DENND10 is occupied within the complex, the inherent flexibility of this region may still allow Rab binding in an alternative conformation (Laulumaa et al.,

2024). Consequently, it is yet to be determined whether DENND10 exhibits GEF (guanine nucleotide exchange factor) activity, or whether it plays a distinct role in the recycling context.

5.7. Relevance of this work

The Retriever-CCC-SNX17 pathway plays a critical role in cargo recycling from endosomes to the plasma membranes. However, the molecular mechanisms by which SNX17 functions as a cargo adapter protein and recruits the Retriever complex was an unresolved question in the field. This thesis uncovers the interaction between SNX17 and Retriever, highlighting the significant roles of SNX17 cargo binding and membrane association in this process.

To date, there has been some debate regarding whether Retriever can function independently of the Commander complex. Some studies point out that the CCC and Retriever complexes are part of a unified multiprotein assembly (Wan et al., 2015b), while others argue that they are functionally distinct, as the CCC complex has been shown to regulate the trafficking of cargos independent of Retriever (Phillips-Krawczak et al., 2015). This ongoing debate underscores the importance of studying the Retriever complex in isolation. For this reason, this research focused solely on the Retriever complex in conjunction with its binding partner, SNX17.

The current uncertainty about Retriever and CCC being or not separable and distinct molecular assemblies makes the analysis of Retriever complex alone to be a conceivable matter of study. For this reason, the present work was only focused in the role of the Retriever complex along with the binding-partner SNX17.

In summary, this study provides a comprehensive model for the recruitment of the Retriever complex to membranes. We suggest that the autoinhibitory conformation of SNX17 prevents the assembly of the entire recycling machinery when SNX17 is in the cytoplasm or loosely associated with nonspecific membranes. SNX17 holds the recycling system in an “off” state, which can be switched to an “on” state by two different mechanisms: either through selective engagement with a cargo protein or by a specific association with membranes containing PI3P (**Figure 85**). We propose that integrating both Retriever recruitment mechanisms might be essential for simultaneous membrane coating and cargo selection. This model illustrates the initial step of cargo inclusion into as yet unidentified membrane transport carriers of the SNX17-Retriever-CCC pathway for transporting the cargo from the endosome to the plasma membrane. Further research is required to decipher the roles of other components of the Commander complex, such as the CCC complex and DEND10 in this initial step of endosomal membrane association for recycling transmembrane cargos from endosomes to the cell surface.

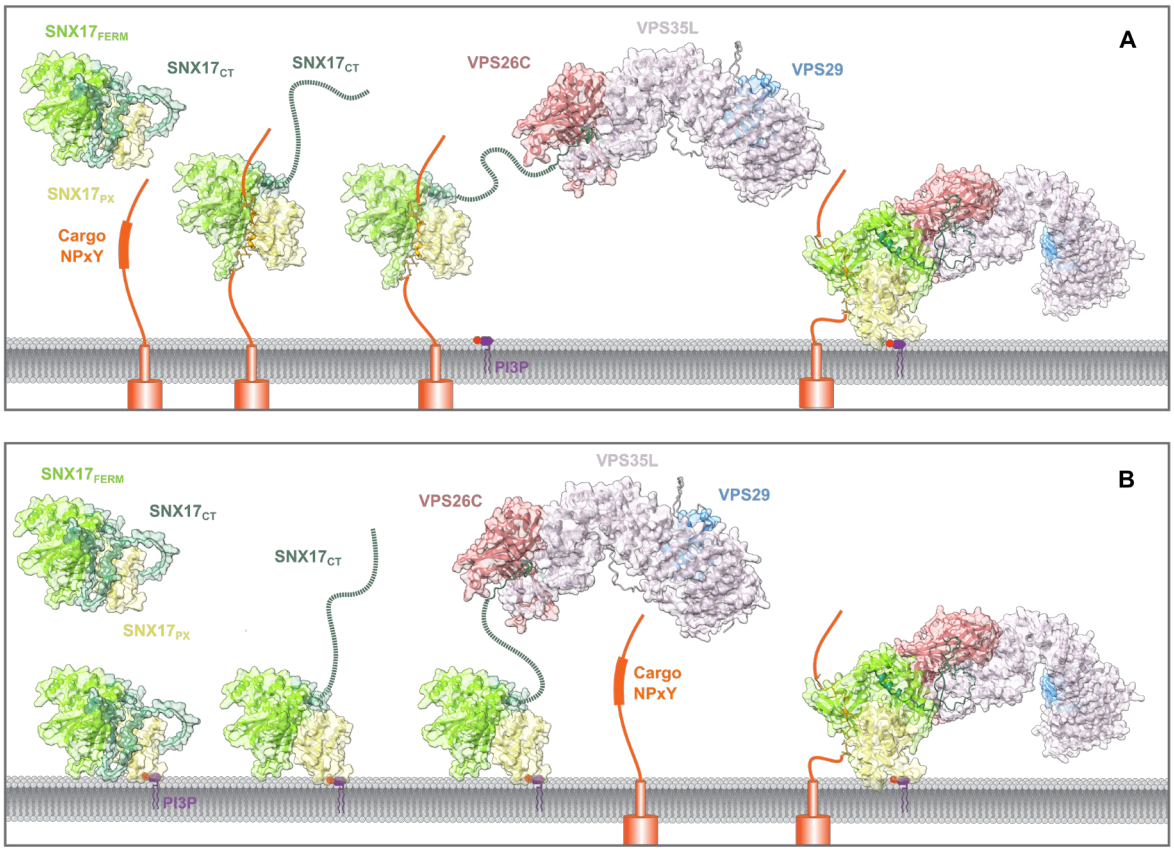

Figure 85. Proposed activation mechanisms for the Retriever-SNX17 interaction. This model illustrates the initial step of cargo incorporation into currently unidentified membrane transport carriers within the SNX17-Retriever-CCC pathway, responsible for transporting cargo from the endosome to the plasma membrane. (**A**) Cargo-mediated activation: SNX17 encounters its cargo, and this interaction through the FERM domain triggers the release of the SNX17 C-terminal region. With the C-terminal residues exposed, SNX17 binds and recruits Retriever. Subsequently, SNX17 binding to PI3P at the membrane through the PX domain promotes the attachment of the complex to the membrane. (**B**) Membrane-mediated activation: SNX17 initially binds to PI3P, leading to its attachment to the membrane and subsequent exposure of the Retriever-binding motif. The movement of the C-terminal residues of SNX17 enables Retriever recruitment and cargo binding. The predicted interaction between VPS26C and SNX17, observed in the AF2-multimer model for the complex SNX17:L2$_{17mer}$:VPS26C:VPS35L$_{110-598}$, was used to illustrate the proposed approach of Retriever to the membrane in (**A**) and (**B**).

Understanding how recycling mechanisms of cargo proteins work in our cells, including both the recognition and transport processes via tubules or vesicles, could pave the way for the development of molecules that target specific components of the recycling complexes responsible for these tasks. These molecules could either promote or inhibit the recycling of particular proteins whose levels have become dysregulated. By focusing on key players in the recycling machinery, we may eventually be able to correct protein imbalances associated with various diseases.

This research is still at the basic science stage, and far from practical applications. However, gaining a deeper understanding of these mechanisms could undoubtedly lay the groundwork for future applied science. Unraveling how protein recycling is regulated will be crucial for developing therapeutic strategies that manipulate protein levels in a controlled and precise manner.

Chapter 6: CONCLUSIONS

Aim 1. Characterization of the structural organization of the Retriever Complex:

- In the Retriever complex, VPS35L functions as the anchor protein, with VPS26C binding to VPS35L through the region spanning amino acids 110-436. VPS29 requires a dual interaction with both the N- and C-terminal regions (residues 1-109 and 599-963), a feature that is evolutionarily conserved.

- The association of VPS35L with either VPS26C or VPS29 is essential from maintaining the structural integrity of VPS35L in solution.

Aim 2. Study of cargo recognition by SNX17:

- SNX17 binds to the cargos L2 (from HPV), LRP1, APP, and INTB1 with different affinities through its FERM domain.

- The presence of the NPxY motif in the cargo sequence is a requisite for SNX17 binding, but neighboring residues also play a decisive role, as exemplified by the VEGFR1 protein, which contains the NPxY motif but shows no binding affinity.

- The L2 protein from HPV displays a high affinity for SNX17 and can outcompete cellular cargos. Two key residues of L2, Y252 and E258, have been identified as responsible for this high affinity, as alanine mutagenesis of these residues induces a 22-fold and 8-fold reduction in binding affinity, respectively.

Aim 3. Analysis of the Retriever-SNX17 Assembly:

- The C-terminal end of SNX17 contacts the VPS35L/VPS26C interface, with critical involvement of the SNX17 C-terminal residues L470, N459, and F462. In VPS35L, residues R248 and W280 are essential for this interaction, and mutations at K157 and R161 result in a 5-fold decrease in binding affinity.

- SNX17's interaction with Retriever is enhanced upon SNX17 binding to the cargo in solution, due to the disruption of an intramolecular autoinhibitory interaction between the C-terminal region of SNX17 and its cargo-binding pocket. This autoinhibition mechanism is evolutionarily conserved. Mutation of H457, part of the cargo-mimicking region, prevents autoinhibition in the absence of cargo.

Aim 4. Study of the membrane association of SNX17 and the Retriever complex:

- Retriever itself lacks membrane-binding ability and does not interact with PI3P.

- SNX17 facilitates Retriever recruitment to membranes containing PI3P, and this recruitment is further enhanced when SNX17 is bound to cargo.

- The first six residues of SNX17, as well as residues R36 and Y37, are critical for binding to PI3P-enriched membranes.

Aim 5. Examination of the role of SNX31 within the Retriever-mediated recycling pathway:

- SNX31 exhibits distinct binding affinity and specificity for the analyzed cargos compared to SNX17.

- The C-terminal regions of SNX17 and SNX31 are not interchangeable.

- Similar to SNX17, SNX31 interacts with the Retriever complex through its C-terminal region, although with lower affinity.

Chapter 7: BIBLIOGRAPHY

1. Adzhubei, I. A., Schmidt, S., Peshkin, L., Ramensky, V. E., Gerasimova, A., Bork, P., Kondrashov, A. S., & Sunyaev, S. R. (2010). A method and server for predicting damaging missense mutations. Nature Methods, 7(4), 248–249. https://doi.org/10.1038/nmeth0410-248

2. Altschul, S. (1997). Gapped BLAST and PSI-BLAST: A new generation of protein database search programs. Nucleic Acids Research, 25(17), 3389–3402. https://doi.org/10.1093/nar/25.17.3389

3. Aubry, L., Guetta, D., & Klein, G. (2009). The Arrestin Fold: Variations on a Theme. Current Genomics, 10(2), 133–142. https://doi.org/10.2174/138920209787847014

4. Baek, M., DiMaio, F., Anishchenko, I., Dauparas, J., Ovchinnikov, S., Lee, G. R., Wang, J., Cong, Q., Kinch, L. N., Schaeffer, R. D., Millán, C., Park, H., Adams, C., Glassman, C. R., DeGiovanni, A., Pereira, J. H., Rodrigues, A. V., van Dijk, A. A., Ebrecht, A. C., … Baker, D. (n.d.). Accurate prediction of protein structures and interactions using a three-track neural network.

5. Bajorek, M., Schubert, H. L., McCullough, J., Langelier, C., Eckert, D. M., Stubblefield, W.-M. B., Uter, N. T., Myszka, D. G., Hill, C. P., & Sundquist, W. I. (2009). Structural basis for ESCRT-III protein autoinhibition. Nature Structural & Molecular Biology, 16(7), 754–762. https://doi.org/10.1038/nsmb.1621

6. Balla, T. (2013). Phosphoinositides: Tiny Lipids With Giant Impact on Cell Regulation. Physiological Reviews, 93(3), 1019–1137. https://doi.org/10.1152/physrev.00028.2012

7. Baños-Mateos, S., Rojas, A. L., & Hierro, A. (2019). VPS29, a tweak tool of endosomal recycling. Current Opinion in Cell Biology, 59, 81–87. https://doi.org/10.1016/j.ceb.2019.03.010

8. Barlow, D. J., & Thornton, J. M. (1983). Ion-pairs in proteins. Journal of Molecular Biology, 168(4), 867–885. https://doi.org/10.1016/S0022-2836(83)80079-5

9. Bar-Peled, L., & Kory, N. (2022). Principles and functions of metabolic compartmentalization. Nature Metabolism, 4(10), 1232–1244. https://doi.org/10.1038/s42255-022-00645-2

10. Barsegian, V., & Kosova, I. (2023). Human papillomavirus infection causing refractory lower urinary tract symptoms in a young female. Indian Journal of Urology, 39(3), 242–244. https://doi.org/10.4103/iju.iju_398_22

11. Bartuzi, P., Billadeau, D. D., Favier, R., Rong, S., Dekker, D., Fedoseienko, A., Fieten, H., Wijers, M., Levels, J. H., Huijkman, N., Kloosterhuis, N., Van Der Molen, H., Brufau, G., Groen, A. K., Elliott, A. M., Kuivenhoven, J. A., Plecko, B., Grangl, G., McGaughran, J., … Van De Sluis, B. (2016). CCC- and WASH-mediated endosomal sorting of LDLR is required for normal clearance of circulating LDL. Nature Communications, 7(1), 10961. https://doi.org/10.1038/ncomms10961

12. Battye, T. G. G., Kontogiannis, L., Johnson, O., Powell, H. R., & Leslie, A. G. W. (2011). iMOSFLM: A new graphical interface for diffraction-image processing with MOSFLM. Acta Crystallographica Section D Biological Crystallography, 67(4), 271–281. https://doi.org/10.1107/S0907444910048675

13. Beetz, C., Ameziane, N., Kdissa, A., Karageorgou, V., Bauer, P., Suleiman, J., Sutton, V. R., & El-Hattab, A. W. (2020). VPS26C homozygous nonsense variant in two cousins with neurodevelopmental deficits, growth failure, skeletal abnormalities, and distinctive facial features. Clinical Genetics, 97(4), 644–648. https://doi.org/10.1111/cge.13690

14. Bergant, M., & Banks, L. (2013). SNX17 Facilitates Infection with Diverse Papillomavirus Types. Journal of Virology, 87(2), 1270–1273. https://doi.org/10.1128/JVI.01991-12

15. Bergant, M., Peternel, Š., Pim, D., Broniarczyk, J., & Banks, L. (2017). Characterizing the spatio-temporal role of sorting nexin 17 in human papillomavirus trafficking. Journal of General Virology, 98(4), 715–725. https://doi.org/10.1099/jgv.0.000734

16. Bergant Marušič, M., Ozbun, M. A., Campos, S. K., Myers, M. P., & Banks, L. (2012). Human Papillomavirus L2 Facilitates Viral Escape from Late Endosomes via Sorting Nexin 17. Traffic, 13(3), 455–467. https://doi.org/10.1111/j.1600-0854.2011.01320.x

17. Betts, G. N., Van Der Geer, P., & Komives, E. A. (2008). Structural and Functional Consequences of Tyrosine Phosphorylation in the LRP1 Cytoplasmic Domain. Journal of Biological Chemistry, 283(23), 15656–15664. https://doi.org/10.1074/jbc.M709514200

18. Bingham, R., McCarthy, H., & Buckley, N. (2024). Exploring Retrograde Trafficking: Mechanisms and Consequences in Cancer and Disease. Traffic, 25(2), e12931. https://doi.org/10.1111/tra.12931

19. Bissig, C., & Gruenberg, J. (2014). ALIX and the multivesicular endosome: ALIX in Wonderland. Trends in Cell Biology, 24(1), 19–25. https://doi.org/10.1016/j.tcb.2013.10.009

20. Boesch, D. J., Singla, A., Han, Y., Kramer, D. A., Liu, Q., Suzuki, K., Juneja, P., Zhao, X., Long, X., Medlyn, M. J., Billadeau, D. D., Chen, Z., Chen, B., & Burstein, E. (2024). Structural organization of the retriever–CCC endosomal recycling complex. Nature Structural & Molecular Biology, 31(6), 910–924. https://doi.org/10.1038/s41594-023-01184-4

21. Boesch, D., Singla, A., Han, Y., Kramer, D., Liu, Q., Suzuki, K., Juneja, P., Zhao, X., Long, X., Medlyn, M., Billadeau, D., Chen, Z., Chen, B., & Burstein, E. (2023). Structural Organization of the Retriever-CCC Endosomal Recycling Complex. In Review. https://doi.org/10.21203/rs.3.rs-3026818/v1

22. Böttcher, R. T., Stremmel, C., Meves, A., Meyer, H., Widmaier, M., Tseng, H.-Y., & Fässler, R. (2012). Sorting nexin 17 prevents lysosomal degradation of β1 integrins by binding to the β1-integrin tail. Nature Cell Biology, 14(6), 584–592. https://doi.org/10.1038/ncb2501

23. Bronnimann, M. P., Chapman, J. A., Park, C. K., & Campos, S. K. (2013). A Transmembrane Domain and GxxxG Motifs within L2 Are Essential for Papillomavirus Infection. Journal of Virology, 87(1), 464–473. https://doi.org/10.1128/JVI.01539-12

24. Buckley et al 2000. (n.d.).

25. Bugarcic, A., Zhe, Y., Kerr, M. C., Griffin, J., Collins, B. M., & Teasdale, R. D. (2011). Vps26A and Vps26B Subunits Define Distinct Retromer Complexes. Traffic, 12(12), 1759–1773. https://doi.org/10.1111/j.1600-0854.2011.01284.x

26. Burstein, E., Hoberg, J. E., Wilkinson, A. S., Rumble, J. M., Csomos, R. A., Komarck, C. M., Maine, G. N., Wilkinson, J. C., Mayo, M. W., & Duckett, C. S. (2005). COMMD Proteins, a Novel Family of Structural and Functional Homologs of MURR1. Journal of Biological Chemistry, 280(23), 22222–22232. https://doi.org/10.1074/jbc.M501928200

27. Buser, D. P., & Spang, A. (2023). Protein sorting from endosomes to the TGN. Frontiers in Cell and Developmental Biology, 11, 1140605. https://doi.org/10.3389/fcell.2023.1140605

28. Cagiada, M., Bottaro, S., Lindemose, S., Schenstrøm, S. M., Stein, A., Hartmann-Petersen, R., & Lindorff-Larsen, K. (2023). Discovering functionally important sites in proteins. Nature Communications, 14(1), 4175. https://doi.org/10.1038/s41467-023-39909-0

29. Cam, J. A., & Bu, G. (2006). [No title found]. Molecular Neurodegeneration, 1(1), 8. https://doi.org/10.1186/1750-1326-1-8

30. Carroni, M., & Saibil, H. R. (2016). Cryo electron microscopy to determine the structure of macromolecular complexes. Methods, 95, 78–85. https://doi.org/10.1016/j.ymeth.2015.11.023

31. Caswell, P. T., Spence, H. J., Parsons, M., White, D. P., Clark, K., Cheng, K. W., Mills, G. B., Humphries, M. J., Messent, A. J., Anderson, K. I., McCaffrey, M. W., Ozanne, B. W., & Norman, J. C. (2007). Rab25 Associates with α5β1 Integrin to Promote Invasive Migration in 3D Microenvironments. Developmental Cell, 13(4), 496–510. https://doi.org/10.1016/j.devcel.2007.08.012

32. Cavalier-Smith, T. (2010). Origin of the cell nucleus, mitosis and sex: Roles of intracellular coevolution. Biology Direct, 5(1), 7. https://doi.org/10.1186/1745-6150-5-7

33. Chandra, M., Chin, Y. K.-Y., Mas, C., Feathers, J. R., Paul, B., Datta, S., Chen, K.-E., Jia, X., Yang, Z., Norwood, S. J., Mohanty, B., Bugarcic, A., Teasdale, R. D., Henne, W. M., Mobli, M., & Collins, B. M. (2019). Classification of the human phox homology (PX) domains based on their phosphoinositide binding specificities. Nature Communications, 10(1), 1528. https://doi.org/10.1038/s41467-019-09355-y

34. Cheever, M. L., Sato, T. K., De Beer, T., Kutateladze, T. G., Emr, S. D., & Overduin, M. (2001). Phox domain interaction with PtdIns(3)P targets the Vam7 t-SNARE to vacuole membranes. Nature Cell Biology, 3(7), 613–618. https://doi.org/10.1038/35083000

35. Chen, K., Healy, M. D., & Collins, B. M. (2019). Towards a molecular understanding of endosomal trafficking by Retromer and Retriever. Traffic, 20(7), 465–478. https://doi.org/10.1111/tra.12649

36. Chi, R. J., Harrison, M. S., & Burd, C. G. (2015). Biogenesis of endosome-derived transport carriers. Cellular and Molecular Life Sciences, 72(18), 3441–3455. https://doi.org/10.1007/s00018-015-1935-x

37. Christ, L., Raiborg, C., Wenzel, E. M., Campsteijn, C., & Stenmark, H. (2017). Cellular Functions and Molecular Mechanisms of the ESCRT Membrane-Scission Machinery. Trends in Biochemical Sciences, 42(1), 42–56. https://doi.org/10.1016/j.tibs.2016.08.016

38. Clairfeuille, T., Mas, C., Chan, A. S. M., Yang, Z., Tello-Lafoz, M., Chandra, M., Widagdo, J., Kerr, M. C., Paul, B., Mérida, I., Teasdale, R. D., Pavlos, N. J., Anggono, V., & Collins, B. M. (2016). A molecular code for endosomal recycling of phosphorylated cargos by the SNX27–retromer complex. Nature Structural & Molecular Biology, 23(10), 921–932. https://doi.org/10.1038/nsmb.3290

39. Collinet, C., Stöter, M., Bradshaw, C. R., Samusik, N., Rink, J. C., Kenski, D., Habermann, B., Buchholz, F., Henschel, R., Mueller, M. S., Nagel, W. E., Fava, E., Kalaidzidis, Y., & Zerial, M. (2010). Systems survey of endocytosis by multiparametric image analysis. Nature, 464(7286), 243–249. https://doi.org/10.1038/nature08779

40. Collins, B. M., Norwood, S. J., Kerr, M. C., Mahony, D., Seaman, M. N. J., Teasdale, R. D., & Owen, D. J. (2008). Structure of Vps26B and Mapping of its Interaction with the Retromer Protein Complex. Traffic, 9(3), 366–379. https://doi.org/10.1111/j.1600-0854.2007.00688.x

41. Collins, B. M., Skinner, C. F., Watson, P. J., Seaman, M. N. J., & Owen, D. J. (2005). Vps29 has a phosphoesterase fold that acts as a protein interaction scaffold for retromer assembly. Nature Structural & Molecular Biology, 12(7), 594–602. https://doi.org/10.1038/nsmb954

42. Conner, S. D., & Schmid, S. L. (2003). Regulated portals of entry into the cell. Nature, 422(6927), 37–44. https://doi.org/10.1038/nature01451

43. Cui, L., Li, H., Xi, Y., Hu, Q., Liu, H., Fan, J., Xiang, Y., Zhang, X., Shui, W., & Lai, Y. (2022). Vesicle trafficking and vesicle fusion: Mechanisms, biological functions, and their implications for potential disease therapy. Molecular Biomedicine, 3(1), 29. https://doi.org/10.1186/s43556-022-00090-3

44. Cui, Q., Liang, S., Li, H., Guo, Y., Lv, J., Wang, X., Qin, P., Xu, H., Huang, T. Y., Lu, Y., Tian, Q., & Zhang, T. (2024). SNX17 Mediates Dendritic Spine Maturation via p140Cap. Molecular Neurobiology, 61(3), 1346–1362. https://doi.org/10.1007/s12035-023-03620-4

45. Cullen, P. J., & Steinberg, F. (2018). To degrade or not to degrade: Mechanisms and significance of endocytic recycling. Nature Reviews Molecular Cell Biology, 19(11), 679–696. https://doi.org/10.1038/s41580-018-0053-7

46. Czubayko, M., Knauth, P., Schlüter, T., Florian, V., & Bohnensack, R. (2006). Sorting nexin 17, a non-self-assembling and a PtdIns(3)P high class affinity protein, interacts with the cerebral cavernous malformation related protein KRIT1. Biochemical and Biophysical Research Communications, 345(3), 1264–1272. https://doi.org/10.1016/j.bbrc.2006.04.129

47. Damen, E., Krieger, E., Nielsen, J. E., Eygensteyn, J., & Van Leeuwen, J. E. M. (2006). The human Vps29 retromer component is a metallo-phosphoesterase for a cation-independent mannose 6-phosphate receptor substrate peptide. Biochemical Journal, 398(3), 399–409. https://doi.org/10.1042/BJ20060033

48. Daniloski, Z., Jordan, T. X., Wessels, H.-H., Hoagland, D. A., Kasela, S., Legut, M., Maniatis, S., Mimitou, E. P., Lu, L., Geller, E., Danziger, O., Rosenberg, B. R., Phatnani, H., Smibert, P., Lappalainen, T., tenOever, B. R., & Sanjana, N. E. (2021). Identification of Required Host Factors for SARS-CoV-2 Infection in Human Cells. Cell, 184(1), 92-105.e16. https://doi.org/10.1016/j.cell.2020.10.030

49. Day, P. M., Baker, C. C., Lowy, D. R., & Schiller, J. T. (2004). Establishment of papillomavirus infection is enhanced by promyelocytic leukemia protein (PML) expression. Proceedings of the National Academy of Sciences, 101(39), 14252–14257. https://doi.org/10.1073/pnas.0404229101

50. Day, P. M., Thompson, C. D., Schowalter, R. M., Lowy, D. R., & Schiller, J. T. (2013). Identification of a Role for the trans -Golgi Network in Human Papillomavirus 16 Pseudovirus Infection. Journal of Virology, 87(7), 3862–3870. https://doi.org/10.1128/JVI.03222-12

51. Derivery, E., Sousa, C., Gautier, J. J., Lombard, B., Loew, D., & Gautreau, A. (2009). The Arp2/3 Activator WASH Controls the Fission of Endosomes through a Large Multiprotein Complex. Developmental Cell, 17(5), 712–723. https://doi.org/10.1016/j.devcel.2009.09.010

52. Doherty, G. J., & McMahon, H. T. (2009). Mechanisms of Endocytosis. Annual Review of Biochemistry, 78(1), 857–902. https://doi.org/10.1146/annurev.biochem.78.081307.110540

53. Dostál, V., Humhalová, T., Beránková, P., Pácalt, O., & Libusová, L. (2023). SWIP mediates retromer-independent membrane recruitment of the WASH complex. Traffic, 24(5), 216–230. https://doi.org/10.1111/tra.12884

54. Elkin, S. R., Lakoduk, A. M., & Schmid, S. L. (2016). Endocytic pathways and endosomal trafficking: A primer. Wiener Medizinische Wochenschrift, 166(7–8), 196–204. https://doi.org/10.1007/s10354-016-0432-7

55. Elliott, A. M., Simard, L. R., Coghlan, G., Chudley, A. E., Chodirker, B. N., Greenberg, C. R., Burch, T., Ly, V., Hatch, G. M., & Zelinski, T. (2013). A novel mutation in KIAA0196: Identification of a gene involved in Ritscher–Schinzel/3C syndrome in a First Nations cohort. Journal of Medical Genetics, 50(12), 819–822. https://doi.org/10.1136/jmedgenet-2013-101715

56. Farfán, P., Lee, J., Larios, J., Sotelo, P., Bu, G., & Marzolo, M. (2013). A Sorting Nexin 17-Binding Domain Within the LRP1 Cytoplasmic Tail Mediates Receptor Recycling Through the Basolateral Sorting Endosome. Traffic, 14(7), 823–838. https://doi.org/10.1111/tra.12076

57. Fedoseienko, A., Wijers, M., Wolters, J. C., Dekker, D., Smit, M., Huijkman, N., Kloosterhuis, N., Klug, H., Schepers, A., Willems Van Dijk, K., Levels, J. H. M., Billadeau, D. D., Hofker, M. H., Van Deursen, J., Westerterp, M., Burstein, E., Kuivenhoven, J. A., & Van De Sluis, B. (2018). The COMMD Family Regulates Plasma LDL Levels and Attenuates Atherosclerosis Through Stabilizing the CCC Complex in Endosomal LDLR Trafficking. Circulation Research, 122(12), 1648–1660. https://doi.org/10.1161/CIRCRESAHA.117.312004

58. Filippone, A., & Praticò, D. (2021). Endosome Dysregulation in Down Syndrome: A Potential Contributor to Alzheimer Disease Pathology. Annals of Neurology, 90(1), 4–14. https://doi.org/10.1002/ana.26042

59. Franch-Marro, X., Wendler, F., Guidato, S., Griffith, J., Baena-Lopez, A., Itasaki, N., Maurice, M. M., & Vincent, J.-P. (2008). Wingless secretion requires endosome-to-Golgi retrieval of Wntless/Evi/Sprinter by the retromer complex. Nature Cell Biology, 10(2), 170–177. https://doi.org/10.1038/ncb1678

60. Frost, A., Unger, V. M., & De Camilli, P. (2009). The BAR Domain Superfamily: Membrane-Molding Macromolecules. Cell, 137(2), 191–196. https://doi.org/10.1016/j.cell.2009.04.010

61. Gabaldón, T., & Pittis, A. A. (2015). Origin and evolution of metabolic sub-cellular compartmentalization in eukaryotes. Biochimie, 119, 262–268. https://doi.org/10.1016/j.biochi.2015.03.021

62. Gallon, M., Clairfeuille, T., Steinberg, F., Mas, C., Ghai, R., Sessions, R. B., Teasdale, R. D., Collins, B. M., & Cullen, P. J. (2014). A unique PDZ domain and arrestin-like fold interaction reveals mechanistic details of endocytic recycling by SNX27-retromer. Proceedings of the National Academy of Sciences, 111(35). https://doi.org/10.1073/pnas.1410552111

63. Gasteiger, E., Hoogland, C., Gattiker, A., Duvaud, S., Wilkins, M. R., Appel, R. D., & Bairoch, A. (2005). Protein Identification and Analysis Tools on the ExPASy Server. In J. M. Walker (Ed.), The Proteomics Protocols Handbook (pp. 571–607). Humana Press. https://doi.org/10.1385/1-59259-890-0:571

64. Gerasimenko, J. V., Tepikin, A. V., Petersen, O. H., & Gerasimenko, O. V. (1998). Calcium uptake via endocytosis with rapid release from acidifying endosomes. Current Biology, 8(24), 1335–1338. https://doi.org/10.1016/S0960-9822(07)00565-9

65. Gershlick, D. C., & Lucas, M. (2017). Endosomal Trafficking: Retromer and Retriever Are Relatives in Recycling. Current Biology, 27(22), R1233–R1236. https://doi.org/10.1016/j.cub.2017.10.004

66. Ghai, R., Bugarcic, A., Liu, H., Norwood, S. J., Skeldal, S., Coulson, E. J., Li, S. S.-C., Teasdale, R. D., & Collins, B. M. (2013a). Structural basis for endosomal trafficking of diverse transmembrane cargos by

PX-FERM proteins. Proceedings of the National Academy of Sciences, 110(8). https://doi.org/10.1073/pnas.1216229110

67. Ghai, R., Bugarcic, A., Liu, H., Norwood, S. J., Skeldal, S., Coulson, E. J., Li, S. S.-C., Teasdale, R. D., & Collins, B. M. (2013b). Structural basis for endosomal trafficking of diverse transmembrane cargos by PX-FERM proteins. Proceedings of the National Academy of Sciences, 110(8). https://doi.org/10.1073/pnas.1216229110

68. Ghai, R., Mobli, M., Norwood, S. J., Bugarcic, A., Teasdale, R. D., King, G. F., & Collins, B. M. (2011). Phox homology band 4.1/ezrin/radixin/moesin-like proteins function as molecular scaffolds that interact with cargo receptors and Ras GTPases. Proceedings of the National Academy of Sciences, 108(19), 7763–7768. https://doi.org/10.1073/pnas.1017110108

69. Gibson, D. G., Young, L., Chuang, R.-Y., Venter, J. C., Hutchison, C. A., & Smith, H. O. (2009). Enzymatic assembly of DNA molecules up to several hundred kilobases. Nature Methods, 6(5), 343–345. https://doi.org/10.1038/nmeth.1318

70. Giridharan, S. S. P., Luo, G., Rivero-Rios, P., Steinfeld, N., Tronchere, H., Singla, A., Burstein, E., Billadeau, D. D., Sutton, M. A., & Weisman, L. S. (2022). Lipid kinases VPS34 and PIKfyve coordinate a phosphoinositide cascade to regulate retriever-mediated recycling on endosomes. eLife, 11, e69709. https://doi.org/10.7554/eLife.69709

71. Gopaldass, N., Chen, K.-E., Collins, B., & Mayer, A. (2024). Assembly and fission of tubular carriers mediating protein sorting in endosomes. Nature Reviews Molecular Cell Biology, 25(10), 765–783. https://doi.org/10.1038/s41580-024-00746-8

72. Greenfield, N. J. (2006). Using circular dichroism spectra to estimate protein secondary structure. Nature Protocols, 1(6), 2876–2890. https://doi.org/10.1038/nprot.2006.202

73. Groppelli, E., Len, A. C., Granger, L. A., & Jolly, C. (2014). Retromer Regulates HIV-1 Envelope Glycoprotein Trafficking and Incorporation into Virions. PLoS Pathogens, 10(11), e1004518. https://doi.org/10.1371/journal.ppat.1004518

74. Guo, Q., Chen, K., Gimenez-Andres, M., Jellett, A. P., Gao, Y., Liu, M., Danson, C. M., Heesom, K. J., Cullen, P. J., & Collins, B. M. (n.d.). Structural basis for coupling of the WASH subunit FAM21 with the endosomal SNX27-Retromer complex.

75. Habuka, M., Fagerberg, L., Hallström, B. M., Pontén, F., Yamamoto, T., & Uhlen, M. (2015). The Urinary Bladder Transcriptome and Proteome Defined by Transcriptomics and Antibody-Based Profiling. PLOS ONE, 10(12), e0145301. https://doi.org/10.1371/journal.pone.0145301

76. Hamada, K. (2000). Structural basis of the membrane-targeting and unmasking mechanisms of the radixin FERM domain. The EMBO Journal, 19(17), 4449–4462. https://doi.org/10.1093/emboj/19.17.4449

77. Hargittai, I. (2010). Structures beyond crystals. Journal of Molecular Structure, 976(1–3), 81–86. https://doi.org/10.1016/j.molstruc.2010.02.009

78. Healy, M. D., Hospenthal, M. K., Hall, R. J., Chandra, M., Chilton, M., Tillu, V., Chen, K.-E., Celligoi, D. J., McDonald, F. J., Cullen, P. J., Lott, J. S., Collins, B. M., & Ghai, R. (2018). Structural insights into the architecture and membrane interactions of the conserved COMMD proteins. eLife, 7, e35898. https://doi.org/10.7554/eLife.35898

79. Healy, M. D., McNally, K. E., Butkovič, R., Chilton, M., Kato, K., Sacharz, J., McConville, C., Moody, E. R. R., Shaw, S., Planelles-Herrero, V. J., Yadav, S. K. N., Ross, J., Borucu, U., Palmer, C. S., Chen, K.-E., Croll, T. I., Hall, R. J., Caruana, N. J., Ghai, R., … Cullen, P. J. (2023). Structure of the endosomal Commander complex linked to Ritscher-Schinzel syndrome. Cell, 186(10), 2219-2237.e29. https://doi.org/10.1016/j.cell.2023.04.003

80. Healy, M. D., Sacharz, J., McNally, K. E., McConville, C., Tillu, V. A., Hall, R. J., Chilton, M., Cullen, P. J., Mobli, M., Ghai, R., Stroud, D. A., & Collins, B. M. (2022). Proteomic identification and structural basis for the interaction between sorting nexin SNX17 and PDLIM family proteins. Structure, 30(12), 1590-1602.e6. https://doi.org/10.1016/j.str.2022.10.001

81. Hierro, A., Rojas, A. L., Rojas, R., Murthy, N., Effantin, G., Kajava, A. V., Steven, A. C., Bonifacino, J. S., & Hurley, J. H. (2007). Functional architecture of the retromer cargo-recognition complex. Nature, 449(7165), 1063–1067. https://doi.org/10.1038/nature06216

82. Higgs, H. N., & Pollard, T. D. (2001). Regulation of Actin Filament Network Formation Through ARP2/3 Complex: Activation by a Diverse Array of Proteins. Annual Review of Biochemistry, 70(1), 649–676. https://doi.org/10.1146/annurev.biochem.70.1.649

83. Hirano, Y., Hatano, T., Takahashi, A., Toriyama, M., Inagaki, N., & Hakoshima, T. (2011). Structural basis of cargo recognition by the myosin-X MyTH4-FERM domain: Myosin-X binding to DCC, integrin and microtubule. The EMBO Journal, 30(13), 2734–2747. https://doi.org/10.1038/emboj.2011.177

84. Hodis, E., Watson, I. R., Kryukov, G. V., Arold, S. T., Imielinski, M., Theurillat, J.-P., Nickerson, E., Auclair, D., Li, L., Place, C., DiCara, D., Ramos, A. H., Lawrence, M. S., Cibulskis, K., Sivachenko, A., Voet, D., Saksena, G., Stransky, N., Onofrio, R. C., … Chin, L. (2012). A Landscape of Driver Mutations in Melanoma. Cell, 150(2), 251–263. https://doi.org/10.1016/j.cell.2012.06.024

85. Hong, W. (2005). SNAREs and traffic. Biochimica et Biophysica Acta (BBA) - Molecular Cell Research, 1744(2), 120–144. https://doi.org/10.1016/j.bbamcr.2005.03.014

86. Hsiao, J.-C., Chu, L.-W., Lo, Y.-T., Lee, S.-P., Chen, T.-J., Huang, C.-Y., Ping, Y.-H., & Chang, W. (2015). Intracellular Transport of Vaccinia Virus in HeLa Cells Requires WASH-VPEF/FAM21-Retromer Complexes and Recycling Molecules Rab11 and Rab22. Journal of Virology, 89(16), 8365–8382. https://doi.org/10.1128/JVI.00209-15

87. Huber, L. A., & Teis, D. (2016). Lysosomal signaling in control of degradation pathways. Current Opinion in Cell Biology, 39, 8–14. https://doi.org/10.1016/j.ceb.2016.01.006

88. Huotari, J., & Helenius, A. (2011). Endosome maturation: Endosome maturation. The EMBO Journal, 30(17), 3481–3500. https://doi.org/10.1038/emboj.2011.286

89. Hynes 2002. (n.d.).

90. Jia, D., Gomez, T. S., Billadeau, D. D., & Rosen, M. K. (2012). Multiple repeat elements within the FAM21 tail link the WASH actin regulatory complex to the retromer. Molecular Biology of the Cell, 23(12), 2352–2361. https://doi.org/10.1091/mbc.e11-12-1059

91. Jia, D., Gomez, T. S., Metlagel, Z., Umetani, J., Otwinowski, Z., Rosen, M. K., & Billadeau, D. D. (2010). WASH and WAVE actin regulators of the Wiskott–Aldrich syndrome protein (WASP) family are controlled by analogous structurally related complexes. Proceedings of the National Academy of Sciences, 107(23), 10442–10447. https://doi.org/10.1073/pnas.0913293107

92. Julkowska, M. M., Rankenberg, J. M., & Testerink, C. (2013). Liposome-Binding Assays to Assess Specificity and Affinity of Phospholipid–Protein Interactions. In T. Munnik & I. Heilmann (Eds.), Plant Lipid Signaling Protocols (Vol. 1009, pp. 261–271). Humana Press. https://doi.org/10.1007/978-1-62703-401-2_24

93. Jumper, J., Evans, R., Pritzel, A., Green, T., Figurnov, M., Ronneberger, O., Tunyasuvunakool, K., Bates, R., Žídek, A., Potapenko, A., Bridgland, A., Meyer, C., Kohl, S. A. A., Ballard, A. J., Cowie, A., Romera-Paredes, B., Nikolov, S., Jain, R., Adler, J., … Hassabis, D. (2021). Highly accurate protein structure prediction with AlphaFold. Nature, 596(7873), 583–589. https://doi.org/10.1038/s41586-021-03819-2

94. Kabsch, W. (2010). XDS. Acta Crystallographica Section D Biological Crystallography, 66(2), 125–132. https://doi.org/10.1107/S0907444909047337

95. Kapust, R. B., & Waugh, D. S. (1999). Escherichia coli maltose-binding protein is uncommonly effective at promoting the solubility of polypeptides to which it is fused. Protein Science, 8(8), 1668–1674. https://doi.org/10.1110/ps.8.8.1668

96. Kato, K., Oka, Y., Muramatsu, H., Vasilev, F. F., Otomo, T., Oishi, H., Kawano, Y., Kidokoro, H., Nakazawa, Y., Ogi, T., Takahashi, Y., & Saitoh, S. (2020). Biallelic VPS35L pathogenic variants cause 3C/Ritscher-Schinzel-like syndrome through dysfunction of retriever complex. Journal of Medical Genetics, 57(4), 245–253. https://doi.org/10.1136/jmedgenet-2019-106213

97. Kendall, A. K., Xie, B., Xu, P., Wang, J., Burcham, R., Frazier, M. N., Binshtein, E., Wei, H., Graham, T. R., Nakagawa, T., & Jackson, L. P. (2020). Mammalian Retromer Is an Adaptable Scaffold for Cargo Sorting from Endosomes. Structure, 28(4), 393-405.e4. https://doi.org/10.1016/j.str.2020.01.009

98. Kim, H. S., Jung, M., Kang, H. N., Kim, H., Park, C.-W., Kim, S.-M., Shin, S. J., Kim, S. H., Kim, S. G., Kim, E. K., Yun, M. R., Zheng, Z., Chung, K. Y., Greenbowe, J., Ali, S. M., Kim, T.-M., & Cho, B. C. (2017). Oncogenic BRAF fusions in mucosal melanomas activate the MAPK pathway and are sensitive to MEK/PI3K inhibition or MEK/CDK4/6 inhibition. Oncogene, 36(23), 3334–3345. https://doi.org/10.1038/onc.2016.486

99. Kingston, D., Chang, H., Ensser, A., Lee, H.-R., Lee, J., Lee, S.-H., Jung, J. U., & Cho, N.-H. (2011). Inhibition of Retromer Activity by Herpesvirus Saimiri Tip Leads to CD4 Downregulation and Efficient T Cell Transformation. Journal of Virology, 85(20), 10627–10638. https://doi.org/10.1128/JVI.00757-11

100. Knauth, P., Schlüter, T., Czubayko, M., Kirsch, C., Florian, V., Schreckenberger, S., Hahn, H., & Bohnensack, R. (2005). Functions of Sorting Nexin 17 Domains and Recognition Motif for P-selectin Trafficking. Journal of Molecular Biology, 347(4), 813–825. https://doi.org/10.1016/j.jmb.2005.02.004

101. Kobe, B., Ve, T., & Williams, S. J. (2015). Fusion-protein-assisted protein crystallization. Acta Crystallographica Section F Structural Biology Communications, 71(7), 861–869. https://doi.org/10.1107/S2053230X15011061

102. Kolanczyk, M., Krawitz, P., Hecht, J., Hupalowska, A., Miaczynska, M., Marschner, K., Schlack, C., Emmerich, D., Kobus, K., Kornak, U., Robinson, P. N., Plecko, B., Grangl, G., Uhrig, S., Mundlos, S., & Horn, D. (2015). Missense variant in CCDC22 causes X-linked recessive intellectual disability with features of Ritscher-Schinzel/3C syndrome. European Journal of Human Genetics, 23(5), 633–638. https://doi.org/10.1038/ejhg.2014.109

103. Koumandou, V. L., Klute, M. J., Herman, E. K., Nunez-Miguel, R., Dacks, J. B., & Field, M. C. (2011). Evolutionary reconstruction of the retromer complex and its function in Trypanosoma brucei. Journal of Cell Science, 124(9), 1496–1509. https://doi.org/10.1242/jcs.081596

104. Kovtun, O., Leneva, N., Bykov, Y. S., Ariotti, N., Teasdale, R. D., Schaffer, M., Engel, B. D., Owen, David. J., Briggs, J. A. G., & Collins, B. M. (2018). Structure of the membrane-assembled retromer coat determined by cryo-electron tomography. Nature, 561(7724), 561–564. https://doi.org/10.1038/s41586-018-0526-z

105. Kowallik, K. V., & Martin, W. F. (2021). The origin of symbiogenesis: An annotated English translation of Mereschkowsky's 1910 paper on the theory of two plasma lineages. Biosystems, 199, 104281. https://doi.org/10.1016/j.biosystems.2020.104281

106. Laakkonen, J. P., Lähteenvuo, J., Jauhiainen, S., Heikura, T., & Ylä-Herttuala, S. (2019). Beyond endothelial cells: Vascular endothelial growth factors in heart, vascular anomalies and placenta. Vascular Pharmacology, 112, 91–101. https://doi.org/10.1016/j.vph.2018.10.005

107. Lane, N., & Martin, W. (2010). The energetics of genome complexity. Nature, 467(7318), 929–934. https://doi.org/10.1038/nature09486

108. Lauffer, B. E. L., Melero, C., Temkin, P., Lei, C., Hong, W., Kortemme, T., & Von Zastrow, M. (2010). SNX27 mediates PDZ-directed sorting from endosomes to the plasma membrane. Journal of Cell Biology, 190(4), 565–574. https://doi.org/10.1083/jcb.201004060

109. Laulumaa, S., Kumpula, E.-P., Huiskonen, J. T., & Varjosalo, M. (2024). Structure and interactions of the endogenous human Commander complex. Nature Structural & Molecular Biology, 31(6), 925–938. https://doi.org/10.1038/s41594-024-01246-1

110. Laulumaa, S., & Varjosalo, M. (2021). Commander Complex—A Multifaceted Operator in Intracellular Signaling and Cargo. Cells, 10(12), 3447. https://doi.org/10.3390/cells10123447

111. Lear, S., & Cobb, S. L. (2016). Pep-Calc.com: A set of web utilities for the calculation of peptide and peptoid properties and automatic mass spectral peak assignment. Journal of Computer-Aided Molecular Design, 30(3), 271–277. https://doi.org/10.1007/s10822-016-9902-7

112. Lee, J., Retamal, C., Cuitiño, L., Caruano-Yzermans, A., Shin, J.-E., Van Kerkhof, P., Marzolo, M.-P., & Bu, G. (2008). Adaptor Protein Sorting Nexin 17 Regulates Amyloid Precursor Protein Trafficking and Processing in the Early Endosomes. Journal of Biological Chemistry, 283(17), 11501–11508. https://doi.org/10.1074/jbc.M800642200

113. Lee, S., Park, H., Zhu, P.-P., Jung, S.-Y., Blackstone, C., & Chang, J. (2020). Hereditary spastic paraplegia SPG8 mutations impair CAV1-dependent, integrin-mediated cell adhesion. Science Signaling, 13(613), eaau7500. https://doi.org/10.1126/scisignal.aau7500

114. Leneva, N., Kovtun, O., Morado, D. R., Briggs, J. A. G., & Owen, D. J. (2021). Architecture and mechanism of metazoan retromer:SNX3 tubular coat assembly. SCIENCE ADVANCES.

115. Lenoir, M., Ustunel, C., Rajesh, S., Kaur, J., Moreau, D., Gruenberg, J., & Overduin, M. (2018). Phosphorylation of conserved phosphoinositide binding pocket regulates sorting nexin membrane targeting. Nature Communications, 9(1), 993. https://doi.org/10.1038/s41467-018-03370-1

116. Li, Y., Calvo, S. E., Gutman, R., Liu, J. S., & Mootha, V. K. (2014). Expansion of Biological Pathways Based on Evolutionary Inference. Cell, 158(1), 213–225. https://doi.org/10.1016/j.cell.2014.05.034

117. Lockstone, H. E., Harris, L. W., Swatton, J. E., Wayland, M. T., Holland, A. J., & Bahn, S. (2007). Gene expression profiling in the adult Down syndrome brain. Genomics, 90(6), 647–660. https://doi.org/10.1016/j.ygeno.2007.08.005

118. Lopez-Robles, C., Scaramuzza, S., Astorga-Simon, E. N., Ishida, M., Williamson, C. D., Baños-Mateos, S., Gil-Carton, D., Romero-Durana, M., Vidaurrazaga, A., Fernandez-Recio, J., Rojas, A. L., Bonifacino, J. S., Castaño-Díez, D., & Hierro, A. (2023). Architecture of the ESCPE-1 membrane coat. Nature Structural & Molecular Biology, 30(7), 958–969. https://doi.org/10.1038/s41594-023-01014-7

119. Lucas, M., Gershlick, D. C., Vidaurrazaga, A., Rojas, A. L., Bonifacino, J. S., & Hierro, A. (2016). Structural Mechanism for Cargo Recognition by the Retromer Complex. Cell, 167(6), 1623-1635.e14. https://doi.org/10.1016/j.cell.2016.10.056

120. Madeira, F., Madhusoodanan, N., Lee, J., Eusebi, A., Niewielska, A., Tivey, A. R. N., Lopez, R., & Butcher, S. (2024). The EMBL-EBI Job Dispatcher sequence analysis tools framework in 2024. Nucleic Acids Research, 52(W1), W521–W525. https://doi.org/10.1093/nar/gkae241

121. Maine, G. N., & Burstein, E. (2007). COMMD Proteins and the Control of the NFκB Pathway. Cell Cycle, 6(6), 672–676. https://doi.org/10.4161/cc.6.6.3989

122. Mallam, A. L., & Marcotte, E. M. (2017). Systems-wide Studies Uncover Commander, a Multiprotein Complex Essential to Human Development. Cell Systems, 4(5), 483–494. https://doi.org/10.1016/j.cels.2017.04.006

123. Manalastas-Cantos, K., Konarev, P. V., Hajizadeh, N. R., Kikhney, A. G., Petoukhov, M. V., Molodenskiy, D. S., Panjkovich, A., Mertens, H. D. T., Gruzinov, A., Borges, C., Jeffries, C. M., Svergun, D. I., & Franke, D. (2021). ATSAS 3.0: Expanded functionality and new tools for small-angle scattering data analysis. Journal of Applied Crystallography, 54(1), 343–355. https://doi.org/10.1107/S1600576720013412

124. Maxfield, F. R., & Yamashiro, D. J. (1987). Endosome Acidification and the Pathways of Receptor-Mediated Endocytosis. In M. Z. Atassi (Ed.), Immunobiology of Proteins and Peptides IV (Vol. 225, pp. 189–198). Springer US. https://doi.org/10.1007/978-1-4684-5442-0_16

125. Mayor, S., & Pagano, R. E. (2007). Pathways of clathrin-independent endocytosis. Nature Reviews Molecular Cell Biology, 8(8), 603–612. https://doi.org/10.1038/nrm2216

126. McDonald, F. J. (2021). Explosion in the complexity of membrane protein recycling. American Journal of Physiology-Cell Physiology, 320(4), C483–C494. https://doi.org/10.1152/ajpcell.00171.2020

127. McGough, I. J., & Cullen, P. J. (2011). Recent Advances in Retromer Biology. Traffic, 12(8), 963–971. https://doi.org/10.1111/j.1600-0854.2011.01201.x

128. McGough, I. J., Steinberg, F., Jia, D., Barbuti, P. A., McMillan, K. J., Heesom, K. J., Whone, A. L., Caldwell, M. A., Billadeau, D. D., Rosen, M. K., & Cullen, P. J. (2014). Retromer Binding to FAM21 and the WASH Complex Is Perturbed by the Parkinson Disease-Linked VPS35(D620N) Mutation. Current Biology, 24(14), 1670–1676. https://doi.org/10.1016/j.cub.2014.06.024

129. McMahon, H. T., & Boucrot, E. (2011). Molecular mechanism and physiological functions of clathrin-mediated endocytosis. Nature Reviews Molecular Cell Biology, 12(8), 517–533. https://doi.org/10.1038/nrm3151

130. McMillan, K. J., Korswagen, H. C., & Cullen, P. J. (2017). The emerging role of retromer in neuroprotection. Current Opinion in Cell Biology, 47, 72–82. https://doi.org/10.1016/j.ceb.2017.02.004

131. McNally, K. E., & Cullen, P. J. (2018). Endosomal Retrieval of Cargo: Retromer Is Not Alone. Trends in Cell Biology, 28(10), 807–822. https://doi.org/10.1016/j.tcb.2018.06.005

132. McNally, K. E., Faulkner, R., Steinberg, F., Gallon, M., Ghai, R., Pim, D., Langton, P., Pearson, N., Danson, C. M., Nägele, H., Morris, L. L., Singla, A., Overlee, B. L., Heesom, K. J., Sessions, R., Banks, L., Collins, B. M., Berger, I., Billadeau, D. D., … Cullen, P. J. (2017). Retriever is a multiprotein complex for retromer-independent endosomal cargo recycling. Nature Cell Biology, 19(10), 1214–1225. https://doi.org/10.1038/ncb3610

133. McPherson, A., & Gavira, J. A. (2014). Introduction to protein crystallization. Acta Crystallographica Section F Structural Biology Communications, 70(1), 2–20. https://doi.org/10.1107/S2053230X13033141

134. Mecozzi, V. J., Berman, D. E., Simoes, S., Vetanovetz, C., Awal, M. R., Patel, V. M., Schneider, R. T., Petsko, G. A., Ringe, D., & Small, S. A. (2014). Pharmacological chaperones stabilize retromer to limit APP processing. Nature Chemical Biology, 10(6), 443–449. https://doi.org/10.1038/nchembio.1508

135. Mellman and Warren 2000. (n.d.).

136. Mercer, J., Schelhaas, M., & Helenius, A. (2010). Virus Entry by Endocytosis. Annual Review of Biochemistry, 79(1), 803–833. https://doi.org/10.1146/annurev-biochem-060208-104626

137. Micsonai, A., Moussong, É., Wien, F., Boros, E., Vadászi, H., Murvai, N., Lee, Y.-H., Molnár, T., Réfrégiers, M., Goto, Y., Tantos, Á., & Kardos, J. (2022). BeStSel: Webserver for secondary structure and fold prediction for protein CD spectroscopy. Nucleic Acids Research, 50(W1), W90–W98. https://doi.org/10.1093/nar/gkac345

138. Mirdita, M., Schütze, K., Moriwaki, Y., Heo, L., Ovchinnikov, S., & Steinegger, M. (2022). ColabFold: Making protein folding accessible to all. Nature Methods, 19(6), 679–682. https://doi.org/10.1038/s41592-022-01488-1

139. Miroux, B., & Walker, J. E. (1996). Over-production of Proteins inEscherichia coli: Mutant Hosts that Allow Synthesis of some Membrane Proteins and Globular Proteins at High Levels. Journal of Molecular Biology, 260(3), 289–298. https://doi.org/10.1006/jmbi.1996.0399

140. Mirrashidi, K. M., Elwell, C. A., Verschueren, E., Johnson, J. R., Frando, A., Von Dollen, J., Rosenberg, O., Gulbahce, N., Jang, G., Johnson, T., Jäger, S., Gopalakrishnan, A. M., Sherry, J., Dunn, J. D., Olive, A., Penn, B., Shales, M., Cox, J. S., Starnbach, M. N., … Engel, J. (2015). Global Mapping of the Inc-Human Interactome Reveals that Retromer Restricts Chlamydia Infection. Cell Host & Microbe, 18(1), 109–121. https://doi.org/10.1016/j.chom.2015.06.004

141. Mishima, M., Maesaki, R., Kasa, M., Watanabe, T., Fukata, M., Kaibuchi, K., & Hakoshima, T. (2007). Structural basis for tubulin recognition by cytoplasmic linker protein 170 and its autoinhibition. Proceedings of the National Academy of Sciences, 104(25), 10346–10351. https://doi.org/10.1073/pnas.0703876104

142. Moreno-Layseca, P., Icha, J., Hamidi, H., & Ivaska, J. (2019). Integrin trafficking in cells and tissues. Nature Cell Biology, 21(2), 122–132. https://doi.org/10.1038/s41556-018-0223-z

143. Naslavsky, N., & Caplan, S. (2018). The enigmatic endosome – sorting the ins and outs of endocytic trafficking. Journal of Cell Science, 131(13), jcs216499. https://doi.org/10.1242/jcs.216499

144. Nayerossadat, N., Maedeh, T., & Ali, P. (2012). Viral and nonviral delivery systems for gene delivery. Advanced Biomedical Research, 1(1), 27. https://doi.org/10.4103/2277-9175.98152

145. Norwood, S. J., Shaw, D. J., Cowieson, N. P., Owen, D. J., Teasdale, R. D., & Collins, B. M. (2011). Assembly and Solution Structure of the Core Retromer Protein Complex. Traffic, 12(1), 56–71. https://doi.org/10.1111/j.1600-0854.2010.01124.x

146. Organ, S. L., & Tsao, M.-S. (2011). An overview of the c-MET signaling pathway. Therapeutic Advances in Medical Oncology, 3(1_suppl), S7–S19. https://doi.org/10.1177/1758834011422556

147. O'Sullivan, M. J., & Lindsay, A. J. (2020). The Endosomal Recycling Pathway—At the Crossroads of the Cell. International Journal of Molecular Sciences, 21(17), 6074. https://doi.org/10.3390/ijms21176074

148. Palovcak, E., Asarnow, D., Campbell, M. G., Yu, Z., & Cheng, Y. (2020). Enhancing the signal-to-noise ratio and generating contrast for cryo-EM images with convolutional neural networks. IUCrJ, 7(6), 1142–1150. https://doi.org/10.1107/S2052252520013184

149. Pantoliano, M. W., Petrella, E. C., Kwasnoski, J. D., Lobanov, V. S., Myslik, J., Graf, E., Carver, T., Asel, E., Springer, B. A., Lane, P., & Salemme, F. R. (2001). High-Density Miniaturized Thermal Shift Assays as a General Strategy for Drug Discovery. SLAS Discovery, 6(6), 429–440. https://doi.org/10.1177/108705710100600609

150. Pearson, M. A., Reczek, D., Bretscher, A., & Karplus, P. A. (2000). Structure of the ERM Protein Moesin Reveals the FERM Domain Fold Masked by an Extended Actin Binding Tail Domain. Cell, 101(3), 259–270. https://doi.org/10.1016/S0092-8674(00)80836-3

151. Pei, J., & Grishin, N. V. (2001). AL2CO: Calculation of positional conservation in a protein sequence alignment. Bioinformatics, 17(8), 700–712. https://doi.org/10.1093/bioinformatics/17.8.700

152. Pei, J., Kim, B.-H., & Grishin, N. V. (2008). PROMALS3D: A tool for multiple protein sequence and structure alignments. Nucleic Acids Research, 36(7), 2295–2300. https://doi.org/10.1093/nar/gkn072

153. Penn, J. S., Madan, A., Caldwell, R. B., Bartoli, M., Caldwell, R. W., & Hartnett, M. E. (2008). Vascular endothelial growth factor in eye disease. Progress in Retinal and Eye Research, 27(4), 331–371. https://doi.org/10.1016/j.preteyeres.2008.05.001

154. Personnic, N., Bärlocher, K., Finsel, I., & Hilbi, H. (2016). Subversion of Retrograde Trafficking by Translocated Pathogen Effectors. Trends in Microbiology, 24(6), 450–462. https://doi.org/10.1016/j.tim.2016.02.003

155. Pettersen, E. F., Goddard, T. D., Huang, C. C., Meng, E. C., Couch, G. S., Croll, T. I., Morris, J. H., & Ferrin, T. E. (2021). UCSF ChimeraX: Structure visualization for researchers, educators, and developers. Protein Science, 30(1), 70–82. https://doi.org/10.1002/pro.3943

156. Phillips-Krawczak, C. A., Singla, A., Starokadomskyy, P., Deng, Z., Osborne, D. G., Li, H., Dick, C. J., Gomez, T. S., Koenecke, M., Zhang, J.-S., Dai, H., Sifuentes-Dominguez, L. F., Geng, L. N., Kaufmann, S. H., Hein, M. Y., Wallis, M., McGaughran, J., Gecz, J., Sluis, B. V. D., … Burstein, E. (2015). COMMD1 is linked to the WASH complex and regulates endosomal trafficking of the copper transporter ATP7A. Molecular Biology of the Cell, 26(1), 91–103. https://doi.org/10.1091/mbc.e14-06-1073

157. Pim, D., Broniarczyk, J., Bergant, M., Playford, M. P., & Banks, L. (2015). A Novel PDZ Domain Interaction Mediates the Binding between Human Papillomavirus 16 L2 and Sorting Nexin 27 and Modulates Virion Trafficking. Journal of Virology, 89(20), 10145–10155. https://doi.org/10.1128/JVI.01499-15

158. Pim, D., Broniarczyk, J., Siddiqa, A., Massimi, P., & Banks, L. (2021). Human Papillomavirus 16 L2 Recruits both Retromer and Retriever Complexes during Retrograde Trafficking of the Viral Genome to the Cell Nucleus. Journal of Virology, 95(3), e02068-20. https://doi.org/10.1128/JVI.02068-20

159. Polishchuk, R. S., Capestrano, M., & Polishchuk, E. V. (2009). Shaping tubular carriers for intracellular membrane transport. FEBS Letters, 583(23), 3847–3856. https://doi.org/10.1016/j.febslet.2009.10.031

160. Popa, A., Zhang, W., Harrison, M. S., Goodner, K., Kazakov, T., Goodwin, E. C., Lipovsky, A., Burd, C. G., & DiMaio, D. (2015). Direct Binding of Retromer to Human Papillomavirus Type 16 Minor Capsid Protein L2 Mediates Endosome Exit during Viral Infection. PLOS Pathogens, 11(2), e1004699. https://doi.org/10.1371/journal.ppat.1004699

161. Prinz, W. A. (2010). Lipid Trafficking sans Vesicles: Where, Why, How? Cell, 143(6), 870–874. https://doi.org/10.1016/j.cell.2010.11.031

162. Prinz, W. A., Toulmay, A., & Balla, T. (2019). The functional universe of membrane contact sites. Nature Reviews Molecular Cell Biology, 21(1), 7–24. https://doi.org/10.1038/s41580-019-0180-9

163. ProteinHandbook.pdfpage48 Walker 2009 triton. (n.d.).

164. Pufall, M. A., & Graves, B. J. (2002). Autoinhibitory Domains: Modular Effectors of Cellular Regulation. Annual Review of Cell and Developmental Biology, 18(1), 421–462. https://doi.org/10.1146/annurev.cellbio.18.031502.133614

165. Punjani, A., Rubinstein, J. L., Fleet, D. J., & Brubaker, M. A. (2017). cryoSPARC: Algorithms for rapid unsupervised cryo-EM structure determination. Nature Methods, 14(3), 290–296. https://doi.org/10.1038/nmeth.4169

166. Rabouille, C. (2017). Retriever fetches integrins from endosomes. Nature Cell Biology, 19(10), 1144–1146. https://doi.org/10.1038/ncb3612

167. Rauch, J. N., Luna, G., Guzman, E., Audouard, M., Challis, C., Sibih, Y. E., Leshuk, C., Hernandez, I., Wegmann, S., Hyman, B. T., Gradinaru, V., Kampmann, M., & Kosik, K. S. (2020). LRP1 is a master regulator of tau uptake and spread. Nature, 580(7803), 381–385. https://doi.org/10.1038/s41586-020-2156-5

168. Rivero-Ríos, P., Tsukahara, T., Uygun, T., Chen, A., Chavis, G. D., Giridharan, S. S. P., Iwase, S., Sutton, M. A., & Weisman, L. S. (2023). Recruitment of the SNX17-Retriever recycling pathway regulates synaptic function and plasticity. Journal of Cell Biology, 222(7), e202207025. https://doi.org/10.1083/jcb.202207025

169. Robert, X., & Gouet, P. (2014). Deciphering key features in protein structures with the new ENDscript server. Nucleic Acids Research, 42(W1), W320–W324. https://doi.org/10.1093/nar/gku316

170. Rojas, R., Van Vlijmen, T., Mardones, G. A., Prabhu, Y., Rojas, A. L., Mohammed, S., Heck, A. J. R., Raposo, G., Van Der Sluijs, P., & Bonifacino, J. S. (2008). Regulation of retromer recruitment to endosomes by sequential action of Rab5 and Rab7. The Journal of Cell Biology, 183(3), 513–526. https://doi.org/10.1083/jcb.200804048

171. Romano-Moreno, M., Astorga-Simón, E. N., Rojas, A. L., & Hierro, A. (2024). Retromer-mediated recruitment of the WASH complex involves discrete interactions between VPS35 , VPS29, and FAM21. Protein Science, 33(5), e4980. https://doi.org/10.1002/pro.4980

172. Romano-Moreno, M., Rojas, A. L., Williamson, C. D., Gershlick, D. C., Lucas, M., Isupov, M. N., Bonifacino, J. S., Machner, M. P., & Hierro, A. (2017). Molecular mechanism for the subversion of the retromer coat by the Legionella effector RidL. Proceedings of the National Academy of Sciences, 114(52). https://doi.org/10.1073/pnas.1715361115

173. Romero-Durana, M., Jiménez-García, B., & Fernández-Recio, J. (2020). pyDockEneRes: Per-residue decomposition of protein–protein docking energy. Bioinformatics, 36(7), 2284–2285. https://doi.org/10.1093/bioinformatics/btz884

174. Ropers, F., Derivery, E., Hu, H., Garshasbi, M., Karbasiyan, M., Herold, M., Nurnberg, G., Ullmann, R., Gautreau, A., Sperling, K., Varon, R., & Rajab, A. (2011). Identification of a novel candidate gene for non-syndromic autosomal recessive intellectual disability: The WASH complex member SWIP. Human Molecular Genetics, 20(13), 2585–2590. https://doi.org/10.1093/hmg/ddr158

175. Saitoh, S. (2022). Endosomal Recycling Defects and Neurodevelopmental Disorders. Cells, 11(1), 148. https://doi.org/10.3390/cells11010148

176. Sartori, F., Hafner, A.-S., Karimi, A., Nold, A., Fonkeu, Y., Schuman, E. M., & Tchumatchenko, T. (2020). Statistical Laws of Protein Motion in Neuronal Dendritic Trees. Cell Reports, 33(7), 108391. https://doi.org/10.1016/j.celrep.2020.108391

177. Schindelin, J., Arganda-Carreras, I., Frise, E., Kaynig, V., Longair, M., Pietzsch, T., Preibisch, S., Rueden, C., Saalfeld, S., Schmid, B., Tinevez, J.-Y., White, D. J., Hartenstein, V., Eliceiri, K., Tomancak, P., & Cardona, A. (2012). Fiji: An open-source platform for biological-image analysis. Nature Methods, 9(7), 676–682. https://doi.org/10.1038/nmeth.2019

178. Seaman, M. N. J. (2007). Identification of a novel conserved sorting motif required for retromer-mediated endosome-to-TGN retrieval. Journal of Cell Science, 120(14), 2378–2389. https://doi.org/10.1242/jcs.009654

179. Seaman, M. N. J., Gautreau, A., & Billadeau, D. D. (2013). Retromer-mediated endosomal protein sorting: All WASHed up! Trends in Cell Biology, 23(11), 522–528. https://doi.org/10.1016/j.tcb.2013.04.010

180. Seaman, M. N. J., Michael McCaffery, J., & Emr, S. D. (1998). A Membrane Coat Complex Essential for Endosome-to-Golgi Retrograde Transport in Yeast. The Journal of Cell Biology, 142(3), 665–681. https://doi.org/10.1083/jcb.142.3.665

181. Shafaq-Zadah, M., Gomes-Santos, C. S., Bardin, S., Maiuri, P., Maurin, M., Iranzo, J., Gautreau, A., Lamaze, C., Caswell, P., Goud, B., & Johannes, L. (2016). Persistent cell migration and adhesion rely on retrograde transport of β1 integrin. Nature Cell Biology, 18(1), 54–64. https://doi.org/10.1038/ncb3287

182. Shaid, S., Brandts, C. H., Serve, H., & Dikic, I. (2013). Ubiquitination and selective autophagy. Cell Death & Differentiation, 20(1), 21–30. https://doi.org/10.1038/cdd.2012.72

183. Sheffield, P., Garrard, S., & Derewenda, Z. (1999). Overcoming Expression and Purification Problems of RhoGDI Using a Family of "Parallel" Expression Vectors. Protein Expression and Purification, 15(1), 34–39. https://doi.org/10.1006/prep.1998.1003

184. Shi, H., Rojas, R., Bonifacino, J. S., & Hurley, J. H. (2006). The retromer subunit Vps26 has an arrestin fold and binds Vps35 through its C-terminal domain. Nature Structural & Molecular Biology, 13(6), 540–548. https://doi.org/10.1038/nsmb1103

185. Shisheva, A. (2008). PIKfyve: Partners, significance, debates and paradoxes. Cell Biology International, 32(6), 591–604. https://doi.org/10.1016/j.cellbi.2008.01.006

186. Siddiqa, A., Broniarczyk, J., & Banks, L. (2018). Papillomaviruses and Endocytic Trafficking. International Journal of Molecular Sciences, 19(9), 2619. https://doi.org/10.3390/ijms19092619

187. Simonetti, B., Danson, C. M., Heesom, K. J., & Cullen, P. J. (2017). Sequence-dependent cargo recognition by SNX-BARs mediates retromer-independent transport of CI-MPR. Journal of Cell Biology, 216(11), 3695–3712. https://doi.org/10.1083/jcb.201703015

188. Singla, A., Fedoseienko, A., Giridharan, S. S. P., Overlee, B. L., Lopez, A., Jia, D., Song, J., Huff-Hardy, K., Weisman, L., Burstein, E., & Billadeau, D. D. (2019). Endosomal PI(3)P regulation by the COMMD/CCDC22/CCDC93 (CCC) complex controls membrane protein recycling. Nature Communications, 10(1), 4271. https://doi.org/10.1038/s41467-019-12221-6

189. Sizova, O., John, L. St., Ma, Q., & Molldrem, J. J. (2023). Multi-faceted role of LRP1 in the immune system. Frontiers in Immunology, 14, 1166189. https://doi.org/10.3389/fimmu.2023.1166189

190. Soppina, V., Rai, A. K., Ramaiya, A. J., Barak, P., & Mallik, R. (2009). Tug-of-war between dissimilar teams of microtubule motors regulates transport and fission of endosomes. Proceedings of the National Academy of Sciences, 106(46), 19381–19386. https://doi.org/10.1073/pnas.0906524106

191. Steinberg, F., Gallon, M., Winfield, M., Thomas, E. C., Bell, A. J., Heesom, K. J., Tavaré, J. M., & Cullen, P. J. (2013). A global analysis of SNX27–retromer assembly and cargo specificity reveals a function in glucose and metal ion transport. Nature Cell Biology, 15(5), 461–471. https://doi.org/10.1038/ncb2721

192. Steinberg, F., Heesom, K. J., Bass, M. D., & Cullen, P. J. (2012). SNX17 protects integrins from degradation by sorting between lysosomal and recycling pathways. Journal of Cell Biology, 197(2), 219–230. https://doi.org/10.1083/jcb.201111121

193. Stelzer, G., Rosen, N., Plaschkes, I., Zimmerman, S., Twik, M., Fishilevich, S., Stein, T. I., Nudel, R., Lieder, I., Mazor, Y., Kaplan, S., Dahary, D., Warshawsky, D., Guan-Golan, Y., Kohn, A., Rappaport, N., Safran, M., & Lancet, D. (2016). The GeneCards Suite: From Gene Data Mining to Disease Genome Sequence Analyses. Current Protocols in Bioinformatics, 54(1). https://doi.org/10.1002/cpbi.5

194. Stiegler, A. L., Zhang, R., Liu, W., & Boggon, T. J. (2014). Structural Determinants for Binding of Sorting Nexin 17 (SNX17) to the Cytoplasmic Adaptor Protein Krev Interaction Trapped 1 (KRIT1). Journal of Biological Chemistry, 289(36), 25362–25373. https://doi.org/10.1074/jbc.M114.584011

195. Stockinger, W. (2002). The PX-domain protein SNX17 interacts with members of the LDL receptor family and modulates endocytosis of the LDL receptor. The EMBO Journal, 21(16), 4259–4267. https://doi.org/10.1093/emboj/cdf435

196. Stuart, S. A., Houel, S., Lee, T., Wang, N., Old, W. M., & Ahn, N. G. (2015). A Phosphoproteomic Comparison of B-RAFV600E and MKK1/2 Inhibitors in Melanoma Cells*. Molecular & Cellular Proteomics, 14(6), 1599–1615. https://doi.org/10.1074/mcp.M114.047233

197. Studier, F. W., & Moffatt, B. A. (1986). Use of bacteriophage T7 RNA polymerase to direct selective high-level expression of cloned genes. Journal of Molecular Biology, 189(1), 113–130. https://doi.org/10.1016/0022-2836(86)90385-2

198. Swarbrick, J. D., Shaw, D. J., Chhabra, S., Ghai, R., Valkov, E., Norwood, S. J., Seaman, M. N. J., & Collins, B. M. (2011). VPS29 Is Not an Active Metallo-Phosphatase but Is a Rigid Scaffold Required for Retromer Interaction with Accessory Proteins. PLoS ONE, 6(5), e20420. https://doi.org/10.1371/journal.pone.0020420

199. Tabuchi, M., Yanatori, I., Kawai, Y., & Kishi, F. (2010). Retromer-mediated direct sorting is required for proper endosomal recycling of the mammalian iron transporter DMT1. Journal of Cell Science, 123(5), 756–766. https://doi.org/10.1242/jcs.060574

200. Tan, J. Z. A., & Gleeson, P. A. (2019). The role of membrane trafficking in the processing of amyloid precursor protein and production of amyloid peptides in Alzheimer's disease. Biochimica et Biophysica Acta (BBA) - Biomembranes, 1861(4), 697–712. https://doi.org/10.1016/j.bbamem.2018.11.013

201. Teasdale, R. D., & Collins, B. M. (2012). Insights into the PX (phox-homology) domain and SNX (sorting nexin) protein families: Structures, functions and roles in disease. Biochemical Journal, 441(1), 39–59. https://doi.org/10.1042/BJ20111226

202. The Cancer Genome Atlas Research Network. (2011). Integrated genomic analyses of ovarian carcinoma. Nature, 474(7353), 609–615. https://doi.org/10.1038/nature10166

203. The UniProt Consortium, Bateman, A., Martin, M.-J., Orchard, S., Magrane, M., Ahmad, S., Alpi, E., Bowler-Barnett, E. H., Britto, R., Bye-A-Jee, H., Cukura, A., Denny, P., Dogan, T., Ebenezer, T., Fan, J., Garmiri, P., Da Costa Gonzales, L. J., Hatton-Ellis, E., Hussein, A., … Zhang, J. (2023). UniProt: The Universal Protein Knowledgebase in 2023. Nucleic Acids Research, 51(D1), D523–D531. https://doi.org/10.1093/nar/gkac1052

204. Trudeau, T., Nassar, R., Cumberworth, A., Wong, E. T. C., Woollard, G., & Gsponer, J. (2013). Structure and Intrinsic Disorder in Protein Autoinhibition. Structure, 21(3), 332–341. https://doi.org/10.1016/j.str.2012.12.013

205. Tseng, H.-Y., Thorausch, N., Ziegler, T., Meves, A., Fässler, R., & Böttcher, R. T. (2014). Sorting Nexin 31 Binds Multiple β Integrin Cytoplasmic Domains and Regulates β1 Integrin Surface Levels and Stability. Journal of Molecular Biology, 426(18), 3180–3194. https://doi.org/10.1016/j.jmb.2014.07.003

206. Uhlén, M., Fagerberg, L., Hallström, B. M., Lindskog, C., Oksvold, P., Mardinoglu, A., Sivertsson, Å., Kampf, C., Sjöstedt, E., Asplund, A., Olsson, I., Edlund, K., Lundberg, E., Navani, S., Szigyarto, C. A.-K., Odeberg, J., Djureinovic, D., Takanen, J. O., Hober, S., … Pontén, F. (2015). Tissue-based map of the human proteome. Science, 347(6220), 1260419. https://doi.org/10.1126/science.1260419

207. Van De Sluis, B. (2002). Identification of a new copper metabolism gene by positional cloning in a purebred dog population. Human Molecular Genetics, 11(2), 165–173. https://doi.org/10.1093/hmg/11.2.165

208. Van Weering, J. R. T., Verkade, P., & Cullen, P. J. (2010). SNX–BAR proteins in phosphoinositide-mediated, tubular-based endosomal sorting. Seminars in Cell & Developmental Biology, 21(4), 371–380. https://doi.org/10.1016/j.semcdb.2009.11.009

209. Vanni, I., Tanda, E. T., Dalmasso, B., Pastorino, L., Andreotti, V., Bruno, W., Boutros, A., Spagnolo, F., & Ghiorzo, P. (2020). Non-BRAF Mutant Melanoma: Molecular Features and Therapeutical Implications. Frontiers in Molecular Biosciences, 7, 172. https://doi.org/10.3389/fmolb.2020.00172

210. Varadi, M., Anyango, S., Deshpande, M., Nair, S., Natassia, C., Yordanova, G., Yuan, D., Stroe, O., Wood, G., Laydon, A., Žídek, A., Green, T., Tunyasuvunakool, K., Petersen, S., Jumper, J., Clancy, E., Green, R., Vora, A., Lutfi, M., … Velankar, S. (2022). AlphaFold Protein Structure Database: Massively expanding the structural coverage of protein-sequence space with high-accuracy models. Nucleic Acids Research, 50(D1), D439–D444. https://doi.org/10.1093/nar/gkab1061

211. Vardarajan, B. N., Bruesegem, S. Y., Harbour, M. E., George-Hyslop, P. St., Seaman, M. N. J., & Farrer, L. A. (2012). Identification of Alzheimer disease-associated variants in genes that regulate retromer function. Neurobiology of Aging, 33(9), 2231.e15-2231.e30. https://doi.org/10.1016/j.neurobiolaging.2012.04.020

212. Vedadi, M., Niesen, F. H., Allali-Hassani, A., Fedorov, O. Y., Finerty, P. J., Wasney, G. A., Yeung, R., Arrowsmith, C., Ball, L. J., Berglund, H., Hui, R., Marsden, B. D., Nordlund, P., Sundstrom, M., Weigelt, J., & Edwards, A. M. (2006). Chemical screening methods to identify ligands that promote protein stability, protein crystallization, and structure determination. Proceedings of the National Academy of Sciences, 103(43), 15835–15840. https://doi.org/10.1073/pnas.0605224103

213. Velasco-Olmo, A., Ormaetxea Gisasola, J., Martinez Galvez, J. M., Vera Lillo, J., & Shnyrova, A. V. (2019). Combining patch-clamping and fluorescence microscopy for quantitative reconstitution of cellular membrane processes with Giant Suspended Bilayers. Scientific Reports, 9(1), 7255. https://doi.org/10.1038/s41598-019-43561-4

214. Vicente-Manzanares, M., Choi, C. K., & Horwitz, A. R. (2009). Integrins in cell migration—The actin connection. Journal of Cell Science, 122(9), 1473–1473. https://doi.org/10.1242/jcs.052894

215. Vieira, N., Deng, F.-M., Liang, F.-X., Liao, Y., Chang, J., Zhou, G., Zheng, W., Simon, J.-P., Ding, M., Wu, X.-R., Romih, R., Kreibich, G., & Sun, T.-T. (2014). SNX31: A Novel Sorting Nexin Associated with the Uroplakin-Degrading Multivesicular Bodies in Terminally Differentiated Urothelial Cells. PLoS ONE, 9(6), e99644. https://doi.org/10.1371/journal.pone.0099644

216. Vos, D. Y., Wijers, M., Smit, M., Huijkman, N., Kloosterhuis, N. J., Wolters, J. C., Tissink, J. J., Pronk, A. C. M., Kooijman, S., Rensen, P. C. N., Kuivenhoven, J. A., & Van De Sluis, B. (2023). Cargo-Specific Role for Retriever Subunit VPS26C in Hepatocyte Lipoprotein Receptor Recycling to Control Postprandial Triglyceride-Rich Lipoproteins. Arteriosclerosis, Thrombosis, and Vascular Biology, 43(1). https://doi.org/10.1161/ATVBAHA.122.318169

217. Waddell, G. L., Drew, E. E., Rupp, H. P., & Hansen, S. D. (2023). Mechanisms controlling membrane recruitment and activation of the autoinhibited SHIP1 inositol 5-phosphatase. Journal of Biological Chemistry, 299(8), 105022. https://doi.org/10.1016/j.jbc.2023.105022

218. Wan, C., Borgeson, B., Phanse, S., Tu, F., Drew, K., Clark, G., Xiong, X., Kagan, O., Kwan, J., Bezginov, A., Chessman, K., Pal, S., Cromar, G., Papoulas, O., Ni, Z., Boutz, D. R., Stoilova, S., Havugimana, P. C., Guo, X., … Emili, A. (2015a). Panorama of ancient metazoan macromolecular complexes. Nature, 525(7569), 339–344. https://doi.org/10.1038/nature14877

219. Wan, C., Borgeson, B., Phanse, S., Tu, F., Drew, K., Clark, G., Xiong, X., Kagan, O., Kwan, J., Bezginov, A., Chessman, K., Pal, S., Cromar, G., Papoulas, O., Ni, Z., Boutz, D. R., Stoilova, S., Havugimana, P. C., Guo, X., … Emili, A. (2015b). Panorama of ancient metazoan macromolecular complexes. Nature, 525(7569), 339–344. https://doi.org/10.1038/nature14877

220. Wang, D., Guo, M., Liang, Z., Fan, J., Zhu, Z., Zang, J., Zhu, Z., Li, X., Teng, M., Niu, L., Dong, Y., & Liu, P. (2005). Crystal Structure of Human Vacuolar Protein Sorting Protein 29 Reveals a Phosphodiesterase/Nuclease-like Fold and Two Protein-Protein Interaction Sites. Journal of Biological Chemistry, 280(24), 22962–22967. https://doi.org/10.1074/jbc.M500464200

221. Wang, J., Billadeau, D. D., & Jia, D. (2022). Two siblings, distinct characteristics. Structure, 30(12), 1559–1560. https://doi.org/10.1016/j.str.2022.11.003

222. Wang, J., Fedoseienko, A., Chen, B., Burstein, E., Jia, D., & Billadeau, D. D. (2018). Endosomal receptor trafficking: Retromer and beyond. Traffic, 19(8), 578–590. https://doi.org/10.1111/tra.12574

223. Wardell, C. P., Fujita, M., Yamada, T., Simbolo, M., Fassan, M., Karlic, R., Polak, P., Kim, J., Hatanaka, Y., Maejima, K., Lawlor, R. T., Nakanishi, Y., Mitsuhashi, T., Fujimoto, A., Furuta, M., Ruzzenente, A., Conci, S., Oosawa, A., Sasaki-Oku, A., … Nakagawa, H. (2018). Genomic characterization of biliary tract cancers identifies driver genes and predisposing mutations. Journal of Hepatology, 68(5), 959–969. https://doi.org/10.1016/j.jhep.2018.01.009

224. Weeratunga, S., Paul, B., & Collins, B. M. (2020). Recognising the signals for endosomal trafficking. Current Opinion in Cell Biology, 65, 17–27. https://doi.org/10.1016/j.ceb.2020.02.005

225. Weissmann, F., Petzold, G., VanderLinden, R., Huis In 'T Veld, P. J., Brown, N. G., Lampert, F., Westermann, S., Stark, H., Schulman, B. A., & Peters, J.-M. (2016). biGBac enables rapid gene assembly for the expression of large multisubunit protein complexes. Proceedings of the National Academy of Sciences, 113(19). https://doi.org/10.1073/pnas.1604935113

226. White, D. P., Caswell, P. T., & Norman, J. C. (2007). Avβ3 and α5β1 integrin recycling pathways dictate downstream Rho kinase signaling to regulate persistent cell migration. The Journal of Cell Biology, 177(3), 515–525. https://doi.org/10.1083/jcb.200609004

227. Wild, K., August, A., Pietrzik, C. U., & Kins, S. (2017). Structure and Synaptic Function of Metal Binding to the Amyloid Precursor Protein and its Proteolytic Fragments. Frontiers in Molecular Neuroscience, 10. https://doi.org/10.3389/fnmol.2017.00021

228. Wong, L. H., Gatta, A. T., & Levine, T. P. (2019). Lipid transfer proteins: The lipid commute via shuttles, bridges and tubes. Nature Reviews Molecular Cell Biology, 20(2), 85–101. https://doi.org/10.1038/s41580-018-0071-5

229. Wozniak, M. A., Modzelewska, K., Kwong, L., & Keely, P. J. (2004). Focal adhesion regulation of cell behavior. Biochimica et Biophysica Acta (BBA) - Molecular Cell Research, 1692(2–3), 103–119. https://doi.org/10.1016/j.bbamcr.2004.04.007

230. Wu, Y., Zhou, Y., Huang, J., Ma, K., Yuan, T., Jiang, Y., Ye, M., & Li, J. (2021). The Role of Sorting Nexin 17 in Cardiac Development. Frontiers in Cardiovascular Medicine, 8, 748891. https://doi.org/10.3389/fcvm.2021.748891

231. Xiang, X., & Qiu, R. (2020). Cargo-Mediated Activation of Cytoplasmic Dynein in vivo. Frontiers in Cell and Developmental Biology, 8, 598952. https://doi.org/10.3389/fcell.2020.598952

232. Xu, Y., Hortsman, H., Seet, L., Wong, S. H., & Hong, W. (2001). SNX3 regulates endosomal function through its PX-domain-mediated interaction with PtdIns(3)P. Nature Cell Biology, 3(7), 658–666. https://doi.org/10.1038/35083051

233. Yang, L., Tan, W., Yang, X., You, Y., Wang, J., Wen, G., & Zhong, J. (2021). Sorting nexins: A novel promising therapy target for cancerous/neoplastic diseases. Journal of Cellular Physiology, 236(5), 3317–3335. https://doi.org/10.1002/jcp.30093

234. Yariv, B., Yariv, E., Kessel, A., Masrati, G., Chorin, A. B., Martz, E., Mayrose, I., Pupko, T., & Ben-Tal, N. (2023). Using evolutionary data to make sense of macromolecules with a "face-lifted" ConSurf. Protein Science, 32(3), e4582. https://doi.org/10.1002/pro.4582

235. Yong, X., Zhao, L., Hu, W., Sun, Q., Ham, H., Liu, Z., Ren, J., Zhang, Z., Zhou, Y., Yang, Q., Mo, X., Hu, J., Billadeau, D. D., & Jia, D. (2021). SNX27-FERM-SNX1 complex structure rationalizes divergent trafficking pathways by SNX17 and SNX27. Proceedings of the National Academy of Sciences, 118(36), e2105510118. https://doi.org/10.1073/pnas.2105510118

236. Yoshimura, S. H., & Hirano, T. (2016). HEAT repeats – versatile arrays of amphiphilic helices working in crowded environments? Journal of Cell Science, 129(21), 3963–3970. https://doi.org/10.1242/jcs.185710

237. Zavodszky, E., Seaman, M. N. J., Moreau, K., Jimenez-Sanchez, M., Breusegem, S. Y., Harbour, M. E., & Rubinsztein, D. C. (2014). Mutation in VPS35 associated with Parkinson's disease impairs WASH complex association and inhibits autophagy. Nature Communications, 5(1), 3828. https://doi.org/10.1038/ncomms4828

238. Zhang, J., Zhang, K., Qi, L., Hu, Q., Shen, Z., Liu, B., Deng, J., Zhang, C., & Zhang, Y. (2019). DENN domain-containing protein FAM45A regulates the homeostasis of late/multivesicular endosomes. Biochimica et Biophysica Acta (BBA) - Molecular Cell Research, 1866(5), 916–929. https://doi.org/10.1016/j.bbamcr.2019.02.006

239. Zhang, P., Monteiro Da Silva, G., Deatherage, C., Burd, C., & DiMaio, D. (2018). Cell-Penetrating Peptide Mediates Intracellular Membrane Passage of Human Papillomavirus L2 Protein to Trigger Retrograde Trafficking. Cell, 174(6), 1465-1476.e13. https://doi.org/10.1016/j.cell.2018.07.031

240. Zhou, C.-Z., Li De La Sierra-Gallay, I., Quevillon-Cheruel, S., Collinet, B., Minard, P., Blondeau, K., Henckes, G., Aufrère, R., Leulliot, N., Graille, M., Sorel, I., Savarin, P., De La Torre, F., Poupon, A., Janin, J., & Van Tilbeurgh, H. (2003). Crystal Structure of the Yeast Phox Homology (PX) Domain Protein Grd19p Complexed to Phosphatidylinositol-3-phosphate. Journal of Biological Chemistry, 278(50), 50371–50376. https://doi.org/10.1074/jbc.M304392200

241. Zhou, Z., Chan, C. H., Ma, Q., Xu, X., Xiao, Z., & Tan, E.-K. (2011). The roles of amyloid precursor protein (APP) in neurogenesis: Implications to pathogenesis and therapy of Alzheimer disease. Cell Adhesion & Migration, 5(4), 280–292. https://doi.org/10.4161/cam.5.4.16986

242. Zhu, Y., Feng, F., Hu, G., Wang, Y., Yu, Y., Zhu, Y., Xu, W., Cai, X., Sun, Z., Han, W., Ye, R., Qu, D., Ding, Q., Huang, X., Chen, H., Xu, W., Xie, Y., Cai, Q., Yuan, Z., & Zhang, R. (2021). A genome-wide CRISPR screen identifies host factors that regulate SARS-CoV-2 entry. Nature Communications, 12(1), 961. https://doi.org/10.1038/s41467-021-21213-4

243. Zivanov, J., Nakane, T., Forsberg, B. O., Kimanius, D., Hagen, W. J., Lindahl, E., & Scheres, S. H. (2018). New tools for automated high-resolution cryo-EM structure determination in RELION-3. eLife, 7, e42166. https://doi.org/10.7554/eLife.42166